

# ASYMMETRY IN NEURAL RESPONSES TO INTERAURALLY TIME-DELAYED STIMULI

---

John Paul Agapiou

PhD Neuroscience

University College London

2007

UMI Number: U592566

All rights reserved

INFORMATION TO ALL USERS

The quality of this reproduction is dependent upon the quality of the copy submitted.

In the unlikely event that the author did not send a complete manuscript and there are missing pages, these will be noted. Also, if material had to be removed, a note will indicate the deletion.



UMI U592566

Published by ProQuest LLC 2013. Copyright in the Dissertation held by the Author.  
Microform Edition © ProQuest LLC.

All rights reserved. This work is protected against  
unauthorized copying under Title 17, United States Code.



ProQuest LLC  
789 East Eisenhower Parkway  
P.O. Box 1346  
Ann Arbor, MI 48106-1346

# ACKNOWLEDGEMENTS

---

I would like to thank my supervisor, Prof David McAlpine, for his infectious confidence and enthusiasm. His door was always open and my ideas were never floccinaucinihilipilificated. He helped improve both my critical and presentation skills, and encouraged me to travel and visit other laboratories. His concern for a convivial yet dialectic atmosphere has made the McAlpine lab a fun and vibrant group to join.

I would like to thank several other individuals for their assistance on this project. Dr Susan Boehnke for providing some of the early data in DNLL. Dr Jennifer Read for a pertinent discussion about binocular disparity tuning that helped put me in the right direction. Torsten Marquardt for several interesting and helpful discussions on a variety of topics. Prof John Rinzel and his lab for hosting an educational and enjoyable three-month visit to NYU. I would also like to thank the Wellcome PhD program committee for their support and advice.

I feel very privileged to have received financial support to pursue my education. This work has been supported by a generous studentship from the Wellcome Trust, who must receive particular thanks. My three-month stay at NYU was funded by both a Charlotte and Yule Bogue scholarship and a contribution from Prof John Rinzel. I also received a Dale and Rushton award from the Physiological Society that allowed me to attend the EU Advanced Course in Computational Neuroscience in 2003.

I would also like to thank several people for general emotional support during my PhD. The McAlpine lab and other colleagues who made working at UCL enjoyable, and my friends outside of work, without whom life would be significantly more boring. Apologies to all those who often came a poor second to this work.

Finally, my love and deepest gratitude to my parents, Anne and Mike, and my grandparents, Fred and Nina, for a lifetime's investment in my education, and for supporting my return to the homestead with grace.

# ABSTRACT

---

The interaural time difference (ITD) between sounds at the two ears is an important cue in low-frequency sound localisation. Sensitivity to ITD is created in the medial superior olive (MSO), where neurons show an ITD-dependent response tuned to some preferred ITD. The traditional model of ITD sensitivity suggests that this *best ITD* arises from a difference in the length of projections from the two ears to the MSO. However, recent experiments in gerbil MSO instead indicate that glycinergic inhibitory mechanisms are responsible for establishing a neuron's best ITD.

This study examined the role of mechanisms thought to underlie the establishment of the best ITD and their effects on shape of ITD tuning curves. The predictions of models of these mechanisms were then compared to responses to both pure-tone and broadband noise stimuli, recorded from binaural nuclei in the midbrain. Asymmetrical responses were observed, indicating some frequency-dependence in the mechanisms determining best delay. In addition, an envelope-sensitive component to the noise responses was observed at lower frequencies than previously reported.

While the observed asymmetry was qualitatively consistent with the effect of carving inhibition, the traditional model of ITD sensitivity could not be distinguished from other mechanisms capable of introducing frequency-dependent delays. However, this study shows that mechanisms usually considered only to affect the best ITD, can have profound effects on ITD tuning curve shape. These effects can have a strong impact on the functional encoding of ITDs beyond the establishment of the best ITD.

# CONTENTS

---

<b>1</b>	<b>INTRODUCTION</b>	<b>6</b>
1.1	Sound localisation	6
1.2	The Jeffress model	7
1.3	The neural origin of ITD sensitivity	8
1.4	Summary	17
<b>2</b>	<b>METHODS</b>	<b>18</b>
2.1	Surgical procedure	18
2.2	Experimental apparatus	19
2.3	Recording procedure	20
2.4	Stimuli	22
<b>3</b>	<b>ASYMMETRY IN RESPONSES TO PURE-TONE STIMULI</b>	<b>25</b>
3.1	Introduction	25
3.2	Modelling the effect of inhibition	27
3.3	Results	38
3.4	Discussion	48
<b>4</b>	<b>ASYMMETRY IN RESPONSES TO NOISE STIMULI</b>	<b>54</b>
4.1	Introduction	54
4.2	The distribution of best ITD	55
4.3	The Gabor model	57
4.4	Envelope asymmetry	63
4.5	Discussion	71
<b>5</b>	<b>THE ORIGIN OF ASYMMETRIES</b>	<b>73</b>
5.1	Introduction	73
5.2	Correlation-dependent nonlinearities	73
5.3	Envelope sensitivity	77

5.4	Discussion	81
<b>6</b>	<b>COMPONENTS OF DUAL-DELAY FUNCTIONS</b>	<b>85</b>
6.1	Introduction	85
6.2	The relative contribution of components	85
6.3	Components of DNLL dual-delay functions	87
6.4	Components of IC dual-delay functions	101
6.5	Discussion	112
<b>7</b>	<b>DISCUSSION</b>	<b>118</b>
7.1	Summary	118
7.2	Differences between IC and DNLL	119
7.3	Relationship to binocular disparity tuning curves	120
7.4	Functional consequences	121
7.5	Future work	124
7.6	Final Words	125
<b>8</b>	<b>MATHEMATICAL APPENDIX</b>	<b>126</b>
8.1	The Gabor model	126
8.2	Phase delayed narrowband signals	127
8.3	Measuring the equivalence contour	128
8.4	Creating envelope sensitivity	128
8.5	Responses to envelope-sensitive inputs	129
	<b>BIBLIOGRAPHY</b>	<b>133</b>

# 1

## INTRODUCTION

---

The theory of sound localisation based on interaural time differences (ITDs) is founded on a central theory (the *Jeffress model*, Jeffress 1948) that has remained unchallenged for over 50 years. However, recent work in the field has highlighted key failings of the Jeffress model, leading to the emergence of a new model of ITD sensitivity. This thesis address the extent to which this new model is a departure from the Jeffress model and the extent to which it constitutes a reshaping of the original theory, with new mechanisms fulfilling the same functional roles.

### 1.1 Sound localisation

Unlike vision, the sensory epithelium of the auditory system does not provide an explicit representation of spatial location. Rather, the spatial position of sounds must be reconstructed from various binaural and monaural cues. Monaurally, some sense of the front/back and elevational position of sources can be determined from the position of spectral notches that arise from the directional filtering of the external ear (the pinna). However, to obtain a more precise idea of the azimuthal position of a sound, it is necessary to combine information from both ears.

The spatial separation of the two ears ensures that a sound source will usually be closer to one ear than to the other. Since the head is acoustically opaque, sound must diffract around the head in order to reach the more distant ear. Thus, sound arriving at the more distant ear will arrive delayed and attenuated relative to the sound arriving at the closer ear, producing both an interaural time difference (ITD) and an interaural level difference (ILD) between the stimuli. Although both these cues provide information about the spatial location of a source, in practice human, and many animal listeners, preferentially use ITDs for low-frequency sounds below 1.5 kHz, and ILDs for high-frequency sounds above 1.5 kHz (Rayleigh 1907). This arises because low-frequency sounds can easily diffract around the head, producing ILDs of only a few decibels, while for high-frequency sounds the head produces a more effective acoustic shadow, leading to ILDs of the order of tens of decibels.

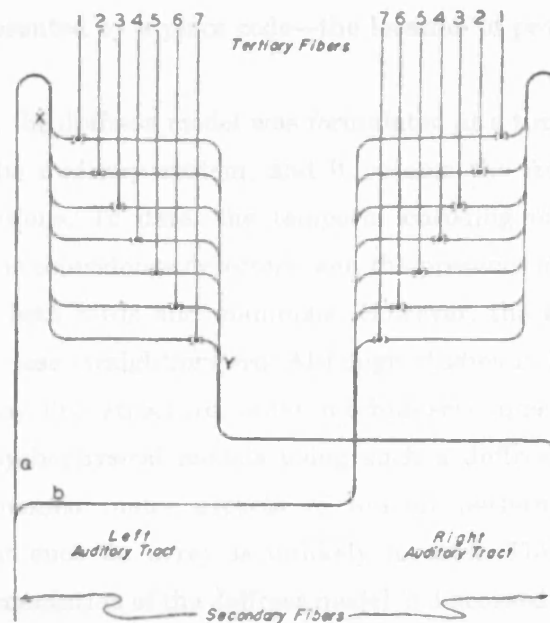


**Figure 1.1 The Jeffress model.**

Incoming sounds are encoded into a train of action potentials that are transmitted to an array of coincidence detector neurons (black dots) through a network of delay lines ("secondary fibers"). The difference in axonal path lengths leading to different neurons introduces an internal interaural delay. Only the neuron for which the internal delay is equal and opposite to the external ITD at the ears will fire, allowing the ITD to be read out from the array. (Figure from Jeffress 1948).

ILD is therefore a more effective cue at high frequencies while ITD is more effective at low frequencies.

## 1.2 The Jeffress model

For over 50 years, the working model of low-frequency sound localisation has been the Jeffress model (Jeffress 1948). In this model (Figure 1.1), the temporal structures of the sounds received at the two ears are encoded as trains of action potentials in *secondary fibres*. These secondary fibres form a network of delay lines projecting to an array of coincidence detector neurons, which fire when action potentials from the two sides arrive synchronously. The hypothesised delay line structure is such that there are differences in propagation time for ipsilateral and contralateral inputs, resulting in an *internal ITD* determined by the position of the coincidence detector in the array. For any given azimuthal position, only the neuron whose internal delay compensates for the ITD will fire, allowing the ITD to be read out from the array. Thus, the model can therefore be broken down into four fundamental concepts:

1. The temporal structure of sound is preserved in the firing patterns of the early stages of the auditory system.
2. There exist binaural coincidence detector neurons, sensitive to the interaural timing of sounds.
3. The input to these neurons is subjected to an internal delay, which arises from a systematic network of delay lines.

4. The ITD is represented by a place code—the location of peak activity in an array of detectors.

Simple and elegant, the Jeffress model was formulated at a time when little was known of the physiology of the auditory system, and it became the framework for subsequent physiological investigations. To date, the temporal encoding of sound, the capacity of certain neurons to act as coincidence detectors, and the presence of internal delays have all been demonstrated in both birds and mammals. However, the evidence regarding other aspects of the model is less straightforward. Although studies in birds have demonstrated the existence of a delay line structure, other mechanisms appear to be at work in the mammal. Although psychophysical models using such a Jeffress-like array of detectors have successfully explained many aspects of human performance, the physiological evidence indicates that such an array is unlikely to exist. This evidence both for and against a neural implementation of the Jeffress model is discussed in the next section.

### 1.3 The neural origin of ITD sensitivity

Although Jeffress initially rejected the idea (Jeffress 1948), the weight of evidence over the last 50 years suggests that principal neurons in the medial superior olive (MSO, a nucleus in the brainstem) fulfil the role of the binaural coincidence detector neurons suggested by the Jeffress model. However, before discussing the physiology and response properties of these neurons that lead to this conclusion, it is important to have some understanding of the anatomy of the brainstem and the properties of its inputs.

The MSO is composed of two morphologically and physiologically distinct cell types: principal neurons, which act as coincidence detectors, and nonprincipal neurons. The principal neurons form a thin, parasagittally oriented, planar structure just a few neurons thick in the mediolateral direction. They are bipolar, with contralateral excitatory inputs innervating their medial dendrites and ipsilateral excitatory inputs innervating their lateral dendrites (Figure 1.2). They are also innervated by somatic inhibitory inputs, which will be discussed later.

Inputs to the MSO originate in the anterior ventral cochlear nuclei (AVCN). The AVCN consists of two groups of neurons, spherical bushy cells (SBCs) and globular bushy cells (GBCs). Both these groups of neurons show temporally precise and highly reproducible patterns of firing in response to pure-tone stimulation. This property is largely inherited from their inputs (auditory nerve fibres), but is often more temporally precise.

Auditory nerve (AN) fibres originate in the cochlea and receive input directly from inner hair cells. The firing rate of these fibres shows a bandpass dependency on sound-frequency that is a consequence of the mechanics of the basal membrane. The frequency at which a response can be evoked at the lowest sound level is known as the fibre's *characteristic frequency* (CF); fibres originating from more apical turns of the cochlea show lower CFs than those originating from more basal turns. This tonotopic organisation is preserved in afferent areas all the way up to auditory cortex, producing separate pathways for the

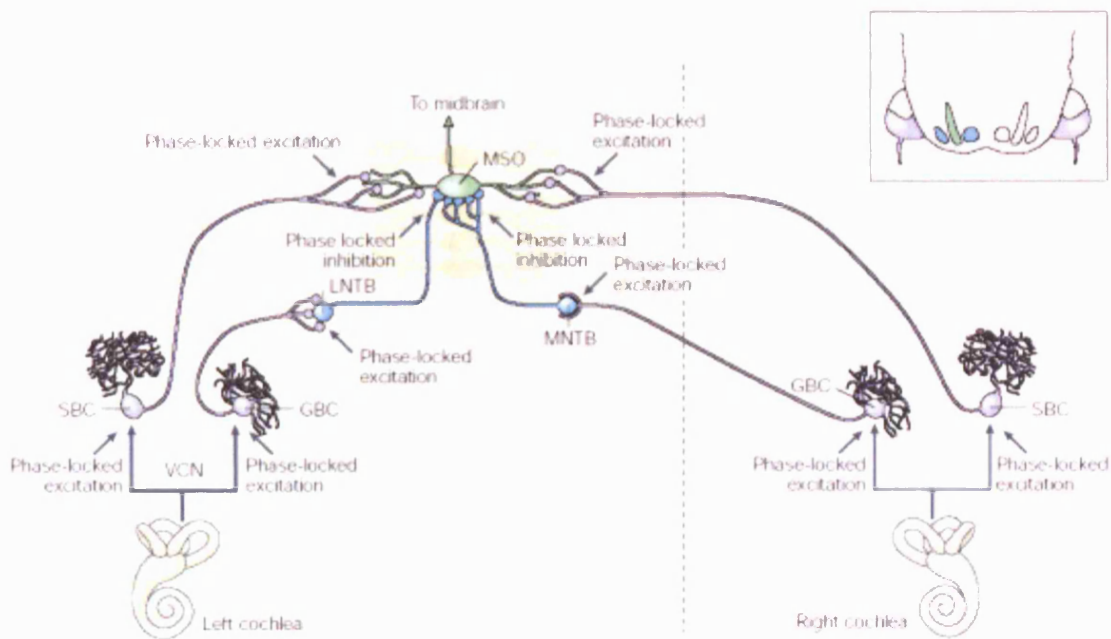


**Figure 1.2** The ITD pathway in the mammalian brainstem.

Incoming sounds are filtered by the cochlea and encoded into a train of action potentials within the auditory nerve, which then innervates the cochlear nucleus. Bipolar principal neurons in the medial superior olive (MSO), thought to act as binaural coincidence detectors, receive spatially segregated excitatory input from the ipsilateral and contralateral SBCs. In addition, these neurons also receive bilateral somatic inhibition from the ipsilateral lateral nucleus of the trapezoid body (LNTB) and the contralateral medial nucleus of the trapezoid body (MNTB). Both these nuclei receive inputs from globular bushy cells (GBCs) in the VCN through large calyceal synapses and show temporally precise patterns of firing. **Inset**, the location of the nuclei in the brain stem (coronal slice): mauve, the auditory nerve and cochlea; blue, trapezoid body nuclei; green, medial superior olive. (Figure from Grothe 2003).

processing of different frequencies. Figure 1.2 can therefore be thought of as showing the ITD pathway for only one narrow-range of sound frequencies.

### 1.3.1 The temporal coding of sound

Much of the work on characterising the temporal properties of the auditory periphery was performed with pure-tone stimuli (Johnson 1980, Joris et al. 1994a, Joris et al. 1994b). Raster plots of auditory nerve responses to pure-tone stimuli (see Figure 1.3c) show a highly regular pattern of firing, with spikes tending to occur at a particular phase of the stimulus. The precision of this *phase locking* can be measured using the vector-strength statistic (Mardia & Jupp 2000), which is zero when the spike times are independent of the phase of the stimulus and one when spikes only occur at a fixed phase. For very low-frequency stimuli, the jitter in spike timing is low relative to the period of the stimulus and so the vector strength is high. However, as the frequency of stimulation increases and the jitter becomes larger relative to the period of stimulation, the phase locking deteriorates. Thus, the stochastic nature of the fibre is an inherent limit to the precision of phase locking. Even so, auditory nerve fibres are highly precise; in the cat, they can show vector strengths of 0.85 at frequencies as high as 1 kHz (Johnson 1980).

An arguably more significant contribution to the limit of phase locking comes from the inability of inner hair cells to follow high-frequency tones (due to their membrane capacitance) which produces a dramatic decrease in vector-strength at higher frequencies.

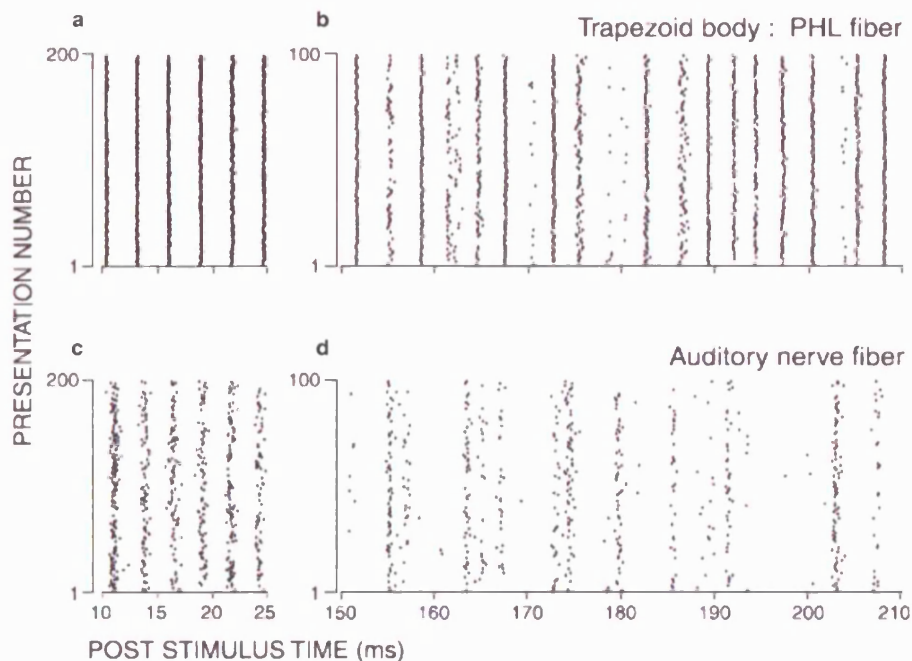


**Figure 1.3** Dot rasters of responses of neurons in the peripheral auditory system of the cat.

Responses to pure tone (a, c) and broadband noise (b, d) stimuli for a trapezoid body fibre originating in the AVCN (top) and an auditory nerve fibre (bottom). CF, threshold and spontaneous rate were 350 Hz, 23 dB<sub>SPL</sub>, and 90 sp s<sup>-1</sup> (top) and 379 Hz, 39 dB<sub>SPL</sub>, and 57 sp s<sup>-1</sup> (bottom). Sound levels (dB<sub>SPL</sub>) were: a, 40; b, 60; c, 60; d, 80. Note that the firing times are regular and highly reproducible, especially in the trapezoid body fibre. (Figure from Louage et al. 2004).

However, if high-frequency tones are amplitude modulated (AM), inner hair cells can follow the envelope of such stimuli. Thus, while high-CF auditory nerve fibres do not phase lock to high-frequency tones they show highly precise phase locking to the low-frequency envelopes of AM stimuli (Joris & Yin 1992).

Surprisingly, at the lowest stimulus frequencies, both spherical and globular bushy cells in the AVCN are even more temporally precise than the AN (Figure 1.3a). In the cat, neurons in the AVCN show vector strengths of over 0.9 for frequencies below 500 Hz, with the lowest frequencies reaching vector strengths as high as 0.98—much higher than the vector strengths observed in the auditory nerve (Joris et al. 1994a). Another difference is that the probability of evoking a spike on any given cycle of the stimulus (the *entrainment*) is vastly improved in AVCN. In the cat, the maximum entrainment is around one for frequencies below 600 Hz, with one spike occurring on every cycle of the stimulus. This means that the firing rate in these neurons is determined by sound-frequency, increasing up to an incredible 600 sp s<sup>-1</sup>. The entrainment in auditory nerve fibres is lower and decreases with increasing sound frequency, producing a constant firing rate of around 250 sp s<sup>-1</sup> (Joris et al. 1994a). This improvement in precision and firing probability is hypothesised to result from monaural coincidence detection across several auditory nerve fibre inputs to the AVCN neuron: highly correlated inputs dominate the firing of the neuron, causing rare high-jitter spikes and uncorrelated spontaneous spikes to be ignored (Joris et al. 1994a).

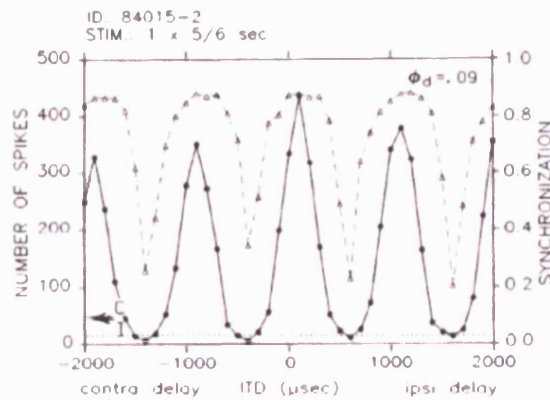


**Figure 1.4** Tone-delay function (solid line) recorded from cat MSO.

The number of coincidences varies as the stimuli move in and out of phase. Since the stimuli are periodic, the tuning curve is also periodic at the same frequency as the stimulating tone (1 kHz). Note that the firing rate can drop below the sum of the contralateral and ipsilateral monaural responses (arrows labelled C and I) indicating an inhibitory influence at these ITDs. The variation of the vector strength of phase locking to the stimulation frequency (triangles), and the spontaneous rate of the neuron (dotted line) are also shown. (Figure from Yin & Chan 1990).

It is clear, therefore, that bushy cells of the AVCN provide precise, reliable, and reproducible patterns of input to the MSO—a firm basis for the processing of interaural timing differences.

### 1.3.2 The medial superior olive

Very few *in vivo* recordings have been obtained from the MSO. Location of the nucleus is hampered by its thinness but, even when located, isolation of single neurons proves difficult. This has been suggested (Yin & Chan 1990) to be due to a low signal-to-noise ratio arising from a combination of strong evoked potentials that are highly correlated with the signal of interest, and a weak somatic contribution to the action potential (resulting in a weak extracellular signal). Recent *in vitro* recordings in the gerbil confirm that the action potential recorded at the soma is weak (10 mV amplitude), suggesting that the site of action potential initiation is axonally located and that back-propagation to the soma is strongly attenuated (Scott et al. 2005). However, existing *in vivo* recordings do offer convincing evidence of the role of these neurons as the Jeffress binaural coincidence detectors.

The *tone-delay function* is a tuning curve recorded by plotting a neuron's firing rate as a function of the interaural time difference (ITD)<sup>1,2</sup> of a binaurally presented pure-tone stimulus. Figure 1.4 shows a tone-delay function for a low-frequency neuron recorded in MSO. As explained in the previous section, the monaural input in response to such a stimulus is a train of action potentials with ISIs distributed around multiples of the period of the stimulus. As the stimuli at each ear move in and out of phase with each other, the chance of two spikes being close enough to be considered coincident varies. Tone-delay functions recorded in MSO reflect this variation in correlation between input spike trains, suggesting that they do indeed act as coincidence detectors. Since the response will be maximal when ipsilateral and contralateral inputs arrive synchronously, any shift in this

<sup>1</sup> Also referred to as the *interaural phase difference* (IPD) when pure-tone stimuli are used.

<sup>2</sup> By convention, positive delays denote a contralateral lead and an ipsilateral lag.

*best ITD*<sup>3</sup> away from zero indicates that an external ITD is required to compensate for an internal delay and bring the inputs into register. Experiments in the dog (Goldberg & Brown 1969), kangaroo rat (Moushegian et al. 1975, Crow et al. 1978), cat (Yin & Chan 1990), rabbit (Batra et al. 1997) and Mongolian gerbil (Spitzer & Semple 1995, Brand et al. 2002) all show a deviation of best ITD away from zero, supporting the existence of internal delays as suggested by Jeffress. Furthermore, as expected, the best ITD can be predicted from the difference between the phases of phase locking under monaural stimulation (Goldberg & Brown 1969, Yin & Chan 1990). The response of MSO neurons to noise and a wealth of data recorded in neurons afferent to the MSO are also consistent with the coincidence detector interpretation.

The ability of principal neurons in the MSO to act as coincidence detectors is a consequence of a low-threshold voltage-activated potassium-current ( $I_{K(LVA)}$ ), which reduces the time-window during which the neurons can integrate their inputs (Smith 1995, Scott et al. 2005). The role of this potassium current in improving coincidence detection has been the subject of several theoretical and experimental studies (Rothman et al. 1993, Rothman & Manis 2003c, Svirskis et al. 2004, Slee et al. 2005). Passively, the increased tonic conductance at rest lowers the membrane time constant of the neuron, producing much briefer excitatory postsynaptic potentials (EPSP). This is enhanced by the active opening of the potassium-channels in response to depolarisation, which inhibits the excitatory input. In order for the neuron to spike, it must depolarise quickly—if the depolarisation is too slow, it will be inhibited by the potassium current and the neuron will be prevented from reaching threshold. Only if the rate of depolarisation is faster than the activation kinetics of the potassium channel can the neuron spike before the channels open. This has the consequence that two EPSPs have a much greater chance of evoking an action potential when they are coincident than when they are not.

### **1.3.3 The lateral superior olive**

In addition to the MSO, a second brainstem nucleus shows ITD-dependent variations in neuronal firing rates. The lateral superior olive (LSO) receives ipsilateral excitation via the ipsilateral AVCN and contralateral inhibition via the ipsilateral MNTB (which is driven by the contralateral AVCN). LSO neurons are sensitive to ILDs and are normally considered to form part of the ILD-processing pathway. However, at low frequencies, LSO neurons can be considered anti-coincidence detectors, with tuning curves that resemble an inverted version of those in MSO (Spitzer & Semple 1995, Batra et al. 1997, Tollin & Yin 2005)—synchronous activation of the inhibitory and excitatory inputs decreases the firing rate while antiphase activation of the inputs increases the firing rate. Neurons in LSO also show high expression of  $I_{K(LVA)}$  (Barnes-Davies et al. 2004) and it is likely that similar membrane properties to those of the MSO shape their response.

---

<sup>3</sup> Also referred to as *best IPD* when pure-tone stimuli are used.

### 1.3.4 Delay lines and inhibition

The strongest evidence for the existence of delay lines comes from studies in the bird. Horseradish peroxidase staining of the axon-fibre tracts from nucleus magnocellularis (NM, the avian homologue of the AVCN) reveals a delay-line like structure in the contralateral projections to the ipsilateral nucleus laminaris (NL, the homologue of MSO) for both chick (Young & Rubel 1983) and barn owl (Carr & Konishi 1990). Single NM neurons innervate both ipsilateral and contralateral neurons along the whole length of both NLs; while the ipsilateral projections show little systematic variation in path-length, the projection to the contralateral NL is shorter for more medial NL neurons than for more ventral NL neurons (the NL is oriented paracoronally). Furthermore, both *in vivo* recordings from NL in the barn owl (Carr & Konishi 1990), and *in vitro* recordings from NL in the chick (Overholt et al. 1992), show a systematic variation in the latencies of inputs along the length of NL consistent with the observed delay-line structure.

However, evidence from *in vivo* recordings in the gerbil MSO casts doubt upon the functional relevance of any such network of delay lines in mammals. Iontophoretic application of strychnine (a glycine receptor antagonist) during recording produces an ITD-dependent increase in firing rate. This has the consequence of shifting the ITD producing the peak firing rate to around 0  $\mu$ s (Brand et al. 2002), suggesting that any internal delay arises chiefly from the action of inhibitory inputs to the neuron and not from the axonal delay lines suggested by the Jeffress model. Anatomical evidence for a delay-line structure in the mammal is weak, with some level of rostrocaudal difference in path-length for some neurons in the cat MSO (Smith et al. 1993, Beckius et al. 1999). While some rostrocaudal variation in best ITD has been reported from tuning curves recorded from cat MSO (Yin & Chan 1990), the subsequent finding that the CF of a neuron and its best ITD are correlated (see next section) raises the possibility that this may be an artefact resulting from a difference in the sampling of CF along this axis. Given that fossil evidence shows the independent evolution of tympanic ears in the ancestors of frogs, birds and mammals (Clack 1997), it is not surprising that mammals and birds could have evolved different mechanisms for the establishment of internal delays.

The MSO receives inhibitory input from both the ipsilateral lateral nucleus of the trapezoid body (LNTB) and the ipsilateral medial nucleus of the trapezoid body (MNTB). The inhibition is binaural in origin since the LNTB receives input from the ipsilateral AVCN and the MNTB receives input from the contralateral AVCN (Grothe & Sanes 1993, Grothe & Sanes 1994; see Figure 1.2). Both nuclei have similar specialisations to those in the AVCN, with heavily myelinated axons and receiving large high-fidelity calyceal synapses. Low-CF neurons in both the LNTB and the MNTB show a phase-locked pattern of firing in response to tonal stimulation (Tsuchitani 1977, Smith et al. 1998), with the MNTB further improving phase-locking above the already impressive level shown by the AVCN (Kopp-Scheinflug et al. 2003). The inhibitory input to MSO is therefore likely to be phase-locked.

It was previously hypothesised that this inhibition may be *out-of-phase* (phase locked at a different phase to the excitatory inputs), due to the fact that minima in MSO tone-delay functions often fell below the level of the response to monaural stimulation (Goldberg & Brown 1969, Yin & Chan 1990; see Figure 1.4 for an example). However, this situation can also arise from excitatory inputs in antiphase producing larger low-threshold potassium currents than monaural stimulation alone (Reyes et al. 1996). That the inhibitory input in the mammal is out-of-phase has been demonstrated by intracellular recordings in the gerbil brain slice (Grothe & Sanes 1994). By stimulating incoming fibres both lateral and medial to MSO, both excitatory and inhibitory pathways are simultaneously activated, allowing an ITD between inputs to be simulated. Application of strychnine reveals a glycinergic inhibitory wake after both the ipsilateral and contralateral excitation; this wake is in part responsible for the observed out-of-phase inhibition. Despite possible differences in the relative timing of excitatory and inhibitory produced by electrical stimulation as opposed to acoustic stimulation, the time course of the spontaneous inhibitory postsynaptic currents (sIPSCs) is slower than that of spontaneous EPSC currents (Magnusson et al. 2005), suggesting that a glycinergic contribution to out-of-phase inhibition will inevitably exist.

Although it has previously been hypothesised that the inhibitory inputs might play a role in the determination of the tuning in MSO neurons (Batra et al. 1997), there is little direct evidence to support a mechanism by which they might do so. Tantalisingly, there is evidence from the gerbil that the distribution of glycine receptors is essential to this mechanism. Before hearing onset, glycine receptors are distributed over both the soma and the dendrites of the MSO neurons. However, shortly after hearing onset, there is a critical period during which the expression of glycine receptors is refined solely to the soma. If an animal is continually exposed to omnidirectional white noise during this critical period, this refinement of expression can be blocked (Kapfer et al. 2002). Juvenile animals, and noise-reared animals for whom this refinement is blocked, have longer IPSC time courses (Magnusson et al. 2005), and the tuning curves of neurons in the dorsal nucleus of the lateral lemniscus<sup>4</sup> (DNLL) of these animals have best ITDs around zero (Seidl & Grothe 2005). There is, therefore, strong evidence that the somatic segregation of the inhibitory inputs is necessary for the determination of the internal delays observed *in vivo*. However, the exact mechanism by which inhibition shifts the tuning curves is unknown.

### **1.3.5 The neural representation of ITD**

That ITD should be encoded by the peak-firing neuron (or group of neurons) with a particular internal delay does not intuitively appear to be an ideal code. Neurons in MSO are broadly tuned, and respond strongly to ITDs slightly off their best ITD (Figure 1.4). Thus, there will not be a single neuron firing in each frequency lamina while all others are silent (as suggested in the Jeffress model), but rather a distribution of firing rates across

---

<sup>4</sup> An area that receives direct excitatory input from the ipsilateral MSO and shows similar tuning curves. It is therefore used as a proxy through which to observe ITD sensitivity.

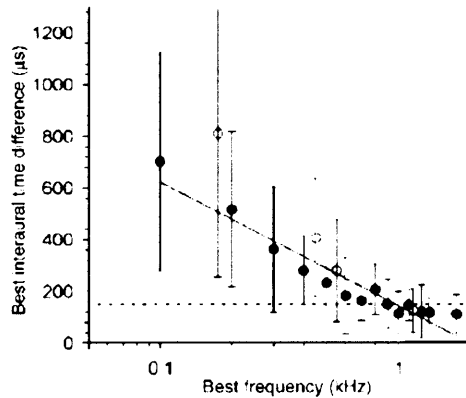


**Figure 1.5 Distribution of the magnitude of best ITD in guinea pig inferior colliculus.**

The best ITD was obtained using interaurally time-delayed broadband noise as a function of characteristic frequency. Both peak-type (filled circles) and trough-type neurons (empty circles) are shown. Note that lower-frequency neurons have larger best ITDs than high-frequency neurons, showing peaks outside the physiological range of ITDs ( $\pm 150 \mu\text{s}$ , dashed line). (Figure from McAlpine et al. 2001).

the whole array of coincidence detectors. The intrinsic noisiness of neural firing rates will therefore make it difficult to confidently identify the peak-firing neuron and thereby the ITD. A coarse estimate of the peak firing neuron would of course be possible, and could be improved by sacrificing a portion of the limited resources available. For example, taking more time to reach a decision, or pooling neurons with the same ITD would allow the intrinsic noise to be averaged out and the maximum firing neuron more accurately determined. However, limiting resources in this way would involve a trade-off: taking longer to decide may lower reaction time, while pooling neurons may lead to some ITDs being underrepresented or more coarsely resolved.

The strongest evidence against the local coding hypothesis of the Jeffress model is the scarcity of low-CF neurons tuned to low ITDs. Although it is reportedly difficult to record single-neuron responses in the MSO, recordings can easily be obtained from the inferior colliculus (IC), a nucleus that receives direct excitatory input from the ipsilateral MSO, and so is often used as a proxy. The internal delay of a neuron can be unambiguously determined from its tuning curve recorded in response to interaurally time-delayed broadband noise stimuli (the *noise-delay function*), since it shows only a single maximum at a single ITD. From a large number of such tuning curves recorded from guinea pig IC, McAlpine et al. found that the best ITD of a neuron (and therefore its internal delay) was correlated with the neuron's CF, such that the best ITD was around an eighth of the period of the neuron's CF ( $0.125 \text{ cyc re } CF^5$ , Figure 1.5, McAlpine et al. 2001). This finding has been replicated in the IC of the cat (Hancock & Delgutte 2004) and for the best ITDs of tone responses recorded at CF in the DNLL and MSO of the gerbil (Seidl & Grothe 2005, Siveke et al. 2006, Brand et al. 2002).

The range of ITDs experienced by an animal is constrained to a narrow *physiological range* that is dependent on head-width (gerbil,  $120 \mu\text{s}$ ; guinea pig,  $150 \mu\text{s}$ ; human,  $650 \mu\text{s}$ ); ITDs outside of this range are rarely experienced. A direct consequence of the CF

<sup>5</sup> Where 1 cyc re CF is an amount of time equivalent to the period of the characteristic frequency of the neuron. Thus for a neuron with a CF of 500 Hz, a range of 0.125 cyc re CF corresponds to  $250 \mu\text{s}$ .

dependence of the internal delay is that the lowest CF neurons are tuned to ITDs outside this physiological range. If the system were to use a place code as suggested by Jeffress, then such neurons outside the range would be largely useless. Instead, based on the observation that the steepest slopes of the tuning curves were distributed around zero, McAlpine et al. suggested a *balance model* of ITD sensitivity (McAlpine et al. 2001) where the ITD is represented by the relative firing rates of the ipsilateral MSO (coding contralateral space) and the contralateral MSO (coding ipsilateral space).

The accuracy with which recorded tuning curves can be used to encode stimuli can be addressed with signal detection theory (Green & Swets 1974). By examining the responses of a neuron to two stimuli with different ITDs, signal detection theory can be used to calculate the probability that an ideal observer could use the neuron to correctly discriminate these two ITDs. Repeating this for a range of ITDs around a reference ITD allows prediction of the *just noticeable difference* (JND)—the smallest change in ITD from the reference that can be correctly discriminated 75% of the time. This predicted JND can then be compared to the JNDs measured from psychophysical experiments. Using responses recorded from the IC of unanaesthetised rabbit, Fitzpatrick et al. tested the JNDs predicted by the Jeffress model (Fitzpatrick et al. 1997). In order to produce JNDs similar those exhibited by humans, it was necessary to estimate ITD using a pool of at least 40 neurons. It was important that these neurons were chosen so that they uniformly sampled the entire range of best ITDs; if chosen randomly, the dearth of low-best ITD neurons would have been expected to result in poor JNDs around zero ITD—the very range at which ITD acuity is greatest (Mossop & Culling 1998). Furthermore, the large pool size reduced the uncertainty introduced by the broad tuning-width of neurons discussed earlier. Thus, for a place-code similar to that suggested by Jeffress to produce low JNDs, it is necessary not only to average over a large number of neurons, but also to artificially choose them so as to undersample the neurons with high best ITDs.

Alternatively, it has been shown that similar JNDs can result from the tuning curves of single neurons when signal detection theory is applied directly to the difference in firing rate for two ITDs (Skottun 1998). This is a consequence of the fact that since the slopes of tuning curves pass through zero, a small change in ITD produces a large difference in firing rate. Applying this method to single-neuron responses to pure-tone stimuli predicts the decrease in JND with stimulus frequency observed in humans, and shows that the lowest JNDs predicted from single neurons (in guinea pig) are comparable with those psychophysically measured for humans (Skottun et al. 2001, Shackleton et al. 2003). This indicates that human performance can be explained by the acuity of single neurons, without the need for any pooling.

The maximally coding part of the tuning curve is not around best ITD, but rather where the gradient of the tuning curve is steep and the noise is low. The distribution of best ITD that results in the optimal representation (the one that, assuming an ideal observer, produces the lowest error in the estimated ITD) is therefore one that results in the

physiological range being tiled by the slopes of the functions. Where the physiological range is narrow relative to the period of the tone stimulus, the optimal distribution of best ITDs is formed by two discrete distributions at around  $\pm 0.125$  cyc re CF. At higher frequencies, where the physiological range is broad relative to the period of the stimulus, a uniform distribution of best ITDs is optimal (Harper & McAlpine 2004). Thus, the optimal distribution for any particular animal is dependent on the physiological range (i.e. the head-width of the animal) and the range of frequencies over which the animal is sensitive to ITDs (i.e. the upper limit on phase locking). Such a finding explains the apparent dichotomy between the bimodal distribution of best ITDs seen in the guinea pig (which can only phase-lock up to around 1 kHz) and the uniform distribution seen in the barn owl (which can phase-lock up to 10 kHz, Wagner et al. 2002).

## 1.4 Summary

The traditional model of ITD sensitivity was developed by Jeffress in 1948, and a large body of evidence supports the existence of the precise temporal coding of sound, and coincidence detectors sensitive to microsecond-scale timing-differences. However, in the last decade or so, doubts have arisen as to the origin of the internal delays observed in these neurons, and the way in which ITD is encoded by the distribution of these internal delays across the neural population. The emerging new model of ITD sensitivity uses inhibitory input to the MSO to set up two separate populations of neurons with best delays distributed roughly around  $\pm 0.125$  cyc re CF. Such an arrangement of best ITDs is determined in an experience-dependent manner, and is optimal for the commonly experienced range of ITDs. An important outstanding problem is to relate these findings by investigating the mechanism through which the inhibition determines the best delay, and how this might affect the coding of ITD.

# 2

## METHODS

---

### 2.1 Surgical procedure

Young-adult pigmented guinea pigs (*Cavia porcella*) with body masses ranging from 0.3 kg to 0.7 kg were anaesthetised with an intraperitoneal injection of urethane ( $1.0 \text{ g kg}^{-1}$  in 25% solution of NaCl; Sigma-Aldrich, Poole, UK), and analgesia was induced with a 0.1 ml intramuscular injection of Hypnorm ( $0.315 \text{ mg ml}^{-1}$  fentanyl citrate and  $10 \text{ mg ml}^{-1}$  fluanosine; Janssen–Cilag Ltd., High Wycombe, UK). Anaesthesia was monitored throughout the experiment via the withdrawal reflex, and was maintained with supplementary 0.1 ml doses of Hypnorm as required. Atropine sulphate (0.1 ml; Animalcare Ltd., York, UK) was administered subcutaneously to reduce fluid secretion. On completion of an experiment, animals were killed with 2 ml Pentoject (sodium pentobarbitone, Animalcare Ltd.).

Guinea pigs were shaved around the ears, top of head, and throat, and administered subcutaneous injections of lignocaine hydrochloride (2%, Martindale Pharmaceuticals, Romford, UK) in these areas. The ear canals were visualised by sectioning the tragi, and cleared of any debris. A tracheotomy was performed to maintain airway patency, and the animal was positioned in a stereotaxic apparatus, housed in a sound attenuating chamber (IAC, Winchester, UK). Custom-made ear bars allowed positioning of the animal within the restraint so that the tympanic membrane could be clearly visualised. A homoeothermic blanket was used to maintain body temperature at  $36 \text{ }^\circ\text{C}$  and a pump was available to provide respiration if required. The skull was levelled stereotaxically, and middle ear pressure was maintained throughout the experiment by ventilating the bullae through small cannulae that were sealed into the bullae with petroleum jelly. In some animals, the posterior fossa was vented to reduce brain pulsation.

A craniotomy above the location of the right IC or the right DNLL was performed, and the dura overlying the cortex removed. A warm 4% agar solution was placed over the craniotomy and allowed to cool. This reduced brain pulsing, and protected the cortical surface from desiccation. An electrode was stereotaxically positioned in the brain above the site of either the IC or the DNLL. Either glass-coated tungsten electrodes (manufactured

in-house) or parylene-coated tungsten electrodes (World Precision Instruments, Stevenage, UK) were used. A brass screw, positioned in the cortex, approximately 10 mm anterior and 5 mm contralateral to the recording site, was used as a ground reference.

## **2.2 Experimental apparatus**

### **2.2.1 Sound delivery and calibration**

Acoustic stimuli were delivered via the ear bars using Beyerdynamic DT48 audiological speaker transducers (Beyerdynamic, Burgess Hill, UK). Small audiological microphones (Knowles FG-series, Knowles Europe, Burgess Hill, UK) were connected to the ear bar channels, 1 mm to 2 mm from the tympanic membrane, by high impedance tubing. The impulse response of these microphones had been previously calibrated with respect to the output of the speakers using a high quality 1/8" microphone (Type 4138, Brüel and Kjær, Stevenage, UK), 1/2" preamplifier (Type 2669, Brüel and Kjær) and measurement amplifier (Type 2610, Brüel and Kjær). On completion of surgery, it was possible to check the transfer function of the system and thereby assess the quality of acoustic coupling. In all experiments, the gain of the transfer function was flat to within  $\pm 3$  dB over the frequency range 0.05 to 2 kHz. No significant interaural phase or level differences arising from the different transfer functions were observed at any of the frequencies presented in this study.

Sound signal construction was originally performed on TDT System 2 hardware (Tucker-Davis Technologies, Alachua, FL, USA), and stimulus generation, stimulus presentation, and data collection was performed using software written by Trevor Shackleton (MRC-IHR, Nottingham, UK). Later experiments were performed using TDT System 3 hardware (Tucker-Davis Technologies), stimulus presentation and data collection were controlled by the Brainware program (Jan Schnupp, University of Oxford, UK). Stimulus generation was performed using Matlab (The Mathworks, Cambridge, UK), via a Brainware interface programmed in Delphi (Borland, Twyford, UK) by the author. Under both systems, all stimuli were generated digitally and loaded onto a digital to analogue converter (DAC). Stimuli were output at the maximum possible gain of the DAC and digitally controlled analogue attenuators were used to set the sound intensity to that required. All stimuli were checked in both the spectral and temporal domains before experimentation using a SR780 spectrum analyser (Stanford Research Systems, Sunnyvale, CA). Stimulus presentation and data collection were synchronously triggered via a TTL pulse from the controller computer.

### **2.2.2 Neural recordings**

All recorded signals were preamplified using a Medusa preamp and RA16 base station (Tucker-Davis Technologies) which 16 bit quantised the signal at a 25 kHz sampling rate. Signals were then filtered and monitored both aurally (over a speaker) and visually (on an oscilloscope). In experiments conducted using the System 2 setup, signals were digitally

highpass filtered at 300 Hz and lowpass filtered at 10 kHz (on the RA16). Filters were implemented using second-order Butterworth filters with 3 dB bandwidths of 10 Hz. An analogue filter (PC1, Tucker-Davies Technologies) was then used to highpass filter at 4.5 kHz. In experiments conducted using the System 3 setup, all filtering was performed on the RA16; spike trains were highpass filtered at 300 Hz and lowpass filtered at 6 kHz.

## 2.3 Recording procedure

### 2.3.1 Isolating single neurons

Auditory areas were easily identified by presenting repeated search stimuli while advancing the electrode through the brain. Two search stimuli were used: either a pure tone (50 ms duration), or a broadband noise stimulus (50 ms duration, 0.05 to 50 kHz bandwidth). Both were presented diotically. Brain regions sensitive to the search stimulus could be detected from the sound of evoked potentials locked in to the presentation period of the search stimulus. Varying the frequency of a search tone allowed the characteristic frequency of the area to be determined, and the electrode was advanced slowly until single neurons could be isolated. For the System 2 setup, putative action potentials were recorded when the first derivative of the recorded voltage trace passed a specified trigger level. For the System 3 setup, putative action potentials were isolated in Brainware based on a template match to the voltage waveform, defined by a negative threshold crossing, a positive threshold crossing, and the time between the negative threshold crossing and the peak of the waveform. All putative action potentials were isolated from the voltage trace and displayed on a separate oscilloscope, in order to allow confirmation of the presence (or absence) of a single-neuron, based on the spike-shape. As a further precaution, the presence of a refractory period was verified from autocorrelograms of recorded spike trains. Isolated action potentials were monitored throughout the recording; whenever the signal-to-noise ratio did not enable clear discrimination of single neurons, the recording was abandoned.

### 2.3.2 Characterising auditory neurons

The *characteristic frequency* (CF) of a neuron was defined as the frequency of the pure-tone stimulus at the lowest sound level able to produce a detectable (audio-visual) change in discharge rate above spontaneous levels. The *threshold* of the neuron was defined as this minimum sound level. A *response-area plot* (RSP) was then recorded for the neuron by recording the firing rate of the neuron in response to a series of diotically presented tone bursts (50 ms duration) that covered a range of frequencies and sound levels. Tone bursts ranged from 4 octaves below CF to 2 octaves above CF with 4 tones per octave frequency sampling, and sound levels covering the range 10 to 100 dB<sub>SPL</sub> in 5 dB<sub>SPL</sub> steps. A typical response area for an IC neuron can be seen in Figure 2.1. The response of the neuron to ipsilateral, contralateral and diotic tone bursts at CF (50 ms duration, 150 repetitions, 20 dB above threshold) was also recorded. The latency of the neuron could then be

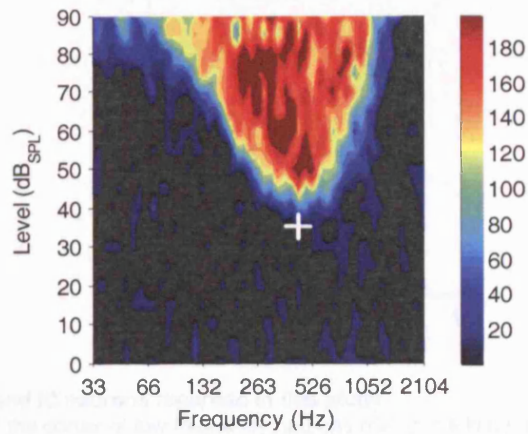


**Figure 2.1** Example of a response area plot from a neuron in IC. Colour indicates firing rate (in  $\text{sp s}^{-1}$ ). The CF (442 Hz) and threshold (35  $\text{dB}_{\text{SPL}}$ ) are indicated by a white cross.

determined as the shortest time it took for the neuron to respond to these stimuli, and the strength of phase locking of the neuron to CF could be determined for all three cases. Finally, the response to a binaural beat stimulus was recorded by presenting a tone at CF to the ipsilateral (to the recording site) ear, and a tone burst 1 Hz above CF to the contralateral ear (3 s duration, 10 repetitions, 20 dB above threshold). This was equivalent to modulating the interaural phase of a CF tone at a rate of 1 Hz. If the recorded response did not appear to be ITD sensitive, the recording was abandoned. All spike isolation and characterisation of neurons was performed using the System 2 setup.

### 2.3.3 Stereotaxic and physiological identification of nuclei

Since the central nucleus of the inferior colliculus is large and unambiguous, precise stereotaxic measurements were not always necessary; however, for twelve animals, careful stereotaxic coordinates were recorded in order to allow comparison with other nuclei. Low-frequency neurons ( $\text{CF} \leq 1.5 \text{ kHz}$ ) in the IC were found at a mean location  $2.5 \pm 0.05 \text{ mm}$  ( $\pm \text{SEM}$ ) lateral and  $0.2 \pm 0.08 \text{ mm}$  rostral of bregma. Neurons were found at a range of depths from 1.8 to 3.8 mm ( $2.7 \pm 0.11 \text{ mm}$ ), relative to a point 8 mm below a calibration point attached to the ear-bars (approximately the level of the surface of the cortex). Low-frequency neurons in the DNLL were recorded from nine animals, at a mean location  $3.1 \pm 0.04 \text{ mm}$  lateral of bregma, and  $0.1 \pm 0.06 \text{ mm}$  rostral of bregma, at a range of depths from around 4.1 to 7.1 mm ( $5.3 \pm 0.13 \text{ mm}$ , interquartile range). The wide range of neuronal depths was most likely a consequence of developmental variations in head size, since the mean depth of DNLL neurons in each animal was strongly correlated with body mass ( $r = 0.87$ ,  $P \leq 0.001$ , Pearson's correlation coefficient), with the DNLL located more ventrally for larger animals. No such correlation was observed for IC ( $P = 0.88$ , Pearson's correlation coefficient). The body masses of the animals used in the DNLL study varied from 0.27 kg to 0.53 kg (median 0.34 kg), while the body mass of the animals in the IC study varied from 0.32 kg to 0.75 kg (median 0.49 kg). Consequently, the apparent

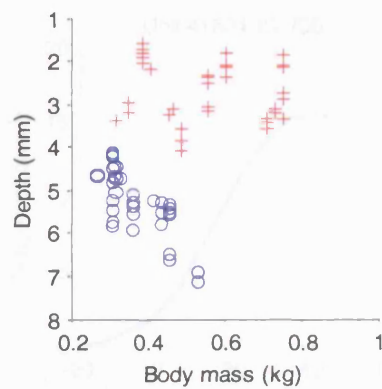


**Figure 2.2 Depth of DNLN and IC neurons recorded in this study**

The depth below the surface of the cortex of low-frequency neurons ( $CF \leq 1.5$  kHz) recorded from the IC (red crosses) and the DNLN (blue circles), as a function of the body mass of the animal. Note that while, the depth of the IC is relatively independent of body mass, the DNLN was located increasingly ventrally as the animal developed.

dorsoventral proximity of the two nuclei was likely to be a consequence of the differing range of head sizes in the two groups (Figure 2.2).

The dorsal approach used in this study made it possible to observe the tonotopic gradient in IC using pure-tone search stimuli. Both the CF of single neurons and the frequency to which the evoked potentials in IC showed the greatest response increased towards higher frequencies at deeper levels. The transition out of the IC and into the lateral lemniscus could be identified from the absence of any action potentials and the increased strength of the evoked potentials. The frequency to which the evoked potentials showed the strongest response was initially high, decreasing ventrally towards the low-frequency area of DNLN, and increasing again below the level of the DNLN. On most penetrations, the lemniscus was interrupted by a large non-auditory area. The DNLN was observed to be distinct from other nuclei, with large, triphasic action potentials, which were easily isolated from the background evoked activity of the lemniscus.

The location of the nucleus determined in this study corresponds to an area that has previously been histologically verified to be the DNLN (Dr SE Boehnke and Prof D McAlpine, unpublished data). In terms of their response properties, DNLN neurons showed shorter latencies, sharper phase locking, and narrower frequency tuning curves in response to pure-tone stimulation than neurons in IC with comparable CFs. Neurons in the VNLL were easily distinguished from those in the DNLN by their high threshold and preference for broadband stimuli. Thus, in terms of both anatomical location and physiological properties, the DNLN could be easily distinguished from other nuclei with a high level of confidence.

## 2.4 Stimuli

### 2.4.1 Tone-delay functions

Tone-delay functions were generated (using the System 2 setup) by varying the interaural phase difference between binaurally presented pure-tone stimuli. Stimuli were presented at

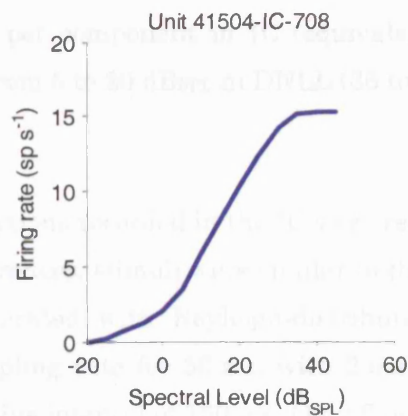


**Figure 2.3** A rate-intensity function obtained from IC using uncorrelated noise stimuli. The threshold of this neuron to pure-tone stimulation at its CF (708 Hz) was 30 dB<sub>SPL</sub>. Responses could be evoked at lower spectral levels because of the broader range of spectral content of the noise stimulus. Noise stimuli for this neuron were presented at a spectral level of 15 dB<sub>SPL</sub> in order to obtain the most linear response.

100 kHz sampling rate, and were 50 ms long, with 2 ms ramped-cosine onsets/offsets, and a minimum inter-stimulus interval of 150 ms. Tone bursts were presented at characteristic frequency and at a level 20 dB above threshold. The IPD was varied between  $\pm 1.5$  cyc and the resultant firing rate on each presentation recorded. The complete set of IPDs was repeated 10 times, in a different pseudorandom order on each repeat.

#### 2.4.2 Noise-delay functions

##### System 3

The majority of noise-delay functions presented in this thesis were generated using the System 3 setup. Noise bursts of 300 ms duration were generated digitally at a sampling rate of 50 kHz via the inverse Fourier transform. The power spectrum of each noise burst was flat, covering a frequency range from 50 Hz to 5 kHz, while the phase spectrum was pseudorandomly distributed from a uniform circular distribution. Stimuli were gated with a 5 ms ramped-cosine window before presentation. Windows were triggered synchronously to ensure that there were no onset time differences between ipsilateral and contralateral stimuli. For each presentation, a new sample of noise was generated and presented ipsilaterally (the right ear). The contralateral (left ear) stimulus was formed by time delaying the ipsilateral noise stimulus for a range of ITDs from  $-1.5$  to  $+1.5$  cyc re CF. The complete set of ITDs was repeated 10 times using a fresh sample of noise for each presentation, and in a different pseudorandom order on each repeat. The minimum inter-stimulus interval was 600 ms, although in practice it was much higher due to the computational overheads of stimulus generation.

The sound level at which the stimuli were presented was determined by binaurally presenting independent (and therefore uncorrelated) samples of the noise stimulus to different ears, and recording the firing rate obtained as the spectral level (the level of each component in the stimulus) was varied from  $-20$  to  $+50$  dB<sub>SPL</sub> (see Figure 2.3). Noise stimuli were presented in the middle of the dynamic range of this function. Spectral levels

ranged from 15 to 45 dB<sub>SPL</sub> per component in IC (equivalent to a stimulus intensity of around 45 to 75 dB<sub>SPL</sub>), and from 5 to 20 dB<sub>SPL</sub> in DNLL (35 to 50 dB<sub>SPL</sub>).

## *System 2*

Eleven of the noise-delay functions recorded in the IC were recorded using the old System 2 setup. With a few minor differences, stimuli were similar to those generated using System 3. The noise bursts were generated with Rayleigh-distributed power spectra, and were presented at a 100 kHz sampling rate for 50 ms, with 2 ms ramped-cosine onsets/offsets, and a minimum inter-stimulus interval of 150 ms. Only five independent samples of noise were pre-calculated for each recording, and each sample was repeated twice. No obvious difference was noticed between responses to the stimuli collected using the different setups.

### **2.4.3 Dual-delay functions**

The dual-delay function is an extension of the noise-delay function, originally used to investigate coincidence detection properties of the MSO (Yin et al. 1987). In this stimulus, in addition to all the underlying components in the noise burst being interaurally time delayed, they are also interaurally phase delayed. Thus, a family of noise-delay functions are obtained, one for each IPD.

Since the System 2 setup did not allow total control over the stimulus spectrum, stimuli were generated using the Matlab programming environment, and loaded into a buffer onboard the System 3 hardware, ready for triggering. Noise bursts were identical to those described in the previous section, except that the contralateral stimulus was formed from the ipsilateral noise stimulus by both time delaying the ipsilateral phase spectrum  $\theta_1(f)$  by  $\tau$  seconds and phase delaying it by  $\phi$  radians

$$\theta_c(f) = \theta_1(f) + 2\pi f\tau + \phi \quad (2.1)$$

This was performed for a range of ITDs from  $-1.5$  cyc re CF to  $+1.5$  cyc re CF in  $0.05$  cyc re CF steps and a range of IPDs from  $-0.375$  cyc to  $0.5$  cyc in  $0.125$  cyc steps. Each ITD/IPD pair was repeated 10 times using a fresh sample of noise for each presentation. On each repeat, all presentations of each ITD/IPD pair were randomly interleaved, to control for any effect of neural adaptation. The level of the stimulus was determined from the response of the neuron to uncorrelated noise as discussed in the previous section.

# 3

## ASYMMETRY IN RESPONSES TO PURE-TONE STIMULI

---

### 3.1 Introduction

Given the widespread use of the Jeffress model in the psychophysical literature, it is tempting to assume that the effect of inhibition in the MSO is to set up a Jeffress delay-line system under some degree of plastic control—a time delay tuned during development to the distribution of ITDs in the environment. However, it has been previously suggested that the delay introduced by the effect of inhibition cannot be described as a pure time delay, but rather is dependent upon the frequency of stimulation. The purpose of this chapter is to examine how inhibition might influence the shape of responses of neurons to interaurally delayed pure-tone stimuli.

#### 3.1.1 Phase plots

As explained in the Introduction (Section 1.3.2), the internal delay can be determined from the *best IPD* (the IPD at which the neuron fires maximally), and is most robustly estimated using the Fourier transform of the response. A *phase plot* is produced by repeating this procedure for the range of frequencies to which the neuron is sensitive, and plotting the best IPD against stimulation frequency. If the internal delay is a pure time delay then the best IPD will be given by the equation

$$\phi(f) = 2\pi f\tau_0 \quad (3.1)$$

where  $f$  is the stimulation frequency and  $\tau_0$  is a time delay referred to as the *characteristic delay* (CD). Thus, the Jeffress model predicts that the phase plot will be linear, and intercept both the x- and y-axes at the origin (Figure 3.1a).

However, such a plot is uncommon. The data are often better described by a model incorporating an additional phase delay known as the *characteristic phase* (CP), which produces a nonzero y-intercept (Figure 3.1b)

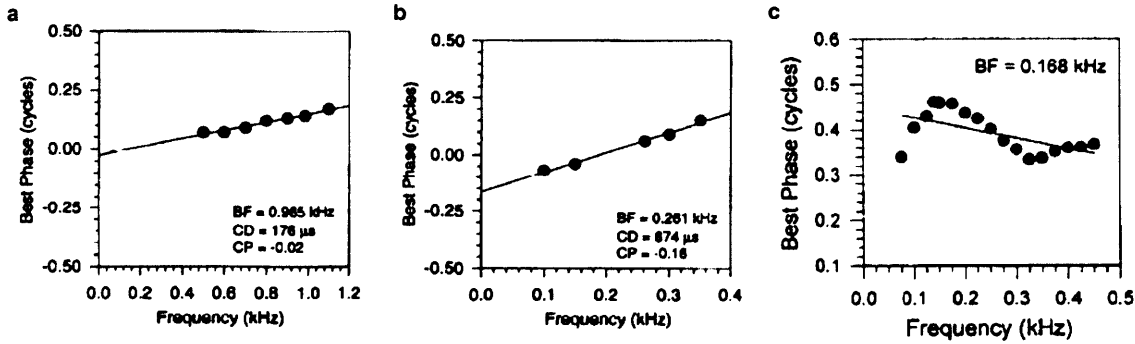


**Figure 3.1** Phase plots recorded from IC.

**a**, a linear phase plot produced by a pure time delay. Note that the regression line intercepts the y-axis around zero. **b**, a linear phase plot with a some phase component to the delay. Note the nonzero y-intercept. **c**, a nonlinear phase plot. (**a** and **b** from McAlpine et al. 1996, **c** from McAlpine et al. 1998).

$$\phi(f) = 2\pi f\tau_0 + \phi_0 \quad (3.2)$$

Neurons recorded from the LSO, for example, show CPs around 0.5 cyc because of their inverted tuning curve shape.

Still, some phase plots are not completely captured by this model, and are better described by a nonlinear dependency of the phase on the frequency of stimulation (Figure 3.1c). Forty percent of ITD sensitive neurons recorded from the superior olivary complex<sup>6</sup> (SOC) show significant deviation from linearity (Batra et al. 1997). In general, there is no typical phase plot in the SOC, the DNLL, or the IC; rather a mixture of linear and nonlinear relationships with a range of CPs (Batra et al. 1997, McAlpine et al. 1998, Kuwada et al. 2006).

### 3.1.2 Mechanisms producing phase delays

The characteristic phase and nonlinear phase plots are clearly deviations away from the pure time delays predicted to arise from axonal conductance delays in the Jeffress model. Batra et al. (Batra et al. 1997) hypothesised that this range of phase plots observed in the SOC was a consequence of the influence of inhibition in the MSO. They suggested that precisely timed inhibition in a fixed temporal relationship with the excitation could shift the best IPD away from that arising from the excitatory inputs alone. The temporal relationship between the inhibition and excitation was hypothesised to arise from a Jeffress-like axonal conductance delay (constant for all frequencies), with the consequence that the timing of the inhibitory input with respect to the phase of the excitatory input would vary as the frequency of stimulation changed. Because of this, a range of both linear and nonlinear phase plots could result. This effect of precisely timed inhibition has been suggested as a mechanism capable of explaining the observed effect of inhibition in the MSO (Grothe 2003). Grothe suggested that while excitatory inputs are identical with no internal delay between them, leading contralateral inhibitory input would *carve out* the leading edge of the contralateral excitatory inputs, effectively delaying the centroid and

<sup>6</sup> The superior olivary complex is a structure consisting of the medial superior olive, the lateral superior olive, and several periolivary nuclei.

introducing an internal delay. Thus if this *carving inhibition* were blocked with strychnine, the internal delay would disappear as observed *in vivo*.

However, alternative explanations for such phase plots also exist. Since sound takes a different amount of time to reach different tonotopic positions on the basilar membrane, then an internal delay will result from any interaural difference in this *group delay* that might be produced by inputs to MSO with mismatched CFs. Since the group delay imposed by the cochlea is frequency-dependent, this *stereausis* mechanism (Shamma et al. 1989) would be expected to yield nonlinear phase plots.

Another alternative is that nonlinear phase plots in the IC can be explained by the convergence of two delay-sensitive inputs on to the same neuron. By selectively suppressing one of two inputs, the area of the phase plot corresponding to the other input can become linear, albeit with some CP (McAlpine et al. 1998, Shackleton et al. 2000). Although this study says little about the phase plots observed in the MSO, it cautions against the use of the IC as a proxy when trying to understand MSO processing.

## 3.2 Modelling the effect of inhibition

Because of its coincidence-detecting properties, the ITD-dependent variation in the firing rate of an MSO neuron is often modelled as the cross-correlation of the cochlea-filtered input stimuli (Colburn 1973, Yin et al. 1987). However, such a model only considers the function of these neurons in terms of spike processing, and does not consider the contribution of sub-threshold synaptic events to spiking. Such a model is therefore inadequate when seeking to address what effect inhibitory inputs might have upon the spiking of a neuron. At the other extreme, a biophysical model exists that is capable of reproducing the carving effect of inhibition, producing contralaterally delayed tuning curves when the inhibition is present, and tuning curves centred around zero when it is not (Brand et al. 2002). However, the time course of the modelled inhibitory synaptic current is unrealistically fast; when set to a more plausible speed, it fails to shift the tuning curve away from zero (Zhou et al. 2005). While this does not disprove the carving hypothesis, it does highlight the flaws inherent in using complex models when a large degree of uncertainty exists over the parameters. The model is based on a model of bushy cells in the AVCN, where only the low threshold potassium channels were characterised for the bushy cells themselves (Rothman et al. 1993). Other channels had kinetics obtained from non-auditory neurons in a variety of species (some amphibian), and some channels known to be present in MSO neurons were omitted (such as the hyperpolarisation-activated nonselective cation channels,  $I_H$ ). Although both updated kinetic schema and alternative biophysical models of MSO are available (Agmon-Snir et al. 1998, Svirskis et al. 2002, Rothman & Manis 2003a, Rothman & Manis 2003b, Rothman & Manis 2003c, Zhou et al. 2005), such complex models are laborious to run and difficult to generalise. It was hoped that a simpler models could provide a more intuitive description of the system (albeit at the expense of accuracy).

The model used by Batra et al. to explain the nonlinear phase plots in the SOC is simple, with few starting parameters, and addresses the sub-threshold integration within the neuron (Batra et al. 1997). The ipsilateral excitatory input  $v_{IE}(t)$ , the contralateral excitatory input  $v_{CE}(t)$ , and the contralateral inhibitory input  $v_{CI}(t)$ , are all described by a sinusoids with different amplitudes (representing different synaptic strengths). The inputs are then interaurally delayed (including any interaural differences in conductance times), summated, and the response of the neuron is proportional to the amplitude of the resulting sinusoid

$$r(\tau) \propto \max_t [v_{IE}(t) + v_{CE}(t + \tau_E + \tau) + v_{CI}(t + \tau_I + \tau)] \quad (3.3)$$

where  $r(\tau)$  is the response of the neuron to an ITD of  $\tau$  ms. By independently varying the interaural delays for the excitation  $\tau_E$  and the inhibition  $\tau_I$ , Batra et al. were able to qualitatively reproduce a range of nonlinear phase plots. With a few modifications, a model such as this can be used to develop an intuition for the sub-threshold effect of inhibition on tuning curve shape, for a variety of stimuli.

### 3.2.1 An ITD energy model

The use of the amplitude to determine the output firing rate of the neuron in (3.3) does not easily generalise to other inputs. Only if all the inputs to (3.3) were pure sinusoids would their sum be a pure sinusoid. For this reason, and others that will shortly become clear, the response was modelled in line with the energy model used to explain the shape of binocular disparity tuning curves (Ohzawa et al. 1990, 1997).

The MSO neuron is considered an inhomogeneous Poisson process, with a probability of firing proportional to the squared sum of the postsynaptic responses originating from the contralateral and ipsilateral inputs. The firing rate of the neuron is therefore given by integrating this value over time

$$r(\tau) \propto \frac{1}{T} \int_0^T dt [v_I(t) + v_C(t + \tau)]_+^2 \quad (3.4)$$

The half-wave rectification nonlinearity (denoted by  $[\cdot]_+$ ) is incorporated to ensure that the probability of firing could not be negative. If the inputs are assumed to be positive, then this half-wave rectification can be ignored, and for large  $T$  and small  $\tau$ , (3.4) can be simplified to yield a predicted tuning curve proportional to the cross-correlation of the postsynaptic responses

$$r(\tau) \propto \frac{1}{T} \int_0^T dt v_I(t) v_C(t + \tau) \quad (3.5)$$

Thus the model in (3.4) is in line with the cross-correlation model of MSO neurons.

In their original model, Batra et al. assume that all inputs follow the same sinusoidal time course, but they allow the amplitude and phases to differ. In order that the tuning curve should peak at zero ITD in the absence of inhibition, it is assumed that any internal delay between the excitatory inputs is zero (i.e.  $\tau_E = 0$  in (3.3)) and (for simplicity) the

excitatory inputs are assumed to be of equal strength. This leaves only two parameters:  $\alpha$ , the strength of the contralateral inhibition relative to that of the excitation, and  $\beta$ , the time lead of the inhibition over the contralateral excitation (denoted as  $\tau_I$  in (3.3)). Since the time course of the inhibition is otherwise identical to that of the contralateral excitation, the contralateral postsynaptic response can be described by a linearly filtered version of the contralateral excitatory input

$$v_C(t) = v_{CE}(t) - v_{CI}(t) = v_{CE}(t) - \alpha v_{CE}(t + \beta) \quad (3.6)$$

Defining the linear kernel

$$\kappa(t) = \delta(t) - \alpha\delta(t + \beta) \quad (3.7)$$

where  $\delta(t)$  is the Dirac delta function, allows (3.4) to be rewritten as

$$r(\tau) \propto \frac{1}{T} \int_0^T dt [v_{IE}(t) + v_{CE}(t + \tau) * \kappa(t + \tau)]_+^2 \quad (3.8)$$

Finally, for the purposes of developing some intuition of the effect, if all inputs are reasonably assumed to follow the same time course  $v(t)$ , and the half-wave rectification is ignored, the response can be expressed as a filtered version of the autocorrelation of the input distribution  $v_X(t)$

$$r(\tau) = a_0 + a_1 v_X(\tau) * \kappa(\tau) \quad (3.9)$$

where  $a_0$  and  $a_1$  are constants of proportionality. Thus, from the definition of  $\kappa(\tau)$ , the ITD tuning curve can be considered to be composed of two components: an excitatory component centred at zero ITD and an inhibitory component centred at  $-\beta$ . The excitatory component arises from the correlation between the excitatory inputs, while the inhibitory component arises from the anti-correlation between the ipsilateral excitatory and the contralateral inhibitory component. Despite (3.9) being an approximation, if the excitatory inputs are considered to be purely positive then the approximation is reasonable, with large differences expected only when the inhibition is unmatched by the excitation, producing a large negative potential. Although it might be desirable to introduce bilateral inhibition into (3.9), this has been avoided since the positive correlation between inhibitory inputs would erroneously raise the firing rates for the approximation.

### 3.2.2 Frequency-dependent delays

If the input  $v(t)$  is a pure sinusoid, from (3.9) the response will be

$$r(\tau) = a_0 + a_1 A_\kappa(f) \cos[2\pi f\tau + \phi_\kappa(f)] \quad (3.10)$$

where  $A_\kappa(f)$  is the amplitude spectrum of  $\kappa(\tau)$  and  $\phi_\kappa(f)$  is its phase spectrum. Since the best IPD of the response to any arbitrary frequency  $f$  is given by  $-\phi_\kappa(f)$ , the effect of the inhibition on the purely sinusoidal stimuli used by Batra et al. can be understood by examining the phase spectrum of  $\kappa(\tau)$

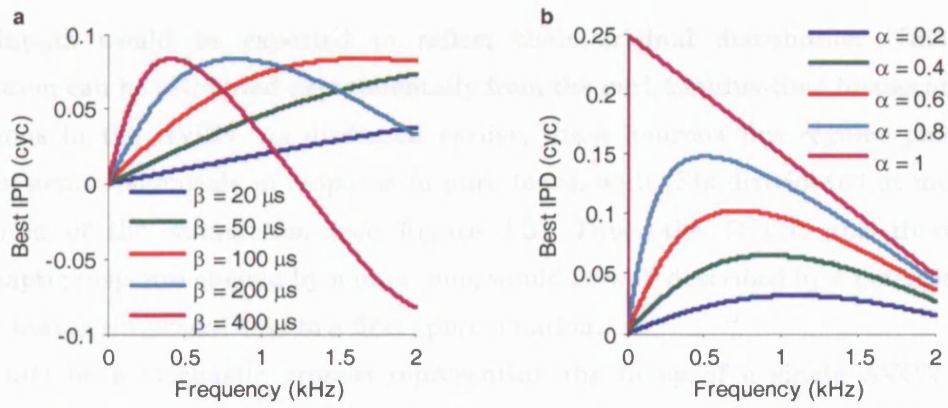


**Figure 3.2 Phase plots predicted by carving inhibition.**

Phase plots produced for sinusoidal inputs by the model in (3.9). **a**, the relative strength of inhibition is fixed at 0.5 and the lead time is allowed to vary. **b**, lead time is fixed at 0.2 ms and the relative strength is allowed to vary. The early portion of the plot is linear and passes through zero, correspond to a pure time delay for low-frequency neurons. However, at some frequencies the gradient of the plot is zero, corresponding to a pure phase delay.

$$\phi_{\kappa}(f) = \arctan \left[ \frac{\alpha \sin(2\pi f\beta)}{\alpha \cos(2\pi f\beta) - 1} \right] \quad (3.11)$$

If inhibition is blocked by setting  $\alpha = 0$ , then  $\phi_{\kappa}(f) = 0$  for all frequencies, producing a flat phase plot. However, for  $\alpha > 0$ , the best IPD will have some level of frequency dependency.

Figure 3.2 shows a variety of phase plots predicted for various values of  $\alpha$  and  $\beta$ . Since any given neuron will only respond to a narrow range of frequencies, the phase plots recorded experimentally would only appear as a small portion of the graphs shown. Clearly, a wide range of resultant phase plots is possible. For one range of frequencies, the phase plot can appear linear with a CP of zero (corresponding to a pure time delay); for others, the gradient of the phase plot can be zero, corresponding to a pure phase delay. Between these two extremes, a large number of intermediate plots are possible with both CD, CP, and varying degrees of curvature—consistent with the majority of phase plots observed in the SOC (Batra et al. 1997). The more complex phase plots are not predicted by (3.11) but are uncommon and are likely to be reproduced by the inclusion of LNTB-mediated ipsilateral inhibition in the model. In general however, the majority of the explanatory power of the model of Batra et al. can be retained without the need for a difference in the axonal conductance delays between excitatory inputs.

### 3.2.3 Modelling the input to MSO

For simplicity, Batra et al. assumed that a sinusoidal pure-tone stimulus would induce a sinusoidal pattern of input to the MSO neuron. However, due to the high precision of phase locking in the AVCN, it is likely that this input would be more tightly distributed than a sinusoid and so contain harmonic distortions. Since the modelled effect of the inhibition introduces frequency dependency into the internal delay, what response would be predicted if more than one frequency were present in the stimulus?

Assuming that the neuron receives a large number of independent but identically distributed inputs, the net postsynaptic response resulting from the combined activity of

these inputs would be expected to reflect their original distribution. This original distribution can be estimated experimentally from the peristimulus-time histogram (PSTH) of neurons in the AVCN. As discussed earlier, these neurons fire regular phase-locked trains of action potentials in response to pure tones, with ISIs distributed at multiples of the period of the stimulation (see Figure 1.3). Thus, the PSTH, and therefore the postsynaptic response elicited by a pure tone, would be well described by a periodic function, but one that is sinusoidal only to a first approximation.

Let  $x(t)$  be a stochastic process representing the firing of a single AVCN input in response to the pure-tone stimulation. Based on studies of the response of the AVCN to pure-tone stimuli (Joris et al. 1994a), it is reasonable to assume that AVCN neurons will tend to fire at a fixed phase of the stimulus (which for simplicity is defined to be zero), with some cycle-to-cycle jitter in the spike timing

$$x(t) = \sum_{n=-\infty}^{\infty} s_n \delta(t - nT - \xi_n) \quad (3.12)$$

where  $T$  is the period of stimulation and the amount of jitter is determined by the random variable  $\xi_n$ , which is unimodally distributed around zero in line with period histograms observed in AVCN (Joris et al. 1994a). The variable probability of firing on any given cycle is modelled using the random variable  $s_n$ , which takes the value one with probability  $\varepsilon$  (the entrainment) and is zero otherwise.  $\xi_n$  and  $s_n$  are assumed to be independent of each other.

The net input arising from a large number of independent AVCN inputs (but with the same phase of phase locking) may therefore be reasonably assumed to be

$$\bar{x}(t) = p(t) * \varepsilon \delta_T(t) \quad (3.13)$$

where  $\delta_T(t)$  is a Dirac comb with period  $T$  and  $p(t)$  is the probability distribution of the jitter. If not all inputs are phase locked to exactly the same phase, but instead are distributed around some common phase, this can be modelled by increasing the variance of the jitter. Finally, the net synaptic response can be determined by convolving the net input distribution with the EPSP or the IPSP appropriate to the polarity and origin of the input

$$v_{IE}(t) = \bar{x}(t) * e_I(t) \quad (3.14)$$

$$v_{CE}(t) = \bar{x}(t) * e_C(t) \quad (3.15)$$

$$v_{CI}(t) = \bar{x}(t) * i_C(t) \quad (3.16)$$

where  $e_I(t)$  and  $e_C(t)$  are the ipsilateral and contralateral EPSPs and  $i_C(t)$  is the contralateral IPSP. For simplicity, it is assumed that

$$e_I(t) = e_C(t) = i_C(t) \quad (3.17)$$

From (3.14)–(3.16), it can be seen that the predicted autocorrelation of the postsynaptic responses  $v_x(\tau)$  in (3.9) is given by

$$v_x(\tau) = \varepsilon \delta_T(\tau) * p_x(\tau) * e_x(\tau) \quad (3.18)$$

where  $p_x(\tau)$  is the autocorrelation of the jitter distribution and  $e_x(\tau)$  is the autocorrelation of the EPSP waveform. Replacing  $\delta_T(\tau)$  by its Fourier series

$$v_x(\tau) = 2f\varepsilon \sum_{n=0}^{\infty} \text{sgn}(n) \cos(2\pi n f \tau) * p_x(\tau) * e_x(\tau) \quad (3.19)$$

it is clear that the autocorrelation (and similarly the input and the response) is formed from the summed activity of filtered harmonics. Since the contralateral and ipsilateral jitter distributions and EPSPs are assumed to be unimodal and identical, then both  $p_x(\tau)$  and  $e_x(\tau)$  will be unimodal and symmetric about  $\tau = 0$ , and will act as lowpass filters, attenuating the harmonics.

Thus, it can be seen that if the phase locking in AVCN is sharp and the synaptic kinetics are fast (relative to the period of stimulation), then significant harmonic activity will be present in the inputs. In contrast, if the phase locking is poor (or equivalently if the distribution of the phase of phase locking is broad), or if the synaptic kinetics are sluggish (again relative to the period of stimulation), then the level of harmonic distortion will be reduced. In practice however, it is unlikely that the harmonics could be eliminated without overly attenuating the fundamental, which, in terms of the output of the neuron, would produce only weak modulation to IPDs and a large IPD insensitive baseline. Since the jitter measured in AVCN is low (Joris et al. 1994a) and the synaptic currents recorded in MSO neurons are fast (Magnusson et al. 2005), it seems likely that some level of harmonic distortion should be present in the postsynaptic response, and more so at the lower frequencies.

If we assume that  $p_x(\tau) * e_x(\tau)$  is Gaussian, then a good model for  $v_x(\tau)$  will be the wrapped normal distribution. Since this is well approximated by a Von Mises distribution (Mardia & Jupp 2000), a more practical form of (3.19) is given by

$$v_x(\tau) \propto \exp[\gamma \cos(2\pi f \tau)] \quad (3.20)$$

where  $\gamma$  is the *concentration parameter*. For large values of  $\gamma$ , the tuning curve is sharp and the harmonic distortion is high; for low values of  $\gamma$ , the tuning curve is broad and the distortion is low. This approximation is satisfactory for values of  $\gamma$  greater than 1.4 (corresponding to vector strengths greater than 0.57, Mardia & Jupp 2000). At lower values, the Von Mises approximation underestimates the degree of harmonic distortion. In lieu of detailed knowledge of the distribution of the jitter and the EPSP shapes, the Von Mises distribution is felt to be reasonable model to use to investigate the possible effects of the carving inhibition.

### 3.2.4 Asymmetric tuning curves

Substituting the Fourier series of  $v_x(\tau)$  into (3.9) gives

$$r(\tau) = a_0 + \sum_{n=1}^{\infty} a_n \cos(2\pi n f \tau) * \kappa(\tau) \quad (3.21)$$

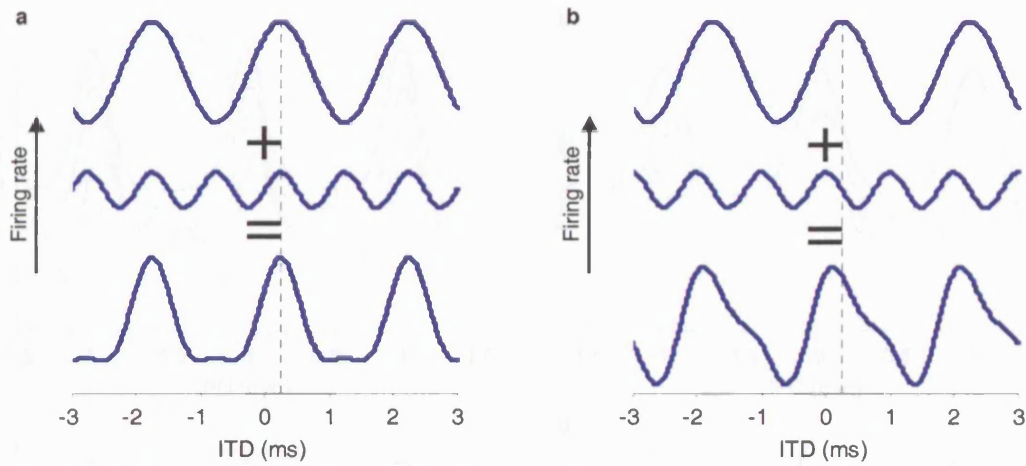


**Figure 3.3** The effect of the second harmonic on tuning curve shape. **a**, both the fundamental (0.5 kHz, top trace) and its second harmonic (1 kHz, middle) are delayed by the same time delay (250  $\mu$ s), resulting in a symmetric function when they are added (bottom). **b**, the fundamental and its harmonic are delayed by different time delays, resulting in a skewed response (bottom).

which is the tuning curve produced by harmonically distorted inputs resulting from pure-tone stimuli.  $v_x(\tau)$  is assumed to be symmetric about  $\tau = 0$  since both  $p_x(\tau)$  and  $e_x(\tau)$  are symmetric about  $\tau = 0$ , as discussed in the last section. This symmetry comes about from the fact that its harmonics are in cosine phase, and so are all symmetric around the line  $\tau = 0$ . However, it can be seen from (3.21) that the effect of inhibition will be to phase delay the fundamental by  $\phi_\kappa(f)$  rad and the  $n^{\text{th}}$  harmonic by  $\phi_\kappa(nf)$  rad. If  $\kappa(\tau)$  were implementing a pure time delay

$$\phi_\kappa(f) = 2\pi f\tau_0 \quad (3.22)$$

each harmonic would be shifted by the same amount of *time*, preserving the symmetry around the line  $\tau = -\tau_0$  (Figure 3.3a). However, if there were some phase component to the delay

$$\phi_\kappa(nf) = 2\pi nf\tau_0 + \phi_0 \quad (3.23)$$

where  $\sin(\phi_0) \neq 0$ , then the fundamental and the harmonics would be shifted by different amounts of time resulting in an asymmetric tuning curve (Figure 3.3b). More specifically, the symmetry will only be preserved when the *phase disparity*

$$\theta_n(f) = \phi_\kappa(nf) - n\phi_\kappa(f) \quad (3.24)$$

between each of the harmonics and the fundamental is either 0 cyc or 0.5 cyc.

Thus, the Jeffress model predicts symmetrical tuning curves, and carving inhibition predicts asymmetric tuning curves. However, whether or not the inhibition does produce an asymmetric tuning curve for any given stimulus is parameter dependent. Consider the set of parameter values resulting in the red curve in Figure 3.2a. For frequencies up to about 0.5 kHz, the curve is approximately linear, with the consequence that there will be no phase disparity between the fundamental and the second harmonic for pure-tone stimuli below 0.25 kHz. If the response is not strongly distorted, any contribution from the third and higher harmonics will be negligible, resulting in a symmetric tuning curve. Thus while

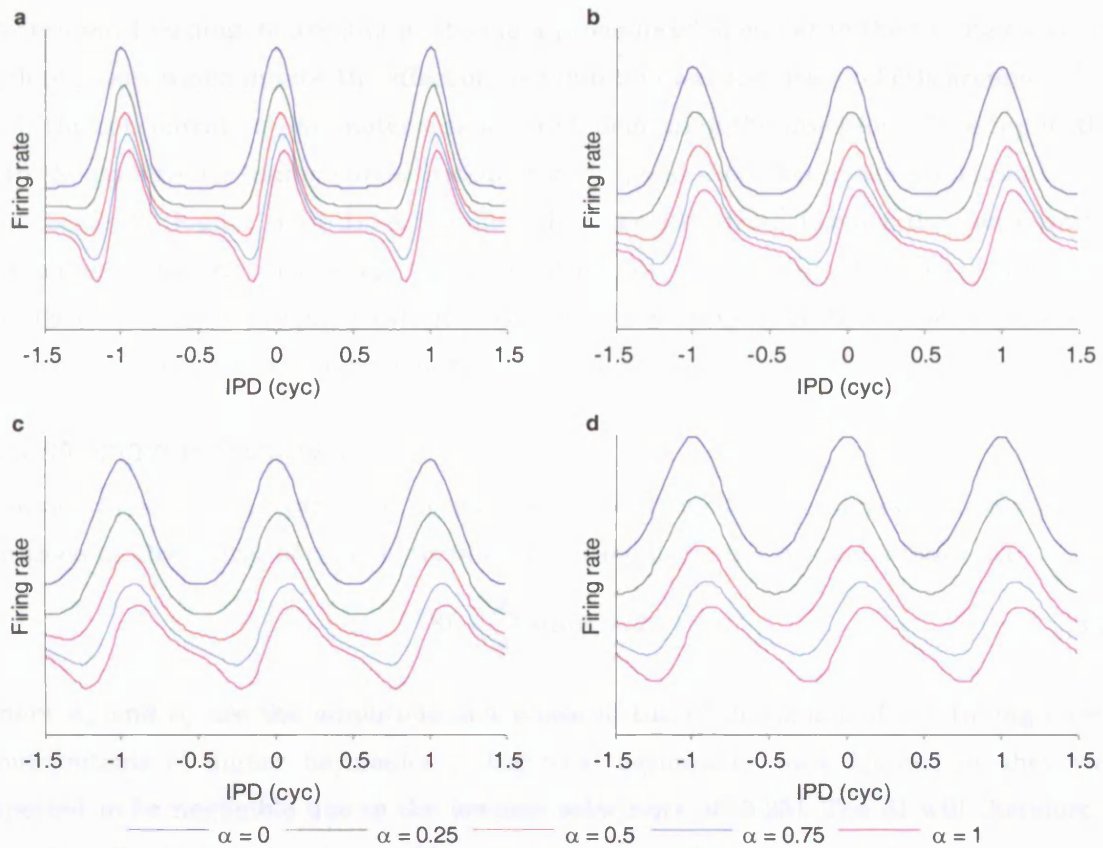


**Figure 3.4** Tone-delay functions predicted for carving inhibition.

Tone-delay functions arising from numerical simulation of (3.8) for an exponentially distorted input (see text for details) of frequency 500 Hz with vector strength: **a**, 0.9; **b**, 0.8; **c**, 0.7; and **d**, 0.6. Inhibition led excitation by 0.2 ms and the relative strength of inhibition varied from 0.2 (blue trace) to 1 (magenta) in 0.2 steps.

the inhibition can produce an asymmetric tuning curve, it will not necessarily do so on every occasion.

### 3.2.5 Simulated tone-delay functions

Since the prediction of asymmetric tuning curves discussed above relied on an approximation, the original model including half-wave rectification (3.8) was numerically integrated for inputs of the form

$$v(t) = \exp[\gamma \cos(2\pi ft)] \quad (3.25)$$

in order to examine the symmetry of the predicted tuning curves. A forward difference method of integration was used with a 10  $\mu$ s time step. Use of (3.25) was motivated by the Von Mises approximation to the wrapped normal discussed earlier for (3.20). The higher the concentration parameter  $\gamma$ , the more precise the phase locking of the input.

Figure 3.4 shows tuning curves resulting from a range of different values of the parameters  $\alpha$ ,  $\beta$  and  $\gamma$ . The effect of inhibition can be seen most clearly for a very precisely phase-locked input (Figure 3.4a). When the inhibition was absent, the tuning curve peaked at zero ITD. As the strength of the inhibition increased, the inhibition began to carve out the tuning curve, affecting contralateral lagging (negative) ITDs more than

contralateral leading delays and producing a pronounced shoulder in the tuning curve. For such precisely timed inputs, the effect of the inhibition was localised to ITDs around  $-\beta$ .

If the concentration parameter was lowered, degrading the precision of the input, then both the underlying tuning curves became broader, and the effect of the inhibition became less localised (Figure 3.4b–d). A similar effect resulted from leaving the concentration parameter fixed but increasing the stimulation frequency. Thus, for the lowest vector strengths (or highest frequencies), the asymmetry resulting from the inhibition was weak, resulting in a gently skewed tuning curve.

### *Quantifying the asymmetry*

In order to assess the variation in the skewness of the tuning curves with the various parameters, the degree of asymmetry was quantified using the *symmetry index* (SI)

$$SI = \frac{A_2}{A_1} \sin(\phi_2 - 2\phi_1) \quad (3.26)$$

where  $A_n$  and  $\phi_n$  are the amplitude and phase of the  $n^{\text{th}}$  harmonic of the tuning curve<sup>7</sup>. Contributions of higher harmonics to the total asymmetry were ignored as they were expected to be negligible due to the lowpass selectivity of (3.25). The SI will therefore be zero if the fundamental and second harmonic are delayed by the same amount of time, or if there is no harmonic distortion. If the second harmonic “leads” the fundamental, sharpening the left-hand slope (relative to the peak) as in Figure 3.3b, then the SI will be positive; if it “lags” the fundamental, sharpening the right-hand slope, then the SI will be negative.

While the phase disparity defined in (3.24) could have been used alone, factoring in the relative amplitude of the second harmonic normalised for the level of modulation. For neural data, this allowed comparison between different neurons and ensured that the effect of harmonics arising from noise was not overstated.

### *The effect of inhibition on the shape of tone-delay functions*

Tuning curves were simulated for a range of parameters over a 65 point sampled range of IPDs from  $-0.5$  to  $+0.5$  cyc. Figure 3.5 shows the variation in the best IPD, the SI, the phase disparity, and the *power ratio* (between the second harmonic and the fundamental) of the simulated tuning curves, as a function of the model parameters. Although the effects of lagging inhibition ( $\beta < 0$ ) are not shown, they can be simply deduced from Figure 3.5 by considering the effect of reflecting the tuning curve in the y-axis. Positive best IPDs and phase disparities will become negative while the power ratio will remain the same, producing negative SI values.

---

<sup>7</sup> The SI is the normalised area inside the Lissajous curve formed by the first two harmonics. If no phase discrepancy exists then the curve will be a parabola and the area will be zero. If some discrepancy exists however, the curve will form a figure-of-eight pattern and the area constrained by the curve will be nonzero.

The simulated tuning curves behaved as expected from the analytical model. The best IPD was largely independent of the degree of phase locking of the input and had a similar form to the predicted phase-plots arising from (3.11) (shown in Figure 3.2). Because of this, the phase disparity showed a similar level of independence. The variation of the power ratio was dependent on all three parameters, although the concentration parameter showed the strongest influence since it determined the level of harmonic activity in the input. The variation of the power ratio with respect to the inhibitory parameters was largely independent of the concentration parameter, and reflected the frequency selectivity of the inhibitory filter. Because of this decrease in the power ratio, the SI also inevitably decreased with the concentration parameter, as the influence of the second harmonic on the tuning curve shape weakened. Similar to the phase-disparity, the variation in the SI value with the inhibitory parameters was largely independent of the degree of phase locking and showed a similar dependency on the inhibitory parameters as the best IPD.

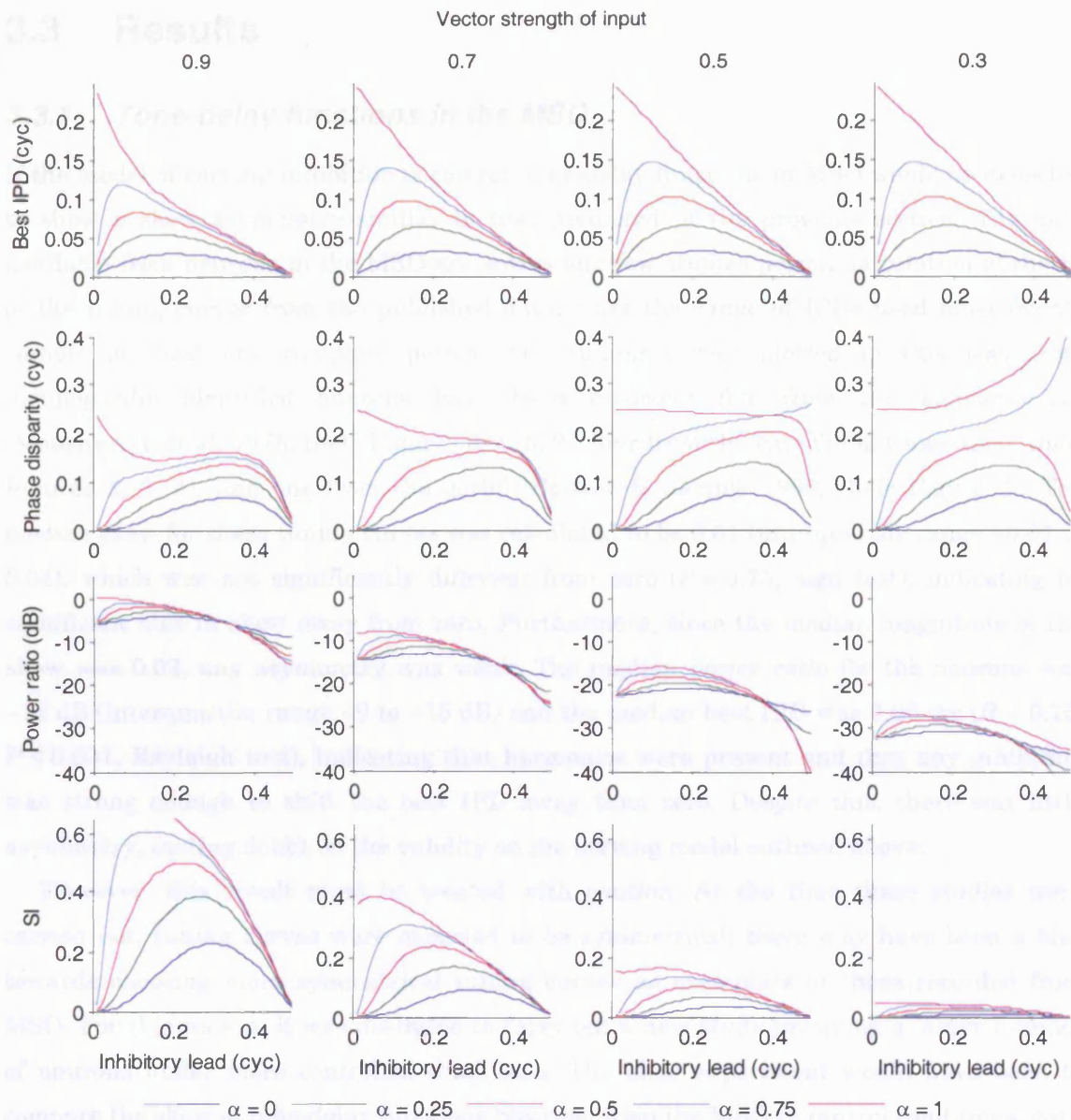


**Figure 3.5 Predicted effect of carving inhibition and phase locking on the shape of tone-delay functions.** Changes in simulated tuning curves as functions of the lead and relative strength of the inhibition for four different strengths of input phase locking (columns). The lead time of the inhibition has been expressed in cycles in order to normalise for stimulus frequency. The best IPD (top row) and the phase disparity (second row) were largely independent of the precision of the input. The power ratio (third row) and SI (bottom row) showed dependency on all three parameters.

In general, precisely phase-locked inputs together with strong inhibition that lead excitation by around 0.25 cyc, produced strong harmonic activity and a pronounced asymmetry. If the precision of phase locking fell (decreasing the harmonic activity), or if the inhibition grew weaker or moved in-phase with the excitation, then the asymmetry was reduced.

### 3.3.2 Tone-delay functions in the DMLL

Tone-delay functions were recorded from 20 neurons in the DMLL. 14 neurons were recorded by the author and 20 neurons were drawn from all results study by Dr. G. S. S. and Prof. D. McAlpine. Unpublished data. Stimuli were presented at the characteristic

## 3.3 Results

### 3.3.1 *Tone-delay functions in the MSO*

If the model of carving inhibition is correct, tone-delay functions in MSO would be expected to show a skew asymmetry similar to that predicted in the previous section. The data available from neurons in the MSO are scarce and few studies permit calculation of the SI of the tuning curves from the published data, since the range of IPDs used must evenly sample at least one complete period. Ten tuning curves plotted in this way from histologically identified neurons have been reported: five from the kangaroo rat (Moushegian et al. 1975; their Figures 3, 4, 5, 9), four from the cat (Yin & Chan 1990; their Figures 2, 3, 4), and one from the gerbil (Spitzer & Semple 1995, their Figure 2). The median skew for these tuning curves was calculated to be 0.01 (interquartile range  $-0.01$  to  $0.04$ ), which was not significantly different from zero ( $P = 0.75$ , sign test), indicating no significant bias in skew away from zero. Furthermore, since the median magnitude of the skew was 0.02, any asymmetry was weak. The median power ratio for the neurons was  $-12$  dB (interquartile range  $-9$  to  $-15$  dB) and the median best IPD was  $0.06$  cyc ( $R = 0.76$ ,  $P \leq 0.001$ , Rayleigh test), indicating that harmonics were present and that any inhibition was strong enough to shift the best IPD away from zero. Despite this, there was little asymmetry, casting doubt on the validity on the carving model outlined above.

However, this result must be treated with caution. At the time these studies were carried out, tuning curves were expected to be symmetrical; there may have been a bias towards choosing more symmetrical tuning curves as exemplars of those recorded from MSO. For this reason, it was desirable to carry out a new study involving a larger number of neurons under more controlled conditions. The ideal experiment would have been to compare the skew of tone-delay functions recorded from the MSO in control conditions, with those recorded during application of strychnine. However, due to the difficulty of isolating neurons in the MSO mentioned earlier, combined with the difficulties inherent in the use of a iontophoresis electrode, it was felt that it would be preferable to record from a proxy nucleus afferent to the MSO. Since it is known that the IC is an unreliable proxy (McAlpine et al. 2001), it was decided to record from the dorsal nucleus of the lateral lemniscus (DNLL). The DNLL is potentially a site of lower convergence than the IC, as suggested by the stronger phase locking and narrower tuning curves reported for the DNLL compared with the IC. It was hoped that this assumption could be tested by comparing results obtained in DNLL with those observed in IC.

### 3.3.2 *Tone-delay functions in the DNLL*

Tone-delay functions were recorded from 38 neurons in the DNLL: 18 neurons were recorded by the author and 20 neurons were drawn from an earlier study (Dr SE Boehnke and Prof D McAlpine, unpublished data). Stimuli were presented at the characteristic

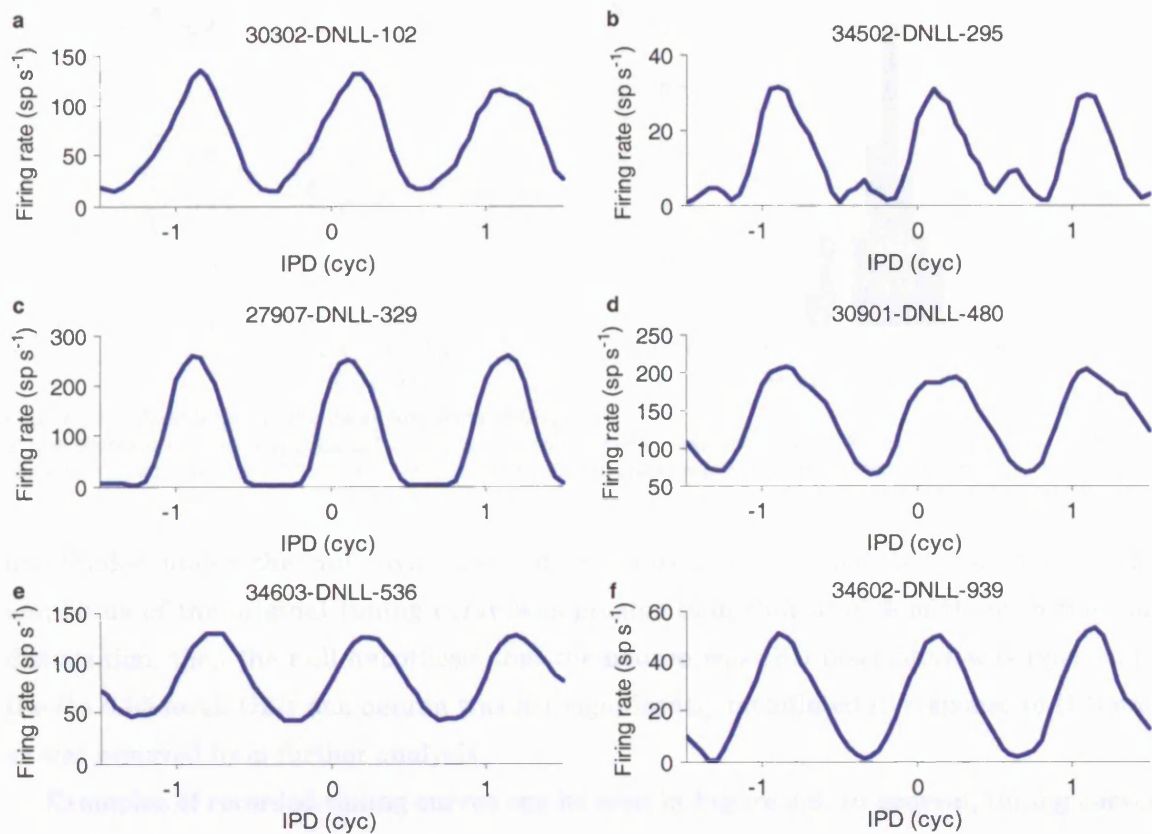


**Figure 3.6** Examples of tone-delay functions recorded from DNLL.

Responses were usually unimodal with positive skew. **a**, a rare example of a negatively skewed response. Note that the right-hand slope of the tuning curve (relative to the peak) is steeper than the left-hand slopes. **b**, a neuron showing strong positive skew (the left-hand slope is steeper). In addition, this neuron shows an unusual bimodal tuning curve (see text for discussion). **c–f**, typical responses showing a slight positive skew for a range of BFs. See Table 3.1 for characteristic frequencies and other measurements.

ID	CF (Hz)	Best IPD (cyc)	SI	Power Ratio (dB)
30302	102	0.13	-0.12	-16
34502	295	0.14	0.11	-6
27907	329	0.13	0.02	-12
30901	480	0.18	0.13	-15
34603	536	0.24	0.06	-22
34602	939	0.14	0.09	-19

**Table 3.1** CFs and tone-delay function properties of neurons shown in Figure 4.6.

frequency of the neuron, at a level 20 dB above threshold. Full details of procedures and stimuli are presented in the Methods chapter (Section 2.4.1).

Tone-delay functions that were not significantly modulated were assumed to be IPD insensitive and were omitted from further analysis. This was tested via a bootstrap test where the tuning curve was resampled by randomly reselecting the firing rate at each IPD from the distribution of firing rates in the original tuning curve (with replacement), effectively eliminating any modulation. This resampling was repeated 1000 times. By measuring the amplitude of modulation at CF for each resample, the distribution of

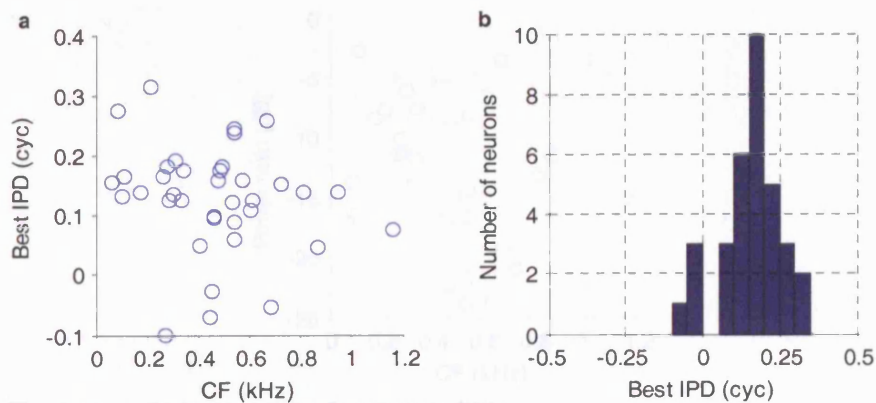


**Figure 3.7 Best IPDs of tone-delay functions in DNLL.**

**a**, the distribution of best IPD as a function of the characteristic frequency. Best IPD was independent of CF. **b**, histogram of recorded best IPD values. For most neurons, best phase was in the range 0 to 0.25 cyc.

amplitudes under the null hypothesis of IPD insensitivity could be estimated. If the amplitude of the original tuning curve was greater than that of 95% of those in the null distribution, then the null hypothesis that the neuron was IPD insensitive was rejected at the  $P \leq 0.05$  level. Only one neuron was not significantly modulated in response to IPD and so was removed from further analysis.

Examples of recorded tuning curves can be seen in Figure 3.6. In general, tuning curves were periodic and unimodal with the exception of two neurons, both of which showed secondary modes half a cycle away from the main peak (see Figure 3.6b). This was not due to post-inhibitory rebound spiking since the onset of firing at these IPDs was consistent with the onset at all other IPDs. The bimodality may have been due to either convergent input, or antiphase-locked firing in the inputs to MSO.

### Best delays

The location of the peak of the tuning curves was estimated by measuring the best IPD of the neuron from the phase of the fundamental (CF) component of the tuning curve. In agreement with other studies in both MSO (Brand et al. 2002) and DNLL (Seidl & Grothe 2005, Siveke et al. 2006), best IPD was independent of characteristic frequency ( $P > 0.1$ , Mardia's linear-circular rank correlation; Mardia & Jupp 2000) with the mean best IPD relatively constant around 0.13 cyc ( $R = 0.86$ ,  $P \leq 0.001$ , Rayleigh test, see Figure 3.7). The majority of neurons ( $30/37$ ) showed best IPDs in the range 0 to 0.25 cyc with only a few neurons peaking at ipsilateral leading delays ( $4/37$  neurons,  $-0.25$  to 0 cyc).

The best IPD can also be defined more in line with the Jeffress model, as the IPD at which the firing rate of the neuron is maximal. In order to estimate this *peak IPD*, the tuning curve was smoothed with a three-point moving-average filter, and the first derivative of the tuning curve at each IPD was estimated from the difference in firing rate of the two neighbouring ITDs. Zero crossings in the first derivative were then located using linear interpolation and the peak ITD was taken to be the positive-to-negative zero crossing corresponding to the highest firing rate. Estimated in this manner, the mean best IPD fell

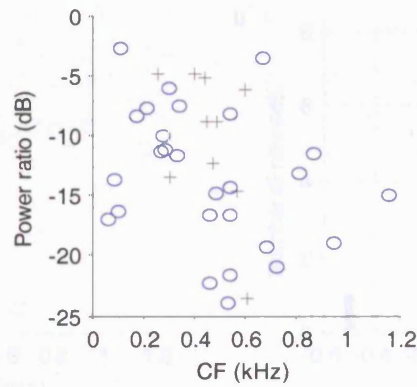


**Figure 3.8** The power ratio for tone-delay functions in DNLL.

The power ratio as a function of the characteristic frequency. Power ratios are shown for both half-wave rectified (grey crosses) and non-rectified (blue circles) tuning curves.

slightly to 0.11 cyc ( $R = 0.84$ ,  $P \leq 0.001$ , Rayleigh test), which was significant ( $P \leq 0.001$ , sign test).

### *Harmonic distortion*

Before analysing the degree of distortion in the tuning curves, several neurons ( $10/37$ ) were excluded from subsequent analysis because they showed half-wave rectification of their tuning curves. Such nonlinearity, potentially arising at the level of the DNLL, would introduce harmonic distortions into the tuning curve, increasing the power ratio and lowering the degree of asymmetry (discussed later). Since such nonlinearity was not accounted for in the model, in order that the recorded responses might be as close as possible to the hypothesised output of MSO, any neurons showing a mean firing rate of 0 sp s<sup>-1</sup> in response to any IPD were excluded.

In order to estimate the degree of harmonic distortion, the ratio of the power in of the second harmonic to the power of the fundamental was calculated using the Fourier transform of the tuning curve. Third and higher order components had little effect on tuning curve shape, accounting for a median 2% of the variance (interquartile range 1% to 3%). Much of this was likely a consequence of noise in the recordings. Individual inputs to the MSO show a decrease in the vector strength of phase locking from 0.99 for the lowest frequencies to around 0.6 at 1 kHz (Joris et al. 1994a). From Figure 3.5, it can be seen that for these input vector strengths, the power ratio should show a decline with CF from around 0 dB to around -15 dB. However, although the power ratio appeared to show a decrease at higher CFs (Figure 3.8) this was not significant ( $P = 0.12$ , Spearman's rank correlation coefficient). Instead, it appeared that the reason for the lack of significant correlation was the presence of only weak distortion in three neurons with the lowest CFs—the very neurons expected to show the highest level of distortion. Excluding these three neurons resulted in a significant negative correlation ( $r = -0.49$ ,  $P = 0.017$ ). However, visual inspection of the tuning curves of these neurons (e.g. Figure 3.6a) revealed no artefactual explanation for the low level of distortion, indicating that these data points were reliable and so could not be considered outliers. In fact, the low-CF data point with the

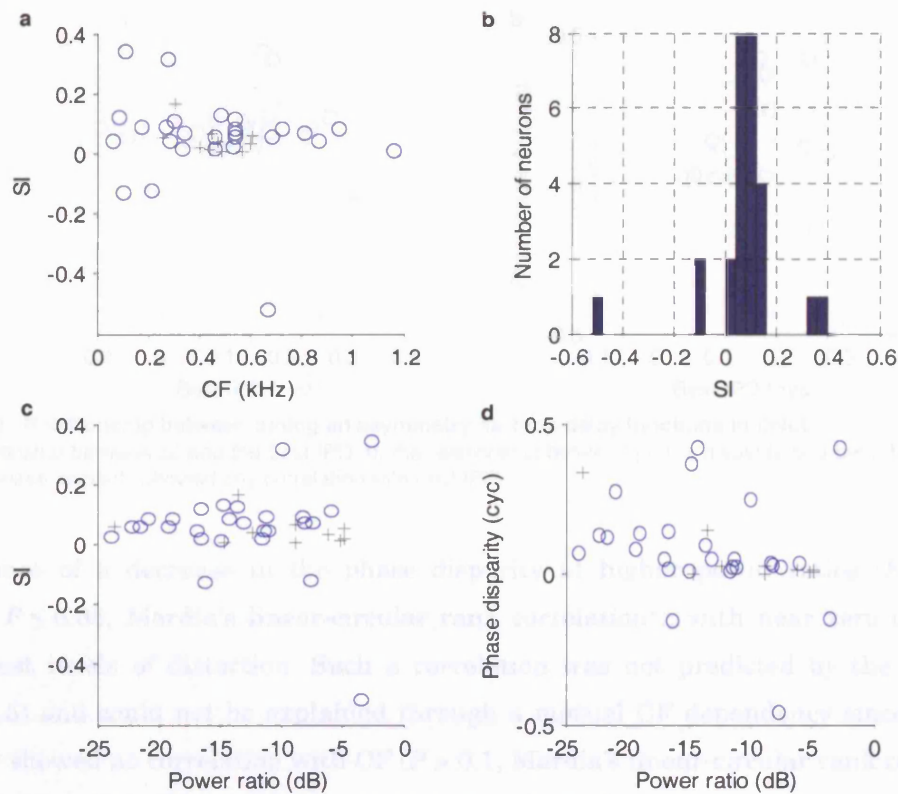


**Figure 3.9** Asymmetry of tone-delay functions in DNLL.

**a**, the distribution of SI as a function of characteristic frequency. Data from both half-wave rectified (grey crosses) and non-rectified (blue circles) tuning curves are shown. The degree of skew was independent of CF. **b**, histogram of SI values. For most neurons, SI was positive and clustered between 0 and 0.2. **c**, variation in SI with power ratio. **d**, the phase disparity as a function of the power ratio. The phase disparity decreased as the degree of distortion increased, suggesting the presence an additional nonlinearity not accounted for in the model.

high power ratio appeared to be more of an outlier, with the high power ratio an artefact of very weak IPD sensitivity and a noisy tuning curve.

### Skewness

The skewness of the tuning curves was measured by the SI, calculated using the Fourier transform of the tuning curves. Since the phase locking of inputs to the MSO decreases with CF, and since the power ratio appeared negatively correlated with CF, it might be expected from (3.26) that the degree of asymmetry should also have decreased with increasing CF. In fact, no significant correlation could be observed between the magnitude of the SI and the CF of the neuron (Figure 3.9a;  $P = 0.076$ , Spearman's rank correlation coefficient). For the majority of neurons the SI was positive ( $24/27$  neurons, Figure 3.9b) leading to a median SI of 0.07, which was significantly different from zero ( $P \leq 0.001$ , sign test). This indicated that although slight, the skew was not an artefact of noise in the recordings and tended to be positive.

The lack of correlation of the magnitude of the SI with CF was surprising given that the magnitude of the SI was defined in (3.26) to be dependent on the power ratio, and that the power ratio appears to decrease with CF. Indeed, the data did show a correlation between the magnitude of the SI and the power ratio ( $r = 0.45$ ,  $P = 0.018$ , Spearman's rank correlation coefficient; Figure 3.9c). The lack of correlation with CF appeared to be a

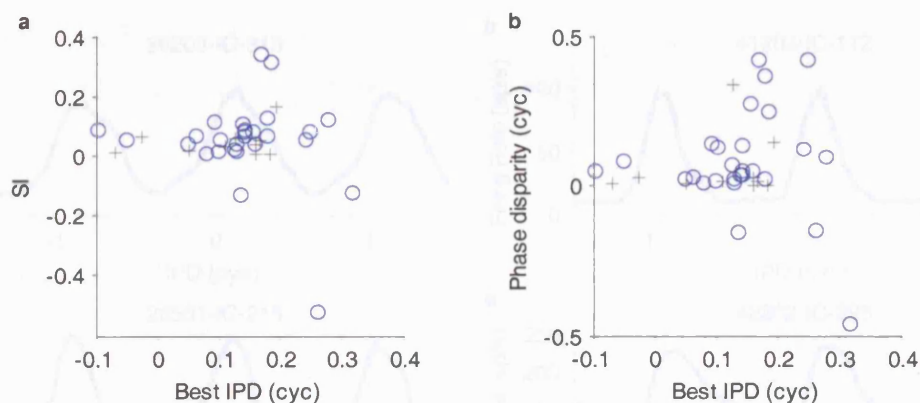


**Figure 3.10 Relationship between tuning an asymmetry for tone-delay functions in DNLL.**

**a**, the relationship between SI and the best IPD. **b**, the relationship between phase disparity and best IPD. Neither the SI nor the phase disparity showed any correlation with best IPD.

consequence of a decrease in the phase disparity at higher power ratios (Figure 3.9d;  $r = 0.29$ ,  $P \leq 0.05$ , Mardia's linear-circular rank correlation<sup>8</sup>), with near zero disparity at the highest levels of distortion. Such a correlation was not predicted by the model (see Figure 3.5) and could not be explained through a mutual CF dependency since the phase disparity showed no correlation with CF ( $P > 0.1$ , Mardia's linear-circular rank correlation).

It is possible that this correlation reflects a static nonlinearity after the level of the MSO, similar to the half-wave rectification discussed earlier. Such a nonlinearity would be expected to introduce harmonic distortions in phase with the fundamental of a skewed tuning curve, which, when combined with the existing distortions, would reduce the phase disparity—an effect that can be seen to be demonstrated by the half-wave rectified tuning curves in Figure 3.9d. Although the exclusion of the half-wave-rectified tuning curves from the analysis means that this particular nonlinearity cannot explain the observed correlation, other nonlinear relationships between input and output cannot be so easily detected. For example, a quadratic input-output dependency in DNLL would introduce second harmonics but could not be distinguished from nonlinearities introduced at an earlier stage. The existence of such nonlinearity would make it difficult to assess the recorded responses in relation to the model outlined previously.

As might be expected from the reduction of both the skew and the phase disparity at higher CFs, no correlation with best IPD was observed for either the skew (Figure 3.10a;  $P > 0.05$ , Mardia's linear-circular rank correlation) or the phase disparity (Figure 3.10b;  $P = 0.56$ , Mardia's circular-circular rank correlation; Mardia & Jupp 2000). In an attempt to control for the effect of any nonlinearity, any data showing a power ratio greater than  $-12$  dB were omitted and this analysis repeated. However, this had little effect on the measured correlations. In the simulations shown in Figure 3.5, for any particular vector strength of input, the SI appeared well correlated with the best IPD. While this correlation may be weak for the recorded data because of a wide range of input vector strengths, the relationship between best IPD and phase disparity was expected to be constant across a

<sup>8</sup> Throughout this text, in the context of Mardia's linear-circular rank correlation,  $r$  refers to the normalised correlation coefficient  $D_n$ .

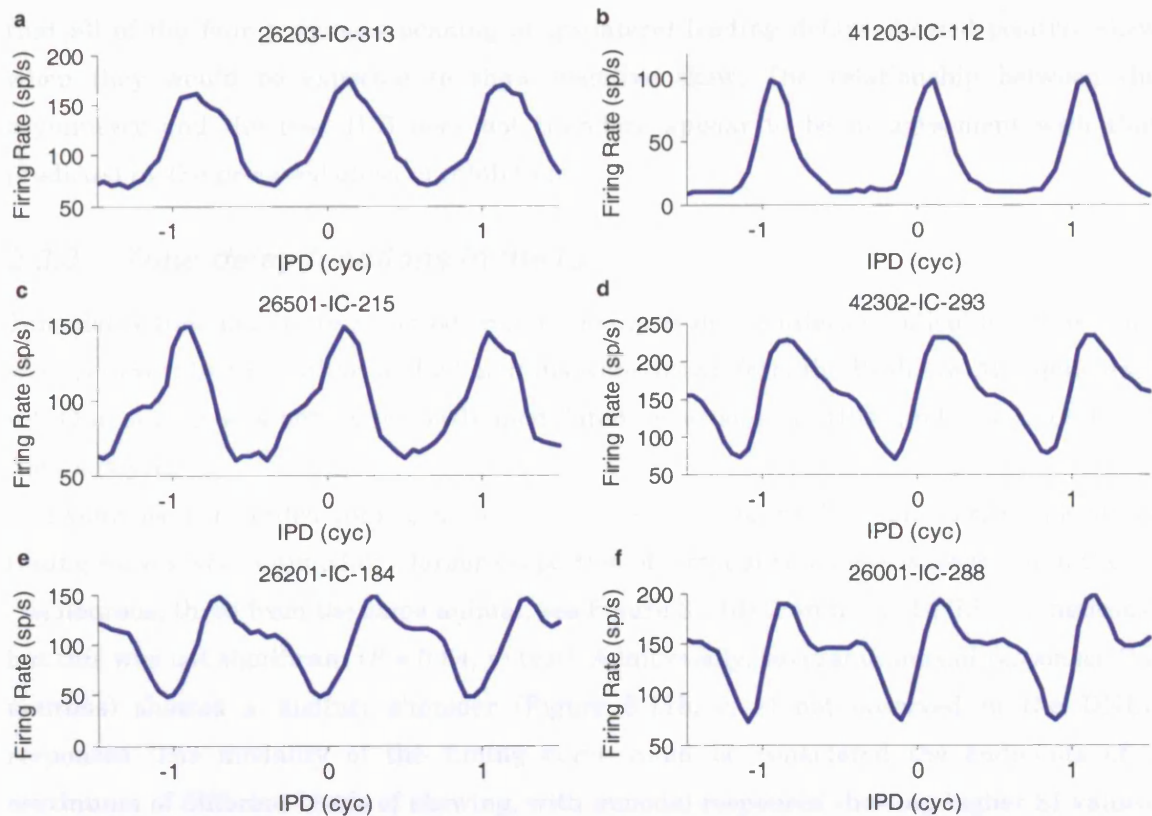


**Figure 3.11** Examples of tone-delay functions recorded from IC.

Tuning curves in IC appeared more skewed than those in DNLL, with curves in IC often showing a shoulder (b, c, e), which was often pronounced enough to become a secondary mode (d). See Table 3.2 for characteristic frequencies and other measurements.

ID	CF (Hz)	Best IPD (cyc)	SI	Power Ratio (dB)
41203	112	0.09	0.05	-5
26201	184	0.41	0.41	-6
26501	215	0.06	-0.26	-10
26001	288	0.31	0.87	0
42302	293	0.25	0.53	-6
26203	313	0.16	0.01	-18

**Table 3.2** CFs and tone-delay function properties of neurons shown in Figure 3.11.

range of input vector strengths. This lack of correlation indicates that the degree of asymmetry and the tuning of the responses may not be determined by the same mechanism.

There were also more general disagreements with the proposed model of the effect of the inhibition, in terms of the direction of skew and the sign of the best IPD. Although the majority of the 33 neurons<sup>9</sup> peaking at contralateral leading delays showed positive skew and were therefore qualitatively consistent with the predicted effect illustrated, some of these neurons ( $\frac{3}{33}$ ) showed strong negative skew. Although, the neuron with the most negative SI was likely to be an outlier (due to a noisy tuning curve), the other two data points appeared to be reliable. Another disagreement with the predictions of the model was

<sup>9</sup> Half-wave rectified responses were included in this analysis. While the nonlinearity will lower the magnitude of the asymmetry, it is not expected to have any systematic effect on the direction of the skew.

that all of the four responses peaking at ipsilateral leading delays showed positive skew when they would be expected to show negative skew. The relationship between the asymmetry and the best IPD does not therefore appear to be in agreement with that predicted by the proposed effect of inhibition.

### 3.3.3 Tone-delay functions in the IC

Tone-delay functions were recorded from 64 neurons in the inferior colliculus: 36 neurons were recorded by the author, and 28 neurons were drawn from the Boehnke–McAlpine data set. One neuron was not significantly modulated in response to IPDs and so was excluded from analysis.

Examples of recorded tuning curves can be seen in Figure 3.11. The large majority of tuning curves were unimodal; a larger proportion of bimodal responses were found in the IC ( $\frac{5}{63}$  neurons, three from the same animal, see Figure 3.11d) than in the DNLL ( $\frac{2}{37}$  neurons), but this was not significant ( $P = 0.94$ ,  $\chi^2$  test). Additionally, several unimodal responses ( $\frac{5}{58}$  neurons) showed a distinct shoulder (Figure 3.11b, c, e) not observed in the DNLL responses. The modality of the tuning curve could be considered the endpoints of a continuum of different levels of skewing, with bimodal responses showing higher SI values. This apparent difference in modality between the IC and the DNLL was therefore expected to be reflected in a difference in the SI statistic.

#### Best delays

Similar to the DNLL, the best IPD was independent of CF ( $P > 0.1$ , Mardia's linear-circular rank correlation) with the mean best IPD relatively constant around 0.14 cyc ( $R = 0.70$ ,  $P \leq 0.001$ , Rayleigh test; see Figure 3.12). Despite this similarity in mean best IPD, the distributions in IC and DNLL were significantly different ( $P = 0.029$ , uniform scores test; Mardia & Jupp 2000), reflecting the broader range of best IPDs in the IC.

When the peak of the tuning curve was used to estimate the best IPD, the mean best IPD was 0.11 ( $R = 0.73$ ,  $P \leq 0.001$ , Rayleigh test), a significant reduction in the estimated value ( $P = 0.043$ , sign test). Interestingly, estimating the mean best IPD from the peak of

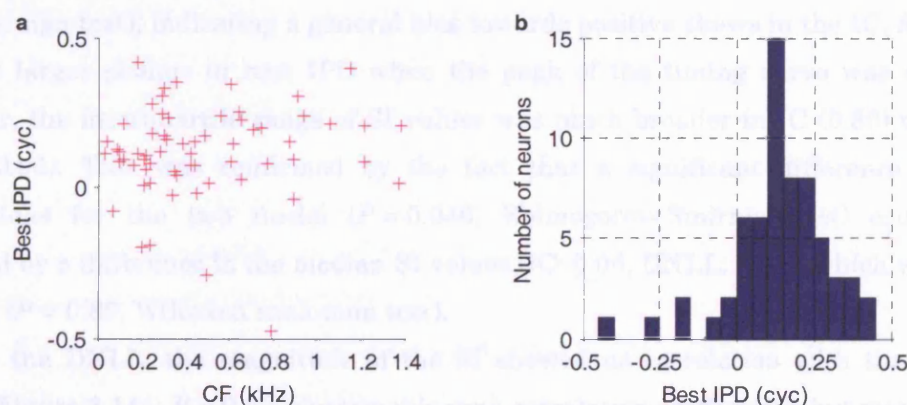


**Figure 3.12 Best IPDs of tone-delay functions in IC.**

**a**, the distribution of best IPD as a function of the characteristic frequency. Best IPD was independent of CF. **b**, Best IPD is clustered roughly around an eighth of a cycle. Note that the range of phases was broader than that in DNLL.

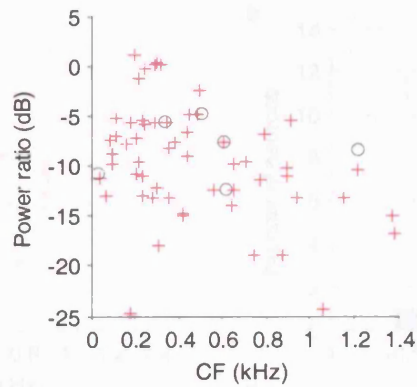


**Figure 3.13 The power ratio for tone-delay functions in IC.**

Variation in the power ratio as a function of the characteristic frequency of neurons in IC. Power ratios are shown for both half-wave rectified (grey circles) and non-rectified (red crosses) tuning curves.

the tuning curve caused the distributions of best IPD for the IC and DNLL to cease to be significantly different ( $P = 0.18$ , uniform scores test). The difference in the phase of the fundamental in the two areas is a reflection of the increased prevalence in IC of highly asymmetric tuning curves with secondary modes and shoulders.

### *Harmonic distortion*

Like the tuning curves in DNLL, third and higher order components had little effect on the tuning curve shape, accounting for a median 2% of the variance (interquartile range 3% to 4%). Again, much of this was likely to arise from noise in the recordings. Unlike the tuning curves in DNLL, the power ratio for the IC tuning curves showed a significant negative correlation with CF (Figure 3.13a;  $r = -0.33$ ,  $P = 0.013$ , Spearman's rank correlation coefficient). However, the distribution in IC was similar to that in DNLL, with low power ratios at the lowest CFs, higher power ratios around 300 Hz, and a fall-off in power ratio at higher frequencies. The median power ratio in IC was 3 dB higher than that in DNLL ( $P = 0.010$ , Wilcoxon rank-sum test) suggesting a higher level of distortion in the tuning curves in IC.

### *Skewness*

The median SI in IC was 0.06 (Figure 3.14b) which was significantly different from zero ( $P = 0.04$ , sign test), indicating a general bias towards positive skews in the IC. As expected from the larger change in best IPD when the peak of the tuning curve was used as an estimator, the interquartile range of SI values was much broader in IC (0.30) than in the DNLL (0.06). This was confirmed by the fact that a significant difference in the SI distributions for the two nuclei ( $P = 0.046$ , Kolmogorov–Smirnov test) could not be explained by a difference in the median SI values (IC: 0.06, DNLL: 0.07), which were nearly identical ( $P = 0.89$ , Wilcoxon rank-sum test).

As in the DNLL, the magnitude of the SI showed no correlation with the CF of the neuron (Figure 3.14a;  $P = 0.67$ , Spearman's rank correlation coefficient), but was correlated with the power ratio as expected from (3.26) (Figure 3.14c;  $r = 0.57$ ,  $P \leq 0.001$ , Spearman's

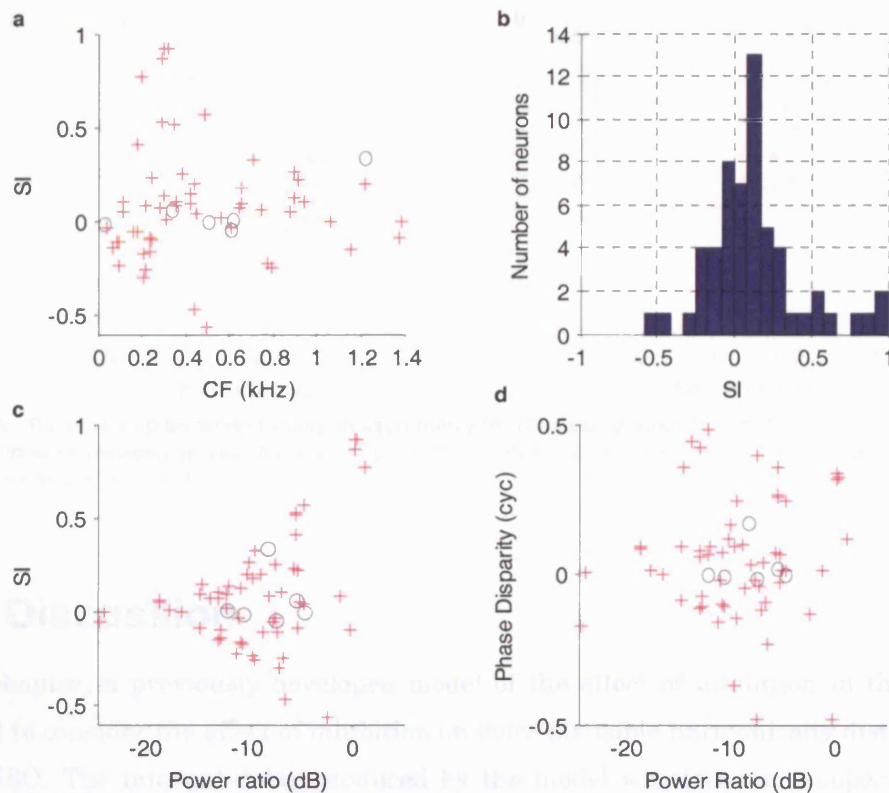


**Figure 3.14 Asymmetry of tone-delay functions in IC.**

**a**, the distribution of SI as a function of the characteristic frequency. Data for both half-wave rectified (grey circles) and non-rectified (red crosses) tuning curves are shown. The degree of skew was independent of the CF. **b**, histogram of SI values. Tuning curves in IC showed a wider range of both positive and negative skews than seen in DNLL. **c**, Distribution of SI as a function of the power ratio. The relationship reflects the fact that, by definition, the magnitude of the SI is determined by the power ratio. **d**, Distribution of the phase disparity as a function of the power ratio. The phase disparity was not correlated with the degree of distortion.

rank correlation coefficient). Unlike DNLL, there was no correlation between the phase disparity and the power ratio (Figure 3.14d;  $P > 0.1$ , Mardia's linear-circular correlation coefficient) indicating that the suggested additional nonlinearity was not present in IC.

In contrast to DNLL, there was a significant correlation between the SI and the best IPD in the IC ( $r = 0.15$ ,  $P \leq 0.05$ , Mardia's linear-circular rank correlation), and a weak but significant positive correlation between the phase disparity and the best IPD ( $r = 0.09$ ,  $P = 0.015$ , Mardia's circular-circular rank correlation coefficient<sup>10</sup>). Visual inspection of the relationship (Figure 3.15a) showed that as the magnitude of the best IPD increased, the asymmetry also increased, in line with the hypothesised effect of the inhibition.

Of the eight responses with negative best IPDs, only four had positive skews. The neuron with the largest SI showed a very eccentric bimodal tuning curve; the other three neurons had best IPDs close to zero, and were consistent with main cluster of data points in the distribution. There was a much greater proportion of neurons with positive best IPDs and negative skews in the IC ( $19/55$  neurons) than in the DNLL ( $P = 0.023$ , Z-test) which did not appear to a consequence of noisy tuning curves. The large number of such neurons indicates that zero SI does not appear to correspond to zero best IPD as predicted by the carving model.

<sup>10</sup> Throughout this text, in the context of Mardia's circular-circular rank correlation,  $r$  refers to the normalised correlation coefficient  $r_0$ .

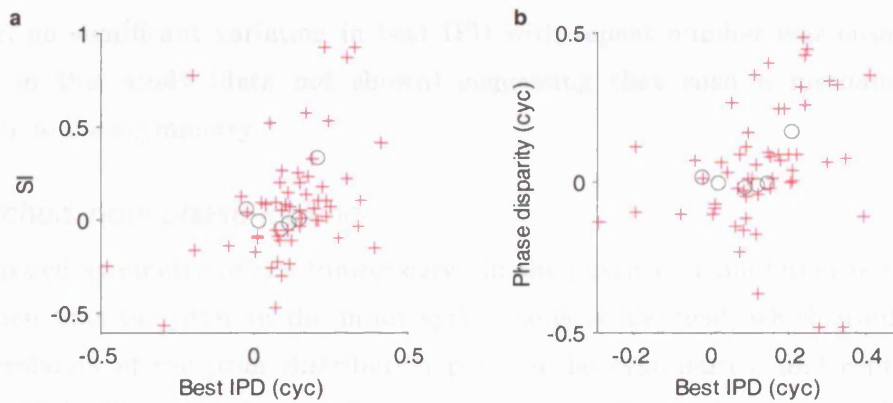


**Figure 3.15 Relationship between tuning an asymmetry for tone-delay functions in IC.** **a**, the relationship between SI and the best IPD. **b**, the relationship between phase disparity and best IPD. The asymmetry increased with best ITD.

## 3.4 Discussion

In this chapter, a previously developed model of the effect of inhibition in the MSO was extended to consider the effect of inhibition on more plausible harmonically distorted inputs to the MSO. The internal delay produced by the model was frequency-dependent and so capable of delaying different harmonic distortions by different time delays, producing an asymmetric tuning curve. Responses recorded in both DNLL and IC showed a bias towards positive best IPDs and positive skews, in broad agreement with the predictions of the model. However, when examined in more detail, the shape of the tuning curve did not appear to agree with that predicted by the model.

### 3.4.1 Alternative sources of asymmetric tuning curves

Before considering what conclusions can be made from the shape of tuning curves observed in IC and DNLL, it is necessary to consider alternative mechanisms capable of generating the observed asymmetry.

#### *Adaptation and plasticity*

A common explanation for a similar asymmetry observed in binaural beat stimuli (where the IPD is dynamically varied) is spike-rate adaptation. In the experiments presented here, any such effects were controlled for by allowing the neuron time to recover between presentations, and by presenting the stimuli in pseudorandom order. It is therefore unlikely that spike-rate adaptation would have had any systematic effect on the tuning curve shape.

An alternative form of adaptation that might explain the asymmetry would be some context-dependent plasticity in the shape of the tuning curve. For example, it is known that neurons in IC adjust their spike-thresholds over time in order to keep the dynamic range of their level tuning curves around recently experienced sound levels (Dean et al. 2005). If the best IPD was not stable over the course of the recording, a skewed tuning curve could result.

However, no significant variation in best IPD with repeat number was observed for the neurons in this study (data not shown) suggesting that such a mechanism did not contribute to the asymmetry.

### *Mismatched input phase-locking*

The supposed symmetry of the tuning curve in the absence of inhibition is based on the assumption that the jitter in the input spike trains is identical, which would cause the cross-correlation of the jitter distribution  $p_x(\tau)$  to be symmetrical and centred at zero. However, if the jitter distributions for the two inputs differed, then this would not be the case— $v_x(\tau)$  would be asymmetrical in (3.9), producing asymmetric tuning curves without the need for inhibition. Such a difference could arise from a difference in the distribution of the phase of phase locking of the inputs, or from differences in the shape of the jitter distribution itself.

### *Mismatched synaptic time courses*

Similar to the above argument, it can be seen from (3.19) that another way to produce an asymmetric tuning curve in the absence of carving inhibition is for the ipsilateral and contralateral inputs to have different EPSP time courses. If the ipsilateral EPSP were faster than the contralateral EPSP (in both rise-time and decay-time) then the autocorrelation  $e_x(\tau)$ , and consequently the tuning curve, would be shifted away from zero and would show positive asymmetry without the need for inhibition. Such a difference in time course is a consequence of the model of the effect of inhibition in the MSO proposed by Zhou et al. (Zhou et al. 2005), where the contralateral EPSP is slowed relative to the ipsilateral EPSP by the high inhibitory conductance at the soma of the neuron.

### *Stereausis*

In its traditional incarnation, stereausis cannot explain the observed asymmetry. Since the stimulation frequency was held constant over the course of the recording and only the ITD was varied, any interaural difference in group delay would have remained constant. Furthermore, since the harmonics would be expected to be created in phase (or in antiphase) with the fundamental, no phase-disparity could exist, and the resultant tuning curve would be symmetric. Any different group delay applied to distortions created in the cochlea would not affect the tuning curve since, due to the frequency selectivity of the cochlea, they would be represented in a separate tonotopic lamina from the fundamental.

However, more generally, there may be some variation in the firing properties of neurons across different frequency lamina. Thus, for example, a mismatch in the CF of the inputs might result in a mismatch in input phase locking, which would produce an asymmetric tuning curve as described above. This could be considered an effect of stereausis, albeit in a different sense to that traditionally suggested.

### *Convergent delay-sensitive input*

The most likely confound of the interpretation of asymmetry in the tuning curves arises from the violation of the assumption that the neurons recorded from only receive a single delay-sensitive input from an MSO principal neuron. From (3.9) it can be seen that the proposed effect of inhibition can be equivalently interpreted as a simple linear combination of two delay-sensitive inputs: one input is excitatory with zero best IPD, and the other is a contralateral inhibitory projection with a negative best IPD. In general, (3.9) can be easily reinterpreted to apply to any pair of convergent inputs—the contralateral inhibitory input can be transformed into an ipsilateral excitatory input by setting  $\alpha < 0$  and  $\beta < 0$ , and since convergent input is not constrained to have zero best IPD, the reference (zero) IPD can be freely redefined. Thus, the carving model can be thought of as a specific instance of a more general convergence model defined by a restricted set of parameters.

#### **3.4.2 Explaining the observed asymmetry**

While there are several possible explanations for the observed asymmetry, it may be possible to distinguish between them based on the expected characteristics of the induced asymmetry. In particular, the degree to which carving inhibition and convergence can be distinguished is of interest, as these were felt to be the most likely contenders.

#### *Asymmetry in IC*

As discussed at the start of this chapter, the effects of convergent delay-sensitive input from neurons with different frequency selectivity are expected to be apparent in the IC data. Consider an IC neuron receiving two excitatory inputs from MSO: one *on-CF*, originating within the same frequency lamina as the IC neuron and strong enough that it determines CF; and one *off-CF*, weaker and tuned to different frequency. The best IPD of either input for a given stimulation frequency  $f$  will be

$$\text{best IPD} = CD \times f + CP \quad (3.27)$$

and will be around 0.125 cyc for a pure tone at the input's own CF (Brand et al. 2002). Thus, while the on-CF input would peak at 0.125 cyc, the off-CF input would be expected to peak at some other IPD, resulting in a mismatch in best IPDs. Assuming simple linear combination of the inputs as in (3.9), the mismatch in best IPD would result in an asymmetric tuning curve and would shift the best IPD away from 0.125 cyc, similar to the effect of carving inhibition (as discussed in the previous section). If both inputs had the same best IPD, then no asymmetry would be expected and the best IPD would not be affected. If the off-CF input had a best IPD 0 to 0.5 cyc greater than that of the on-CF input, then positive asymmetry would result and the best IPD would be shifted up towards higher values. If the off-CF input had a best IPD 0 to 0.5 cyc less than that of the on-CF input, then negative asymmetry would result and the best IPD would be shifted down towards lower values. The larger the mismatch in best IPD, the stronger the asymmetry and the further the deviation in best IPD.

Such a pattern of convergence would predict the correlation between phase disparity and best IPD seen in Figure 3.15d, with positively skewed tuning curves biased towards higher best IPDs and negatively skewed tuning curves biased towards lower best IPDs, but with zero asymmetry occurring around some positive best IPD. A similar correlation would be predicted for an inhibitory off-CF input.

While, for convergent inputs, the best IPD measured from the phase of the fundamental would not reflect the best IPD of either input, the best IPD measured from the peak of the tuning curve would be largely determined by the best IPD of the stronger on-CF component. This provides an explanation for the fact that the distribution of best IPD estimated from the peak was narrower than that estimated from the phase of the fundamental—the peak ITD reflects the distribution of the best IPD of inputs from a single lamina. This potentially large discrepancy raises the question of which of the two methods should be used to estimate best IPD in IC. Estimating the best IPD from the peak of the tuning curve would better reflect the tuning of a single input and could have a significant effect on the shape of phase plots in the IC.

Finally, for high input power ratios and large differences in best IPD, convergent input would result in a bimodal tuning curve, with each mode produced by the peaks of the underlying tuning curves. Such neurons are responsible for the observed power ratios of around 0 dB, which show roughly the same degree of modulation to the second harmonic as to the fundamental.

### *Asymmetry in DNLL*

The negative correlation between the phase disparity and the power ratio observed in the DNLL was not predicted by the model of carving inhibition. One possible explanation is that this correlation was introduced by nonlinear processing in MSO or DNLL not accounted for by the model. If the firing rate of a DNLL neuron were nonlinearly sensitive to an input with an asymmetric tuning curve

$$r_{\text{DNLL}}(\tau) = f[r_{\text{asym}}(\tau)] \quad (3.28)$$

then additional harmonics would be created by the nonlinearity  $f[\cdot]$ . These harmonics would be created in phase with the fundamental and so decrease the phase disparity of the harmonics, reducing the asymmetry. While some neurons might be strongly nonlinear, with tuning curves showing a high power ratio and a low phase disparity, others may be more linear, showing a lower power ratio and a higher phase disparity. This different degree of linearity in the population could explain the reduction in phase disparity at higher power ratios. Any additional nonlinearity could also arise in the MSO from a different relationship between subthreshold response and spike output than that described in the model.

An alternative explanation that does not require additional nonlinearity is that the correlation could be a consequence of convergence in the DNLL. If a neuron in DNLL received two excitatory inputs from MSO, with symmetric tuning curves and similar best

IPDs, then the asymmetry of the resulting tuning curve would be slight but the power ratio would be high. If the best IPDs were moved slightly further apart, then the asymmetry would increase and the power ratio would decrease, since the second harmonics of the two inputs would be closer to being in antiphase than would the fundamentals. Thus, the correlation between the phase disparity and the power ratio could be a consequence of a variation in the difference in best IPD of convergent inputs. Such a mismatch in best IPD may arise from random differences in best IPD for neurons of the same CF, or it may result from a small mismatch in the CF of the inputs. It is worth noting that if the output of DNLL were additionally nonlinearly dependent on the sum of its convergent inputs, then a further reduction in the asymmetry at higher power ratios would be expected.

Both the model of carving inhibition and the proposed pattern of convergence illustrated above predict a positive correlation between the best IPD of the tuning curve and the phase disparity. Such a correlation was not observed in DNLL, which favours an origin of asymmetry unrelated to any mechanism affecting best IPD.. However, the narrow range of best IPDs in DNLL and any reduction in the phase disparity by an additional nonlinearity would have made it difficult to observe any correlation. With more data, such a correlation may have become apparent.

There is evidence that a relationship between ITD tuning and asymmetry does exist. In agreement with the findings here, Seidl and Grothe (Seidl & Grothe 2005) found that the maximum slopes of DNLL tuning curves in the gerbil were on the left-hand slope of the tuning curve implying that they were positively skewed. More interestingly, for animals with abnormal development of inhibitory synapses in MSO (due to being reared in omnidirectional white noise), the peak of the tuning curves was distributed around zero and that the maximum slope was on the side of the curve *nearest zero* as would be expected from the carving model. However, this does not rule out a convergence mechanism as any effect on the tuning curves in MSO would also influence the pattern of convergence in DNLL.

While the presence of convergent delay-sensitive input has been previously observed in IC (McAlpine et al. 1998), this was only possible for inputs where there was a large difference in CF. Because of the narrow range of SI values and best IPDs observed in DNLL compared to IC, it seems likely that any mismatch in CF in DNLL is likely to be small and that a similar approach would be unlikely to be successful. Another approach, if the convergent input were of mixed polarity, would be to use the iontophoretic application of inhibitory neurotransmitter antagonists in the DNLL to attempt to reveal a change in the symmetry. However, if some asymmetry remained, it would still not be possible to determine whether this was due to asymmetry in the MSO tuning curve or due to the convergence of excitatory inputs.

### *Asymmetry in MSO*

The negligible asymmetry demonstrated by neurons recorded in studies in MSO suggests that the model of carving inhibition presented here is inadequate at predicting the effect of inhibition at the MSO. However, the analysed data set may be biased towards more symmetric tuning curves. Firstly, there is a possibility that other authors may have had an unconscious preference for more symmetric tuning curves when selecting exemplars. Secondly, the median best IPD for the available data was only 0.06 cyc, suggesting a bias towards low best IPD neurons, which are expected to show lower asymmetries. Finally, the median power ratio was  $-12$  dB, which, for the DNLL, would lie within the range for which the phase-disparity was highly attenuated. Comparing the data from MSO with that from DNLL, little difference was observed between the tuning curves in MSO and those obtained from high power ratio, low best IPD neurons in DNLL. Thus, the lack of asymmetry in MSO may be explained by a biased data set or a consequence of an additional nonlinearity not accounted for in the model. However, without direct evidence from the MSO it is impossible to determine which (if any) of these possibilities is the case.

### **3.4.3 Conclusion**

The proposed mechanism of carving inhibition can produce a frequency-dependent delay that can lead to asymmetry in the tuning curves of delay-sensitive neurons. However, a similar effect is predicted by the convergence of multiple delay-sensitive inputs at the level of the IC and the DNLL. While the DNLL appeared to be a better proxy for the MSO than the IC, it was not possible to be certain that the observed asymmetry was due to carving inhibition. In order to progress on this particular question, it is necessary to record directly from the MSO. However, as stated earlier this is an unattractive option due to the difficulty involved.

# 4

## ASYMMETRY IN RESPONSES TO NOISE STIMULI

---

### 4.1 Introduction

So far, the analysis of the tuning properties of neurons has focused upon their responses to interaurally delayed pure-tone stimuli. However, neurons show sensitivity to a broad range of sound-frequencies, the response to each of which can be subjected to a different internal delay despite travelling through the same pathways. The purpose of the study presented in this chapter was to address the effect of frequency-dependent delays on spectrally rich stimuli containing multiple frequency components.

The *noise-delay function* is a tuning curve recorded from a neuron by presenting a broadband-noise stimulus binaurally and varying the interaural time difference. It is ethologically more relevant than pure tones, since neurons can respond to the frequencies in which they are more interested (as defined by their frequency tuning curves). The noise-delay function takes the form of a damped sinusoid with a carrier frequency around the CF of the neuron (Figure 4.1). The degree of damping reflects the bandwidth of the frequency selectivity of the neuron, with broader bandwidths producing more damped responses (Yin et al. 1986, Chan et al. 1987, Yin et al. 1987, Joris et al. 2005). It is similar in appearance to the *composite delay function* formed from the sum of several tone-delay functions recorded for pure-tones across the range of frequencies for which the neuron is sensitive. However, there is disagreement as to how similar these two different tuning curves actually are.

Neurons in IC are often divided into *peak-type* neurons (Figure 4.1a) and *trough-type* neurons (Figure 4.1b). The majority of neurons recorded in IC are peak type, which make show a dominant central peak in their noise-delay function, and are thought to inherit their ITD sensitivity from MSO. Trough-type neurons show a prominent central trough in their noise-delay functions, and are thought to inherit their ITD sensitivity from LSO.

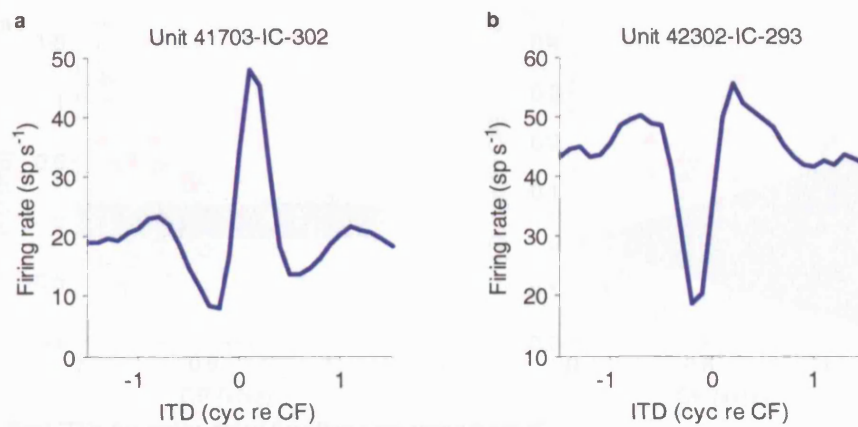


**Figure 4.1** Examples of noise-delay functions recorded from IC.

**a**, a peak-type response. The response showed a prominent central peak at positive ITDs. The CF for this neuron was 302 Hz. **b**, a trough-type response. The response showed a prominent central trough at negative ITDs. The CF for this neuron was 293 Hz.

## 4.2 The distribution of best ITD

The *best ITD* is defined as the ITD at which the noise-delay function is maximal. For peak-type neurons, it provides a measure of the internal delay of the MSO neuron from which the neuron under investigation inherits its ITD sensitivity.

Noise-delay functions were obtained for 28 IC neurons and 14 DNLL neurons. Full details of procedures and stimuli are presented in the Methods chapter (Section 2.4.2). Briefly, broadband noise stimuli (0.05 to 5 kHz) were digitally generated, and binaurally presented with some time delay applied to the stimulus in the contralateral ear. Three IC neurons were trough-type and so were excluded from analysis.

The best ITD was determined for each neuron by smoothing the noise-delay function and locating zero crossings in its first derivative (see Section 3.3.2 for detailed methods). The ITD at which the gradient of the function was maximal (most positive) was also of interest, and so was determined from zero crossings in the second derivative of the tuning curve.

### 4.2.1 The distribution of best ITD in IC

The distribution of best ITD observed in IC was in line with previous findings in the IC of the guinea pig (McAlpine et al. 2001) and cat (Hancock & Delgutte 2004). Best ITDs were largely outside of the physiological range ( $\pm 150 \mu\text{s}$ ) and showed a negative correlation with CF (Figure 4.2a;  $r = -0.60$ ,  $P = 0.0016$ , Spearman's rank correlation coefficient). Based on a much larger sample size, McAlpine et al. concluded that the best ITD was relatively constant when expressed in terms of cycles of CF and distributed around 0.125 cyc re CF (McAlpine et al. 2001, Palmer et al. 2002). Figure 4.2b shows the best ITD expressed in cyc re CF. While the median value was 0.14 cyc re CF (interquartile range 0.09 to 0.17 cyc re CF) there was still significant correlation with CF ( $r = 0.46$ ,  $P = 0.020$ , Spearman's rank correlation coefficient). This also appeared to be true for the data in the

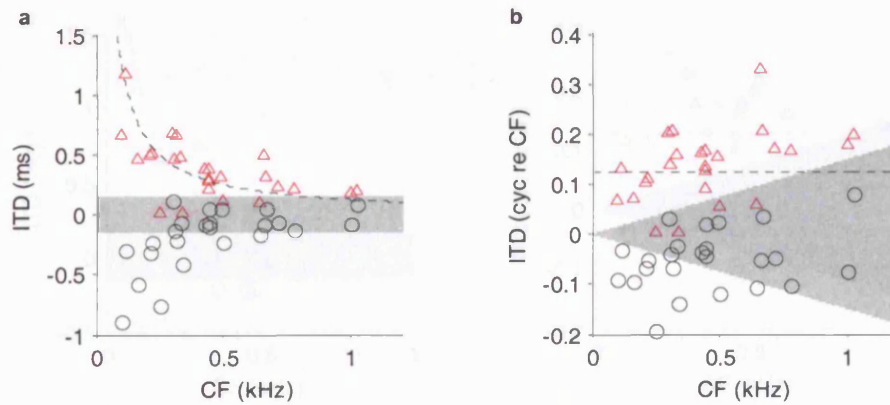


**Figure 4.2 Best ITDs for noise-delay functions recorded from IC.**

**a**, the distribution of the best ITD (red triangles) of peak-type neurons as a function of CF. The ITD at which the tuning curve has maximum gradient is also shown (black circles). Both the best ITD and slope ITD were CF-dependent. **b**, the same data as in **a**, expressed in terms of the period of CF. Note that while the best ITD was largely outside the physiological range (grey area), the slope ITD was inside the physiological range at the higher frequencies. The dotted line represents the inverse relationship between best ITD and CF where best ITD is 0.125 cyc re CF. The data only loosely followed this relationship.

### 4.3 The Gabor model

original study (McAlpine et al. 2001) but was not discussed. Thus the assertion that the data is distributed around 0.125 cyc re CF is only a coarse description of the distribution.

The ITD of maximum gradient (the *slope ITD*) was positively correlated with CF ( $r = 0.59$ ,  $P = 0.002$ , Spearman's rank correlation coefficient), but largely confined to the physiological range. When the slope ITD was expressed in units of cyc re CF, this correlation disappeared ( $P = 0.41$ ), and the slope ITD showed a median value of  $-0.05$  cyc re CF (interquartile range  $-0.09$  to  $-0.03$  cyc re CF). While the distribution of the obtained values of slope ITD are in agreement with those obtained by others, the CF dependence of this slope ITD is a novel finding.

#### 4.2.2 The distribution of best ITD in DNLL

Figure 4.3a shows the location of best ITD (measured in ms) as a function of the CF for 14 neurons in the DNLL. In agreement with the IC, the best ITD was negatively correlated with CF ( $r = -0.66$ ,  $P = 0.013$ , Spearman's rank correlation coefficient), and all but one neuron showed best ITDs outside of the physiological range. After being converted into units of cyc re CF (Figure 4.3b), the best ITD was found to be independent of CF ( $P = 0.23$ ) with a median value of 0.16 cyc re CF (interquartile range 0.12 to 0.18 cyc re CF). However, the best ITDs observed in DNLL did not appear to be different from those in observed in IC.

Unlike the IC, the slope ITD in DNLL was independent of CF (Figure 4.3a;  $P = 0.33$ , Spearman's rank correlation coefficient), with a median value of  $-90$   $\mu$ s (interquartile range  $-10$  to  $-220$   $\mu$ s). The median slope ITD was not significantly different from zero ( $P = 0.057$ , sign test) suggesting that the distribution was centred at 0  $\mu$ s. However, the observed distribution did not appear to be different from that observed in IC, and the lack of correlation with CF was likely a consequence of fewer recordings of the very lowest frequency neurons from the DNLL.

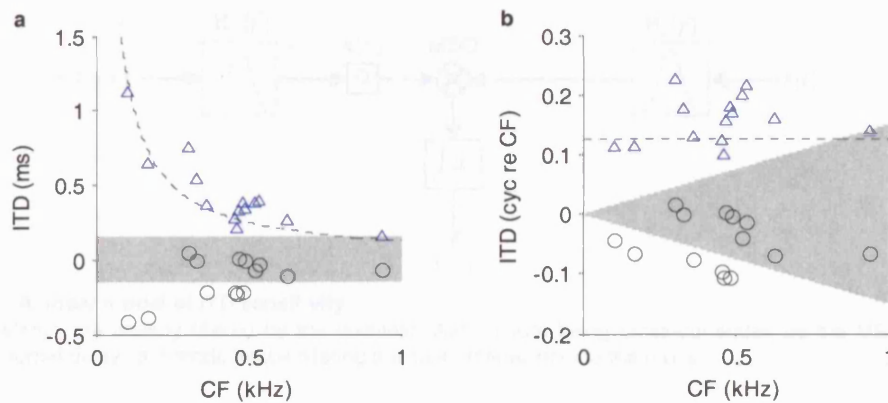


**Figure 4.3 Best ITDs for noise-delay functions recorded from DNLL.** **a**, the distribution of best ITD (blue triangles) of peak-type neurons as a function of CF. The ITD producing the maximum gradient (black circles) is also shown. **b**, the same data as in **a**, expressed in cyc re CF. The relationship was similar to that observed in IC (Figure 4.2).

### 4.3 The Gabor model

If the Jeffress model were correct, the delay line system would have to be such that neurons with lower CFs would have larger path-length differences than neurons with higher CFs. The time delay introduced by these path-length differences would therefore result in the observed CF dependency of the best ITD. In contrast, the model of carving inhibition presented in Chapter 3 is capable of producing both time and phase delays, depending on the timing and strength of the inhibitory input. This provides an alternate explanation for the CF-dependence of the best ITD observed in mammals. If units with different CFs all received carving inhibition that resulted in a phase delay of 0.125 cyc, then an inverse relationship between CF and best ITD would be produced. It was therefore of interest to examine the contribution of time and phase delays to noise-delay functions, to establish which played the dominant role in the determination of best ITD.

Gabor functions (Gabor 1946) have been previously used in visual neuroscience to model simple cell receptive fields (Marcelja 1980) and binocular disparity tuning curves (Sanger 1988, Nieder & Wagner 2000). In the temporal domain, Gabor functions are sinusoids modulated by Gaussian envelopes, which appear similar to noise-delay functions. Because a Gabor function is expressed in the frequency domain by a Gaussian power spectrum and a linear phase spectrum, it can be thought of as a model of the composite curve resulting from the sum of sinusoidal tone-delay functions for a neuron with a linear phase plot and a Gaussian frequency-tuning curve. If the system were linear, then the noise-delay function would be expected to be identical to this composite curve. By fitting Gabor functions to noise-delay functions, various parameters of interest can be estimated (McAlpine & Palmer 2002), including the relative contributions of phase and time delays to the best ITD (Wagner & Frost 1993).

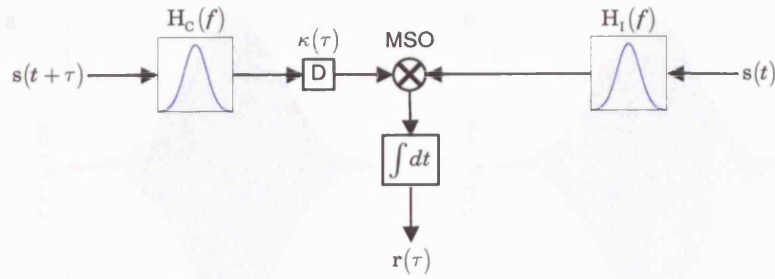


**Figure 4.4** A linear model of ITD sensitivity.

Input noise stimuli are linearly filtered by the cochlear filters before being cross-correlated by the MSO. Frequency-dependent internal delays are modelled by filtering the contralateral input to the model.

### 4.3.1 Derivation of the model

The suitability of the Gabor function as a model of noise-delay functions can be derived by extending the model introduced in the previous chapter (Section 3.2) to noise stimuli. Compared to peripheral responses to tones, little is known about the peripheral response to noise. For simplicity, the input was assumed to be narrowband filtered by the cochlea, and it was assumed that the postsynaptic response in the MSO would follow the shape of the resulting waveform. The MSO itself was modelled as a cross-correlator (as in the previous chapter), and rather than modelling carving inhibition, a more general frequency-dependent internal delay was modelled by filtering the contralateral input to the MSO. A schematic of the resulting model is shown in Figure 4.4.

Assuming that the input stimulus  $s(t)$  is sufficiently broadband so as to be correlated with itself only at zero lag, the predicted response of the neuron will given by

$$r(\tau) = a_0 + a_1 h_x(\tau) * \kappa(\tau) \quad (4.1)$$

where  $h_x(\tau)$  is the cross-correlation of the impulse responses of the cochlear filters and  $\kappa(\tau)$  is a filter implementing the frequency-dependent delay. If the cochlear filters are assumed to be identical (i.e. no stereausis) and to have Gaussian frequency selectivity, then  $h_x(\tau)$  will be a Gabor function

$$h_x(\tau) = \exp[-\pi b^2 \tau^2] \cos(2\pi f_c \tau) \quad (4.2)$$

where  $f_c$  is the centre frequency of the cochlear filters and  $b$  is their *equivalent rectangular bandwidth*<sup>11</sup> (Appendix 8.1). For simplicity, the frequency-dependent delay is assumed to be linear with a nonzero characteristic phase, and any frequency selectivity of  $\kappa(\tau)$  is ignored. This produces the prediction that the output of the MSO can be described by the Gabor function

$$r(\tau) = a_0 + a_1 \exp[-\pi b^2 (\tau - \tau_0)^2] \cos[2\pi f_c (\tau - \tau_0) + \phi_0] \quad (4.3)$$

where  $a_0$ ,  $a_1$  are linear coefficients, and  $\tau_0$  and  $\phi_0$  are the characteristic delay and the characteristic phase of the internal delay.

<sup>11</sup> The equivalent rectangular bandwidth (ERB) of a filter is defined as the width in hertz of a boxcar filter with equivalent total power and equivalent peak power as the filter in question.

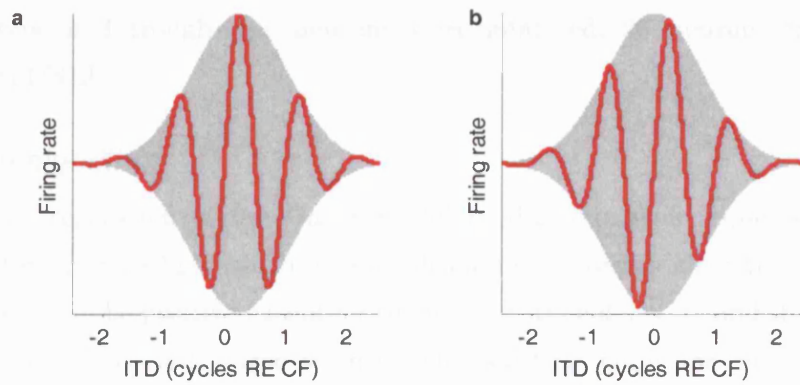


**Figure 4.5** Noise-delay functions predicted by the Gabor model.

Noise-delay functions (red curve) with best ITDs of 0.25 cyc re CF implemented by **a**, a pure time delay and **b**, a pure phase delay. The time delay shifts both the envelope (grey) and the carrier (red), whereas the phase delay only shifts the carrier, leaving the envelope peaking at zero ITD. Note the asymmetric side peaks and side troughs in **b**.

Since the noise-delay functions of interest are obtained from either the IC or DNLL, the neuron being recorded from may have some effect on the tuning curve. For simplicity, it is assumed that each neuron receives only a single delay-sensitive input and that the output firing rate of the neuron is linearly related to the input firing rate. However, since neurons cannot fire at negative firing rates, the response is half-wave rectified. This gives the final model for IC and DNLL responses

$$r(\tau) = \left\{ a_0 + a_1 \exp\left[-\pi b^2 (\tau - \tau_0)^2\right] \cos\left[2\pi f_c (\tau - \tau_0) + \phi_0\right] \right\}_+ \quad (4.4)$$

While this model makes several assumptions that might not be reasonably expected to hold, it was hoped that it would serve as a reasonable approximation and thereby provide estimates of the parameters of interest when regressed to data obtained from DNLL and IC.

### 4.3.2 Phase delays and carrier asymmetry

The CD and CP parameters of the Gabor model provide a means through which to estimate the time and phase contributions to the best ITD. If the internal delay for a given neuron were purely composed of a Jeffress-like time delay with no CP (i.e. if  $\phi_0$  were zero), then the carrier component of the response would peak at the same delay as the envelope, resulting in side troughs and side peaks of equal height (Figure 4.5a). However, if there were some characteristic phase, it can be seen from (4.4) that the sinusoid would be shifted within the envelope, causing the side peaks and side troughs to be different heights (Figure 4.5b). Since such carrier asymmetry is often observed in IC noise-delay functions (see Figure 4.1), it was felt that there could be a strong phase contribution to the internal delay that was not evident when probing the system using tones.

### 4.3.3 Results

The model in (4.4) was then fitted to the recorded noise-delay functions by finding the parameters which minimised the sum-squared error between the estimate and the data.

Both peak-type and trough-type neurons were analysed, 28 neurons from IC and 14 neurons from DNLL.

### *Regression algorithm*

The nonlinear regression of the Gabor model to the data was implemented using the Matlab function `lsqnonlin`, which uses a subspace trust-region algorithm. All parameters were constrained to be positive except for the internal time delay  $\tau_0$  and the internal phase delay  $\phi_0$ , which were left unconstrained. The starting point for each regression was determined from a rough estimate of the parameters of each tuning curve. The initial carrier frequency  $f_c$  (measured in kHz) was set to the CF of the neuron and the bandwidth  $b$  (in kHz) was then estimated from  $f_c$  using the equation

$$b = 0.3f_c^{0.56} \quad (4.5)$$

which gives the ERB bandwidth of guinea-pig auditory-nerve frequency-tuning curves as a function of their characteristic frequency (Evans 2001). The baseline firing rate in response to uncorrelated noise was estimated from the response to the most negative ITD presented, and a rough estimate of the envelope of the function was then constructed by smoothing the squared deviation of the data from this baseline with a five-point moving average filter. The centroid of this envelope was then used as an estimate of the internal time delay  $\tau_0$ . The internal phase delay  $\phi_0$  was then estimated from the phase of the frequency component of the response with frequency  $f_c$ , adjusted for  $\tau_0$ . Estimates for  $a_0$  and  $a_1$  were initially set to zero and one respectively; by performing a linear regression of the Gabor function produced from (4.3) using these estimates to the data, it was possible to improve the estimates of the linear coefficients  $a_0$  and  $a_1$ .

### *Results of regression*

Some examples of fits resulting from the regression procedure are shown in Figure 4.6 and the fitted parameter values in Table 4.1. The regression converged for all neurons within a median 15 iterations. The median  $R^2$  statistic for the IC data was 0.82 (interquartile range 0.73 to 0.91) and 0.91 (0.85 to 0.94) for the DNLL. The  $R^2$  statistic was significantly higher for the DNLL fits than the IC fits ( $P = 0.018$ , Wilcoxon rank-sum test), suggesting that the DNLL data were better described by the Gabor model. However, although a large amount of the variance was explained by the model, the residuals showed significant ITD-dependence for most of the responses (DNLL:  $\frac{9}{14}$  neurons, IC:  $\frac{19}{28}$  neurons;  $P > 0.05$ , Wald-Wolfowitz runs test). This indicated that the Gabor model did not completely capture the shape of the noise-delay functions.

For many of the fits (Figure 4.6a–c, f), the majority of the explained variance arose from fitting only the main peak and main trough of the data. The regression algorithm achieved this by overestimating the bandwidth parameter, which narrowed the envelope of the fitted function so that it covered fewer periods of the sinusoidal component than were present in the data. Any periods outside the envelope were effectively ignored, fitted with a flat line.

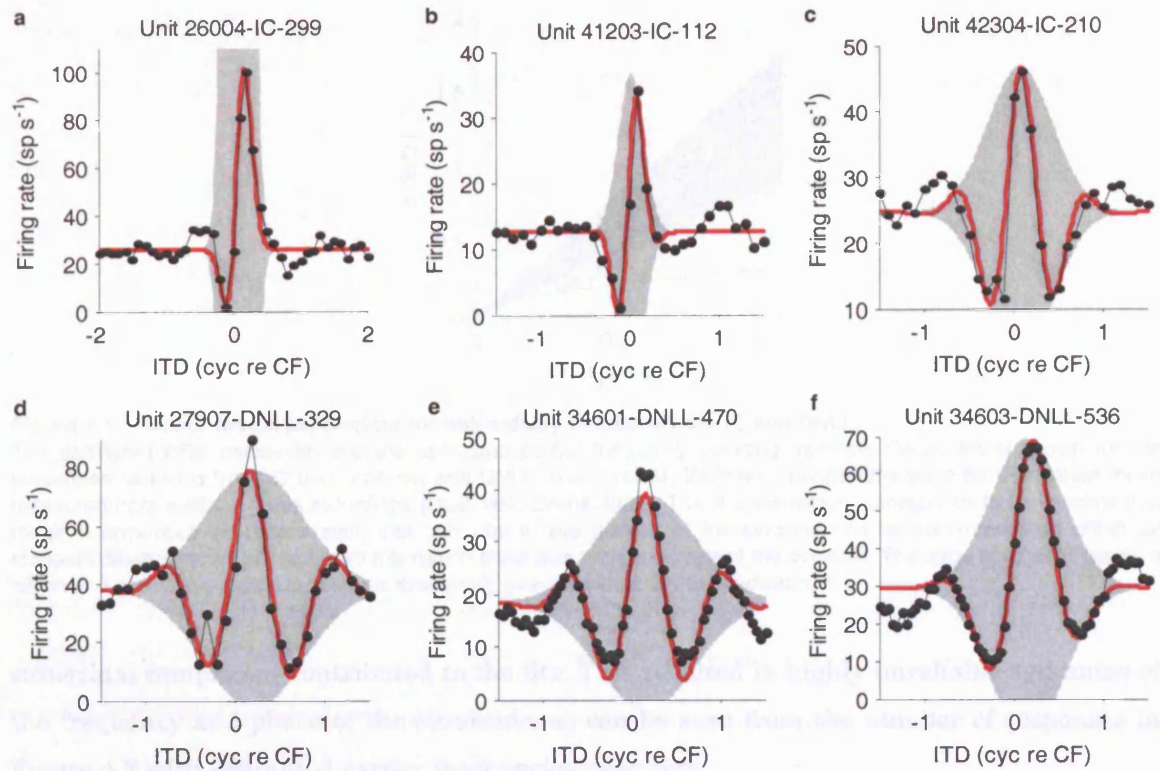


**Figure 4.6** Gabor fits of noise-delay functions from IC and DNLL.

Recorded noise-delay functions (black) from the IC (top row) and DNLL (bottom row) are shown overlaid on top of the fitted Gabor functions (red). The envelope structure of the fitted waveform is shown in grey. See Table 4.1 for estimated parameters, characteristic frequencies, and  $R^2$  values. The bandwidths of the responses were overestimated leading to non-central peaks and troughs being ignored. This is most evident in a, where the overestimation of the bandwidth resulted in a large underestimation of the carrier frequency.

ID	CF (Hz)	$R^2$	Parameter Estimates					
			$a_0$ (sp s <sup>-1</sup> )	$a_1$ (sp s <sup>-1</sup> )	$f_c$ (Hz)	$b$ (Hz)	$\tau_0$ ( $\mu$ s)	$\phi_0$ (cyc)
26004	299	0.94	25	1178	23	895	277	0.24
41203	112	0.88	12	24	186	310	234	0.17
42304	220	0.81	25	22	268	228	376	0.03
27907	329	0.89	38	41	332	237	662	-0.05
34601	470	0.91	18	21	516	347	364	-0.01
34603	536	0.92	29	40	461	525	283	-0.07

**Table 4.1** Results of the Gabor fits in Figure 4.6.

This neglect of the response at more extreme ITDs had little impact on the total squared error, due to comparatively little of the total variance being present at these ITDs.

This overfitting of the central portion of the response can be seen for the population as a whole from the range of bandwidth parameters resulting from the regression (Figure 4.7). The estimated bandwidths were all higher than expected from auditory nerve recordings in the guinea pig (Evans 2001). Many bandwidths were so broad that fewer than two cycles of the sinusoid occurred within  $\pm 2$  standard deviations of the envelope, suggesting that at least one of the side peaks or side troughs visible in the response was ignored by the fitted model. For some neurons (Figure 4.6a), the estimated envelope was narrower than half the period of the sinusoid, with the consequence that only a single maxima or minima of the

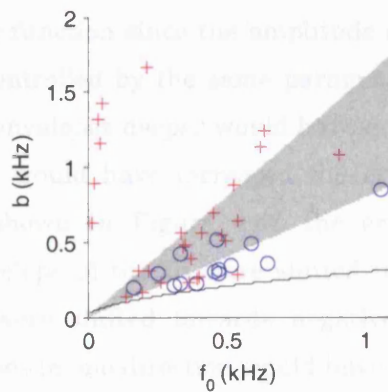


**Figure 4.7 Gabor model parameters for noise-delay functions from IC and DNLL.**

The estimated ERB bandwidth and the estimated carrier frequency resulting from the Gabor fits is shown for the responses recorded from IC (red crosses) and DNLL (blue circles). Estimated bandwidths were far wider than those measured from auditory nerve recordings (black line, Evans 2001). The shaded region corresponds to bandwidths that result in envelopes so narrow such that only one to two periods of the sinusoid can be accommodated within  $\pm 2$  standard deviations. All points above this region show less than one cycle of the sinusoid. The large number of neurons within and above this region indicates a systematic overestimation of the bandwidth.

sinusoidal component contributed to the fits. This resulted in highly unreliable estimates of the frequency and phase of the sinusoids, as can be seen from the number of responses in Figure 4.7 with estimated carrier frequencies near zero.

One possible reason for the tendency to focus on the data at more central ITDs was the higher intrinsic variance of such data points due to their higher firing rates. In order to compensate for this ITD dependency in the underlying variance, the fitting was repeated using a least-squares regression that was unweighted by the inverse square of the firing rate at each ITD. However, this change made little difference to the results, suggesting that this was not the factor responsible for the overestimation the bandwidth.

Another possible reason for the overestimation of the bandwidth was that the regression algorithm might have converged upon a local solution. In order to attempt to locate any global minimum, a number of variations on the regression procedure were tested: different methods for estimating the initial parameters, different regression algorithms, and taking the best of several regressions obtained using different initial estimates. Although inaccurate initial estimates could lead to very poor fits, the results presented in this chapter were generally robust. In a final attempt to force the algorithm not to ignore the side peaks of the response, the bandwidth was constrained to lie within a likely range of values. However, in such cases the algorithm set the bandwidth to the maximum possible, which produced a lower  $R^2$  than when the bandwidth was unconstrained. Thus, the overestimation of the bandwidth did not result from a failure to find the global minimum in the parameter space.

Instead, the main reason for the failure appeared to be a difference between the envelope structure of the responses and the envelope structure of the Gabor model. For example, while what appeared to be a reasonable fit was achieved for the response shown in Figure 4.6e, the error could have been reduced further if the *positive envelope* (the upper envelope) of the fit were made a little deeper and narrower, and the *negative envelope* (the lower envelope) a little shallower and broader. However, these are clearly contradictory

transformations for the Gabor function since the amplitude and width of both the positive and negative envelopes are controlled by the same parameters and are constrained to be identical. While making both envelopes deeper would have decreased the error arising from the peaks of the response, it would have increased the error arising from the troughs. Similarly for the response shown in Figure 4.6f, the error could have been further minimised if the positive envelope of the fit were shifted towards positive ITDs and the negative envelope estimate were shifted towards negative ITDs. Again, this was not possible. Shifting both envelopes in one direction would have decreased the error arising on one side of zero but would have increased it on the other. By overestimating the bandwidth, thereby narrowing both envelopes, any areas of the response that contradicted the Gabor model could effectively be ignored by the minimisation algorithm. The failure to increase the explained variance at extreme ITDs was compensated for by concentrating on the fine-detail of the response at central ITDs. The overestimation of bandwidth (and the significant residual variance) indicates that Gabor functions are not suitable models of noise delay responses in the IC and the DNLL.

## 4.4 Envelope asymmetry

The *dual-delay function* (Yin et al. 1987) is the tuning curve recorded in response to a binaurally presented noise stimulus with both an interaural time difference (ITD) and an additional interaural *phase* difference (IPD). This is achieved by presenting a noise stimulus that has been both time and phase shifted (via the Fourier transform) to one ear and the original stimulus to the other. For the linear Gabor model, a phase delay of one of the input stimuli is equivalent to an internal phase delay of the same magnitude. Such a stimulus would therefore be expected to result in a family of noise-delay functions where the carrier for each function is phase-shifted within the envelope of the response (Figure 4.8).

This has the consequence that for a close sampling of IPD, the envelope structure of the response can be clearly observed. It was hoped that this would allow the time and phase contributions to the internal delay to be directly measured from the peak of the envelope and the offset of the sinusoid within the envelope, without having to fit a model to the response. In addition, since this envelope structure appeared responsible for the failure of the regression of the Gabor model, it was hoped that it would reveal those aspects of the Gabor model that made it unsuitable for modelling noise-delay functions.

### 4.4.1 A linear model of dual-delay functions

Before proceeding, it is necessary to consider what form the response to the dual-delay stimulus would take if some of the assumptions underlying the Gabor model were incorrect. The Gabor model can be considered a specific instance of a more general linear model defined by constraining the cochlear filters to be identical with Gaussian frequency

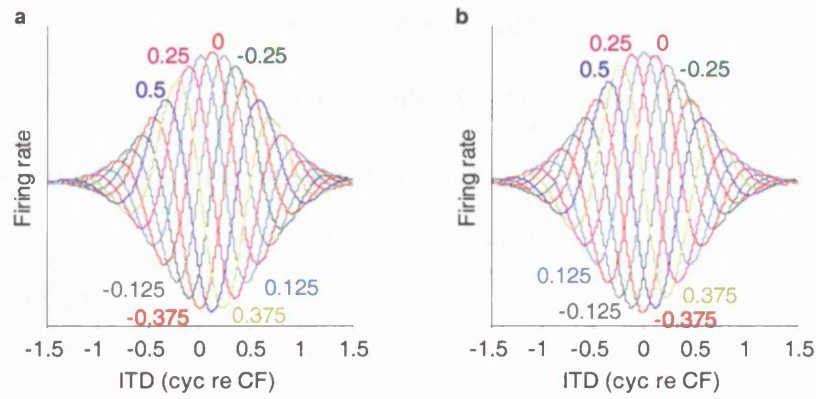


**Figure 4.8** Examples of dual-delay functions predicted by the Gabor model.

The response takes the form of a family of phase-delayed Gabor functions. Coloured numbers indicate the IPD (in cycles) for which the corresponding curve was predicted. **a**, Response predicted for a Gabor model for which the internal delay is a pure time delay (c.f. Figure 4.5a). **b**, Response predicted for a Gabor model for which the internal delay is a pure phase delay (c.f. Figure 4.5b).

selectivity and constraining the internal delay to be linear. The more general model presented in (4.1) is not novel—the filtered and delayed cross-correlation is a common conceptual model for the response of MSO neurons. The addition of the  $\kappa(\tau)$  filter merely allows various internal delay mechanisms to be incorporated.

Since the modelled cochlear filtering is linear, the effect of phase delaying the contralateral noise stimulus relative to the ipsilateral noise stimulus is equivalent to leaving the noise stimulus unchanged but incorporating an additional phase delay into the phase-spectrum of the contralateral filter. This, in turn, will produce an equivalent phase shift in the cross-correlation of the two filters. Thus, for a dual-delay stimulus with an interaural time difference  $\tau$  and an interaural phase difference (IPD)  $\phi$ , the response predicted from (4.1) would be

$$r(\tau | \phi) = a_0 + a_1 h_x(\tau | \phi) * \kappa(\tau) \quad (4.6)$$

where  $h_x(\tau | \phi)$  is the phase-delayed cross-correlation of the cochlear-filter impulse responses and  $\kappa(\tau)$  is an arbitrary filter that can implement any internal delay mechanism.

Since the cochlear filters are expected to be narrowband then the response will be of the form

$$r(\tau | \phi) = a_0 + a_1 e(\tau) \cos[2\pi f_c \tau + \theta(\tau) + \phi] * \kappa(\tau) \quad (4.7)$$

where  $f_c$  is the carrier frequency,  $e(\tau)$  is the *amplitude envelope* and  $\theta(\tau)$  is the *instantaneous phase* of the response (see Appendix 8.2). If  $\kappa(\tau)$  implements linear delay with CD  $\tau_0$  and CP  $\phi_0$ , the response will be given by

$$r(\tau | \phi) = a_0 + a_1 e(\tau - \tau_0) \cos[2\pi f_c (\tau - \tau_0) + \theta(\tau - \tau_0) + \phi - \phi_0] \quad (4.8)$$

Clearly, for such a response, the positive envelope  $+e(\tau - \tau_0)$  and the negative envelope  $-e(\tau - \tau_0)$  are symmetrical.

This can be shown for the more general case in (4.6), without making assumptions about the form of  $\kappa(\tau)$ . If the positive and negative envelopes of the response are defined as the maximum and minimum responses at each ITD

$$e_+(\tau) = \max_{\phi} [r(\tau | \phi)] \quad (4.9)$$

$$e_-(\tau) = \min_{\phi} [r(\tau | \phi)] \quad (4.10)$$

From the linearity of (4.6), it can be seen that since

$$h_x(\tau | \phi + \pi) = -h_x(\tau | \phi) \quad (4.11)$$

it can be shown that

$$e_+(\tau) = a_0 - e_-(\tau) \quad (4.12)$$

Thus, a more general model of the response, based on the filtered cross-correlation of the stimulus and capable of modelling any nonlinear phase plot, predicts that the envelopes should be the same (complementary) shape. This would be expected to hold regardless of the form of the cochlear filters and regardless of whether the delay arose from stereausis, Jeffress-like time delays or carving inhibition.

#### 4.4.2 Results

Dual-delay functions were recorded for 21 neurons from the IC and 15 neurons from the DNLL. Full details of recording procedures and stimuli parameters can be found in the Methods chapter (Section 2.4.3). Briefly, 300 ms noise bursts were presented roughly 20 dB above each neuron's threshold to uncorrelated noise. The ITD between the noise bursts was varied from  $-1.5$  to  $1.5$  cyc re CF while the IPD was varied from  $-0.375$  to  $0.5$  cyc in  $0.125$  cyc steps. All stimuli were presented in pseudorandom order, and a new sample of noise was generated on each presentation.

Examples of responses recorded from DNLL can be seen in Figure 4.9 and examples from IC in Figure 4.10. All responses appeared to be modulated by IPDs, which was confirmed using a modified version of the bootstrap test presented in Chapter 3 ( $P \leq 0.05$ ). This was unsurprising, however, since any neurons not showing IPD-sensitive responses to pure-tone stimuli were abandoned before recording the dual-delay function.

#### *Responses are not symmetrical*

Nearly all of the illustrated responses showed deviation away from the envelope structure predicted by the Gabor model shown in Figure 4.8. In most responses, the positive envelope was deeper than the negative envelope or vice versa (*rate asymmetry*; Figure 4.9b–f; Figure 4.10a–d, f). Furthermore, in many neurons the maximum of the positive envelope and the minimum of the negative envelope were at different ITDs (*delay asymmetry*; Figure 4.9b–c; Figure 4.10b–c), often occurring on opposite sides of zero ITD. Some envelope shapes often did not match at all—in the responses shown in Figure 4.9d and Figure 4.10d, one envelope was bimodal while the other was unimodal.

Such asymmetries provide an explanation of the inability of the Gabor model to fit the responses. In particular, the poor fit to the main peak of the type shown in Figure 4.6e was

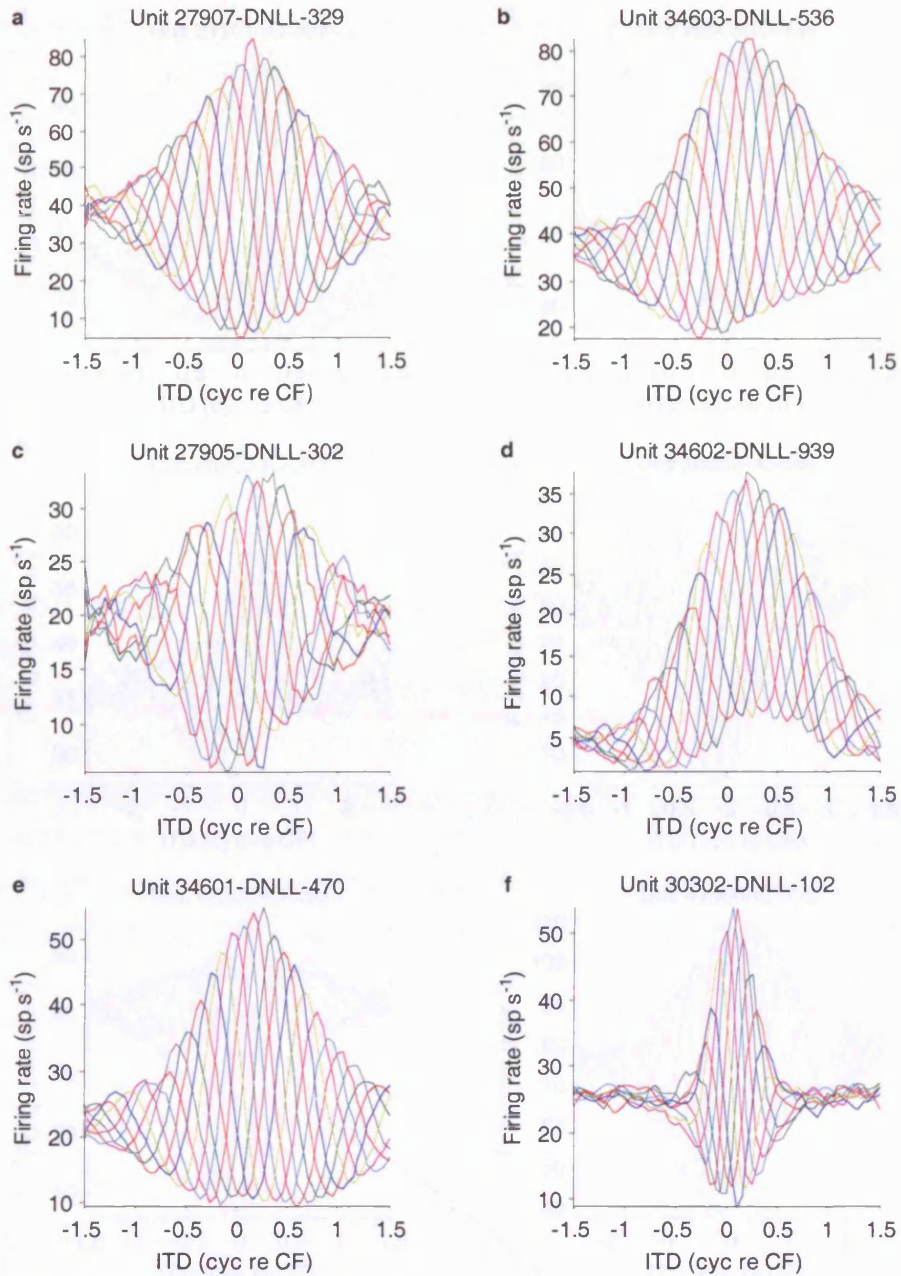


**Figure 4.9** Dual-delay functions recorded from DNLL.

The characteristic frequencies of the neurons were: **a**, 329 Hz; **b**, 536 Hz; **c**, 302 Hz; **d**, 939 Hz; **e**, 470 Hz; and **f**, 102 Hz. Envelope structures were asymmetric; positive and negative envelopes showing different depths, and maxima and minima often at different delays (see the predicted tuning curve in Figure 4.8 for a comparison and colour key).

a consequence of rate asymmetry, and the poor fits in Figure 4.6a, b, f can be accounted for by the presence of the delay asymmetry.

### *Responses are not linear*

Such asymmetries contradicted the prediction that the envelopes should be of the same shape. In order to test whether the data could be described by a linear model, the DC response  $r_0(\tau)$  was determined at each ITD by averaging the responses over IPD. If a response was of the form in (4.6), then when averaging over IPD, antiphasic pairs of stimuli should cancel, producing a constant response independent of the ITD

$$r_0(\tau) = \langle r(\tau | \phi) \rangle_\phi = a_0 \quad (4.13)$$

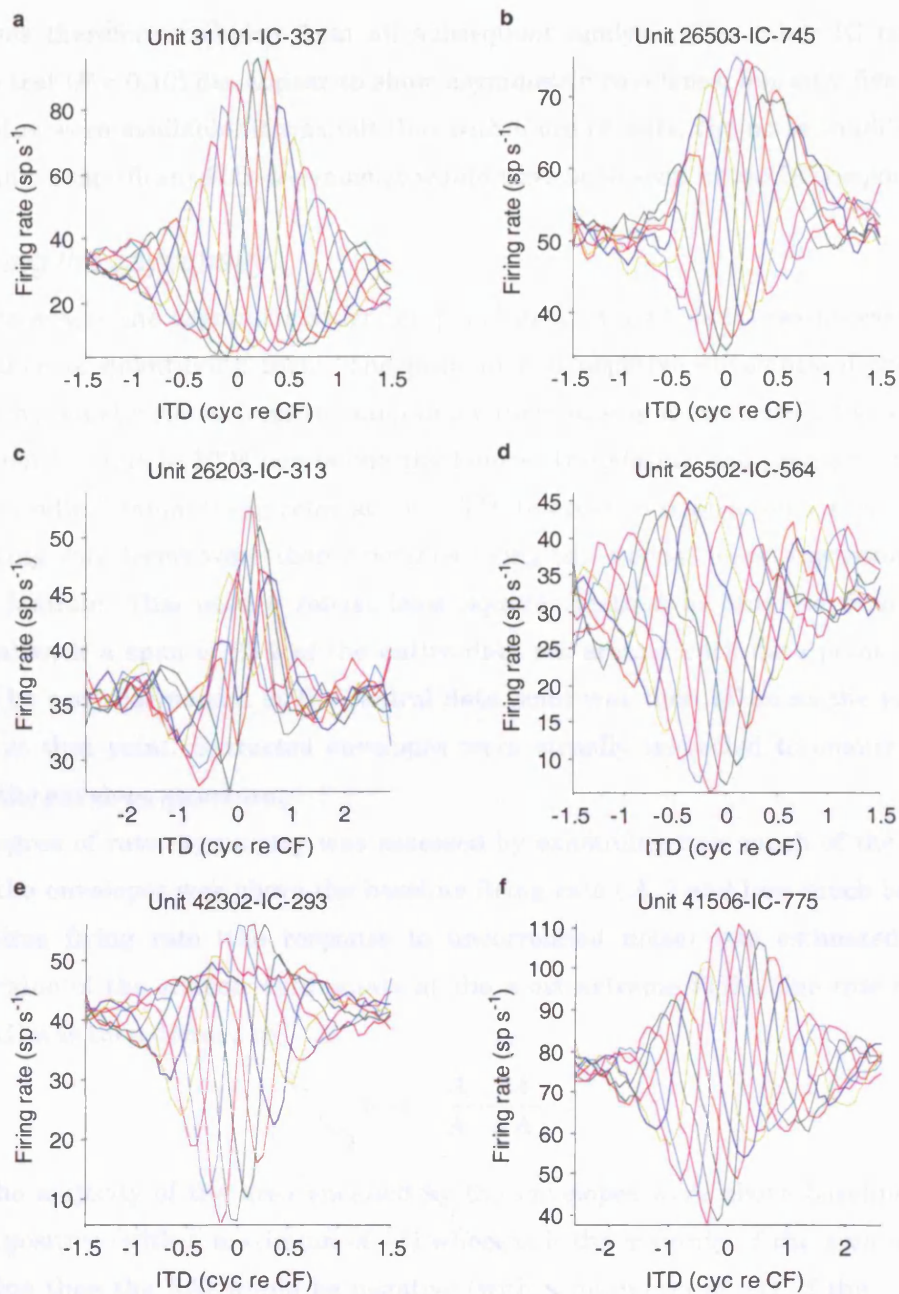


**Figure 4.10** Dual-delay functions recorded from IC.

The characteristic frequencies of the neurons were: **a**, 337 Hz; **b**, 745 Hz; **c**, 313 Hz; **d**, 564 Hz; **e**, 775 Hz; and **f**, 293 Hz. Again, responses showed asymmetric envelope structures (see the narrowband tuning curve in Figure 4.8 for a comparison and colour code).

This was tested using Friedman's non-parametric ANOVA. The use of Friedman's test allowed the ANOVA to be performed *within repeats*, thus controlling for any differences in firing rate that might arise between repeats due to adaptation effects. Significant variation in  $r_0(\tau)$  was observed for  $^{19}_{21}$  neurons in the IC and  $^{15}_{15}$  neurons in the DNLL ( $P \leq 0.05$ ). This significant variation in the DC response as a function of ITD indicates that the recorded responses in the IC and DNLL cannot be well described by a linear narrowband response of the form in (4.6).

Of the two IC neurons that failed the test, one was unusual since it showed only a weak, labile response to interaurally time-delayed noise, producing a noisy tuning curve. This

neuron was therefore excluded from all subsequent analysis. The other IC neuron that failed the test ( $P = 0.10$ ) did appear to show asymmetric envelopes, but only five repeats of the stimulus were available. It was felt that with more repeats, the noise would have been reduced and a significant ITD-dependence would have been seen in the DC response.

### *Quantifying the asymmetry*

In order to assess the asymmetries for the population as a whole it was necessary to find some method of quantifying them. The positive and negative envelopes of the recorded responses were determined from the dual-delay functions by interpolating the sampling of IPD up from 8 points to 1024 points (via the Fourier transform), and then determining the maximum and minimum firing rates at each ITD. In order to remove some of the noisiness, the resulting waveforms were then smoothed using the “robust loess” algorithm (smooth function, Matlab). This used a robust least squares method in order to fit a quadratic polynomial with a span of 25% of the entire data set around each data point. The value predicted by each polynomial at the central data point was then taken as the value of the envelope at that point. Extracted envelopes were visually inspected to ensure that they matched the envelope structure.

The degree of rate asymmetry was assessed by examining how much of the total area between the envelopes was above the baseline firing rate ( $A_+$ ) and how much below ( $A_-$ ). The baseline firing rate (the response to uncorrelated noise) was estimated from the average value of the sixteen data points at the most extreme ITDs. The *rate asymmetry index* (RAI) was then defined as

$$\text{RAI} = \frac{A_+ - A_-}{A_+ + A_-} \quad (4.14)$$

Thus if the majority of the area enclosed by the envelopes were above baseline, the RAI would be positive (with a maximum of +1) whereas if the majority of the area were below the baseline then the RAI would be negative (with a minimum of -1). If the areas above and below baseline were equal then the RAI would be zero, indicating no rate asymmetry.

The existence of multimodality in some of the envelopes made it difficult to define the delay asymmetry and so it was measured only for tuning curves where both envelopes were unimodal. It was therefore necessary to visually inspect the envelopes to determine the level of modality in each envelope before the delay asymmetry could be calculated. The delay asymmetry was measured as the difference in ITD between the peak of the positive envelope and the trough of the negative envelope

$$\text{Delay Asymmetry} = \text{Peak ITD} - \text{Trough ITD} \quad (4.15)$$

The peak of the positive envelope and the trough of the negative envelope were located from zero crossings in their first derivatives, using the same method used to locate the peak of the tone-delay functions in Chapter 3 (Section 3.3.2).

### *The degree of asymmetry in dual-delay functions in IC and DNLL*

The measured RAI for neurons in both the DNLL and IC can be seen in Figure 4.11a. The majority of RAI values in the DNLL were above zero, and the RAI was positively correlated with CF ( $r = 0.69$ ,  $P = 0.006$ , Spearman's rank correlation coefficient), with little or no asymmetry at the lowest CFs. Neurons in the IC, however, often showed negative RAI values ( $\frac{7}{20}$  neurons) and showed no correlation with CF ( $P = 0.43$ , Spearman's rank correlation coefficient).

In the DNLL, both envelopes were unimodal for  $\frac{10}{15}$  neurons, and  $\frac{4}{15}$  neurons showed unimodal positive envelopes but multimodal negative envelopes. The remaining neuron showed a unimodal positive envelope but a relatively flat negative envelope. Thus for the DNLL any multimodality was restricted to the negative envelope. In the IC, both envelopes were unimodal for  $\frac{15}{20}$  neurons,  $\frac{3}{20}$  neurons showed multimodality in one or both of envelopes, and  $\frac{2}{20}$  neurons showed one envelope that appeared relatively unmodulated by ITD.

The delay asymmetries measured for the responses where both envelopes were unimodal are shown in Figure 4.11b. Responses in the DNLL showed a range of delay asymmetries—both positive and negative—resulting in a median DA of 0.05 cyc re CF that was not significantly different from zero ( $P = 1.00$ , sign test). In the IC however, the majority of responses showed positive asymmetry with their positive envelopes peaking at more positive ITDs than those at which their negative envelopes showed a trough. The median delay asymmetry was 0.17 cyc re CF, which showed a significant bias towards positive values ( $P = 0.007$ , sign test). For IC, with the exception of a single high-frequency data point, the DA appeared to be correlated with the CF. Ignoring the sign of the delay asymmetry, a correlation between the magnitude of the DA and the CF of the neuron could be seen ( $r = 0.75$ ,  $P = 0.002$ , Spearman's rank correlation coefficient). A similar correlation appeared to exist for the DNLL but this was not significant ( $P = 0.2$ , Spearman's rank correlation coefficient).

The reason for this CF dependency in delay asymmetry could be seen by examining the location of the peaks of unimodal positive envelopes (Figure 4.11c) and the troughs of the unimodal negative envelopes (Figure 4.11d). The locations of the peaks showed no variation with CF in either DNLL ( $P = 0.42$ , Spearman's rank correlation coefficient) or IC ( $P = 0.56$ ), remaining relatively constant at around 0.14 cyc re CF and 0.13 cyc re CF respectively. However, in both nuclei, the location of the trough of the negative envelope appeared to shift away from zero ITD with increasing CF, with a significant correlation between the magnitude of the trough ITD and the CF for both DNLL ( $r = 0.70$ ,  $P = 0.031$ , Spearman's rank correlation coefficient) and IC ( $r = 0.74$ ,  $P \leq 0.001$ ). Thus, the CF dependence of the delay asymmetry appeared arise from a CF-dependent shift in the trough ITD of the negative envelope.

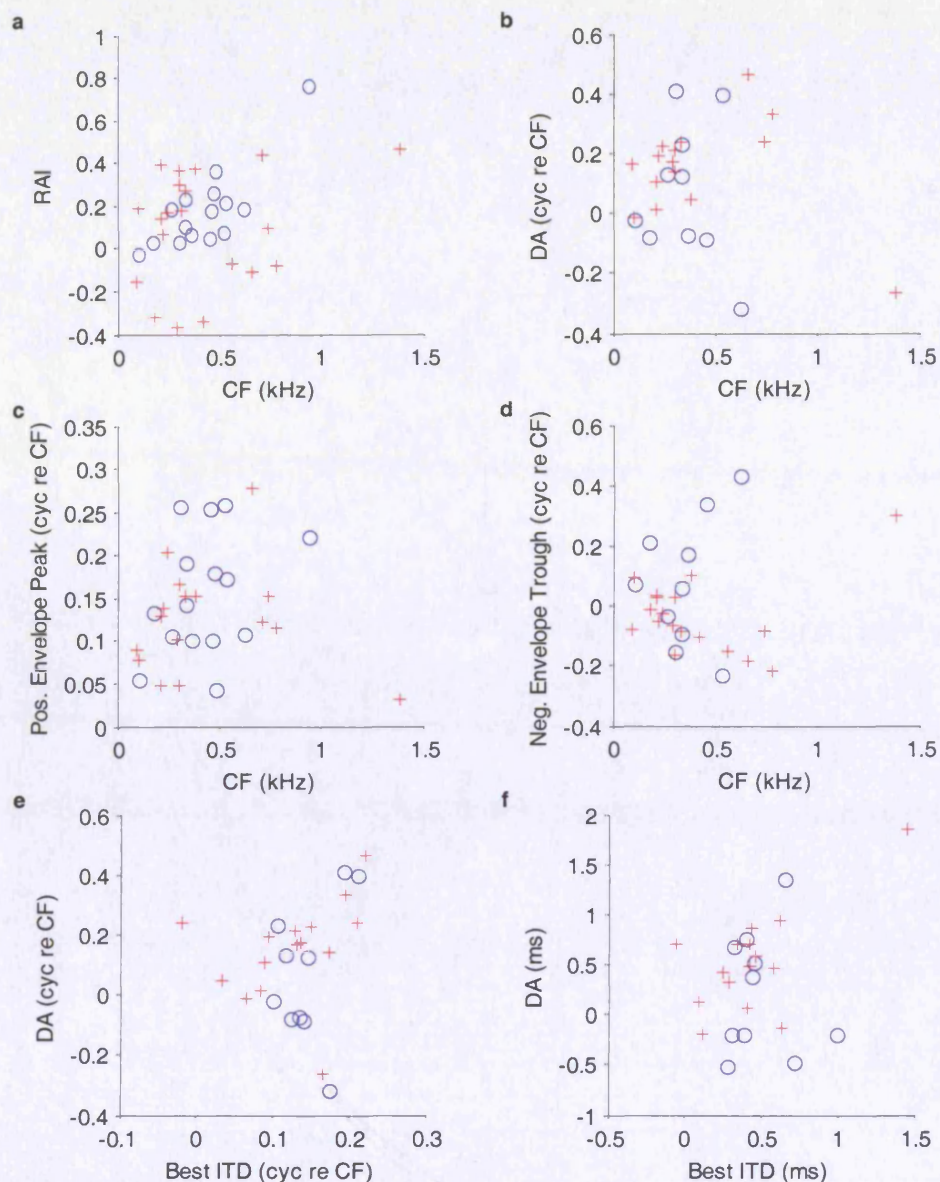


**Figure 4.11 Measures of asymmetry in dual-delay functions from IC and DNLL.**

**a**, the distribution of the Rate Asymmetry Index as a function of the CF for neurons in DNLL (blue circles) and IC (red crosses). The RAI increased with CF for the DNLL. **b**, the distribution of the degree of delay asymmetry (in cycles re CF) as a function of CF. The magnitude of the delay asymmetry appeared to increase with CF for both IC and DNLL. **c**, The distribution of the peak ITD of the positive envelope as a function of CF. **d**, The distribution of the trough ITD of the negative envelope as a function of CF. The outward shift in the negative envelope trough combined with the constancy of the positive envelope peak was responsible for the increase in delay asymmetry with CF. **e**, the degree of delay asymmetry as a function of the best ITD. Larger best ITDs appear to produce larger delay asymmetries. **f**, the same data as in **e** expressed in milliseconds. The delay asymmetry and the best ITD no longer appear correlated.

The magnitude of the delay asymmetry was correlated with the best ITD (Figure 4.11e) for both the IC ( $r = 0.67$ ,  $P = 0.008$ , Spearman's rank correlation coefficient) and the DNLL ( $r = 0.67$ ,  $P = 0.039$ ). This suggested that whatever mechanism was responsible for shifting the best ITD away from zero was also responsible for producing the delay asymmetry. However, when expressed in milliseconds (Figure 4.11f), there was no correlation between the two measures in either IC ( $P = 0.11$ ) or the DNLL ( $P = 0.73$ ), suggesting that any correlation may have arisen from the co-dependence of both the delay asymmetry and the best ITD on the CF of the neuron.

## 4.5 Discussion

### 4.5.1 *Best ITD and slope ITD*

The distribution of best ITD and slope ITD in IC was in accordance with that previously observed (McAlpine et al. 2001, Hancock & Delgutte 2004). The distribution of best ITD in DNLL was the same as that in IC, suggesting that the distribution in MSO would also be similar. While the peaks of tone-delay functions in the MSO and DNLL have previously been described as being distributed around 0.125 cyc re CF, this is only a crude approximation. In fact, the best ITD (in  $\mu\text{s}$ ) was not inversely proportional to the CF and even when converted to cycles of CF, the median value in both IC and DNLL was greater than 0.125 cyc re CF.

Arguably, too much attention has been paid to the location of the best ITDs and this detracts from the more striking distribution of the slope ITDs. In both IC and DNLL the slope ITDs are more tightly clustered around the midline than best ITDs are around their median. Thus, a systematic variation in best ITD may not in of itself be the goal of the system, but rather a means through which effect the more functionally important position of the slope ITDs can be established. However, the tighter distribution of the slope ITDs around zero comes from a weaker dependence on the CF (compared to that of the best ITDs). While for most of the data the slope ITDs are only slightly below zero ITD, for the very lowest CFs the slope ITDs can be outside of the physiological range. Since noise-delay functions provide the greatest acuity at ITDs more negative than their slope ITD (Shackleton et al. 2003), these neurons do not appear to efficiently encode ITDs within the commonly experienced range. This would be expected to result in poorer midline JNDs at these lowest frequencies.

### 4.5.2 *Gabor fits*

The difference in side-trough depth often observed in responses to noise was thought to indicate the presence of a strong phase component to the internal delay. It was hoped that such a finding might provide an explanation for the observed phase-like dependency of the best ITD on CF. Although the Gabor function used to model the data and estimate the phase delays explained a large fraction of the variance, this appeared to be an artefact of overfitting the response at central ITDs. This overfitting lead to unreliable parameter estimates, suggesting that the Gabor function was not suitable for the purpose it was intended. The reason for the failure of the Gabor model to fit the data appeared to be the large degree of asymmetry observed in IC and DNLL. It was therefore not possible to determine whether the observed difference in side-trough depth was a consequence of a phase component to the internal delay or a consequence of the delay asymmetry.

### **4.5.3 Asymmetry in noise-delay functions**

Only two dual-delay functions have been previously illustrated, both recorded from cat IC (Yin et al. 1987). The symmetry of one of these cannot be observed since the negative envelope cannot be seen and the other appears largely symmetrical. Twelve dual-delay functions were recorded in the Yin et al. study and some would be expected to have shown the asymmetry observed here. However, any asymmetry (or lack thereof) is not mentioned. Since the purpose of that study was to highlight the similarity of the response to that expected from a cross-correlation model (with particular reference to any phase modulation), it is possible that any asymmetry was overlooked. Delay-asymmetric tuning curves can be clearly observed in several examples of low-frequency neurons recorded from a similar study in the IC of the cat (Joris et al. 2005), indicating that the asymmetries observed in this study are present and are not unique to the guinea pig.

Since the more general linear model presented in this chapter also predicted symmetrical envelopes, the failure of the Gabor model was not merely a failure to use the correct parameters for the cochlear filters or the delay mechanism. Instead, the observed shape of the noise responses suggests that some mechanism not accounted for in the linear model is playing a significant role. Possible mechanisms underlying these asymmetries will be discussed in the next chapter.

# 5

## THE ORIGIN OF ASYMMETRIES

---

### 5.1 Introduction

While the linear model in the previous chapter suggested that it should be possible to use noise-delay functions to investigate the nature of the internal delay, this was hindered by the presence of the rate and delay asymmetries in the noise-delay functions. In order to progress it was necessary to understand the origin of these asymmetries and, ideally, to factor them in to new model of ITD processing.

The symmetrical envelope structure predicted by the general model presented in the previous chapter arises from its linearity. Any interaural phase-shift of the input stimuli produces an equivalent phase shift of the output (with the exception of the DC component), and so (4.11) holds and the envelopes remain symmetrical. In order to produce asymmetrical envelopes it is necessary to introduce distortions are not put into antiphase by an interaural phase shift of the input stimuli of 0.5 cyc. This requires the introduction of nonlinearity into the model.

### 5.2 Correlation-dependent nonlinearities

One of the simplest ways of producing rate asymmetric responses, is for the output of the MSO to be nonlinearly dependent on the cross-correlation of the cochlea-filtered input stimuli

$$r(\tau | \phi) = f_x[h_x(\tau - \tau_0 | \phi)] \quad (5.1)$$

For simplicity, the effect of inhibition has been ignored. A response of this form has the potential to produce rate-asymmetric responses as illustrated in Figure 5.1. In this example, the positive envelope has been stretched and the negative envelope compressed, resulting in a positive rate asymmetry.

However, responses of the form in (5.1) cannot produce delay asymmetric responses. Since the envelopes of delay-symmetric functions are unimodal, it can be concluded that  $f_x(\cdot)$  is a monotonic function over the range of input correlations. Because of this, the peak of the positive envelope and the trough of the negative envelope of the response will occur

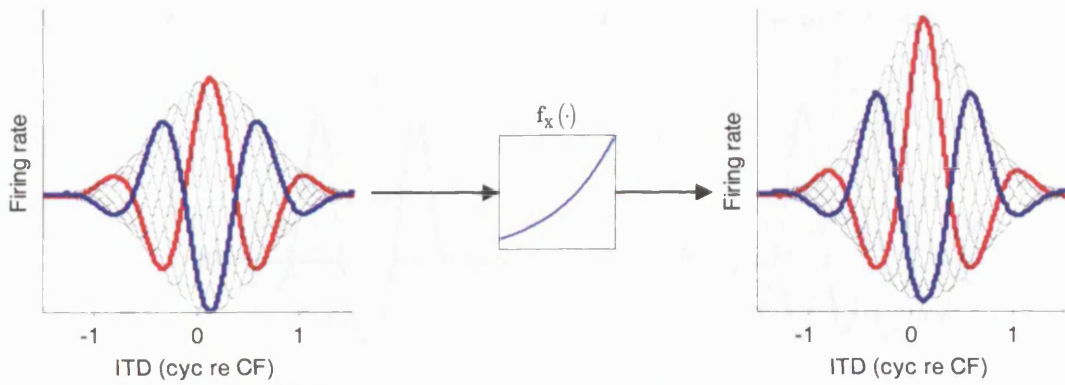


**Figure 5.1 Rate-asymmetric response produced by a correlation-dependent nonlinearity.**

The linear narrowband response (left) becomes rate asymmetric (right) after being stretched by an expansive correlation-dependent nonlinearity (middle). Responses to 0 cyc IPD (red) and 0.5 cyc IPD (blue) are highlighted, all other IPDs are shown in grey.

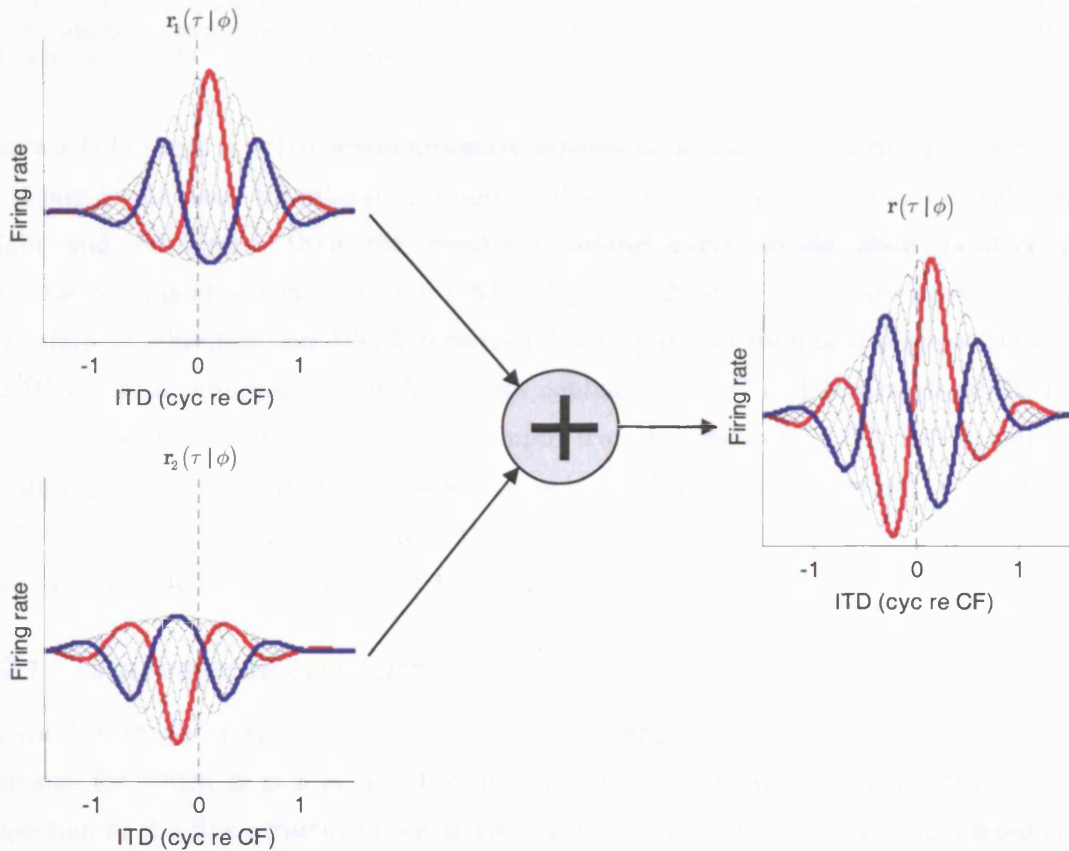


**Figure 5.2 Delay-asymmetric response produced by convergence.**

A combination of an ipsilaterally originating excitatory input (top left) and a contralaterally originating inhibitory input (right) can produce a response with a positive delay-asymmetry (right). Responses to 0 cyc IPD (red) and 0.5 cyc IPD (blue) are highlighted, all other IPDs are shown in grey.

at the same ITDs as those of the input. Thus, since  $h_x(\tau|\phi)$  is delay-symmetric (Section 4.4.1), the response will also be delay-symmetric.

The observed delay asymmetry can be produced by the convergence of rate-asymmetric delay-sensitive inputs. If neurons in DNLL and IC receive two inputs from two different MSO neurons, then the noise-delay response can be modelled as the sum of two rate-asymmetric noise-delay responses

$$r(\tau|\phi) = a_0 + a_1 r_1(\tau|\phi) + a_2 r_2(\tau|\phi) \quad (5.2)$$

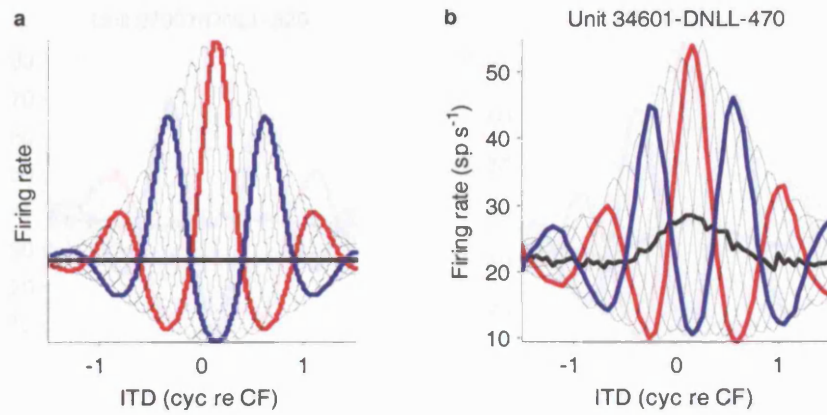


**Figure 5.3 Rate asymmetry cannot be explained by correlation-dependent nonlinearities.**

**a**, A rate-asymmetric tuning curve simulated by passing a Gabor function through an exponential nonlinearity. **b**, A rate-asymmetric tuning curve obtained from a neuron in DNLL. Note the equivalence contour (black) formed by the intersection of antiphase ITD functions. For the tuning curve simulated using a correlation-dependent nonlinearity, the crossing points lie along the zero-correlation line. For the recorded response, these crossing points are ITD dependent, elevated above the zero-correlation line at central ITDs. Responses to 0 cyc IPD (red) and 0.5 cyc IPD (blue) are highlighted, all other IPDs are shown in grey.

where  $r_1(\tau|\phi)$  and  $r_2(\tau|\phi)$  are nonlinearly dependent on the cross-correlation as in (5.1).

If one input were ipsilateral in origin and excitatory, and the other contralateral in origin and inhibitory, then the resultant tuning curve would show positive delay asymmetry as is observed in IC and DNLL (Figure 5.2). Both nuclei are known to receive contralateral inhibition: the DNLL receives inhibitory inputs from contralateral DNLL, and the IC receives inhibitory input from both contralateral IC and contralateral DNLL. In addition, the IC also receives excitatory input from contralateral LSO, which, due to the trough-type responses from this nucleus, would produce a similar effect to contralateral inhibition. Thus, it is plausible that the observed delay asymmetry is a product of the convergence of delay-sensitive input at the level of the DNLL and IC.

### 5.2.1 Equivalence contours

Figure 5.3 shows a rate-asymmetric response simulated using (5.1), and the recorded response for which it is a model. Despite the similarity of the envelope structure, close inspection of the fine structure reveals an important distinction. For the simulated tuning curve, pairs of ITD functions recorded at antiphase IPDs all intersect each other at the same firing rate. This is because, from (4.11) and the monotonicity of  $f_x(\cdot)$ , such crossing points correspond to an underlying correlation of zero

$$f_x[h_x(\tau - \tau_0 | \phi)] = f_x[h_x(\tau - \tau_0 | \phi + \pi)] \Rightarrow h_x(\tau - \tau_0 | \phi) = h_x(\tau - \tau_0 | \phi + \pi) = 0 \quad (5.3)$$

Since the nonlinearity is dependent only on the underlying correlation, the firing rate at these intersections (the *equivalence contour*) is expected to be identical to the response of the neuron to uncorrelated noise—a constant, independent of the ITD. In contrast, the recorded tuning curve shows a distinct ITD dependence in this equivalence contour, suggesting that correlation-dependent nonlinearity is not an adequate model of delay-symmetric dual-delay functions.

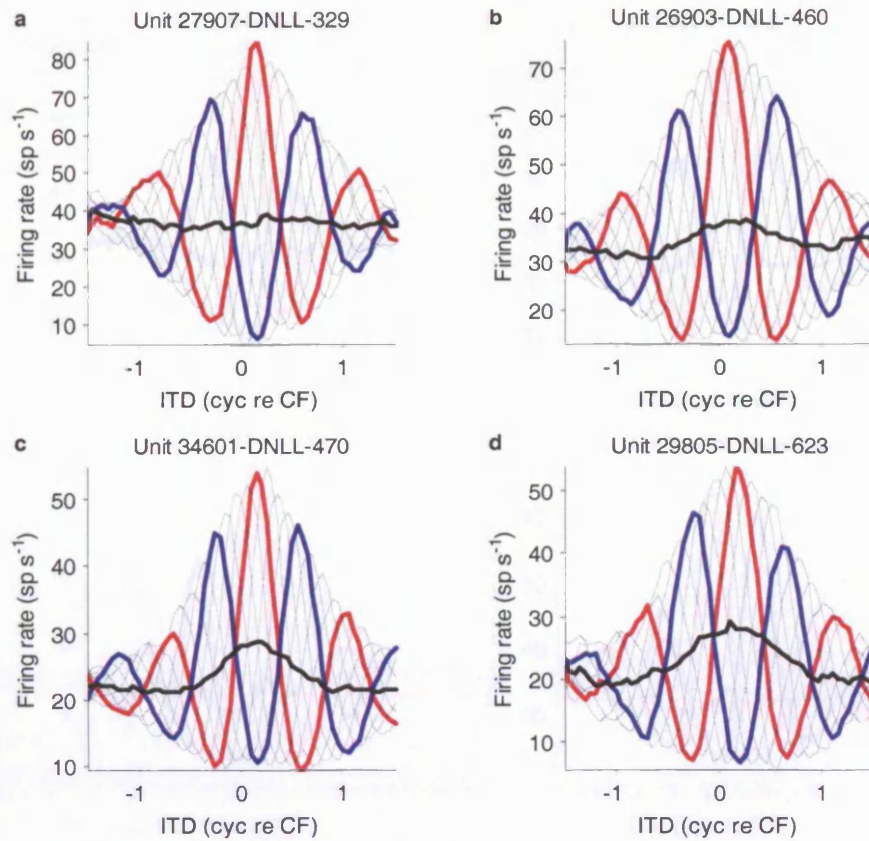


**Figure 5.4** Equivalence contours of four delay-symmetric dual-delay functions from DNLL.

Responses to 0 cyc IPD (red) and 0.5 cyc IPD (blue) are highlighted, all other IPDs are shown in grey. The black line shows the equivalence contour. All neurons showed significant ITD dependency in the predicted response ( $p < 0.001$ ) with the exception of **a** ( $p = 0.90$ ). CFs of the neurons were: **a**, 329 Hz; **b**, 460 Hz; **c**, 470 Hz; and **d**, 623 Hz. The responses at all other IPDs are shown in grey.

In order to investigate the equivalence contour for all recorded neurons, the Fourier series of each response

$$r(\tau | \phi) = \sum_{n=0}^4 a_n(\tau) \cos[n\phi + \theta_n(\tau)] \quad (5.4)$$

was determined using the Fourier transform, and the equivalence contour calculated as

$$z(\tau) = a_0(\tau) - a_2(\tau) + a_4(\tau) \quad (5.5)$$

If a response is well described by a nonlinear function of correlation as in (5.1), then this equivalence contour would be expected to be independent of ITD and would intersect phasic and antiphase noise-delay functions at the same points, thus meeting the looser definition given earlier (see Appendix 8.3).

Equivalence contours are shown for four neurons from DNLL in Figure 5.4, and for four neurons from IC in Figure 5.5. None of these neurons appeared to show a strong delay asymmetry. With the exception of the response shown in Figure 5.4a, all of the responses showed significant ITD dependency in their equivalence contours ( $P \leq 0.05$ , Wald-Wolfowitz runs test).

Although flat equivalence contours were only expected for delay-symmetric tuning curves, all were tested. The majority of neurons in IC ( $18/20$  neurons) and DNLL ( $12/15$  neurons) showed significant variation in their equivalence contours ( $P \leq 0.05$ ). Any lack of

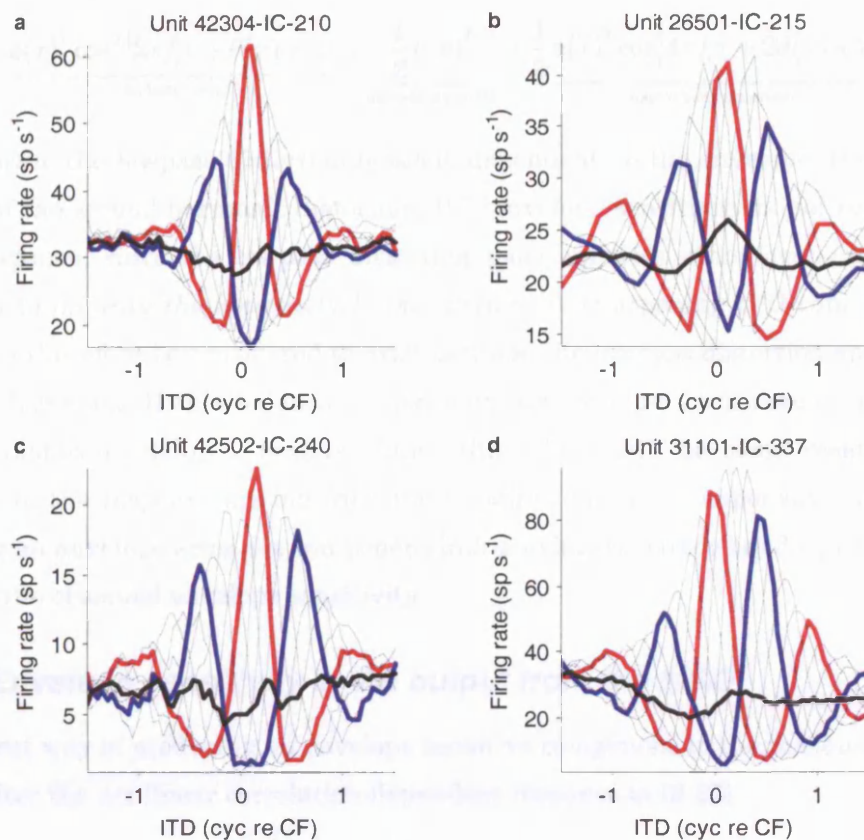


**Figure 5.5** Equivalence contours of four delay-symmetric neurons from IC.

Responses to 0 cyc IPD (red) and 0.5 cyc IPD (blue) are highlighted, all other IPDs are shown in grey. The black line shows the equivalence contour. All neurons showed significant ITD dependency in the predicted response ( $p < 0.01$ ). CFs of the neurons were: **a**, 210 Hz; **b**, 215 Hz; **c**, 240 Hz; and **d**, 337 Hz.

significant variation appeared to be a consequence of noise in the equivalence contour swamping any slower ITD dependency (with the exception of Figure 5.4a). This finding indicated that few of the recorded tuning curves were well described by the nonlinear model described in (5.1), either because of their delay asymmetry or, where delay-symmetric, because of the ITD dependency of the equivalence contour.

### 5.3 Envelope sensitivity

Since the correlation-dependent nonlinearity cannot adequately describe the observed rate-asymmetric responses as proposed in the previous section, a new model of ITD processing is required. In particular, the new model must be able to account for the ITD-sensitive, IPD-insensitive offset of the equivalence contour. One likely explanation for such an offset is an additional component to the response that is not sensitive to the carrier of the response but is sensitive to correlations in the envelopes of the input stimuli to MSO. Such an *envelope-sensitive* component has been previously demonstrated for high-CF neurons in the IC (Joris 2003).

An envelope sensitive component can be introduced into a narrowband signal through a combination of nonlinear distortion and lowpass filtering (Appendix 8.4). This can be simply seen from the quadratic term of any nonlinearity, which is separable into a lowpass distortion and a second-harmonic narrowband distortion

$$\underbrace{e(\tau)^2 \cos^2[2\pi f_c \tau + \theta(\tau) + \phi]}_{\text{quadratic term}} = \underbrace{\frac{1}{2} e(\tau)^2}_{\text{lowpass distortion}} + \underbrace{\frac{1}{2} e(\tau)^2 \cos[4\pi f_c \tau + 2\theta(\tau) + 2\phi]}_{\text{narrowband distortion}} \quad (5.6)$$

On its own, the lowpass distortion is solely dependent on the envelope. However, in the presence of the second-harmonic distortion, this envelope sensitivity is not reflected in the overall response, since the lowpass distortion pairs up with other even-order harmonic distortions to *improve the sensitivity to the carrier* (by sharpening IPD tuning). A kind of balance can therefore be considered to exist between the lowpass distortion and the second-harmonic distortion. If this balance is disrupted, for example by attenuating the second-harmonic distortion using a lowpass filter, then there will be some residual envelope sensitivity in the response arising from the unpaired lowpass component. This method of generating an envelope-sensitive component in a previously narrowband signal can be used to explain the observed envelope sensitivity

### 5.3.1 Envelope sensitivity in the output from the MSO

The simplest way of producing an envelope sensitive component to the response would be to lowpass filter the nonlinear correlation-dependent response in (8.22)

$$r(\tau | \phi) = f_x [h_x(\tau - \tau_0 | \phi)] * \lambda(\tau) \quad (5.7)$$

where  $\lambda(\tau)$  is some lowpass filter. As in the example above, this lowpass filtering would remove the harmonic distortions, leaving a residual envelope-sensitive lowpass component. Thus (5.7) provides a model of rate-asymmetric responses capable of producing an ITD-dependent equivalence contour. Delay-asymmetric responses could be produced by convergence as suggested earlier.

However, while such a mechanism may explain the observed responses, it is hard to discern what process could plausibly fulfil the role of the lowpass filter  $\lambda(\tau)$ . While the filtering arising from the membrane time constant is lowpass, it is a temporal filter and  $\lambda(\tau)$  requires interaction between responses at different ITDs. Since these different ITDs were presented in pseudorandom order, it is hard to see how any temporal filter could fulfil the role of  $\lambda(\tau)$ . The only obvious way to effect interaction across ITD after the level of the MSO is through convergence of delay-sensitive input. Convergence of a large degree of inputs with identical CFs might be expected to show a distribution of best ITDs around 0.125 cyc re CF, effectively producing a lowpass filter.

### 5.3.2 Envelope sensitivity in the input to MSO

A more plausible way of creating an envelope-sensitive component to the response would be to introduce an envelope sensitive component into the input to the MSO. As discussed in the previous section this can be done through a combination of nonlinear distortion and lowpass filtering of the inputs to MSO

$$v_I(t) = f_I [h_I(t) * s(t)] * \lambda_I(t) \quad (5.8)$$

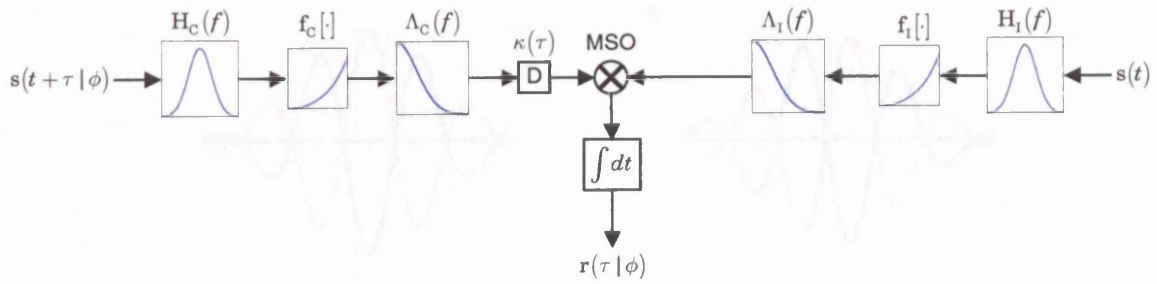


**Figure 5.6 An envelope-sensitive model of ITD sensitivity.** Filtered input stimuli are nonlinearly processed and lowpass filtered to model an envelope-sensitive component into the MSO. Frequency-dependent internal delays are modelled by filtering the contralateral input to the model and the MSO is modelled as a cross-correlator.

$$v_c(t + \tau | \phi) = f_c[h_c(t + \tau | \phi) * s(t)] * \lambda_c(t) \quad (5.9)$$

A schematic of the resulting model is shown in Figure 5.6. Since this introduces an envelope-sensitive component to the input, the response

$$r(\tau | \phi) = v_1(t) * v_c(t | \phi) = v_x(\tau | \phi) \quad (5.10)$$

would be expected to contain a term sensitive to the cross-correlation of these envelope-sensitive components, in addition to a term sensitive to the cross-correlation of the carrier-structure sensitive components (and several cross-terms).

Such a model is easier to justify mechanistically than that in the previous section. At high frequencies, (5.8) and (5.9) can be thought of as modelling the cochlear envelope sensitivity. Such a process has been previously suggested to explain the phase locking to the envelope of high-frequency sounds in the auditory nerve: the stereocilium kinetics distort the injected current to the inner hair cell creating harmonics, which when lowpass filtered by the membrane time-constant, results in a membrane potential that follows the envelope of the input stimulus. This cochlear envelope sensitivity has been proposed to explain the high-CF ITD sensitivity observed in the IC (Joris 2003).

However, cochlear envelope sensitivity is unlikely to explain the low-CF envelope sensitivity observed here. In Chapter 4, the input to MSO was assumed to vary linearly with the cochlea-filtered input stimulus. However, as discussed in Chapter 3 (Section 3.2.3) earlier, a similar assumption for pure-tone stimuli underestimated the degree of phase locking in the input to MSO. In order to model a higher degree of phase locking, the input was assumed to be nonlinearly dependent on the output of the cochlea, and the postsynaptic response arising from each side was determined by convolving the input spike distribution with the EPSP (or IPSP) for those inputs. This reasoning, applied to noise responses, provides an alternate justification for inputs of the form (5.8) and (5.9).

### 5.3.3 Envelope sensitivity and tuning curve asymmetry

The envelope-sensitive component to a response can directly create the rate-asymmetries observed in the previous chapter by offsetting the envelope of the fine structure sensitive component of the response in an ITD dependent manner. Figure 5.7 shows an example of

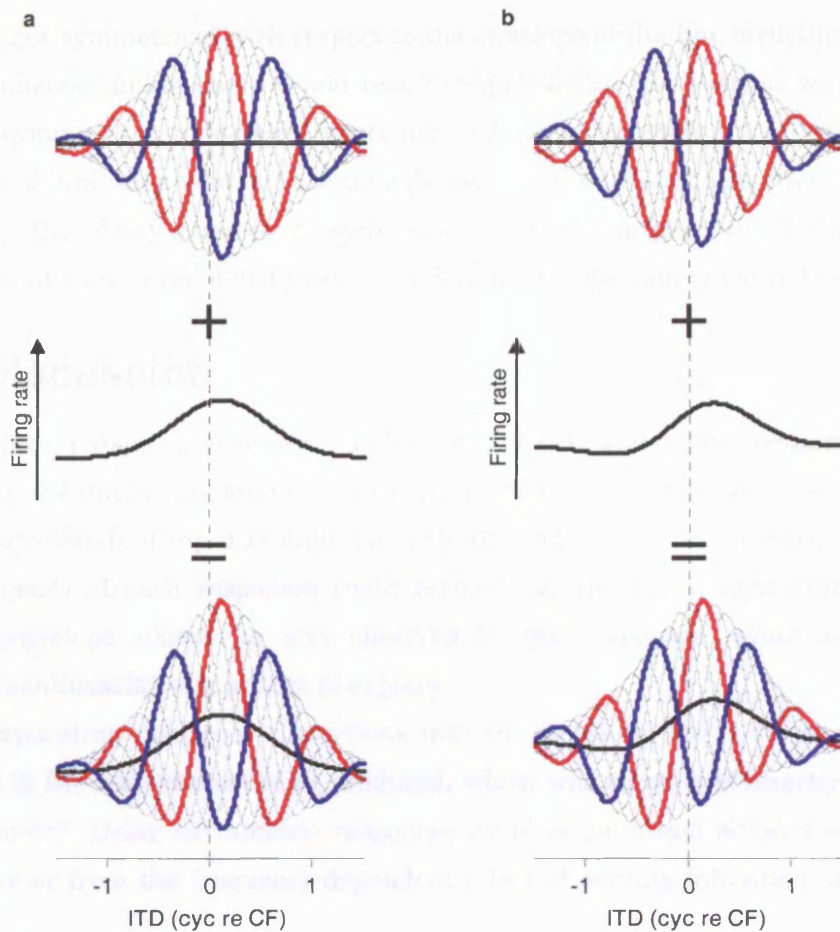


**Figure 5.7 Envelope sensitivity can produce rate and delay asymmetric responses.**

**a**, Example of the creation of rate asymmetry by envelope sensitivity. The envelope-sensitive component to the response (middle) directly offsets the otherwise symmetrical linear component (top), resulting in a rate-asymmetric response (bottom) with a ITD-dependent equivalence contour. Note that both components have been delayed by the same time delay. **b**, Example of the creation of delay asymmetry by envelope sensitivity. The envelope-sensitive component to the response (middle) is asymmetric with respect to the envelope of the linear component (top), as a consequence of the frequency-dependent delay arising from carving inhibition. This results in a delay-asymmetric response (bottom). The components in **b** were produced from those in **a** using the model of carving inhibition with a lead time of 0.125 cyc re CF and relative strength 0.8.

how rate asymmetry can be introduced into an otherwise symmetrical fine-structure sensitive response, by an envelope-sensitive component of the response.

Having reproduced the rate asymmetry, the delay asymmetry can be simply reproduced through convergence as discussed for the nonlinear model (Figure 5.2a). However, carving inhibition may also provide an explanation for the asymmetry. In the first model, the distortions are created after the level of the MSO; thus, carving inhibition would not be expected to make a difference to the symmetry of the tuning curve. However, in the second model, where the envelope sensitivity is present in the input to the MSO, carving inhibition becomes a potential cause of delay asymmetry. Factoring the carving inhibition in to the contralateral input in (5.10) produces a response of the form

$$\mathbf{r}(\tau | \phi) = \mathbf{v}_x(\tau | \phi) * \kappa(\tau) \quad (5.11)$$

Since the lowpass envelope-sensitive distortion is of a lower frequency than the linear fine-structure-sensitive component, the two would be differently affected by the frequency-dependent delay arising from the carving inhibition. If the envelope-sensitive component

were no longer symmetrical with respect to the envelope of the fine-structure component, a delay asymmetric tuning curve would result (Figure 5.2b). However, as was the case with the skew asymmetry in tone-delay functions, no delay asymmetry would result if the effect of the carving inhibition were a pure time-delay, or if the level of distortion were negligibly low. Thus, the delay-symmetric responses observed (largely in DNLL) may be a consequence of a low level of distortion, or a dominant time component to the internal delay.

## 5.4 Discussion

In this chapter, possible mechanisms underlying the rate and delay asymmetry observed in responses to the dual-delay stimulus were investigated. A simple nonlinear dependency on the cross-correlation of input stimuli was able to produce rate asymmetric responses, and the convergence of such responses could account for the delay asymmetry. However, a degree of envelope sensitivity was observed in the responses, which the correlation-dependent nonlinearity was unable to explain.

By incorporating nonlinear distortions into the input to MSO, an envelope-sensitive component to the response could be produced, which was capable of directly producing the rate asymmetry. Delay asymmetric responses could be produced either from convergence mechanisms or from the frequency-dependent effect of carving inhibition on the distorted input.

### 5.4.1 *The origin of envelope sensitivity*

An envelope-sensitive component to ITD tuning curves has been previously demonstrated for high-CF neurons in the cat IC (Joris 2003). Joris showed that the strength of this envelope-sensitive component increased with increasing CF, to the extent that for CFs greater than 2 kHz, the response was completely insensitive to changes in IPD. In order to investigate whether the cochlear envelope sensitivity was responsible for this envelope component in the IC response, Joris examined the cross-correlation of responses to noise recorded in the auditory nerve. By cross-correlating spike trains recorded from a single neuron in response to both correlated and anticorrelated noise stimuli, the 0 cyc IPD and 0.5 cyc IPD noise-delay functions expected from such inputs could be determined. While these correlograms also showed a CF-dependent degree of envelope sensitivity, the CF of the transition from carrier to envelope sensitivity was higher for these auditory nerve derived responses than for IC, and there was little envelope sensitivity for CFs less than 1 kHz.

Cross-correlograms produced for low-CF auditory nerve fibres and low-CF AVCN neurons are shown in Figure 5.8. While the AN correlograms show little or no ITD-dependence in their equivalence contours, the AVCN correlograms show equivalence contours that drop *below* the response to uncorrelated noise. The failure of these correlograms to show an elevated equivalence contour, together with the lower CF of

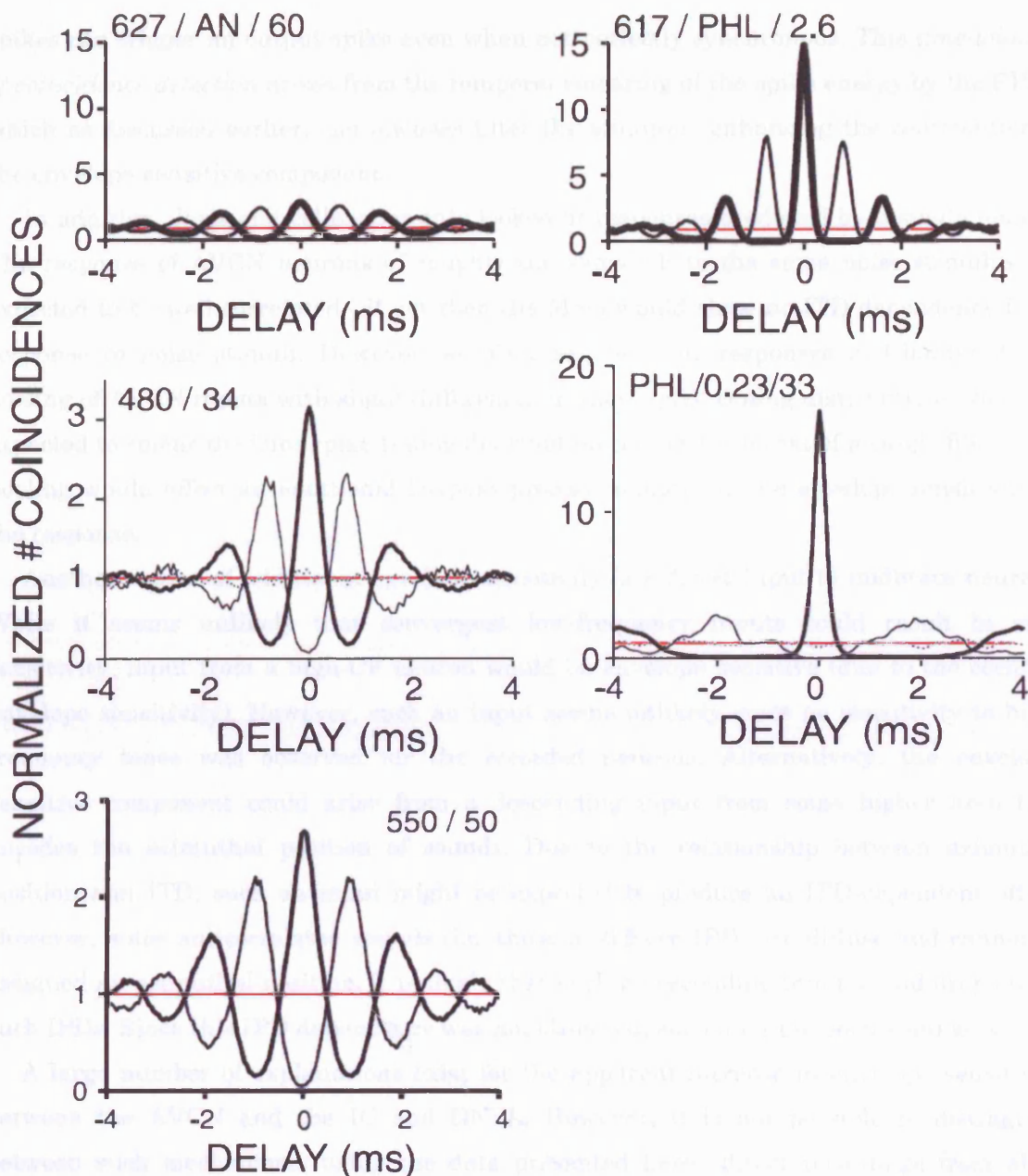


**Figure 5.8** Cross-correlograms of peripheral responses to noise.

The cross-correlograms recorded for both AN (left column) and AVCN (right column) in response to correlated (thick black line) and anticorrelated (thin black line) noise. The average level of the response to uncorrelated noise (normalised to 1) has been superimposed in red. Middle plots also show the recorded response to anticorrelated noise (dotted black line). Note that for AN the equivalence contour is similar to the response to uncorrelated noise. In the AVCN the equivalence contour dips below the response to uncorrelated noise at central ITDs. In neither case does the response resemble that in the IC or the DNLL, suggesting that there is an enhancement of envelope sensitivity in the MSO. (Figure adapted from Louage et al. 2004, 2005, 2006).

transition from carrier to envelope sensitivity observed in AN compared to IC, indicates the input to MSO is not sufficient to explain the envelope sensitivity observed in the responses in IC and DNLL. This suggests an enhancement of envelope sensitivity at or after the level of MSO.

One possible explanation for the observed difference in envelope sensitivity is that the cross-correlograms produced from the AN and AVCN responses effectively model an MSO neuron as a perfect coincidence detector, firing an output spike only when two input spikes are perfectly synchronous. In reality, coincidence detection in MSO is imperfect: two input

spikes can trigger an output spike even when not perfectly synchronous. This *time-window of coincidence detection* arises from the temporal smearing of the spike energy by the EPSP, which as discussed earlier, can lowpass filter the stimulus, enhancing the contribution of the envelope-sensitive component.

In addition, Joris and colleagues only looked at responses predicted by a single neuron. The response of AVCN neurons of roughly the same CF to the same noise stimulus are expected to be well correlated—if not then the MSO would show no ITD dependency in its response to noise stimuli. However, as discussed for tone responses in Chapter 3, the pooling of AVCN inputs with slight differences in their spike timing distributions would be expected to smear the joint spike timing distribution compared to that of a single fibre. This pooling would effect an additional lowpass process, enhancing the envelope sensitivity in the response.

Another source of additional envelope sensitivity is a direct input to midbrain neurons. While it seems unlikely that convergent low-frequency inputs could result in such sensitivity, input from a high-CF neuron would be envelope sensitive (due to the cochlear envelope sensitivity). However, such an input seems unlikely since no sensitivity to high-frequency tones was observed for the recorded neurons. Alternatively, the envelope-sensitive component could arise from a descending input from some higher area that encodes the azimuthal position of sounds. Due to the relationship between azimuthal position and ITD, such an input might be expected to produce an ITD-dependent offset. However, since anticorrelated sounds (i.e. those at 0.5 cyc IPD) are diffuse and cannot be assigned an azimuthal position, it is likely that such a descending input would drop out at such IPDs. Since this IPD dependency was not observed, such an input seems unlikely.

A large number of explanations exist for the apparent increase in envelope sensitivity between the AVCN and the IC and DNLL. However, it is not possible to distinguish between such mechanisms using the data presented here—direct recordings from MSO would be required to test most of these hypotheses.

#### **5.4.2 “Envelope sensitivity”**

Traditionally, “envelope sensitivity” has referred to the responses of neurons to sinusoidally amplitude modulated pure-tone stimuli (SAM). Applying the term “envelope sensitivity” to the IPD-insensitive responses observed in this study is misleading in several ways. While the SAM stimulus itself has an easily-observed envelope, the noise stimulus itself does not. Instead, the envelope is imposed by the narrowband filtering on the basilar membrane. Furthermore, while responses to SAM stimuli reflect the shape of the stimulus envelope, the IPD-insensitive component of the dual delay responses is unlikely to directly reflect the envelope imposed by the cochlea. Thus, while a largely semantic point, it is felt that the term *coarse-structure sensitivity* is a preferable description of the IPD-insensitive component observed in responses to noise stimuli.

### **5.4.3 *The source of tuning curve asymmetry***

If the model incorporating nonlinearity in the input to MSO is correct, then it is hard to make any strong conclusions based on the existence of delay-asymmetric responses. The large number of spectral components arising from distorted noise stimuli produces a large number of cross-terms in the cross-correlation and makes it difficult to obtain a neat closed-form expression for the responses (Appendix 8.5). In general, if the cochlear filters are identical (i.e. no stereausis), the EPSPs are identical (i.e. no Zhou-style inhibition) and if the delay is purely a Jeffress-like time delay, then the inputs to MSO would be identical. The predicted response would therefore be an autocorrelation, symmetrical about best ITD with rate-asymmetry but no delay-asymmetry. Thus, delay-asymmetry in MSO responses is inconsistent with this traditional model. However, since the neurons in IC and DNLL may receive convergent delay-sensitive input, then this traditional model cannot be rejected. Distinguishing between these two mechanisms would require direct recordings from MSO.

# 6

## COMPONENTS OF DUAL-DELAY FUNCTIONS

---

### 6.1 Introduction

By characterising dual-delay functions in terms of their Fourier series expansion, it was hoped that a phenomenological model of ITD tuning curves responses could be produced that would allow the factors responsible for the asymmetry to be determined. Each dual-delay function was analysed with respect to the Fourier series expansion

$$\begin{aligned} r(\tau | \phi) &= \sum_{n=0}^4 a_n(\tau) \cos[n\phi + \theta_n(\tau)] \\ &= \sum_{n=0}^4 r_n(\tau | \phi) \end{aligned} \quad (6.1)$$

where each component  $r_n(\tau | \phi)$ , its amplitude envelope  $a_n(\tau)$ , and its phase response  $\theta_n(\tau)$  were obtained from the Fourier transform of the dual-delay function  $r(\tau | \phi)$  with respect to the IPD  $\phi$ . Of particular interest were the *lowpass component*  $r_0(\tau | \phi)$ , the coarse-structure sensitive component of the response, and the *linear component*  $r_1(\tau | \phi)$ , which is linearly dependent on IPD. Because of this linearity, it was hoped that this component could provide a measure of the time and phase components of the internal delay, fulfilling the original purpose of the Gabor model.

### 6.2 The relative contribution of components

The contribution of each component to the response as a whole can be assessed from the proportion of the total variance that it contributes. Figure 6.1a shows the proportion of explained variance for each component and Figure 6.1b shows the cumulative sum of these contributions—the proportion of variance explained by the  $n^{\text{th}}$ -order and lower components. The same data set was used as in Chapter 4, 20 neurons from IC and 15 neurons from DNLL. Four neurons showing half-wave rectification of their tuning curves were omitted

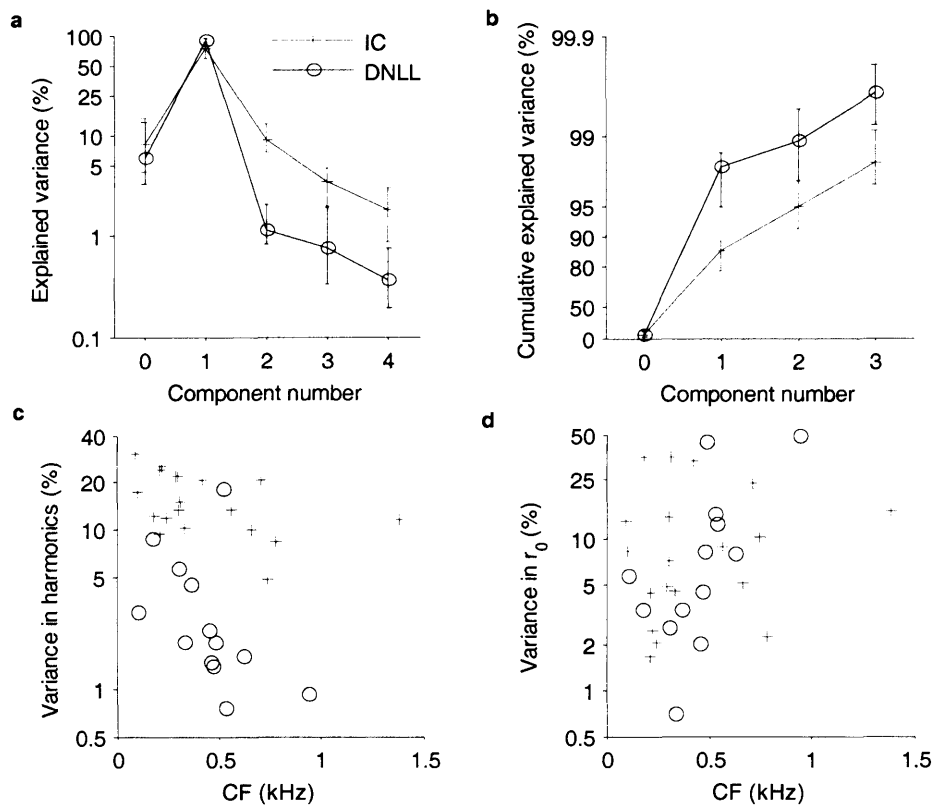


**Figure 6.1 Contribution of distortions to the total variance of DNLL dual-delay functions.**

**a**, the median proportion of explained variance for each component of the response. Error bars show interquartile range. **b**, the median cumulative explained variance for each additional component. Error bars show interquartile range. **c**, the proportion of explained variance in the harmonic (2<sup>nd</sup>-order and higher) components as a function of the CF of the neuron. Data for both the IC (red squares) and the DNLL (blue circles) is shown. Harmonic components make less contribution at higher CFs. **d**, the proportion of explained variance in the lowpass component as a function of the CF of the neuron. In the DNLL, the contribution of the lowpass component increases with CF.

from this analysis in order to avoid overestimating the level of distortion that might be present in the MSO ( $\frac{1}{20}$  IC neurons,  $\frac{3}{15}$  DNLL neurons).

The DNLL showed very little harmonic distortion (i.e. the 2<sup>nd</sup>-order and higher components were low), with the lowpass distortion  $r_0(\tau)$  and the linear component  $r_1(\tau|\phi)$  accounting for a median 98% of the variance, indicating that the response could be well described by just the first two components. The IC on the other hand showed more harmonic activity with the first two components only accounting for a median 87% of the total variance. The inclusion of the second-order component  $r_2(\tau|\phi)$  increased the proportion of explained variance to 95% for the IC, but only slightly increased it for the DNLL to 99%. This suggested that while a first-order model was sufficient to describe most of the DNLL responses, a second-order model was required in order to describe responses in IC with a similar level of accuracy.

Figure 6.1c shows the total variance explained by the harmonic (2<sup>nd</sup>-order and higher) components. The explained variance in the harmonics decreased as a function of the characteristic frequency of the neuron for both the DNLL ( $r = -0.59$ ,  $P = 0.038$ , Spearman's rank correlation coefficient) and the IC ( $r = -0.51$ ,  $P = 0.028$ ). Such a correlation was likely a reflection of the decrease in phase locking observed at higher CFs. If this were simply a decrease in the strength of the nonlinearity in the system then the proportion of variance

explained by the lowpass distortion would also be expected to decrease at higher CFs. Instead, it can be seen for the DNLL (Figure 6.1d) that as the CF of the neuron increased, more of the variance of the response was explained by the lowpass distortion ( $r = 0.73$ ,  $P = 0.007$ , Spearman's rank correlation coefficient) suggesting that this was not the case. In the IC no significant positive correlation was observed ( $P = 0.48$ , Spearman's rank correlation coefficient).

## 6.3 Components of DNLL dual-delay functions

Each component of the responses was examined in order to determine its contribution to the shape of the tuning curve. Particular attention was paid to the linear component, since as shown in the previous section, it made the dominant contribution to the shape of the response. Since the contribution of third-order and higher distortions was negligible, they were not analysed.

### 6.3.1 The linear component

#### *Phase response*

All responses in DNLL appeared to show a linear phase response as evidenced by the fact that the cosine-transformed phase responses of the linear components were near perfect sinusoids (Figure 6.2). In order to test this, the phase of the linear component  $\theta_1(\tau)$  was fitted to the model

$$\hat{\theta}_1(\tau) = 2\pi f_c \tau - \theta_c \quad (6.2)$$

by finding the values of the parameters  $f_c$  (the carrier frequency) and  $\theta_c$  (the carrier phase) which maximised the equation

$$\sum_{i=0}^N w_i \cos[\theta_1(\tau_i) - \hat{\theta}_1(\tau_i)] \quad (6.3)$$

Assuming that the residuals had a von Mises distribution, estimates resulting from the maximisation of (6.3) corresponded to the maximum-likelihood estimates of the parameters of (6.2) (Gould 1969, Mardia & Jupp 2000). To compensate for the uncertainty in the measured phase response, resulting from the relatively stronger contribution of noise at extreme ITDs, the amplitude envelope at each ITD was used as a weighting factor

$$w_i = a_1(\tau_i) \quad (6.4)$$

The regression was performed as for the Gabor fits in Chapter 3, using the Matlab function `fminunc` to maximise (6.3) via a subspace trust-region algorithm. All parameters were unconstrained in the regression, with initial estimates determined from the highest-power component in the Fourier transform of  $r_1(\tau|0)$ . Helical regression to a circular variable is highly sensitive to initial parameters (Gould 1969), since the helix can make several complete loops between each data point; resulting in multiple solutions for  $f_c$ .

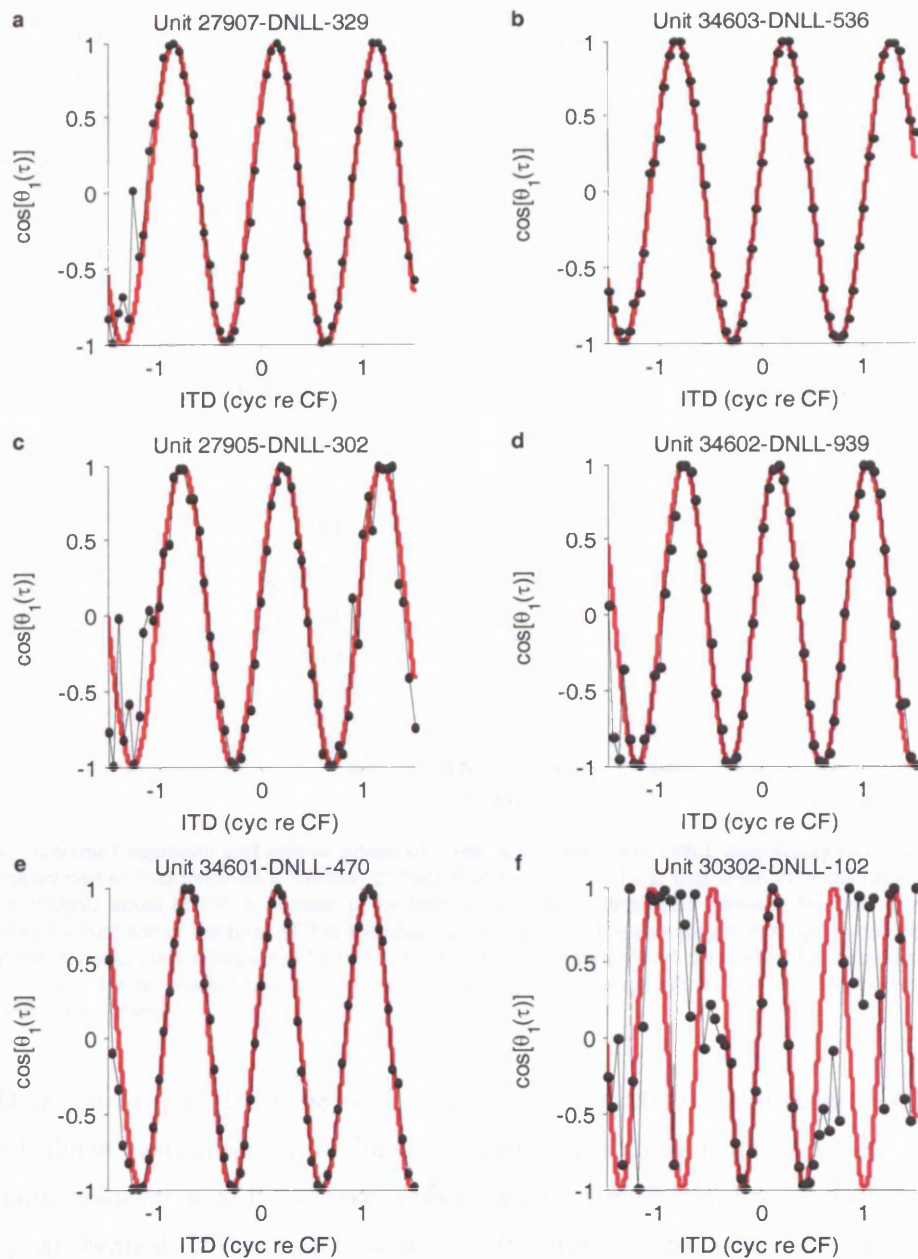


**Figure 6.2** Carriers of linear components of DNLL dual-delay functions.

Cosine transformed phase spectra are shown (black) together with fitted sinusoids (red). Weighted  $R^2$  values for the fits were: a, 0.99; b, 1.00; c, 0.97; d, 0.99; e, 0.99; and f, 0.82. Original dual-delay functions shown in Figure 4.9.

However, since different solutions were at least a factor of 10 apart for this data set, the correct solution could be assumed to be that with an  $f_c$  nearest CF.

The regression converged and was significant for all neurons ( $P \leq 0.05$ , F-test). Goodness-of-fit was assessed using a circular version of the  $R^2$  statistic—the proportion of the (weighted) circular variance explained by the model, as a fraction of the total (weighted) circular variance. This  $R^2$  value for the fits ranged from 0.81 to 1.00 with a median value of 0.97 (interquartile range 0.91 to 0.99) indicating that the phase was linear with respect to ITD over the central region of the response (see Figure 6.2). Although there were large errors at the more extreme ITDs, these made little contribution to the residual (circular) variance because of the weighting factors. However, these errors did not appear to be a consequence of noise. For  $13/15$  neurons, the residuals showed a showed systematic deviation

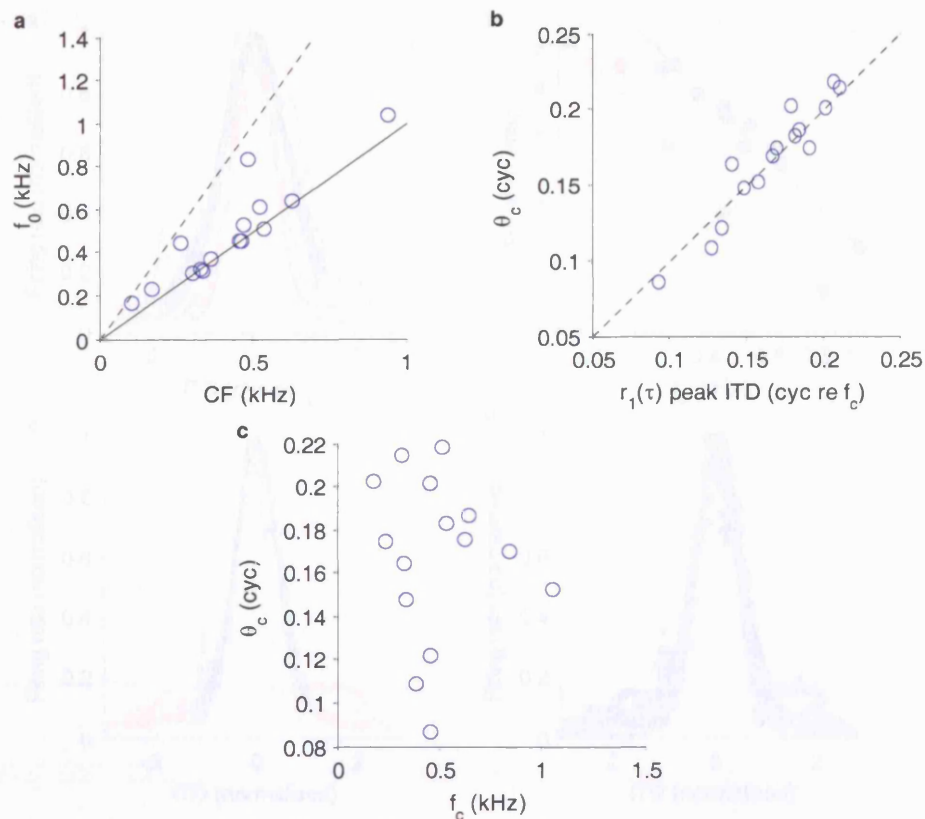


**Figure 6.3 Carrier frequency and carrier phase of linear components of DNLL dual-delay functions.** **a**, the estimated carrier frequency as a function of the CF of the neuron. Note that while for most neurons the carrier frequency is roughly equal to CF, a number of neurons show a large difference between the two. **b**, the estimated carrier phase as a function of the peak ITD of the linear component (expressed in cycles of the carrier frequency). The similarity of the two measures is expected from the fact that the linear component dominates the response and the peak response is expected when the sinusoidal component of the response is maximal. **c**, The joint distribution of the carrier frequency and carrier phase.

with ITD ( $P \leq 0.05$ , circular runs test; Mardia & Jupp 2000), indicating that there was significant phase modulation in the linear components of these neurons, albeit with a weak effect. Visual inspection of these responses showed a broad increase in the instantaneous frequency at central ITDs, which was largely captured by the fits. The majority of unexplained variance therefore arose from the slower instantaneous frequency in the tails of the tuning curves.

The estimated carrier frequency (Figure 6.3a) was significantly higher than the CF ( $P = 0.035$ , sign test), with a median carrier frequency to CF ratio of 1.1 (interquartile range 1.0 to 1.3). Several neurons appeared to respond at carrier frequencies around twice the CF, with ratios between 1.7 and 1.8. No secondary modes were visible at antiphase IPDs in the tone-delay functions of these neurons, so this was not an artefact of the processes responsible for the bimodal tuning curves in Chapter 3.

The estimated carrier phase (Figure 6.3b) determined the location of the peak ITD of the linear component, with no significant difference between the two measures ( $P = 0.67$ , sign test). The carrier phase was independent of  $f_c$  ( $P > 0.1$ , Mardia's linear-circular rank correlation coefficient) with median value 0.18 cyc (interquartile range 0.15 to 0.20 cyc).

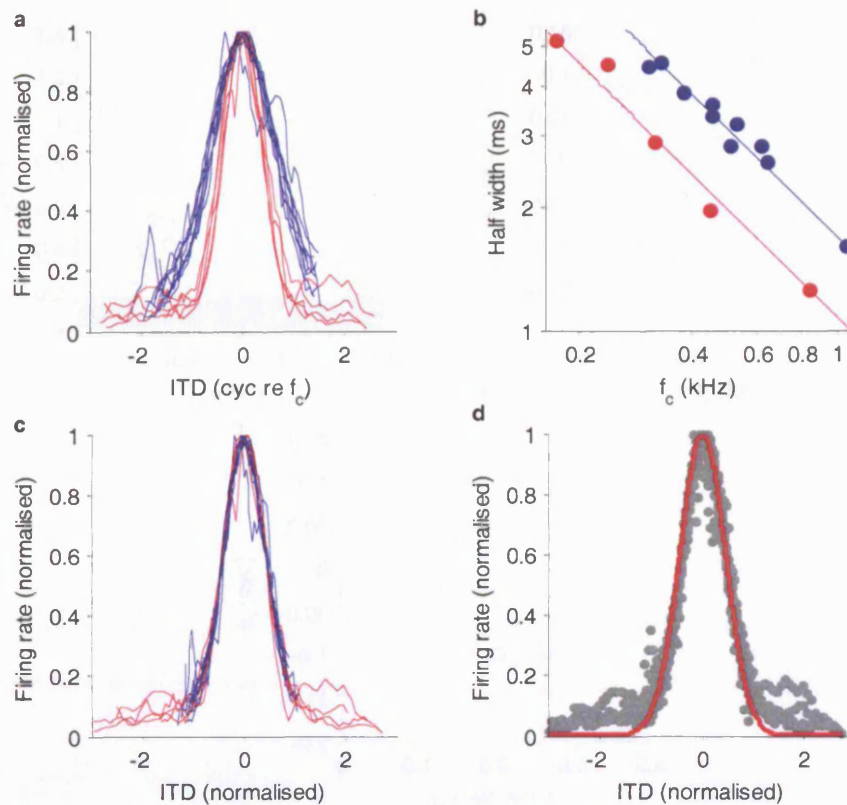


**Figure 6.4 Amplitude envelopes of linear components of DNLL dual-delay functions.**

**a**, the smoothed amplitude envelopes for all 15 neurons recorded from DNLL, normalised by the maximum firing rate. The ITD has been expressed in  $\text{cyc re } f_c$  and adjusted so that the centroid of the square of each envelope occurs at zero. The data fall into two groups: a broadly tuned group (blue) and a more narrowly tuned group (red). **b**, the distribution of the half-widths of the envelopes in **a** as a function of the carrier frequency. **c**, the same data as in **a** where the ITD has been normalised so that the half-width of each envelope is one. **d**, a Gaussian fit to the normalised envelopes in **c**.

### Amplitude envelope

The degree of damping in the amplitude envelope of the linear component is an indication of the bandwidth of the neuron. Figure 6.4a shows the normalised envelopes of the linear components, where the ITD is expressed in terms of cycles of  $f_c$  ( $\text{cyc re } f_c$ ). The envelopes were smoothed by a three-point moving-average filter and shifted so that the centroid of the squared function occurred at zero ITD. Two distinct clusters of responses were distinguishable—one that was narrowly tuned with half-widths less than  $1.2 \text{ cyc re } f_c$  ( $5/15$  neurons), and one that was more broadly tuned ( $10/15$  neurons).

A power-law relationship of the form  $y = kx^c$  existed between the carrier frequency and the half-width of the envelopes (Figure 6.4b). An analysis of covariance performed on the log-transformed data revealed no significant difference in the power-term  $c$  for the two groups ( $P = 0.23$ ), but did reveal a difference in the scaling-constant  $k$  ( $P \leq 0.001$ ). The fitted power-term was  $-0.89 (\pm 0.05, \text{SEM})$ , meaning that the half-width in both groups was approximately inversely proportional to the carrier frequency, as reflected by their close within-group correspondence in Figure 6.4a. The scaling-constant was 1.1 for the narrowly tuned group and 1.7 for the broadly tuned group—while the former showed two complete cycles of the carrier in their tuning curves, the latter showed around half a cycle extra.

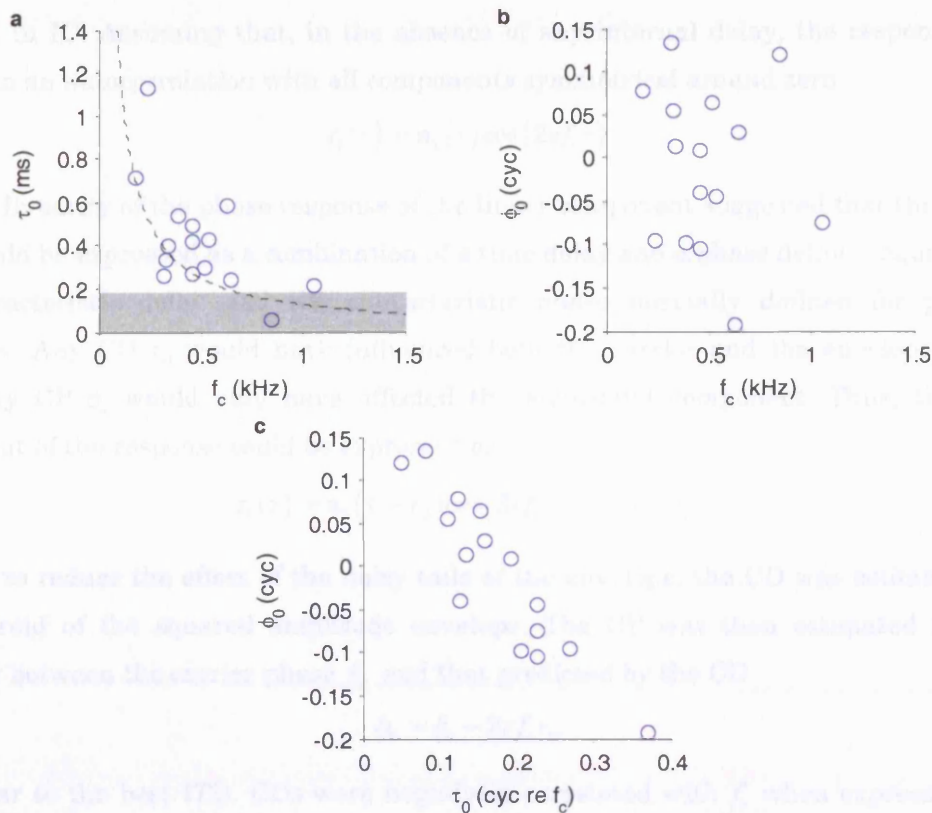


**Figure 6.5 Characteristic delay and characteristic phase of linear components of DNLL dual-delay functions.** **a**, distribution of the estimated characteristic delay as a function of the carrier frequency of the linear component. The physiological range is shown in grey and the black dotted line indicates the relationship expected for best ITD. **b**, the estimated characteristic phase as a function of the carrier frequency of the linear component. **c**, joint distribution of the estimated CD and CP. Note that the combined effect of the CD and the CP produces a narrower range of carrier phases than produced by either alone.

Figure 6.4c shows the data in Figure 6.4a normalised to have a half-width of one unit. The envelopes for both the broadly tuned and narrowly tuned groups were the same structure, and could be transformed onto one another through a combination of translation and dilation. Although a Gaussian (as used in the Gabor model) fitted this envelope shape well ( $r = 0.96$ , Figure 6.4d), the majority of the explained variance occurred at central ITDs and the broad tails of the envelopes could not be captured. To determine if the tails were an artefact of a noise floor, preventing the envelope from reaching zero at extreme ITDs, the neurons were visually examined for any obvious sinusoidal variation of the carrier within the tail. However, because the range of ITDs presented to each neuron was scaled by CF, the tails could only be observed for the five neurons with narrowly tuned envelopes. While  $\frac{3}{5}$  of these neurons showed noisy responses in the tails, for  $\frac{2}{5}$  neurons the carrier within the tail was modulated at a lower frequency than it was at central ITDs (see discussion of frequency modulation in previous section). However, extrapolation from these two neurons to the population as a whole is unlikely to be reliable, particularly since they are drawn from the minority of narrowly tuned responses.

### *Characteristic delay and characteristic phase*

The original reason for fitting the Gabor model to noise-delay functions was to investigate the composition of the delay responsible for the CF-dependent distribution of best ITDs

observed in IC. Assuming that, in the absence of any internal delay, the response would have been an autocorrelation with all components symmetrical around zero

$$r_1(\tau) = a_1(\tau) \cos(2\pi f_c \tau) \quad (6.5)$$

then the linearity of the phase response of the linear component suggested that the internal delay could be expressed as a combination of a time delay and a phase delay—equivalent to the characteristic delay and the characteristic phase normally defined for pure-tone responses. Any CD  $\tau_0$  would have influenced both the carrier and the envelope equally, while any CP  $\phi_0$  would only have affected the sinusoidal component. Thus, the linear component of the response could be expressed as

$$r_1(\tau) = a_1(\tau - \tau_0) \cos[2\pi f_c(\tau - \tau_0) - \phi_0] \quad (6.6)$$

In order to reduce the effect of the noisy tails of the envelope, the CD was estimated from the centroid of the squared amplitude envelope. The CP was then estimated from the disparity between the carrier phase  $\theta_c$  and that predicted by the CD

$$\phi_0 = \theta_c - 2\pi f_c \tau_0 \quad (6.7)$$

Similar to the best ITD, CDs were negatively correlated with  $f_c$  when expressed in ms (Figure 6.5a;  $r = -0.53$ ,  $P = 0.044$ , Spearman's rank correlation coefficient). When expressed in cyc re  $f_c$ , the CD was independent of the carrier frequency ( $P = 0.35$ ), with a median value of 0.16 cyc re  $f_c$  (interquartile range 0.12 to 0.23 cyc re  $f_c$ ), which was consistent with that expected for the best ITD.

The characteristic phase (Figure 6.5b) was clustered around zero with a mean value of  $-0.01$  cyc ( $R = 0.84$ ,  $P \leq 0.001$ , Rayleigh test), and was strongly correlated with the characteristic delay (Figure 6.5c;  $r = 0.44$ ,  $P \leq 0.05$ , Mardia's linear-circular correlation coefficient). The combined effect of the CD and the CP produced a tighter distribution of carrier phases than expected from either acting alone.

### 6.3.2 The lowpass component

The lowpass components for the six neurons from DNLL illustrated in Figure 4.9 are shown in Figure 6.6. All but one of the components showed significant modulation to ITD ( $P \leq 0.05$ , Wald–Wolfowitz runs test); the one neuron that failed (Figure 6.6c,  $P = 0.078$ ) appeared to do so due to a combination of the narrow tuning of the response and a high level of noise. Strongly asymmetric neurons showed more asymmetric lowpass components, with a deep trough to the left of the central peak (Figure 6.6b, c). Interestingly, the lowpass component often appeared Mexican-hat shaped (Figure 6.6e, f), with suppression of the firing rate either side of the main peak. While some lowpass components appeared to lack this suppression, this may have been a consequence of the narrow range of ITDs sampled ( $\pm 1.5$  cyc re CF), and a wider range of sampling may have revealed the side-toughs. The lowpass distortions were visually assessed in order to determine whether such a structure was likely.  $10/15$  neurons in the DNLL showed a lowpass distortion that appeared to have a

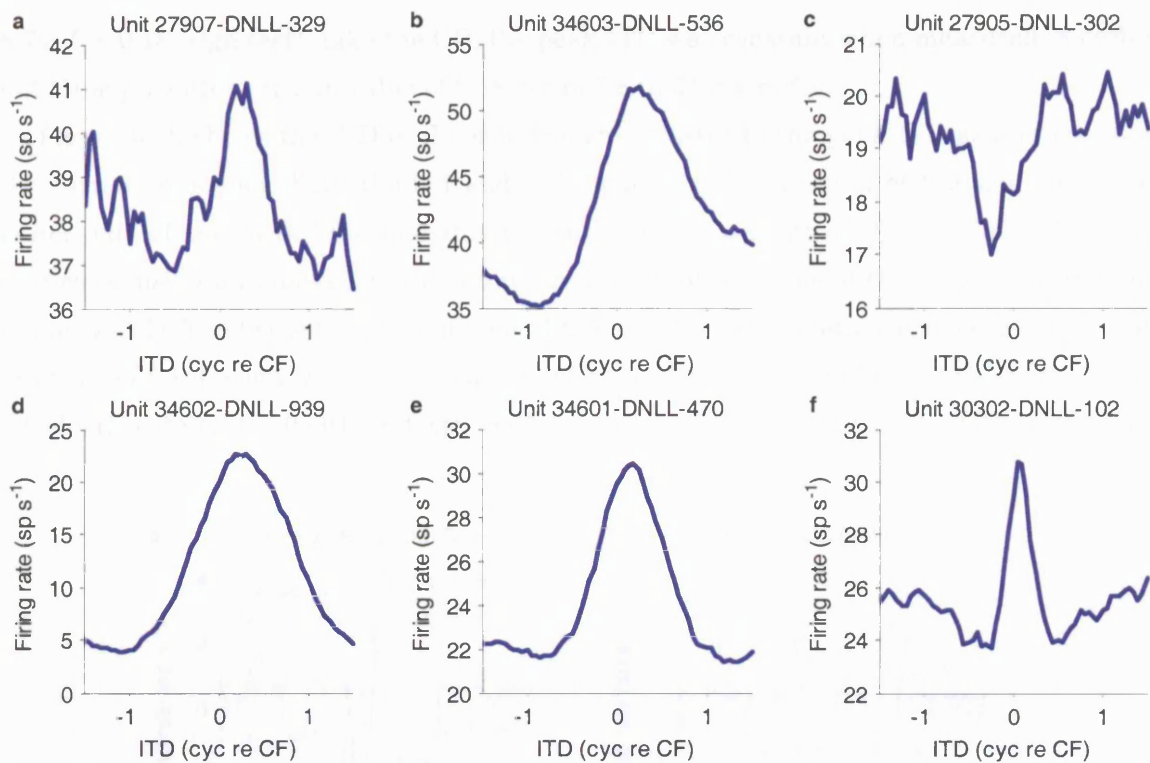


**Figure 6.6** Lowpass components of DNLL dual-delay functions.

The responses can often be seen to be Mexican-hat shaped with a suppression of the response either side of the main peak (e.g. e, f). Original dual-delay functions shown in Figure 4.9.

trough either side of the main peak (e.g. Figure 6.6a, e, f),  $\frac{4}{15}$  neurons showed only one trough to the left of the main peak, but appeared likely to be triphasic (e.g. Figure 6.6b, d). Only  $\frac{1}{15}$  neurons appeared unlikely to be Mexican hat shaped (Figure 6.6c).

To investigate any dependency of the shape of the lowpass component on CF, the peaks and troughs were identified by smoothing the lowpass components using a three-point moving-average filter and locating zero crossings in the first derivative (see Section 3.3.2 for a more detailed method). One neuron (Figure 6.6c) was omitted since it was not possible to reliably locate the peak in the response.

The peak ITD of the lowpass component occurred around the peak ITD of the envelope of the linear component (i.e. the CD), with no significant difference between the two (Figure

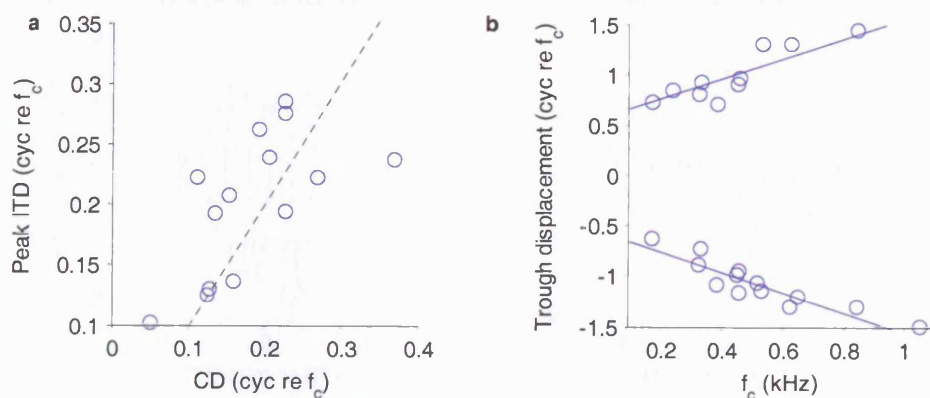
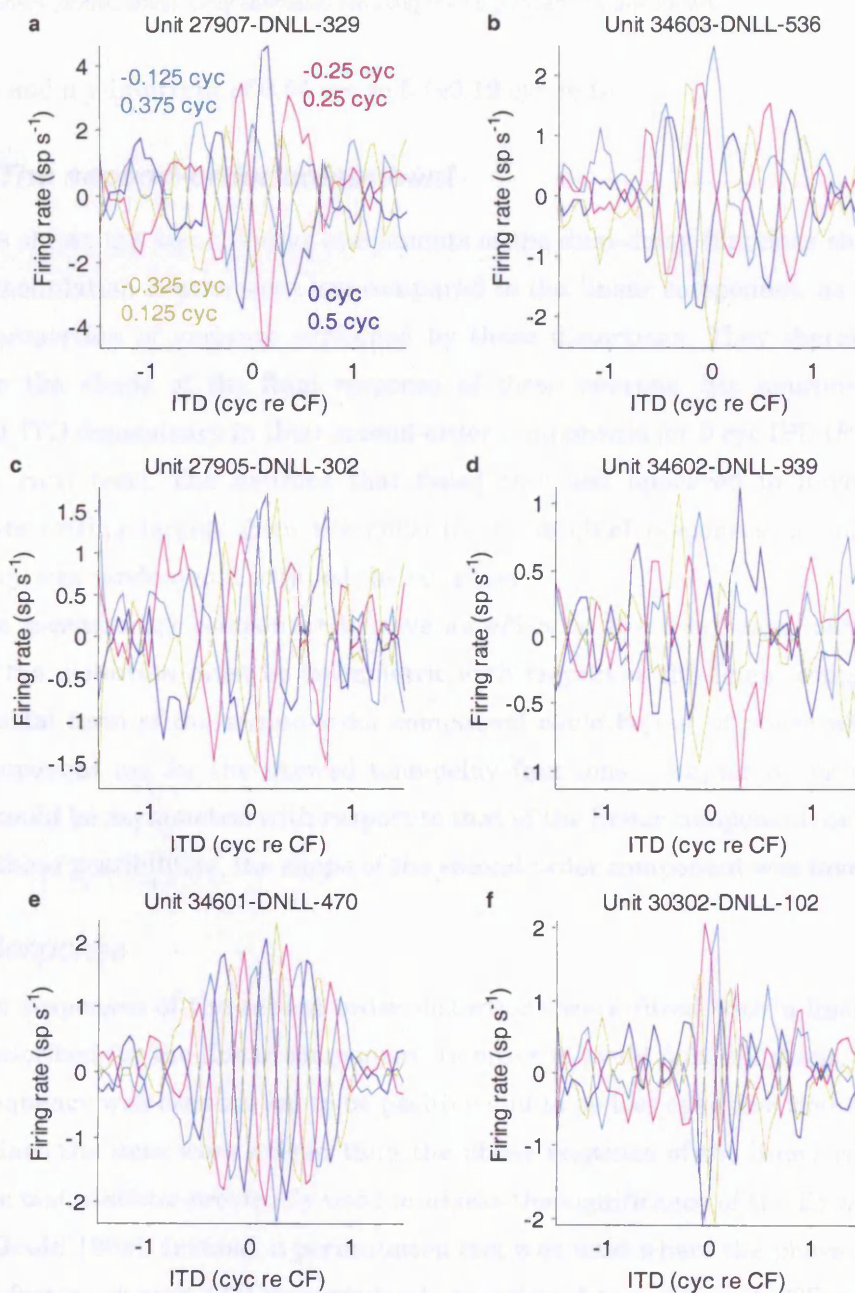


**Figure 6.7** Shape characteristics of the lowpass component of DNLL dual-delay functions.

**a**, the peak ITD of the lowpass component compared to the characteristic delay measured for the linear component. the dotted line indicates the line of equality. **b**, the ITD of the side-troughs as a function of the carrier frequency of the linear component.

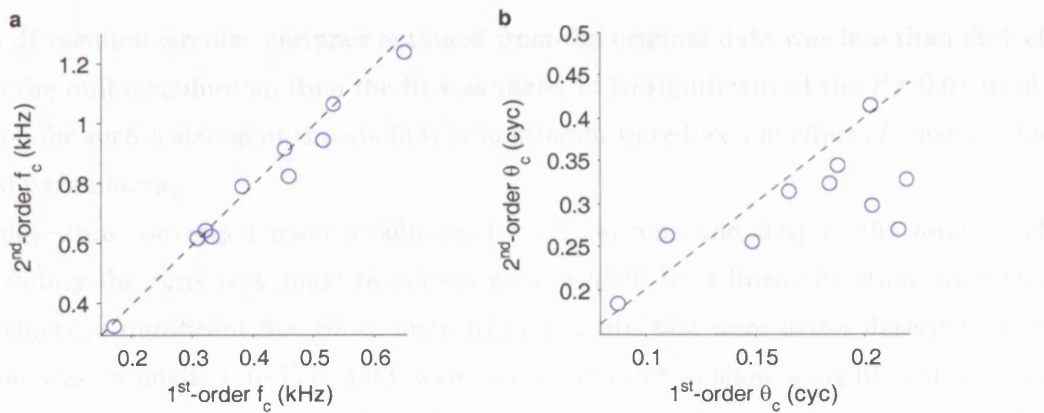
6.7a;  $P = 0.18$ , sign test). Like the CD, the peak ITD was constant when measured in cycles of CF (or  $f_c$ ) with a median value of 0.18 cyc re CF (0.21 cyc re  $f_c$ ).

Figure 6.7b shows the ITD of the side troughs relative to the peak ITD as a function of the carrier frequency. Both the left and right side troughs occurred at the same distance either side of the peak ITD, and this distance was dependent on  $f_c$  (and CF). This was confirmed using an analysis of covariance on the absolute value of the displacement from the peak ITD. The two sets of data did not differ significantly in terms of slope ( $P = 0.27$ ), or in terms of y-intercept ( $P = 0.55$ ). Consequently, both groups could be fit by a single linear trend ( $R^2 = 0.91$ ,  $P \leq 0.001$ , F-test), with a slope of 1.0 ms ( $\pm 0.2$  ms, 95% confidence



**Figure 6.8 Second-order components of DNLL dual-delay functions.**

Responses are dependent on twice the IPD, resulting in identical responses at antiphasic IPDs. A colour key for the IPD is given in a. All neurons showed significant ITD dependency in the 0 cyc IPD response, with the exception of c and d.  $P$  values resulting from the significance test were: a,  $P < 0.001$ ; b,  $P = 0.014$ ; c,  $P = 0.55$ ; d,  $P = 0.11$ ; e,  $P = 0.008$ ; and f,  $P = 0.047$ . Original dual-delay functions shown in Figure 4.9.



**Figure 6.9 Comparison of carriers of linear and second-order components of DNLL dual-delay responses.** **a**, the estimated carrier frequency for the 2<sup>nd</sup>-order component as a function of that of the linear (1<sup>st</sup>-order) component. **b**, the estimated carrier phase. Note that both parameters appear to be roughly twice the value of those obtained for the linear component (dotted lines). Only estimates resulting from significant fits are shown.

intervals) and a y-intercept of 0.54 cyc re  $f_c$  ( $\pm 0.12$  cyc re  $f_c$ ).

### 6.3.3 The second-order component

Figure 6.8 shows the second-order components of the dual-delay functions shown in Figure 4.9. The modulation depths were low compared to the linear component, as expected from the low proportion of variance explained by these distortions. They therefore had little impact on the shape of the final response of these neurons. Six neurons (15%) showed significant ITD dependency in their second-order components for 0 cyc IPD ( $P \leq 0.05$ , Wald–Wolfowitz runs test). The neurons that failed this test appeared to have second-order components arising largely from the noise in the original responses; as such, their ITD dependency was random and so failed the runs test.

For the second-order component to have an effect on the delay asymmetry of the total response, the distortion must be asymmetric with respect to the linear component. Either the sinusoidal term of the second-order component could be out of phase with that of the linear component (as for the skewed tone-delay functions, Chapter 3), or the amplitude envelope could be asymmetric with respect to that of the linear component, or both. In order to assess these possibilities, the shape of the second-order component was investigated.

#### Phase Response

The phase responses of the second order distortions were fitted with a linear function of ITD, as described for the linear component. In order to avoid false solutions, the estimated carrier frequency was constrained to be positive and to be less than five times the CF of the neuron. Since the data were noisier than the phase response of the linear component, the asymptotic test statistic previously used to assess the significance of the fit was unlikely to be valid (Gould 1969). Instead, a permutation test was used where the phase response (and weighting factor) at each ITD was randomly reassigned to a different ITD and then fitted by the linear model. This was repeated 100 times in order to estimate the null distribution of the residual circular variance under the null hypothesis of no ITD sensitivity in the

response. If residual circular variance obtained from the original data was less than 99% of values in the null distribution, then the fit was taken to be significant at the  $P \leq 0.01$  level. The reason for such a stringent threshold was to attempt to reduce the effect of noise on the measured parameters.

The algorithm converged upon a solution for all neurons and despite the number of neurons failing the runs test, most responses were well fit by a linear function, with  $10/15$  neurons showing significant fits. Since neurons failing this test were better described by a model that was insensitive to ITD, they were considered not to show a significant second-order component and were rejected from all subsequent analysis. The median  $R^2$  value for the significant fits was 0.53 (interquartile range 0.49 to 0.63) and only one neuron ( $1/10$ ) showed any significant ITD-dependence in its residuals ( $P = 0.048$ , circular runs test). Thus, for most neurons the linear approximation was sufficient to describe the phase response. Although this was likely due to a low signal-to-noise ratio for these second-order components rather than a lack of any phase modulation, the fits gave a good indication of the shape of the second-order components.

The estimated carrier frequency of the second-order component was distributed around twice that of the linear component (Figure 6.9a), with no significant difference between the two ( $P = 1.00$ , sign test). In addition there was little phase-disparity between the second-order and linear components (Figure 6.9b), with the majority of neurons showing estimated carrier phases that were around twice the value of that estimated for the linear component ( $P = 0.34$ , sign test). Only three neurons appeared to deviate from this trend (Figure 6.8b-d), at least two of which were strongly affected by noise. The sinusoidal component of the second-order component in the DNLL was therefore largely symmetric with respect to that of the linear component.

### Amplitude envelope

For some responses, it appeared that the amplitude envelopes for the second-order

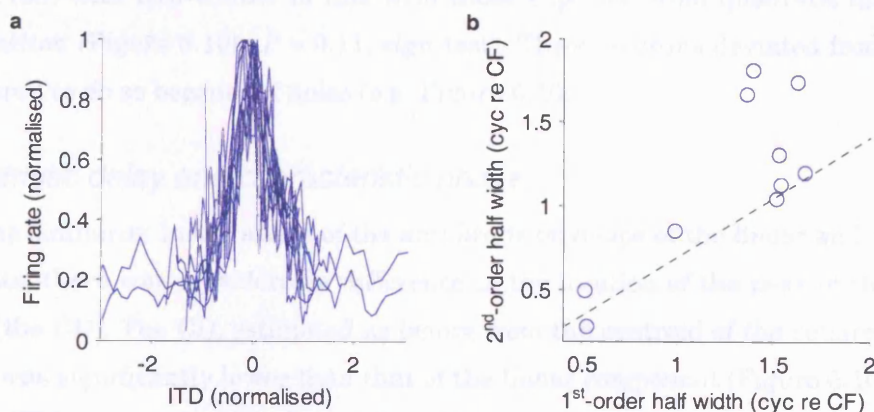


**Figure 6.10 Amplitude envelopes of second-order components of DNLL dual-delay functions.**

**a**, smoothed amplitude envelopes for all 11 neurons showing significant modulation to ITD, normalised by maximum firing rate. The ITD has also been normalised so that the half-width of each envelope is one. **b**, the distribution of half-widths of the amplitude envelopes of the second-order components, compared to those for the linear components. The dotted line shows the half-width predicted for the second-harmonic component of a Gabor function that has been distorted by a quadratic nonlinearity.

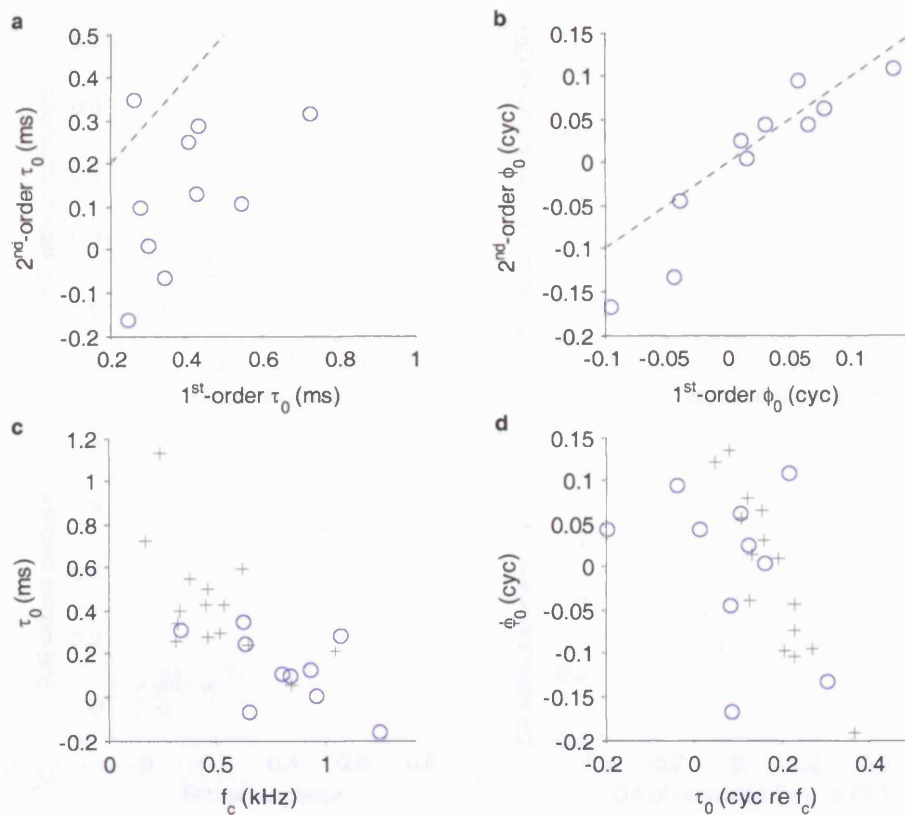


**Figure 6.11 Comparison of characteristic delay and characteristic phase of linear and second-order components of DNLL dual-delay functions.**

**a**, the CD estimated from the second-order component compared to that from the linear component. The dotted line indicates the line of equality. The two different components provide different estimations of CD. **b**, the CP estimated from the second-order component compared to that from the linear component. A similar estimate is provided by the different components. **c**, The distribution of the CD (in ms) as a function of the carrier frequency for both the second-order component (blue circles) and the linear component (grey crosses). Note that both distributions appear to form a continuum. **d**, the distribution of CP as a function of the CD for both the second harmonic (blue circles) and the linear components (grey crosses).

component were quite dissimilar to those of the corresponding linear component. For example, the responses in Figure 6.8b, and f appeared to be bimodal while their linear components showed only unimodal envelopes. However, such features could have been an artefact of noise in the recording. The majority of amplitude envelopes were unimodal (Figure 6.10a) with half-widths in line with those expected from quadratic distortion of a Gabor function (Figure 6.10b;  $P = 0.11$ , sign test). Three neurons deviated from this trend, but appeared to do so because of noise (e.g. Figure 6.10c).

### *Characteristic delay and characteristic phase*

Despite the similarity in the shape of the amplitude envelope of the linear and second-order components, there was considerable difference in the location of the peak of the amplitude envelope (the CD). The CD, estimated as before from the centroid of the squared amplitude envelope, was significantly lower than that of the linear component (Figure 6.10a;  $P = 0.022$ , sign test). This was surprising since the CD is presumed to be constant, regardless of spectral content. Instead, the lower CD appeared attributable to an apparent continuation of the carrier-frequency dependency of the CD observed for the linear component (Figure 6.10c).

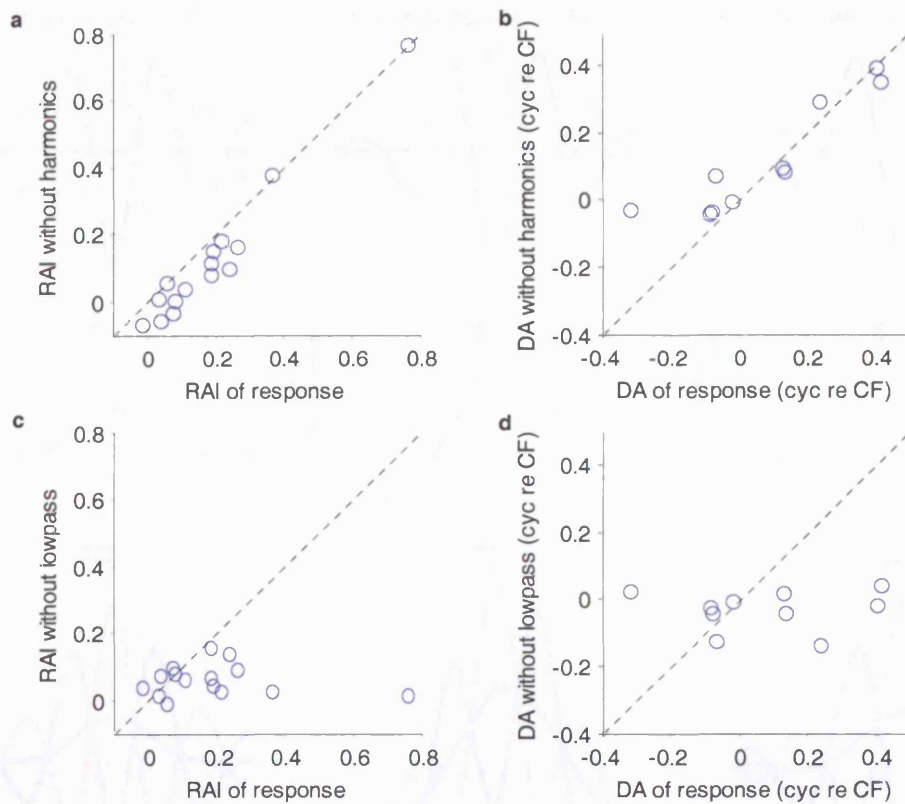


**Figure 6.12 Contribution of distortions to the degree of asymmetry in DNLL dual-delay functions.** **a**, The RAI of an approximation formed by only the lowpass and linear components, compared to the RAI of the original response. **b**, The delay asymmetry of the same lowpass approximation, compared to that of the original response. **c**, The RAI of an approximation formed by only the harmonic (second-order and higher) and linear components, compared to the RAI of the original response. **d**, The delay asymmetry of the harmonic approximation, compared to that of the original response. Note that when the lowpass component is present, the approximation retains the original asymmetry; when absent, the approximation is more symmetrical.

6.10c). Expressed in cycles of the carrier frequency (of the second distortion), the CD had a median value of 0.09 cyc re  $f_c$  (interquartile range 0.01 to 0.16 cyc re  $f_c$ ).

The CP of the second-order component was not significantly different to that of the linear component (Figure 6.10b;  $P = 0.34$ , sign test), indicating that the CP was the same, independent of spectral content. However, any difference may have been missed because of the test being underpowered. Unlike the linear component, no systematic covariation in CD and CP was observed (Figure 6.10d;  $P > 0.1$ , Mardia's linear-circular rank correlation coefficient).

### 6.3.4 The origin of asymmetry in DNLL dual-delay functions

The asymmetries observed in DNLL chiefly arose from the lowpass component—components third-order and greater were negligible, and the contribution of the second-order component was weaker and more indirect than that of the lowpass component. While removing the harmonic components from the responses produced little change in asymmetry, removing the lowpass component produced a much more symmetrical response (Figure 6.12). The envelope structure of the final response was therefore formed by direct summation of the envelope structure of the linear component and the lowpass component (Figure 6.13).

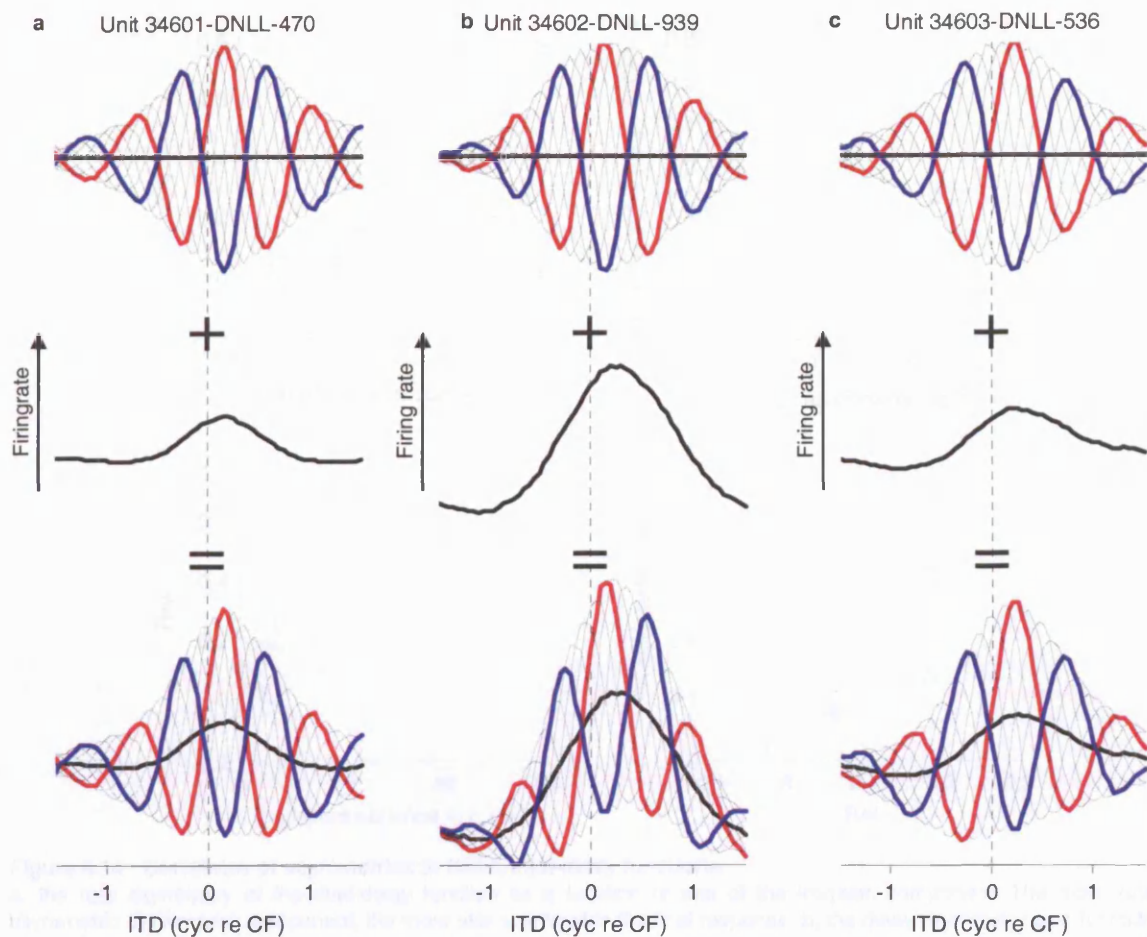


**Figure 6.13 The origin of asymmetry for DNLL dual-delay functions.**

Responses in DNLL are well approximated by the sum of the linear component (top) and the lowpass component (middle). Original responses shown in Figure 4.9. **a**, if the lowpass distortion is symmetrical with respect to the linear response then it will not produce any delay asymmetry. However, it will affect the positive envelope more than the negative envelope, producing a rate asymmetry. **b**, if the magnitude of the distortion is large, then bimodality can result in the lower envelope. **c**, if the lowpass distortion is asymmetric with respect to the linear response, a delay asymmetry is produced.

### Rate asymmetry

When the lowpass component was symmetrical with respect to the envelope of the linear component then a rate-asymmetric function resulted (Figure 6.13a). Since the linear component itself is rate symmetric, any rate asymmetry is expected to come directly from the lowpass component. In order to measure its rate-asymmetry, the RAI was calculated for the lowpass component. The baseline firing rate was determined from the average firing rate at the two most extreme ITDs. The RAI was then measured as before, using (4.14) where  $A_+$  was the area above the baseline and below the lowpass component and  $A_-$  was the area below the baseline and above the lowpass component. The RAI of the lowpass component was correlated with the RAI of the whole function (Figure 6.14a;  $r = 0.68$ ,  $P = 0.007$ , Spearman's rank correlation coefficient), confirming its determinant role in producing the rate-asymmetry.

Since the side troughs were shallow, the majority of the lowpass component was above the baseline response to uncorrelated noise. Thus, the stronger the contribution of the lowpass component to the shape of the tuning curve, the more positive the RAI. This

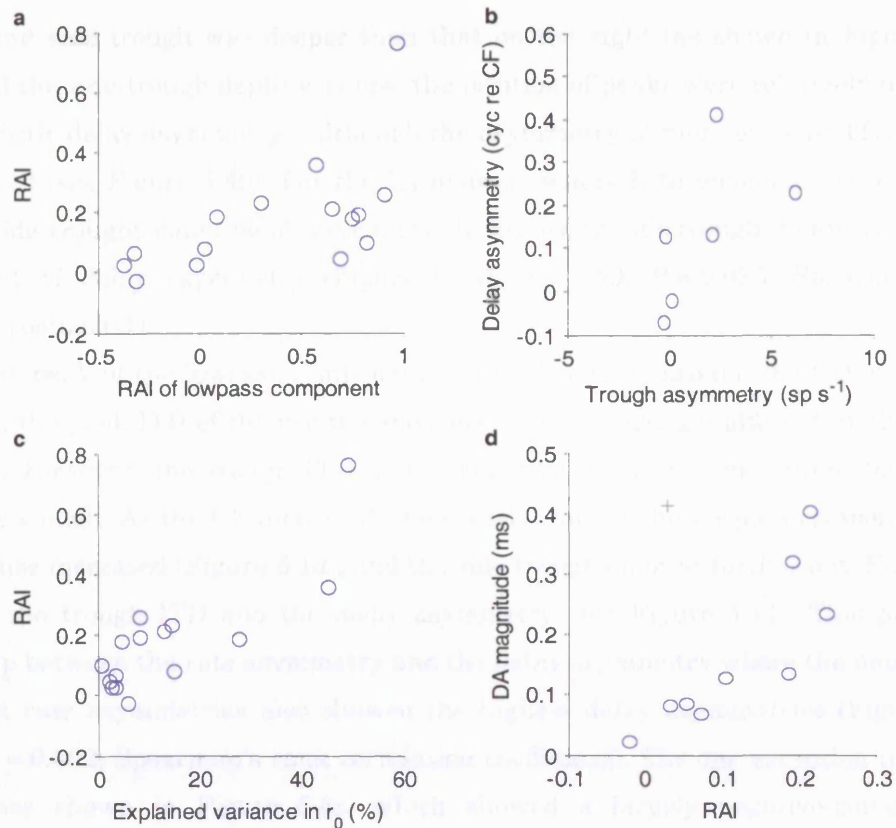


**Figure 6.14 Correlates of asymmetries in DNLL dual-delay functions.**

**a**, the rate asymmetry of the dual-delay function as a function of that of the lowpass component. The more rate asymmetric the lowpass component, the more rate asymmetric the final response. **b**, the delay asymmetry as a function of the difference in side-trough depths. As the left side-trough becomes deeper, the delay asymmetry becomes more positive. **c**, the RAI as a function of the proportion of explained variance in the lowpass component. The stronger the lowpass component, the stronger the rate asymmetry. **d**, the magnitude of the delay asymmetry as a function of the rate asymmetry. The larger the rate asymmetry, the more pronounced the delay asymmetry.

relationship can be seen from Figure 6.14c, which shows a positive correlation of the RAI with the proportion of variance explained by the lowpass component ( $r = 0.71$ ,  $P = 0.004$ , Spearman's rank correlation coefficient). The increase in RAI with CF observed in the DNLL (Figure 4.11) was therefore a consequence of the stronger contribution of the lowpass component at higher CFs (Figure 6.1d). This was confirmed by the fact that, after adjusting for the proportion of variance explained by the lowpass component, the correlation between CF and RAI was no longer significant ( $P > 0.1$ , Spearman's rank correlation coefficient).

### *Bimodality*

Because of their side troughs, the lowpass components were narrower than the envelope of the linear component. Thus, a strong lowpass component could result in bimodality in the negative envelope (Figure 6.13b). Since the lowpass component in DNLL was largely above the baseline (with the exception of Figure 6.6c), bimodality was only observed in the negative envelope of DNLL (Section 4.4.2).

### *Delay asymmetry*

Delay asymmetry resulted when the lowpass component was asymmetric with respect to the envelope of the linear component (Figure 6.13c). For the more dramatic asymmetries,

the left hand side trough was deeper than that on the right (as shown in Figure 6.13c). However, if the side-trough depth was low, the position of peaks were relatively unaffected, producing little delay asymmetry—although the asymmetry at more extreme ITDs could be quite marked (see Figure 5.4b). For the  $\frac{6}{14}$  neurons where both envelopes were unimodal and both side troughs could be observed, the difference in side-trough depth was a strong determinant of delay asymmetry (Figure 6.14b;  $r = 0.89$ ,  $P = 0.033$ , Spearman's rank correlation coefficient).

Since the peak of the lowpass component occurred roughly around the CD of the linear component, the peak ITD of the positive envelope was not strongly affected by the lowpass component. However, the trough ITD of the negative envelope was shifted towards the deeper side trough. As the CF increased, the contribution of the lowpass component to the final response increased (Figure 6.1d), and the side troughs moved further out (Figure 6.7b), increasing the trough ITD and the delay asymmetry (see Figure 4.11). This produced a relationship between the rate asymmetry and the delay asymmetry where the neurons with the highest rate asymmetries also showed the highest delay asymmetries (Figure 6.14d;  $r = 0.90$ ,  $P = 0.002$ , Spearman's rank correlation coefficient). The one exception to this was the response shown in Figure 6.6c, which showed a largely negative-going lowpass component. This reduced the RAI compared to that expected from the magnitude of its delay asymmetry.

Given that the RAI is correlated with CF, and that the degree of delay asymmetry is correlated with the RAI, it is perhaps surprising that the degree of delay asymmetry is not correlated with CF (Figure 4.11). However, the degree of delay asymmetry is not solely determined by CF-dependent factors such as the RAI, but will also be affected by factors showing no apparent correlation with CF, such as the difference in side-trough depths in the lowpass component and the offset of the peak ITD of the lowpass component relative to the CD. It is these CF-independent factors that are likely responsible for lack of a significant relationship between the CF and the magnitude of delay asymmetry.

## 6.4 Components of IC dual-delay functions

The dual-delay functions recorded from IC were analysed in the same manner as those recorded from DNLL. Unlike the DNLL, the second-order component had a stronger contribution to the response and so it was likely that this would play a more prominent role in determining the symmetry of the dual-delay function.

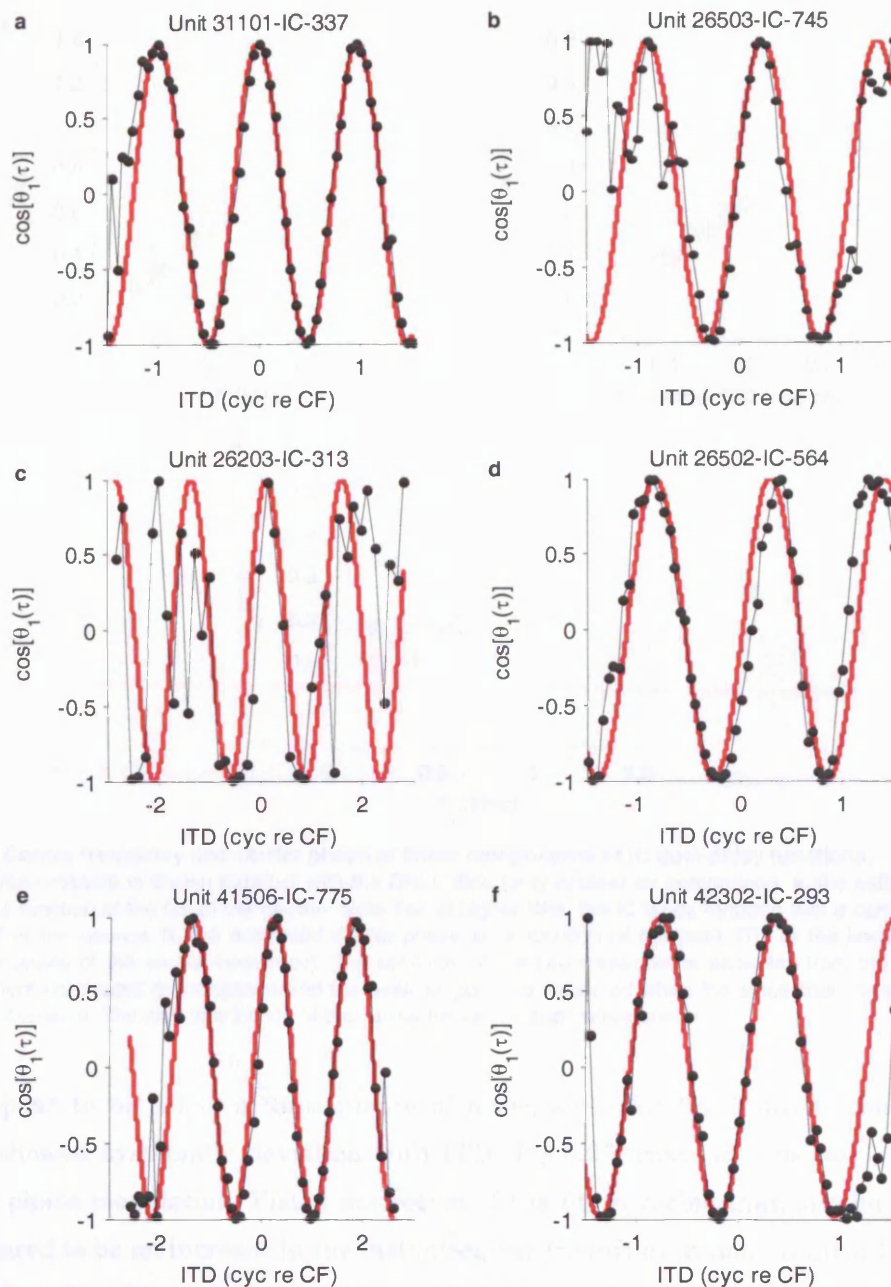


**Figure 6.15** Carriers of linear components of IC dual-delay functions.

Cosine transformed phase spectra are shown (black) together with fitted sinusoids (red). Weighted  $R^2$  values for the fits were: a, 0.99; b, 0.89; c, 0.70; d, 0.91; e, 0.96; and f, 0.96. Original dual-delay functions shown in Figure 4.10.

### 6.4.1 The linear component

#### Phase response

The phase response of the linear component of the IC dual-delay functions was fitted with a linear model as for those in DNLL. Figure 6.15 shows the results of the regression for the neurons illustrated in Figure 4.10. The regression converged for all neurons and was significant ( $P \leq 0.05$ , F-test). The  $R^2$  value for the fits ranged from 0.37 to 0.99 with a median value of 0.91 (interquartile range 0.81 to 0.96). Like the DNLL, the phase was largely linear over the central region of the response, with the unexplained variance arising at the extreme ITDs where the noise was having the strongest effect. However, these errors

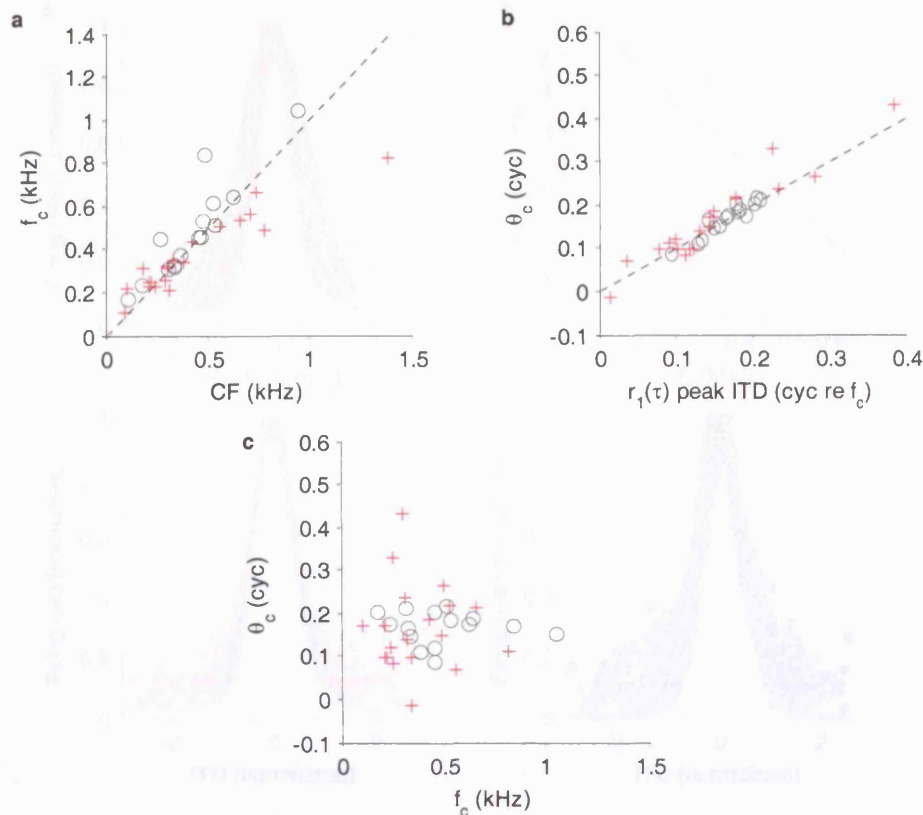


**Figure 6.16 Carrier frequency and carrier phase of linear components of IC dual-delay functions.**

The IC data (red crosses) is shown together with the DNLL data (grey circles) for comparison. **a**, the estimated carrier frequency as a function of the CF of the neuron. Note that at higher BFs, the IC tends to respond with a carrier frequency below the CF of the neuron. **b**, the estimated carrier phase as a function of the peak ITD of the linear component (expressed in cycles of the carrier frequency). The similarity of the two measures is expected from the fact that the linear component dominates the response and the peak response is expected when the sinusoidal component of the response is maximal. **c**, The joint distribution of the carrier frequency and carrier phase.

did not appear to be solely a consequence of noise, since for  $15/20$  neurons the residuals showed a systematic deviation with ITD ( $P \leq 0.05$ , circular runs test), indicating significant phase modulation. Visual inspection of the fits revealed that, similar to DNLL, there appeared to be an increase in the instantaneous frequency at more central ITDs.

The median  $R^2$  value in IC was 0.06 lower than the median  $R^2$  value in DNLL ( $P = 0.005$ , Wilcoxon rank-sum test). However, it was impossible to say whether this was due to a difference in phase modulation, or the higher level of noise in IC compared to DNLL.

The estimated carrier frequencies (Figure 6.16a) were greater than CF at low CFs and lower than CF at high CFs, this was significant since the difference between CF and  $f_c$  was correlated with CF ( $r = 0.86$ ,  $P \leq 0.001$ , Spearman's rank correlation coefficient). This relationship was similar to that observed in the DNLL at low frequencies, but the limiting of carrier frequency at higher ITDs appeared to be unique to the IC. Because this limiting did not appear to be present in DNLL, it is unlikely that this reflected a limit to phase locking in the peripheral auditory system.

The estimated carrier phase can be seen in Figure 6.16b. As expected, the carrier phase determined the peak ITD of the linear component, producing no significant difference between the two measures ( $P = 0.12$ , sign test). There was some overestimation of the peak

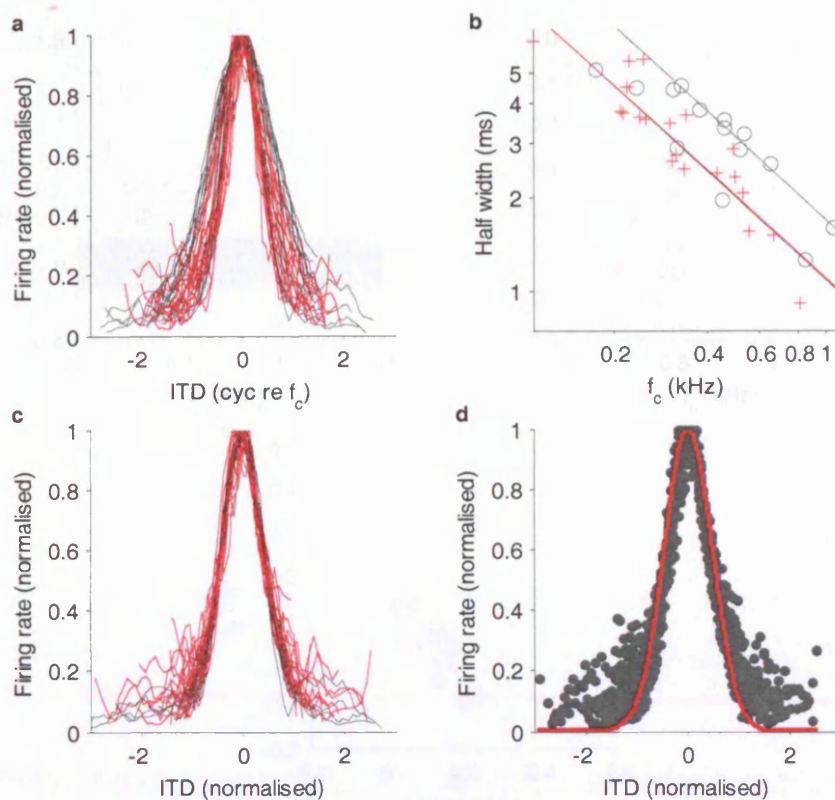


**Figure 6.17 Amplitude envelopes of linear components of IC dual-delay functions.**

**a**, the normalised smoothed amplitude envelopes for all 20 neurons recorded from IC (red curves). Curves for the DNLL are shown for comparison (grey). The ITD has been expressed in cyc re  $f_c$  and adjusted so that the centroid of the square of each envelope occurs at zero. **b**, the distribution of the half-widths of the envelopes in **a** as a function of the carrier frequency (red crosses). The DNLL data is shown for comparison (grey circles). The regression line for the IC data is shown in red. **c**, the same data as in **b** where the ITD has been normalised so that the half-width of each envelope is one. **d**, a Gaussian fit to the normalised IC envelopes in **c**.

ITD (e.g. Figure 6.15b) due to phase modulation of the sinusoidal component not captured by the regression.

### Amplitude envelope

Figure 6.17a shows the normalised envelopes of the linear components in the IC, where the ITD is expressed in terms of cycles of  $f_c$  and the envelope has been shifted so that the centroid of the squared function falls at zero ITD. Similar to the narrowly tuned group in DNLL, a clear power-law relationship of the form  $y = kx^c$  was present between the carrier frequency and the half-width of the envelope, with an estimated value of  $k$  of 1.1 and  $c$  of  $-0.90$  (Figure 6.17b;  $P \leq 0.001$ , F-test). An analysis of covariance revealed no significant difference between the IC neurons and the narrowly tuned group of DNLL neurons for either the power term ( $P = 0.83$ ) or the scaling-constant ( $P = 0.90$ ).

The shape of the envelope appeared to be consistent with those from other IC neurons and those in the DNLL (Figure 6.17c). The envelope shape was loosely Gaussian (Figure 6.17d,  $R^2 = 0.89$ ), but again there were problems with broad tails to the distribution. Several neurons showed modulation of the sinusoid within these tails, which was inconsistent with a mere noise floor. It therefore appeared that while a Gabor model could

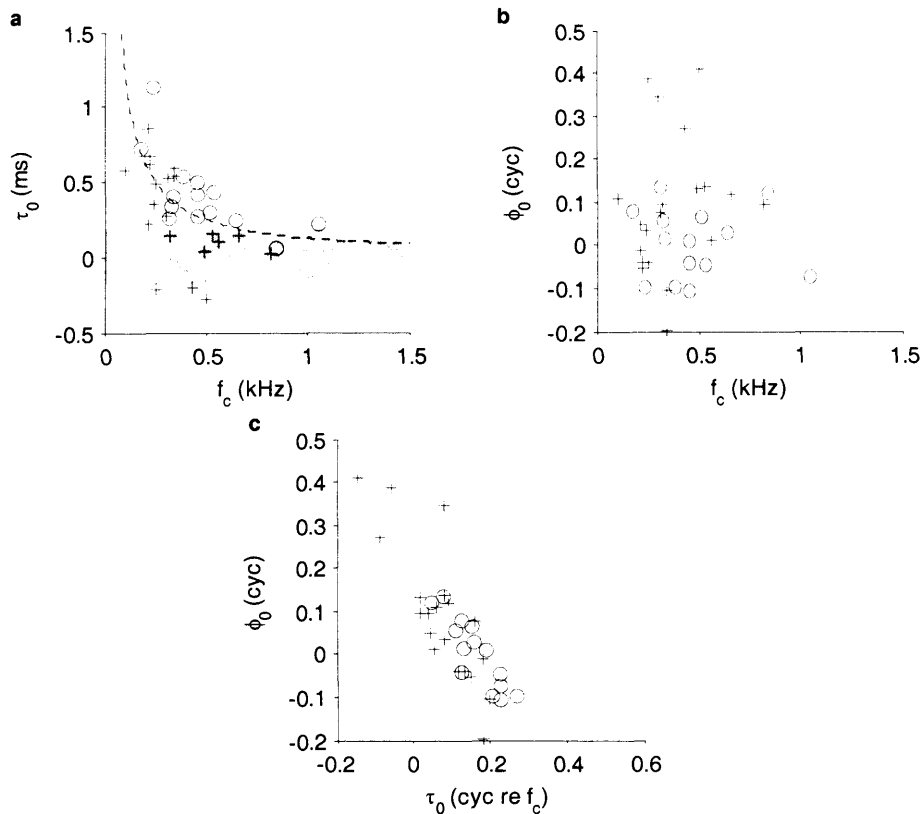


**Figure 6.18 Characteristic delay and characteristic phase of linear components of IC dual-delay functions.**

IC data (red crosses) is shown along with the DNLL data for comparison (grey circles). **a**, distribution of the estimated characteristic delay as a function of the carrier frequency of the linear component. The physiological range is shown in grey and the black dotted line indicates the relationship expected for best ITD. **b**, the estimated characteristic phase as a function of the carrier frequency of the linear component. **c**, joint distribution of the estimated CD and CP. Note that the combined effect of the CD and the CP produces a narrower range of carrier phases than produced by either alone.

capture much of the variance of the linear component, its suitability would be restricted to central ITDs.

### *Characteristic delay and characteristic phase*

The distribution of CD for the linear components in IC (Figure 6.18a) was similar to that observed for DNLL, except for the larger proportion of neurons with CDs inside the physiological range. Furthermore, the trough-type units in IC showed negative CDs, indicating that their amplitude envelope peaked at ipsilateral-leading delays. The distribution of CP (Figure 6.18b) was also similar, except for the few neurons with CPs near 0.5. As expected, both the large CPs and negative CDs arose from the trough-type neurons, consistent with a joint distribution of CD and CP similar to that observed in DNLL (Figure 6.18c). Thus, in both IC and DNLL, the combined effect of the two different delays is preserved so that the peak ITD of the linear component is relatively constant across CF.

### **6.4.2 The lowpass component**

The lowpass components for the six IC neurons shown in Figure 4.10 are shown in Figure 6.19. The IC showed a higher degree of heterogeneity in the shape of these components than was observed in DNLL, with only 5/20 responses appearing likely to be Mexican-hat

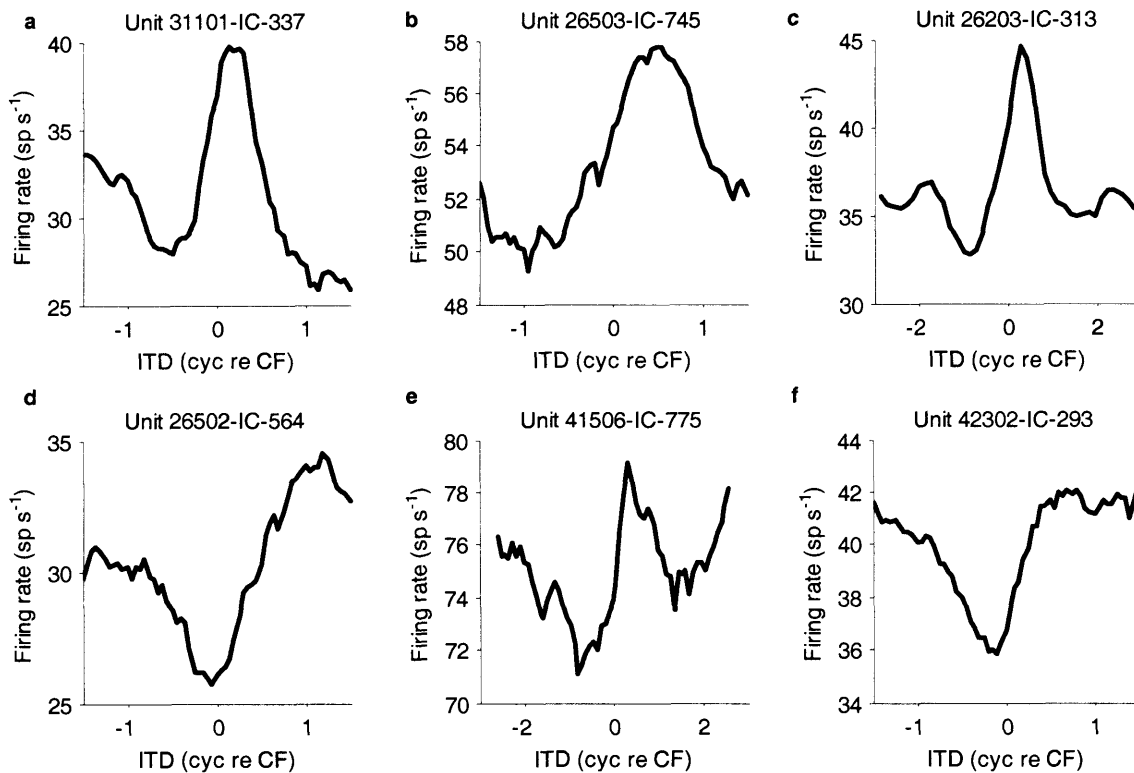


**Figure 6.19 Lowpass components of IC dual-delay functions.**

The responses appear more heterogeneous than those observed in DNLL, with more pronounced side troughs. Original dual-delay functions shown in Figure 4.10.

shaped. While the majority of neurons showed a pronounced peak at central ITDs ( $12/20$  neurons; Figure 6.19b, c), a few showed a pronounced trough ( $4/20$  neurons; Figure 6.19d, f), and several neurons showed both a prominent peak and a prominent trough ( $4/20$  neurons; Figure 6.19a, e). Most of the responses showed at least one peak and at least one trough in the range of ITDs recorded:  $7/20$  neurons showed side troughs on both the left and the right of the largest peak (Figure 6.19c, e),  $2/20$  neurons showed only a right side trough, and  $4/20$  neurons showed only a left side trough (Figure 6.19b, d). Of the remaining neurons,  $4/20$  neurons showed only a peak and  $3/20$  neurons showed only a trough (Figure 6.19f). Other oddities could also be identified, for example  $2/20$  of the responses appeared to show several peaks and troughs (Figure 6.19c), and  $3/20$  of the responses showed a large difference in response at extreme ITDs of opposite sign (Figure 6.19a).

Even when strongly modulated, the lowpass components in IC were less smooth than those recorded in DNLL, making reliable analysis of the shape of curves difficult. Broadly speaking, the lowpass component could produce an asymmetric either by being asymmetric, or, if symmetrical, by having its axis of symmetry offset from the peak of the envelope of the linear component. Figure 6.20a shows the deviation from CD of the closest peak or trough. There was usually either a peak or a trough around the characteristic delay, with no systematic difference between the two ( $P = 1.00$ , sign test), although for some neurons the difference could be large. The three trough-type neurons that showed negative CDs and CPs around 0.5 cyc showed troughs in their lowpass component around CD.

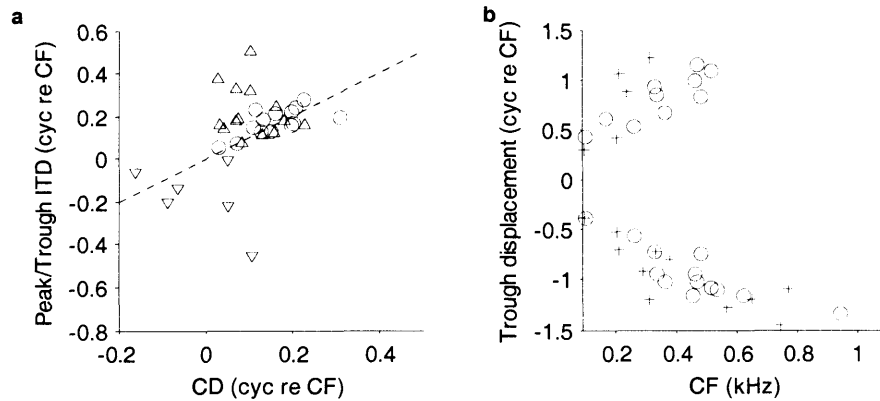


**Figure 6.20 Shape characteristics of the lowpass component of IC dual-delay functions.**

IC data (red) is shown along with the DNLL data for comparison (grey). **a**, The distribution of the ITD of the nearest peak (upwards triangles) or trough (downwards triangles) to the characteristic delay measured for the linear component. The dotted line indicates the line of equality. **b**, the ITD of the side-troughs as a function of the carrier frequency.

The majority of neurons showed asymmetric lowpass components with one prominent peak and one prominent trough. Figure 6.20b shows the variation in the position of the identifiable side troughs with respect to the peak of the lowpass component. The position of the side trough was identical to that in DNLL when viewed in terms of cycles of CF, with no difference in either the slope of the relationship ( $P = 0.97$ , analysis of covariance) or the y-intercept ( $P = 0.29$ ). Both sets of data were therefore fit by a single linear trend ( $R^2 = 0.63$ ,  $P \leq 0.001$ , F-test), with a slope of 1.2 ms ( $\pm 0.3$  ms, 95% confidence intervals) and a y-intercept of 0.41 cyc re CF ( $\pm 0.13$  cyc re CF). The similarity between the IC and the DNLL decreased slightly when the data were compared in terms of  $f_c$ , due to the difference in the CF-dependence of  $f_c$  for the two nuclei. While  $f_c$  is useful for comparing the structure of the linear components of the two nuclei, it is clearly less useful when comparing the lowpass components.

### 6.4.3 The second-order component

Figure 6.21 shows the second-order components for the dual-delay functions shown in Figure 4.10. As expected from the higher explained variance, the second-order components in IC made a stronger contribution to the shape of the dual-delay function than those in DNLL, with modulation depths on a par with those of the lowpass components. The majority of responses in IC ( $11/20$  neurons) showed significant ITD dependency in their second-order components at 0 IPD ( $P \leq 0.05$ , Wald–Wolfowitz runs test), indicating that for these responses, the second-order components were not a consequence of noise in the recording.

#### Phase response

The phase spectrum of the second-order components in IC were well fit by a linear function, with  $14/20$  neurons showing significant fits ( $P \leq 0.01$ , bootstrap test), with a median  $R^2$  value of 0.66 (interquartile ranges 0.44 to 0.81). Neurons failing this test were considered to show negligible second-order components and were excluded from subsequent analysis. Only four

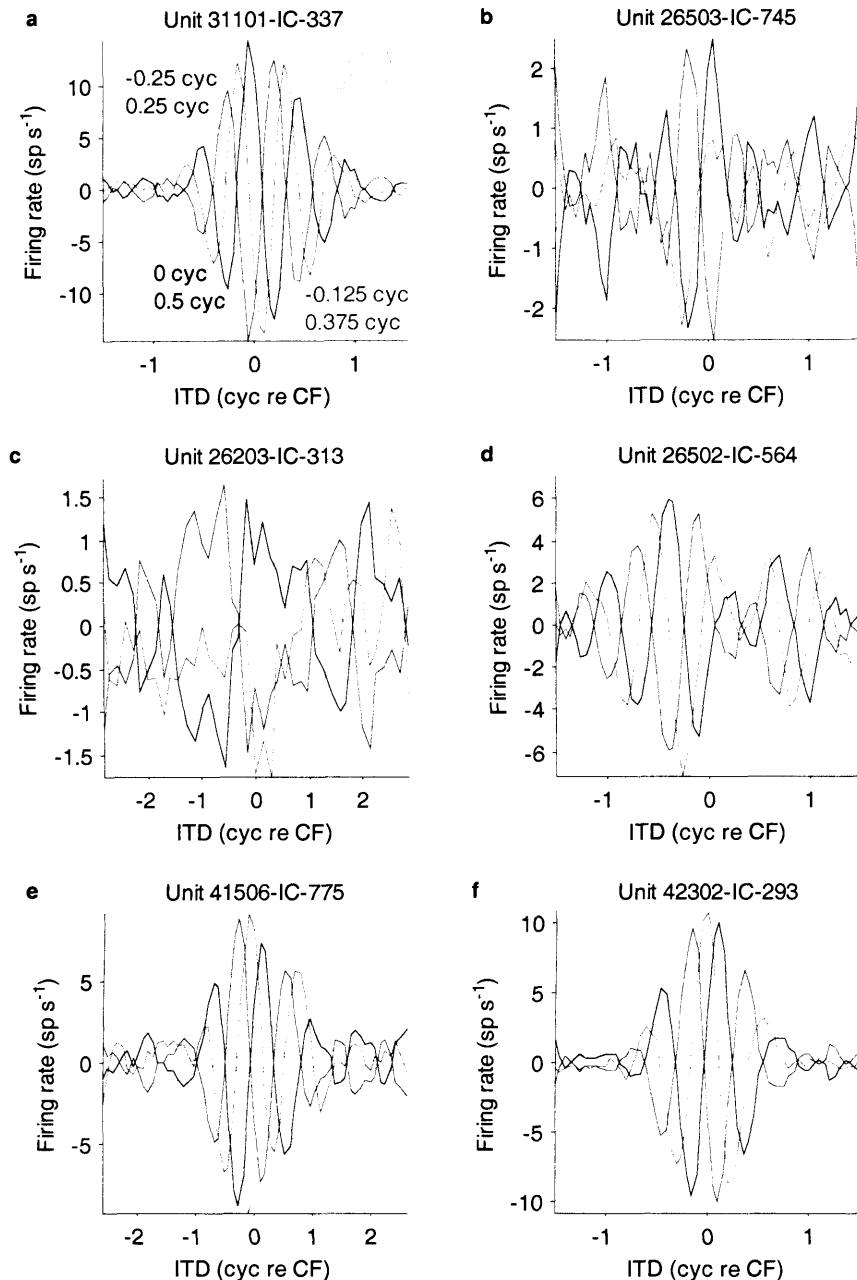


**Figure 6.21 Second-order components of IC dual-delay functions.**

A colour key for the IPD is given in **a**. All neurons showed significant ITD dependency in the 0 cyc IPD response, with the exception of **b**. *P* values resulting from the significance test were: **a**,  $p=0.015$ ; **b**,  $p=0.080$ ; **c**,  $p=0.043$ ; **d**,  $p=0.002$ ; **e**,  $p=0.002$ ; and **f**,  $p<0.001$ . Original dual-delay functions shown in Figure 4.10.

of the significant fits showed significant variation in their residuals ( $P \leq 0.05$ , circular runs test), indicating no significant phase modulation.

Similar to the DNLL, the estimated carrier frequency of the second-order component was around twice that of the linear component (Figure 6.22a), with no significant difference between the two ( $P = 1.00$ , sign test). While there was no significant phase disparity for the population as a whole ( $P = 0.79$ , sign test), several neurons in IC appeared to show a high degree of phase disparity, which did not appear to be a consequence of noise. The sinusoid of the second-order component was therefore more asymmetric with respect to that of the linear component in IC than in DNLL.

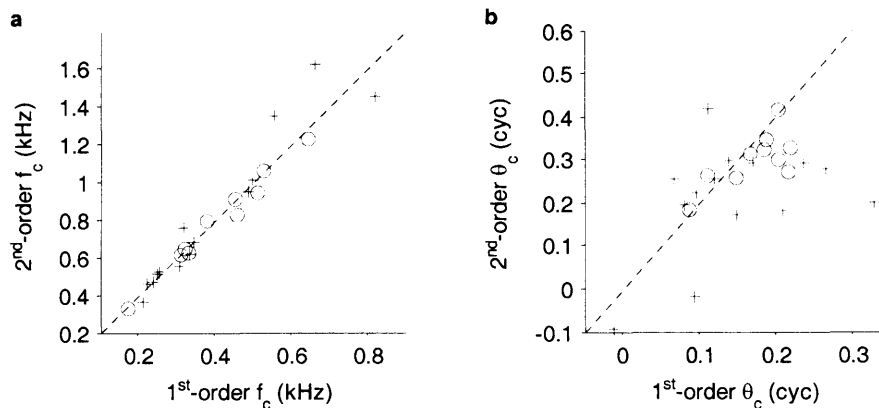


**Figure 6.22 Comparison of carriers of linear and second-order components of IC dual-delay responses.**

IC data (red crosses) is shown along with the DNLL data for comparison (grey circles). **a**, the estimated carrier frequency for the 2<sup>nd</sup>-order component as a function of that of the linear (1<sup>st</sup>-order) component. **b**, the estimated carrier phase. Note that both parameters appear to be roughly twice the value of those obtained for the linear component (dotted lines). Only estimates resulting from significant fits are shown.

### *Amplitude envelope*

The majority of amplitude envelopes were roughly unimodal as can be seen from Figure 6.23a. The half-width of the majority these envelopes was roughly equal to that expected from quadratic distortion of a Gabor function (Figure 6.10b;  $P = 0.057$ , sign test). Six neurons deviated from this trend, showing higher half-widths. Only one of these appeared to do so because of multimodality (Figure 6.21d), the higher half-widths for the other five appeared to be a measurement artefact arising from the noisiness of the amplitude envelopes (e.g. Figure 6.21b).

### *Characteristic delay and characteristic phase*

The distribution of the CD observed in IC was similar to that in DNLL, with a lower CD for the second-order component than for the linear component (Figure 6.24a). Although, this difference in CD for the two components was not significant ( $P = 0.057$ , sign test), the lower CD appeared to be a continuation of the  $f_c$  dependency of the CD observed for the linear

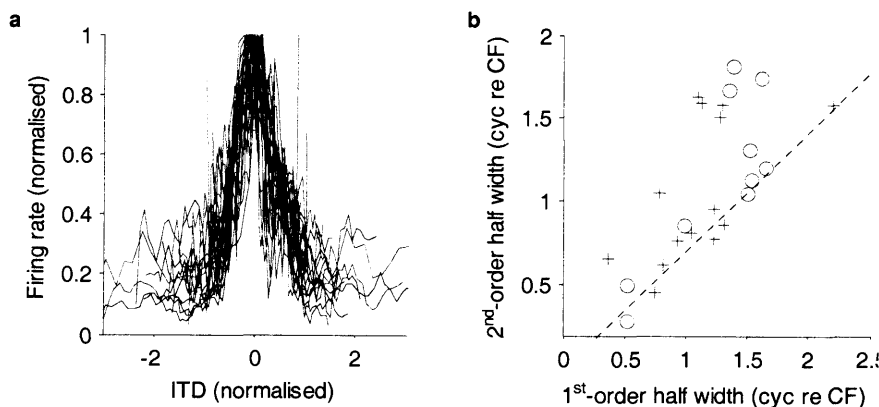


**Figure 6.23 Amplitude envelopes of second-order components of IC dual-delay functions.**

IC data (red) is shown along with the DNLL data for comparison (grey). **a**, smoothed amplitude envelopes for all 14 neurons showing significant modulation to ITD, normalised by maximum firing rate. The ITD has also been normalised so that the half-width of each envelope is one. **b**, the distribution of half-widths of the amplitude envelopes of the second-order components, compared to those for the linear components. The dotted line shows the half-width predicted for the second-harmonic component of a Gabor function that has been distorted by a quadratic nonlinearity.

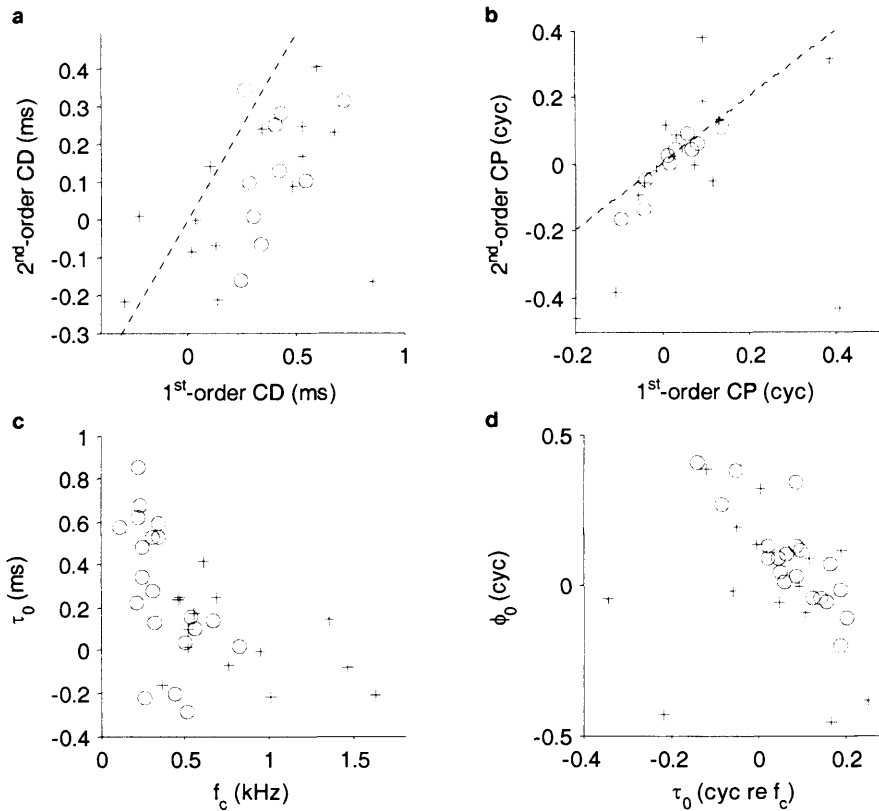


**Figure 6.24 Comparison of characteristic delay and characteristic phase of linear and second-order components of IC dual-delay functions.**

**a**, the CD estimated from the second-order component compared to that from the linear component. IC data (red) is shown along with the DNLL data for comparison (grey). The dotted line indicates the line of equality. The two different components provide different estimations of CD. **b**, the CP estimated from the second-order component compared to that from the linear component. IC data (red) is shown along with the DNLL data for comparison (grey). A similar estimate is provided by the different components. **c**, The distribution of the CD (in ms) as a function of the carrier frequency for both the second-order component (red crosses) and the linear component (grey circles). Note that both distributions appear to form a continuum. **d**, the distribution of CP as a function of the CD for both the second harmonic (red crosses) and the linear components (grey circles).

component (Figure 6.24c).

Although there were outliers, the CP of the second-order component was not significantly different from that of the linear component (Figure 6.24b;  $P = 0.42$ , sign test). No systematic covariation in CD with CP was observed for the second-order component (Figure 6.24d;  $P > 0.1$ , Mardia's linear-circular rank correlation coefficient).

#### 6.4.4 The origin of asymmetry in IC dual-delay functions

In the IC, the second-order component explained as much variance as the lowpass distortion, suggesting a stronger contribution to the response than in the DNLL. A large degree of asymmetry persisted when either the lowpass or the harmonic distortions were removed from the responses (Figure 6.25), suggesting that both components had some effect on the asymmetry.

When the harmonics were removed the RAI decreased slightly for all neurons ( $P = 0.041$ , sign test), indicating that the harmonics were sharpening the linear component, as expected from the fact that the carrier of the second-order component was closer to being in phase with that of the linear component than in antiphase. Removing the harmonics

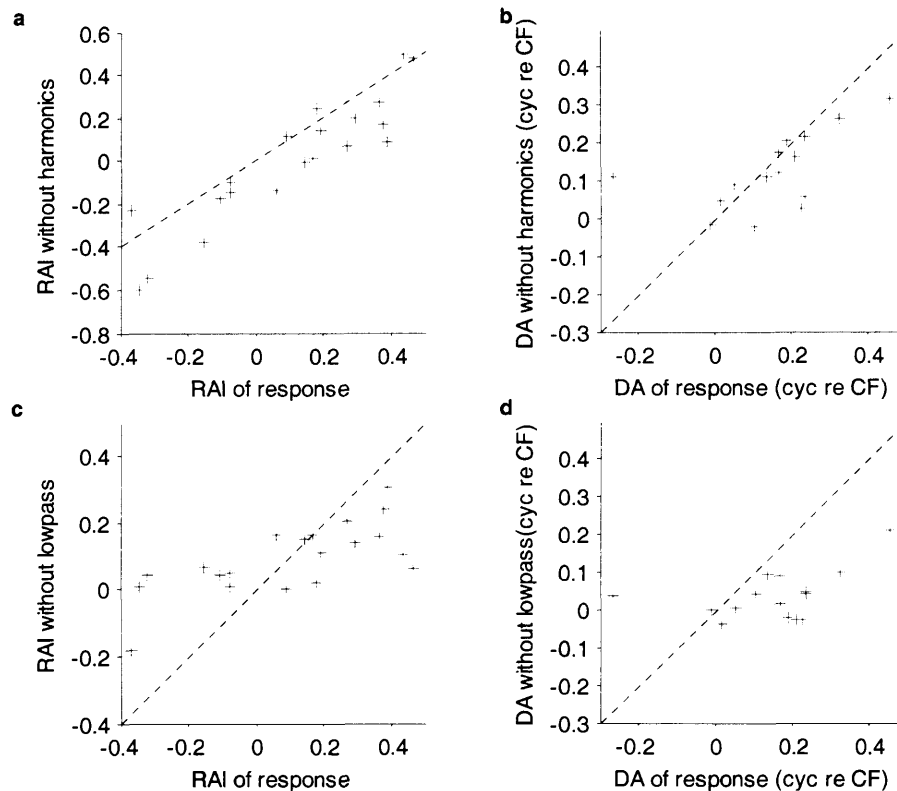


**Figure 6.25 Contribution of distortions to the degree of asymmetry in IC dual-delay functions.**

**a**, The RAI of an approximation formed by only the lowpass and linear components, compared to the RAI of the original response. **b**, The delay asymmetry of the same lowpass approximation, compared to that of the original response. **c**, The RAI of an approximation formed by only the harmonic (second-order and higher) and linear components, compared to the RAI of the original response. **d**, The delay asymmetry of the harmonic approximation, compared to that of the original response. Note that when the lowpass component is present, the approximation retains the original rate asymmetry; when absent, the approximation is more symmetrical. However, both the harmonic and lowpass components appear to play a role in determining the delay asymmetry.

attenuated the rate asymmetry, but it was not eliminated and there was a residual correlation between the RAI of the approximation and that of the original response ( $r = 0.69$ ,  $P < 0.001$ , Spearman's rank correlation coefficient).

Both removing the harmonic components and removing the lowpass component each had a small effect of on the delay asymmetry. The lowpass component appeared to make the stronger contribution, which might be expected given the deep left hand side trough observed in most responses.

### Rate Asymmetry

Asymmetry in IC appeared to be have been largely produced by the lowpass component through similar mechanisms to that in DNLL (Figure 6.26). Similar to the DNLL, the rate asymmetry was largely determined by the lowpass component, with the RAI showing a strong correlation with the RAI of the lowpass component (Figure 6.27a;  $r = 0.93$ ,  $P < 0.001$ , Spearman's rank correlation coefficient). Unlike DNLL, in IC there was no bias towards positive RAI values in IC (Figure 4.11). This was because the IC showed more trough-type responses, which produced lowpass components with more prominent negative-going portions than positive-going portions. An inverse relationship between the RAI and the CP of the linear component was observed (Figure 6.27b;  $r = 0.49$ ,  $P < 0.01$ , Mardia's linear-

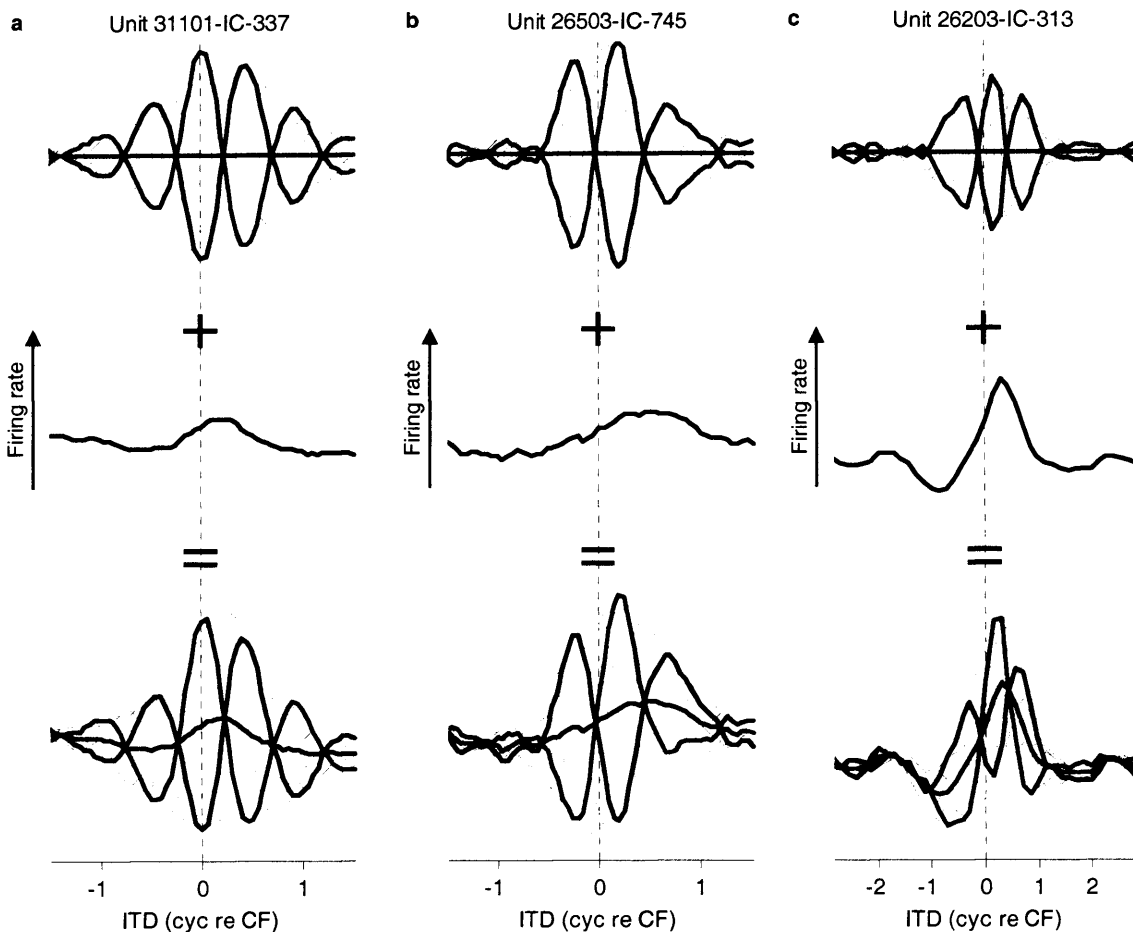


**Figure 6.26 The origin of asymmetry for IC dual-delay functions.**

Responses in IC are well approximated by the sum of the linear component (top) and the lowpass component (middle). Original functions shown in Figure 4.10. **a**, if the lowpass distortion is relatively symmetrical with respect to the envelope of the linear response then any delay asymmetry will be low. However, it will affect the positive envelope more than the negative envelope, producing a rate asymmetry. **b**, if the lowpass distortion is asymmetric with respect to the envelope of the linear response, a more delay asymmetric response is produced. **c**, if the magnitude of the lowpass component is large, then bimodality can result.

circular rank correlation coefficient), indicating that the more trough-type the neuron, the more negative its RAI; the more peak-type the neuron, the more positive its RAI.

### *Bimodality*

The higher incidence of bimodality in IC, and the fact that it could occur in either envelope, was a consequence of the more complex and varied shape of the lowpass components. While the DNLL showed stereotyped lowpass components with only a single peak and at most two troughs, the lowpass component in the IC could show multiple troughs and peaks that could produce bimodality in either envelope (e.g. Figure 6.26c).

### *Delay Asymmetry*

The delay asymmetry in IC could be produced through an offset of the peak ITD of the lowpass component relative to the CD of the linear component (Figure 6.26b), or by a prominent side trough (Figure 6.26c). Since the side troughs moved further out as CF increased (Figure 6.20), a similar shift might be expected to be produced in the negative

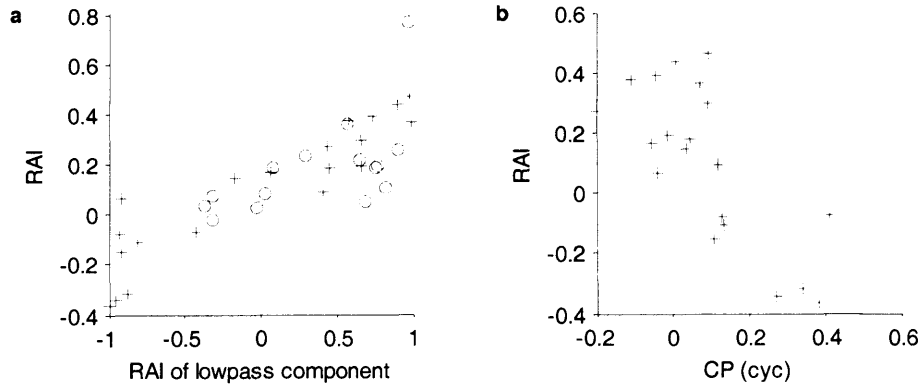


**Figure 6.27 Correlates of rate-asymmetry in IC dual-delay functions.**

**a**, the rate asymmetry of IC dual-delay functions as a function of that of the lowpass components (red crosses). The more rate asymmetric the lowpass component, the more rate asymmetric the final response. DNLL data (grey circles) shown for comparison. **b**, the rate asymmetry as a function of the characteristic phase of the linear component. The closer the CP is to 0 cyc (i.e. peak-type), the more positive the rate asymmetry, the closer the CP is to 0.5 cyc (trough-type), the more negative the RAI.

envelope of the response. This provided a possible explanation of the observed CF dependency of the delay asymmetry observed in IC (Figure 4.11). However, the heterogeneity of the observed lowpass components made it difficult to identify a single parameter that was a strong determinant of the delay asymmetry in IC. This may also have been a consequence of a significant contribution from the second-order component for some neurons.

## 6.5 Discussion

The linear component appeared to be well described by a Gabor function and, accordingly, the  $R^2$  values produced by the Gabor fits to the noise-delay functions reflected the proportion of explained variance in the linear component. The significant residual variation resulting from the Gabor fits therefore largely arose from the distortion terms, particularly the IPD-insensitive lowpass component. This coarse-structure-sensitive component is the main contributor to the asymmetry of the dual-delay functions.

In the DNLL, at higher CFs, the fall off of the variance explained by the higher-order components, and the simultaneous increase in the variance explained by the lowpass component, suggested that the coarse-structure sensitivity arose from the lowpass filtering of distortions, as suggested in the last chapter. With distortions introduced by nonlinearity but with higher-order distortions filtered out by some lowpass process. In such a model, if the corner-frequency of this lowpass filter were reasonably constant for different CFs (as would be expected if it were determined by EPSP time-course), then as the CF increased the harmonics would be more attenuated, increasing the contribution of the relatively unattenuated lowpass distortion.

In IC, no such increase with CF in the variance explained by the lowpass component was observed. However, differing patterns of convergence for different neurons may explain this lack of correlation.

### 6.5.1 *The linear component*

#### *Carrier frequency*

From the assumptions underlying the linear model presented in Chapter 4, the carrier frequency of the response of the neuron was expected to be the same as its CF. However, in DNLL the carrier frequency was in fact greater than the CF, possibly indicating a systematic underestimation of the true CF.

The CF was determined from the *dichotically presented* pure tone capable of eliciting a response at the lowest sound intensity. Consider two tone-delay functions recorded for frequencies from the same neuron, if both were equally well modulated and had the same best ITD (producing different best IPDs), then the response at 0 cyc IPD would be weaker for the higher frequency stimulus. Thus, the choice of CF is biased towards frequencies slightly lower than the true CF, due to their stronger response at 0 cyc IPD. To eliminate such a bias it would be necessary to present a range of IPDs when determining CF. However, any such errors in CF estimation are likely to be small since the lower modulation depth at frequencies off-CF should limit the bias.

For CFs below 500 Hz, the carrier frequency observed in IC was greater than CF, similar to that in DNLL. However, at CFs above this level, the carrier frequency was lower than CF. Although this could have arisen from a shift from a systematic underestimation of CF to a systematic overestimation, it is not clear why this should have occurred for IC and not DNLL. One possibility is that the carrier frequency in IC may be lowered by an input whose own CF is a constant fraction of that of the other (on-CF) input. Thus, the difference between the resultant carrier frequency and the CF would be CF-dependent; combined with any systematic underestimation of CF, this could produce the relationship observed in IC.

The relationship observed here for the IC, was not observed in a similar study in the IC of the cat (Joris et al. 2005). In that study, at low frequencies, the carrier frequency was approximately equal to CF, and while at higher CFs the carrier frequency did fall below CF, this did not begin to happen until around 2 kHz. While this may reflect different limits to phase locking in the two species, it may also arise from different methods of estimating the carrier frequency. Joris et al. used a Fourier transform of the linear component to estimate CF, which is less sensitive to the phase modulation at central ITDs than the method used here. Thus, the apparent underestimation of CF may arise from the carrier frequency reported here being more sensitive to the increased instantaneous frequency observed at central ITDs.

#### *The half-width of the amplitude envelope and stimulus intensity*

The bandwidth of the cochlear filters is known to increase with CF (Evans 2001), and this is reflected in the CF-dependent decline in half-width for the linear components in both IC and DNLL. The half-widths observed in IC were narrower than most in DNLL, suggesting a broader bandwidth in IC relative to DNLL. Since the IC data were obtained using stimuli

a median 15 dB higher than the DNLL data, it is possible this difference in half-width could be a consequence of an increase in bandwidth at higher sound levels. This is supported by the finding that narrowly tuned neurons observed in the DNLL were recorded using stimuli a median 10 dB higher than those for the more broadly tuned group. Furthermore, this narrowly tuned group contained the three neurons that showed carrier frequencies furthest from CF, suggesting that this too could have been a consequence of the higher sound level for these stimuli. If the carrier frequency were determined by the *best modulation frequency*—the frequency at which the tone-delay function has the greatest modulation depth—then the data may reflect a suprathreshold shift of this best modulation frequency towards frequencies above CF.

However, both the half-width and the carrier frequency in IC is independent of sound intensity (Joris et al. 2005) suggesting that the broader bandwidth in IC and the neurons with the high carrier frequencies are not artefacts of higher stimulus intensities. An alternative explanation for the broader bandwidths would be more across-CF convergence in IC than in DNLL. This would be a source of off-best-IPD input, which was proposed in Chapter 3 (Section 3.4.2) to account for the higher skew of tone-delay functions in IC.

For the same spectral level, more of the total power of the stimulus would be captured by higher bandwidth neurons and so a lower threshold would be expected. In fact, the higher bandwidth IC neurons showed *higher* thresholds, possibly because of convergent inhibition or different spike-thresholds in these neurons. To ensure that all neurons received the same effective sound level, higher thresholds were compensated for by presenting stimuli at higher levels. The use of the same sound level in both nuclei would have meant presenting stimuli near threshold in IC and near saturation in DNLL. While adaptation mechanisms in IC can shift the IC intensity tuning curve, the threshold cannot be reduced below that measured here (Dean et al. 2005), and it is not known whether such mechanisms could shift the threshold in DNLL up to levels equivalent to that in IC. Thus, the level of stimuli used here was felt to be the best method of ensuring a robust response from both nuclei.

### *The composition of the internal delay*

From the linearity of the phase responses of the linear component, the internal delay could be seen to be composed of a time delay (the CD) and a phase delay (the CP). The CD played the major role in establishing the best ITD of the neuron, which then appeared to be tuned by the CP to produce the required distribution of best ITDs (and therefore slope ITDs). A similar co-dependence was previously observed from phase-plots recorded in the IC (McAlpine et al. 1996). Whether the CD and CP measured in this way are the same as those measured for a tone stimulus cannot be addressed with the available data.

### 6.5.2 *The second-order component*

The noisiness in the estimated parameters for the second-order components makes confident statements about the general shape of the second-order component difficult. The observed second-order components appeared to be in line with that expected from quadratic distortion of the linear components, with the exception that the CD obtained was much lower than expected. This appeared to be due to a CD that was dependent on the carrier frequency of each component, and not a constant as would be expected for an axonal conductance delay. While this is suggestive of frequency-dependent mechanisms discussed in earlier chapters, a lack of a clear model of the effect of inhibition on this component makes it difficult to interpret this finding.

### 6.5.3 *The lowpass component*

#### *The lowpass component in DNLL*

In the presence of carving inhibition, the lowpass component of the response would be expected to be of the form

$$r_0(\tau) = g(\tau) * \kappa(\tau) = g(\tau) - \alpha g(\tau - \beta) \quad (6.8)$$

where  $g(\tau)$  is the lowpass distortion in the absence of any internal delay. Since the envelope of the linear component was unimodal,  $g(\tau)$  might also be expected to be unimodal, and so from (6.8), the lowpass response would be expected to be biphasic, with the inhibition creating a deep side trough to the left of the main peak. However, the lowpass components observed in DNLL appeared to be largely triphasic with two side troughs.

This Mexican-hat shape could be produced by allowing the inhibitory second term in (6.8) to be broader than the excitatory first term. In terms of the model, this would correspond to a broader lowpass filter for the cross-correlation of the contralateral inhibitory input and the ipsilateral excitatory input, than for the cross-correlation of the excitatory inputs to MSO. This could be justified as corresponding to the longer synaptic time course for inhibition than excitation (Magnusson et al. 2005).

Alternatively since the low threshold potassium channels are known to highpass filter input to the MSO (Slee et al. 2005), this could combine with the lowpass processes to create a more bandpass frequency-selectivity in MSO. This attenuation of the lowest frequencies in the input would result in a periodic lowpass component as observed in DNLL. Similarly,  $g(\tau)$  itself could have bandpass selectivity due to processing before the level of the MSO (although this appears unlikely from the responses recorded in AVCN).

A more obvious source of such a lowpass component would be the convergence of a broadly tuned contralateral inhibitory input with a more narrowly tuned ipsilateral excitatory input. The broader tuning of the inhibitory input could indicate that the inhibitory input is from a lower frequency lamina.

### *The lowpass component in IC*

The lowpass component in IC was more heterogeneous than that in DNLL, but it usually showed at least one dominant trough and one dominant peak around zero ITD. Such a pattern could have formed from the convergence of two delay-sensitive inputs: one peak-type input and one trough-type input. Peak type inputs to IC are provided by excitatory projections from ipsilateral MSO and trough-type inputs can arise from either an inhibitory projection from contralateral IC or DNLL, or an excitatory projection from contralateral LSO. Neurons receiving a stronger peak-type input would show a higher peak in the lowpass component, neurons receiving a stronger trough-type input a deeper trough, and neurons receiving a balance of the two somewhere in the middle. Such a process would affect both the CP of the linear component and the rate-asymmetry of the response and so could explain the negative correlation between the RAI and CP. For responses not entirely determined by a single peak- or trough-type input, delay asymmetry would also be expected. Thus, *intermediate-type responses* hypothesised to arise from such convergence appear to be responsible for the delay symmetry in IC.

# 7

## DISCUSSION

---

### 7.1 Summary

For over half a century, the Jeffress model has served as the framework for the investigation of neurophysiological mechanisms of ITD processing. While much of the model has proved remarkably prescient in the light of current understanding, other aspects of the model have been found wanting. In mammals in particular, both the mechanism through which the internal delay is established and the neural representation of ITDs have been shown to be different from those proposed in the Jeffress model. Internal delays are produced not by a delay-line network but by the effect of inhibition in MSO neurons. ITDs are encoded not by the most active neuron in a continuous array, but by the relative activity of two discrete populations of neurons. This study plays an important role in attempting to relate these recent observations by addressing how inhibitory internal-delay mechanisms might affect tuning curve shape.

The model of carving inhibition presented in Chapter 3 was capable of producing a variety of phase plots depending on the timing and strength of the inhibitory input. While for some parameter ranges, the inhibition could effect a time delay, at others it could result in a more phase-like delay. This provided a possible explanation for the CF-dependence of the best ITD observed in mammals. If units had similar parameters across all the CF laminae that resulted in a large phase component to the best ITD, then this could produce the almost inverse relationship between CF and best ITD. However, the phase contribution to the best ITD was found to be low, suggesting instead that a CF-dependent variation in the time component of the delay was largely responsible.

However, the effect of the inhibition could not entirely be described by a time delay. In the IC and DNLL, both the ITD tuning curves recorded for pure-tone stimuli and those recorded in for noise stimuli were asymmetric. In both of these cases, frequency dependency in the delay resulting from the effect of inhibition in the MSO could provide a qualitative explanation for the asymmetry. Tone-delay functions were skewed by a second-harmonic component for which carving inhibition resulted in a different time-delay than for the fundamental component. For noise-delay functions, the asymmetric envelope structures

observed could be accounted for by a different effect of carving inhibition on the coarse-structure-sensitive component than on the fine-structure sensitive component.

If the DNLL is an accurate reflection of the output of the MSO, these asymmetries suggest that inhibition in the MSO cannot be considered a replacement for the axonal delay lines in the original Jeffress model since it affects not only the best ITD but the entire shape of the tuning curve. Understanding the impact of the carving inhibition on the shape of ITD tuning curves is important in understanding how the neural representation for ITD is constructed.

## 7.2 Differences between IC and DNLL

This study adds to a growing body of work examining the properties of neurons in the DNLL in non-echolocating mammals (Brugge et al. 1970, Seidl & Grothe 2005, Siveke et al. 2006, Kuwada et al. 2006). Little is known of the function of the DNLL in these animals. It is thought to provide feed-forward delay-sensitive GABAergic inhibition to the IC in order to sharpen ITD tuning curves, but iontophoretic applications of SR95531 (“gabazine”, a GABA<sub>A</sub> antagonist) in the inferior colliculus in guinea pig have not revealed the changes in ITD tuning expected for such inputs (Ingham & McAlpine 2005). This is surprising, since the DNLL is estimated to be the source of one third of the inhibitory afferents to the IC in cat (Shneiderman & Oliver 1989). However, this may reflect a species difference or may be a consequence of local inhibition within the inferior colliculus dominating any inhibition originating in the DNLL.

### 7.2.1 Convergence

Responses in the DNLL were more symmetrical than responses in IC, with lower levels of skew in their tone-delay functions and lower delay asymmetry in their noise-delay functions. Tuning curve shapes were more homogenous compared to IC and showed less extreme features. One possible explanation of this is that convergence in DNLL is either absent, or at lower than in IC and restricted to a narrow range of CFs. This would produce a narrower range of input best ITDs, resulting in a more symmetrical tuning curve shape. Furthermore, lower convergence would provide an explanation for the narrower frequency-tuning curves in DNLL and the broader envelopes observed in the noise responses. It is unlikely that any convergent inputs to DNLL can be dissociated using the suppression method of McAlpine et al. (McAlpine et al. 1998) due to the similarity of the CFs of the inputs.

In comparison, the IC would be expected to receive input with a broad range of best ITDs. Since the delay asymmetry in IC was usually positive, with the peak of the negative envelope at ipsilateral leading delays, it seems likely that these neurons in IC receive an ipsilateral excitatory projection from MSO, and an inhibitory projection from contralateral IC or DNLL (or an excitatory projection from the contralateral LSO). Such patterns of

inhibition may be discernable using iontophoresis in IC. However, if the secondary input is excitatory then it will be mediated by the same neurotransmitter as the primary input making dissociation of the inputs via the use of antagonists impossible.

### **7.2.2 Distortion**

The contribution of the second-order component to the final response was consistently higher in IC than in DNLL. While this may have been an artefact of a higher noise floor, it may also be an indication of additional nonlinear processing in IC. Another explanation is convergence: at some delays, a secondary input could have enhanced the second-harmonic component of the primary input while suppressing the fundamental component.

### **7.2.3 Noise**

Tuning curves in IC were noisier than in DNLL, as evidenced by the higher noise floor observed in the power spectrum of the responses. Isolation of neurons is harder in IC than in DNLL due to the smaller spike height and stronger evoked potentials. However, since great care was taken during the experiments to ensure clean single-neuron recordings, the noisiness of IC compared to DNLL cannot be explained by rogue spikes in the recording. In addition, since firing rates in DNLL were higher than in IC, the higher noise could not be explained by a simple firing-rate-dependent noise process.

Analysis of the trial-to-trial variability (around the mean response over all trials) showed that for responses to both tones and noise, the variability of the response in IC on the initial trial was much higher than on subsequent trials, whereas in the DNLL the degree of variability was the same on each trial (data not shown). This difference in variability could reflect either a change in tuning curve shape or a change in the mean firing rate on each trial. However, since for tone stimuli, there was no change in the best IPD over the repeats (Section 3.4.1). It is more likely that this was more reflective of spike-rate adaptation rather than any adaptation in the underlying tuning parameters.

Interestingly, this suggests that the apparent noisiness of IC tuning curves could be due to such adaptation. Experiments using binaural stimuli have demonstrated that the IC is likely to show strong spike-rate adaptation (Ingham & McAlpine 2004). If such adaptation is weaker or absent in DNLL, then the lower degree of a stationary in the IC could explain the noisier tuning curves.

## **7.3 Relationship to binocular disparity tuning curves**

Interestingly, both the rate and delay asymmetries observed here for ITD tuning curves can also be observed in binocular-disparity (BD) tuning curves recorded from cat visual cortex (Cumming & Parker 1997). The mechanism suggested to explain the rate-asymmetry for BD tuning curves is half-wave rectification of the input before the cross-correlation stage in simple cells (Read et al. 2002). The convergence of two simple cells on one complex cell

therefore produces the observed delay asymmetry (i.e. a convergence mechanism). Such a model does not predict the elevated equivalence contours for rate asymmetric responses. However, it is difficult to determine from the published responses whether these contours are elevated for rate-asymmetric BD tuning curves. Whatever mechanisms are at work in one modality may well be applicable in the other. It would therefore be of interest to record from BD-sensitive neurons using dual-delay functions and compare them to the results obtained here.

## 7.4 Functional consequences

### 7.4.1 Asymmetry and psychophysical acuity

One of the studies most directly relevant to these findings is that of Hancock and Delgutte (Hancock & Delgutte 2004). Hancock and Delgutte constructed a model of IC based on a population of symmetrical noise delay responses of the form

$$r(\tau) = f_x[h_x(\tau - \tau_0)] \quad (7.1)$$

where  $h_x(\tau)$  was the bandpass function resulting from the cross-correlation of two identical fourth-order gammatone filters, and  $f_x(\cdot)$  was a quadratic correlation-dependent nonlinearity. They simulated a population of neurons for a range of CFs and best ITDs (sampled in cycle re CF), the distribution of which was estimated by regression of the model to a large number of tuning curves recorded in cat IC. For each tuning curve in the model, its ability to discriminate between two ITDs was determined from the difference in firing rates at these two ITDs (using the  $d'$  statistic). These values were combined across neurons (assuming an ideal observer) producing the probability that the two ITDs could be correctly discriminated for the model as a whole. The just noticeable difference in ITD from a particular reference ITD was then determined, by finding change in ITD that could be correctly discriminated from the reference ITD with a probability of 75%. These model JNDs were then compared with the JNDs measured for human psychophysical performance.

While human JNDs for noise stimuli are lowest around a reference ITD of zero and increase as the reference ITD increases to more positive values (Mossop & Culling 1998), the JNDs obtained from the model were relatively independent of the reference ITD. This was a consequence of the symmetry of the tuning curves and the broad range of best ITDs in the model. Because of the symmetry, slopes either side of best ITD provided equally good discriminability, and the wide range of best ITDs ensured that some of these falling slopes fell into the physiological range. Because of the ideal observer assumption, low acuity neurons were effectively ignored, producing little difference between the acuity at zero ITD and that at nonzero ITDs. In order to predict the ITD dependent increase in JND, the model was modified by pooling (i.e. summing) the tuning curves across CF before calculating  $d'$  values, thereby producing asymmetric tuning curves and reducing the acuity

off zero ITD. Hancock and Delgutte therefore concluded that pooling across CF in higher auditory areas is necessary to explain the poorer human JNDs away from zero ITD.

However, the Hancock and Delgutte model has several shortcomings, which challenge this conclusion. In particular, their model incorporates neither the delay asymmetry, nor the coarse-structure sensitivity observed in this study. Much as the failure of the Gabor model to incorporate these characteristics lead to unreliable parameter estimates, here too any delay asymmetry or coarse-structure sensitivity would be compensated for in the fit by a combination of a nonzero CP and overestimation of the bandwidth or the degree of nonlinearity. Although they reported a mean  $R^2$  value of 0.93, this was likely due to a bias towards low-frequency neurons and overfitting of the central ITDs as observed for the Gabor model. The inadequacy of such a model will be especially pronounced for CFs above 1 kHz, where the coarse-structure sensitivity arising from the cochlear envelope sensitivity begins to dominate the response (Joris 2003). Ironically, since the range of ITDs tested was around 600  $\mu$ s, it is these very neurons that provide falling slopes within the physiological range—the source of the unwanted acuity. Furthermore, responses observed for neurons with CFs greater than 2 kHz—not considered by Hancock and Delgutte—show *only* coarse-structure sensitive responses, with one slope through zero and the other outside the physiological range (Joris 2003). These neurons will selectively increase the acuity around zero ITD only. Thus, the finding that the JNDs do not increase with ITD is highly dependent on the generalisation of low-CF fine-structure sensitivity to CFs where the tuning curves are likely to be very different.

The tuning curves used by Hancock and Delgutte also did not contain any delay asymmetry, and this alone may be sufficient to explain the improved JND at the midline. Since positive and negative envelopes in IC peak on opposite sides of zero, the rising slope is sharpened relative to the falling slope, leading to higher acuity around zero ITD and lower acuity at larger ITDs. Furthermore, Hancock and Delgutte did not include the contralateral IC in their model. The best ITD distribution for this population of neurons will be the mirror image of that shown in this study, with high acuity rising slopes around the midline and falling slopes at *negative* ITDs. They would therefore improve acuity around zero but not at the higher (more positive) ITDs, further amplifying the ITD dependency of the JNDs.

It is likely that factoring the findings of this study (and others), the model of Hancock and Delgutte could produce the ITD dependent increase in Human JNDs without recourse to pooling over CF.

#### **7.4.2 The optimal neural representation of ITD**

When Harper and McAlpine (Harper & McAlpine 2004) investigated the optimal encoding of IPDs of tones, they modelled the tone-delay functions symmetrically, fitting only the rising slope of responses recorded from IC. Although their findings are sufficiently general that asymmetric tuning curves will make little difference to the predicted distributions of

best ITD, it would be of interest to determine how asymmetry could co-vary with best IPD to improve coding (by introducing a second harmonic with its own independent best IPD). For example, at low CFs the optimal asymmetry would be expected to sharpen only the slopes within the physiological range; at CFs where the homogenous distribution occurs, both slopes are required for coding so either no asymmetry (or an equal amount of both positive and negative asymmetry) may be preferable.

A more productive course of investigation would be to consider the optimal encoding of noise stimuli. Although Harper and McAlpine reported similar best ITD distributions arising from a Gabor model of noise-delay functions, this did not consider coarse-structure sensitivity. By allowing the best ITD of coarse- and fine-structure sensitive components to vary independently, the optimal distribution of each could be determined. While it would be interesting to determine whether the observed asymmetry is predicted, the predicted distribution of the coarse-structure best ITDs of high-CF neurons would be of particular interest. This distribution is unknown and would provide a strong test of both the optimal encoding model and the slope coding hypotheses.

If the increasing JNDs with ITD discussed in the previous section were not predicted, then it would be interesting to determine why the more optimal representation is not used. One possibility is that that tuning curves are not as free to vary in nature—where there may be ethological or physiological costs to any changes—as they are in the model. In particular, if the existence of (low-CF) coarse-structure sensitivity results in a suboptimal solution, then it could be considered an undesirable side effect of slower EPSP time courses. However, the energetic costs to increasing these time courses (higher resting membrane conductance, faster glutamate reuptake) may be too great to justify an increase in the efficiency of the code.

### **7.4.3 The four-channel model**

One suggested method of encoding both the interaural correlation and the interaural delay of stimuli is the *four-channel model* (Marquardt & McAlpine 2001). This model uses four IPD-tuned channels for each frequency lamina: two channels sensitive to correlated inputs, tuned to  $\pm 0.125$  cyc (representing the two MSOs); and two other channels tuned to  $\pm 0.125$  cyc, but sensitive to anti-correlated inputs (representing the two LSOs). The combined activity of the four channels within each frequency band thereby provides a quadrature representation of the temporal coherence of the noise stimuli and the instantaneous interaural phase difference within that band.

However, the results presented in Chapter 6 indicate that the phase-like variation of best ITD with CF is not due to a phase delay, but is largely attributable to a time delay tuned to the CF of the neuron. If the bandwidth of the neuron is narrow, then the difference between the responses obtained for a pure time delay will be little different from those obtained with a pure phase delay. Both the internal delays and the coarse-structure

sensitivity observed in this study should be factored into the model to determine what impact they may have.

## 7.5 Future work

### 7.5.1 *The DNLL as a proxy nucleus for MSO*

Although the lower degree of asymmetry in DNLL compared to IC suggests that it is a *better* proxy, exactly how good it is will likely depend on the question being addressed. While it may be reasonable for general insights into the nature of ITD tuning, for more detailed questions, such as those examined here, direct recordings from MSO are preferable.

The most significant limitation of this study was inability to discern between the effect of convergence and the effect of the inhibition, due to lack of direct recordings from MSO. Since the hurdle to obtaining single-neuron recordings in MSO is the high background noise and low-amplitude action potentials, cell-attached recordings *in vivo* may be a productive method of obtaining clean, high-quality recordings from this area.

However, for conclusive answers about the role of inhibition in determining the tuning properties of MSO, it is necessary to obtain *in vivo* intracellular recordings from neurons in the MSO. Despite the significant difficulties posed by the thinness of the MSO and the heavy myelination in the area, such recordings are thought possible. While the patch-clamp method is the preferred method of obtaining intracellular recordings (due to the minimal disruption of the plasma membrane), there has recently been some success in obtaining sharp-microelectrode recordings from nucleus laminaris, the avian homologue of MSO (Funabiki & Konishi 2005). Such experiments are likely to be difficult and low yield, but they would allow direct investigation of the role of inhibition and other mechanisms in establishing the tuning of MSO.

### 7.5.2 *Modelling dual-delay functions*

This study was motivated by a fundamental problem in neuroscience: that of addressing the impact of cellular level processes—such as the biophysical effect of inhibition—upon the tuning curve of a neuron. While the effect can be demonstrated with complex biophysical models, such models take a long time to simulate and the level of understanding obtained is conditional—the complexity of such models may lead to a lack of robustness, with a high dependency upon a specific configuration of input parameter values. In many models (e.g. Brand et al. 2002), there is a large degree of uncertainty around the true parameter values. There is also little knowledge about the representation of noise stimuli in the peripheral auditory system. This uncertainty was found to be a major limiting factor when attempting to investigate dual-delay functions predicted by biophysical models of MSO.

The solutions to these problems attempted in this study, were to make assumptions about the response of the AVCN to noise based on the response to tones, and to attempt to simplify the cellular level processes in order to capture the behaviour of the neuron with a

much smaller and more general set of starting assumptions. While a reasonable approach, the level aimed for was arguably overly simplified. The combination of generality and uncertainty meant that a closed form for the response could not be determined, limiting the possible analysis.

While one solution would be to better characterise the response of AVCN neurons to noise, an alternative line of enquiry would be instead to use a different stimulus. Sinusoidally amplitude modulated (SAM) stimuli contain far fewer spectral components, which would allow more detailed quantitative modelling and analysis. A couple of responses for such stimuli were recorded in IC by the author, and showed the expected rate- and delay-asymmetries. Since the envelope can be varied by changing the beat frequency, it may be easier to investigate the mechanisms underlying the envelope sensitivity.

With a more accurate model of the input to the MSO, it would be more feasible to investigate biophysical models of carving inhibition. Nevertheless, to get around the uncertainty over the parameters, a simple Morris-Lecar type model could be used (Agmon-Snir et al. 1998), which has relatively fewer parameters to investigate. Such a model could more realistically capture aspects of the inhibition that may play an important role such as its interaction with the low-threshold voltage-activated potassium channels. Another use for such a model would be to inject simulated inputs into MSO neurons *in vitro* to try to reproduce the ITD tuning curves, allowing a more direct investigation the effect of carving inhibition.

## 7.6 Final Words

The original aim of this study was to identify the effect of inhibition in the MSO on the ITD tuning curves. While it was not possible to isolate the effect of inhibition from similar frequency-dependent processes, an unexpected outcome to this study was the discovery of coarse-structure sensitivity in the responses of low-CF neurons, which indicated a limit to the temporal precision of the MSO at lower timescales than previously considered. While this coarse-structure sensitivity may arise as a side effect of a physiological limit on the temporal precision, an alternative possibility is that it improves the coding of ITD. In order to better understand the neural representation of ITD, further investigation of both the origin of this coarse-structure sensitivity and the role of inhibition in the MSO is necessary.

# 8

## MATHEMATICAL APPENDIX

---

### 8.1 The Gabor model

#### 8.1.1 Derivation of the Gabor model

In order to derive the Gabor model, it is assumed that ipsilateral and contralateral cochlear filters are identical (i.e. no stereausis) with power spectrum

$$|\mathbf{H}(f)|^2 = \frac{1}{2}[\Upsilon(f - f_c) + \Upsilon(f + f_c)] \quad (8.1)$$

where  $f_0$  is the centre frequency, and  $\Upsilon(f)$  is a Gaussian with zero DC gain, unit integral, and equivalent rectangular bandwidth  $b$

$$\Upsilon(f) = \frac{1}{b} \exp(-\pi f^2 / b^2) \quad (8.2)$$

The cross-spectrum of the impulse response of the filter is obtained from the Wiener-Khinchin theorem

$$\begin{aligned} \mathcal{F}_\tau[\mathbf{h}_x(\tau)](f) &= |\mathbf{H}(f)|^2 \\ &= \frac{1}{2}[\Upsilon(f - f_c) + \Upsilon(f + f_c)] \end{aligned} \quad (8.3)$$

and from the modulation theorem of the Fourier transform, the autocorrelation  $\mathbf{h}_x(\tau)$  can be defined in terms of an amplitude modulated sinusoid

$$\mathbf{h}_x(\tau) = \mathcal{F}_f^{-1}[\Upsilon(f)](\tau) \cdot \cos(2\pi f_c \tau) \quad (8.4)$$

Using the identity

$$\mathcal{F}_x[\exp(-ax^2)](k) = \sqrt{\frac{\pi}{a}} \exp(-\pi^2 k^2 / a) \quad (8.5)$$

it can be seen that the envelope of (8.4) is Gaussian and that  $\mathbf{h}_x(\tau)$  is a Gabor function

$$\mathbf{h}_x(\tau) = \exp(-\pi b^2 \tau^2) \cos(2\pi f_c \tau) \quad (8.6)$$

### 8.1.2 Effect of internal delays

Since the model is time invariant, the effect of an internal time delay  $\tau_0$  can be simply incorporated by translating the entire response

$$h_x(\tau) = \exp\left[-\pi b^2 (\tau - \tau_0)^2\right] \cos[2\pi f_c (\tau - \tau_0)] \quad (8.7)$$

Differences in interaural phase caused by an internal phase delay  $\phi_0$  can be modelled by phase delaying only the contralateral signal. Since the system is linear, this is equivalent to phase delaying the cross-spectrum. Thus, from Appendix 8.2, provided the bandwidths of the cochlear filters are sufficiently narrow, the response will be given by

$$h_x(\tau) = \exp\left[-\pi b^2 (\tau - \tau_0)^2\right] \cos[2\pi f_c (\tau - \tau_0) - \phi_0] \quad (8.8)$$

## 8.2 Phase delayed narrowband signals

### 8.2.1 Phase delayed signals

Let  $s(t)$  be a signal with Fourier transform  $S(f)$

$$s(t) \xleftrightarrow{\mathcal{F}} S(f) \quad (8.9)$$

If each frequency component in  $S(f)$  is phase delayed by  $\phi$ , the resulting spectrum will be of the form

$$\begin{aligned} S(f | \phi) &= S(f) \exp[i \operatorname{sgn}(f) \phi] \\ &= S(f) \cos(\phi) + i \operatorname{sgn}(f) S(f) \sin(\phi) \end{aligned} \quad (8.10)$$

where  $\operatorname{sgn}(f)$  enforces the conjugate symmetry of  $S(f)$  ensuring that  $s(t)$  remains real valued. Given that

$$\mathcal{H}[s(t)] \xleftrightarrow{\mathcal{F}} -i \operatorname{sgn}(f) S(f) \quad (8.11)$$

where  $\mathcal{H}[s(t)]$  is the *Hilbert transform* of  $s(t)$ , the phase delayed signal can be seen to be expressed in the temporal domain by

$$s(t | \phi) = s(t) \cos(\phi) - \mathcal{H}[s(t)] \sin(\phi) \quad (8.12)$$

### 8.2.2 Narrowband signals and phase delays

A *narrowband* signal  $s(t)$  is a signal that has limited support in the frequency domain such that  $S(f)$  is nonzero only in the range  $0 < f \leq 2f_c$ , where  $f_c$  is the carrier frequency of the signal. Using Bedrosian's Theorem it can be shown (Hahn 1996) that for a narrowband signal

$$s(t) = e(t) \cos[2\pi f_c t + \theta(t)] \quad (8.13)$$

the Hilbert transform is given by

$$\mathcal{H}[s(t)] = e(t) \sin[2\pi f_c t + \theta(t)] \quad (8.14)$$

Thus, from (8.12), the phase delayed narrowband signal will be given by

$$s(t | \phi) = e(t) \cos(2\pi f_c t + \theta(t) + \phi) \quad (8.15)$$

Therefore, it can be seen from (8.15) that for narrowband signals, a phase delay does not affect the envelope of the response but merely phase shifts the carrier.

### 8.3 Measuring the equivalence contour

If a purely rate asymmetric response can be described by a nonlinear dependency on the narrowband cross-correlation then it can be expressed in terms of a power series

$$r(\tau | \phi) = \sum_{n=0}^{\infty} a_n e(\tau)^n \cos^n[\theta(\tau) + \phi] \quad (8.16)$$

This in turn can be represented in terms of a Fourier series (in terms of  $\phi$ ) by substituting in the Fourier series of the raised-power cosine terms

$$r(\tau | \phi) = \sum_{n=0}^{\infty} f_n [e(\tau - \tau_0)] \cos[n\phi + n\theta(\tau - \tau_0)] \quad (8.17)$$

where  $f_n[\cdot]$  are a series of polynomials whose exact form depends on the coefficients  $a_n$  (see Appendix 8.4 for derivation). Since at any point on the equivalence contour the underlying correlation will be zero

$$e(\tau) \cos[\theta(\tau) + \phi] = 0 \quad (8.18)$$

the equivalence contour for any ITD can be found by substituting the value of  $\phi$  necessary to satisfy (8.18) into (8.17)

$$\begin{aligned} z(\tau) &= \sum_{n=0}^{\infty} f_n [e(\tau - \tau_0)] \cos\left(\frac{n\pi}{2}\right) \\ &= \sum_{n=0}^{\infty} f_{2n} [e(\tau - \tau_0)] (-1)^n \end{aligned} \quad (8.19)$$

Thus for a response that can be described by the 4<sup>th</sup>-order Fourier series

$$r(\tau | \phi) = \sum_{n=0}^4 a_n(\tau) \cos[n\phi + \theta_n(\tau)] \quad (8.20)$$

it follows that if (8.16) holds then

$$z(\tau) = a_0(\tau) - a_2(\tau) + a_4(\tau) = f_x(0) \quad (8.21)$$

The equivalence contour defined in this way is therefore expected to be equivalent to the response to uncorrelated noise and to be independent of ITD.

## 8.4 Creating envelope sensitivity

### 8.4.1 The Fourier series of distorted narrowband signals

If a narrowband signal  $s(t)$ , is phase delayed by some phase  $\phi$  before being nonlinearly distorted, the resulting signal  $v(t | \phi)$  can be written as a power series

$$v(t | \phi) = f[s(t | \phi)] = \sum_{n=0}^{\infty} a_n e(t)^n \cos^n [2\pi f_c t + \theta(t) + \phi] \quad (8.22)$$

Since the Fourier series of the raised power cosine terms is given by

$$\cos^n(x) = \sum_{u=0}^n E_u^n \cos(ux) \quad (8.23)$$

with Fourier coefficients

$$E_u^n = \begin{cases} 0 & n + u \text{ is odd} \\ 2^{1-n} \operatorname{sgn}(u) \binom{n}{(n+u)/2} & n + u \text{ is even} \end{cases} \quad (8.24)$$

(8.22) can be rewritten as a Fourier series

$$\begin{aligned} v(t | \phi) &= \sum_{u=0}^{\infty} \left( \sum_{n=u}^{\infty} a_n E_u^n e(t)^n \right) \cos[2\pi u f_c t + u\theta(t) + u\phi] \\ &= \sum_{u=0}^{\infty} f_u [e(t)] \cos[2\pi u f_c t + u\theta(t) + u\phi] \end{aligned} \quad (8.25)$$

Thus, it can be seen that the effect of the correlation-dependent nonlinearity is to introduce a series of harmonic distortions into the response. For  $u > 0$  each distortion is narrowband with a carrier frequency that is a harmonic of that of the original signal. The distortion generated for  $u = 0$  is lowpass, independent of the IPD, and dependent solely on the envelope of the original signal

$$v_0(\tau | \phi) = f_0 [e(\tau - \tau_0)] \quad (8.26)$$

### 8.4.2 Envelope sensitivity

As can be seen from (8.24), the odd-power terms in (8.22) contribute only to the odd-order distortions in (8.25), and the even-power terms contribute only to the even-order distortions. The envelope-sensitive lowpass distortion is therefore generated entirely by the even-power terms. In isolation, the lowpass distortion is envelope sensitive, but this envelope sensitivity is not reflected in the overall response. In the presence of the other even-order distortions, the lowpass distortion pairs up with other even-order harmonic distortions to *improve the sensitivity to the carrier* (by sharpening IPD tuning). A kind of balance can therefore be considered to exist between the even-order terms in (8.25). If this balance is disrupted, then the even-order distortions will no longer combine to produce the even-power terms of (8.22) and the unmatched lowpass component will produce a residual envelope-sensitive component in the response. Closer inspection of (8.19) reveals that it is this unmatched lowpass component that is measured by the equivalence contour.

## 8.5 Responses to envelope-sensitive inputs

The purpose of this section is to attempt to produce an expression for the response predicted for inputs to MSO containing envelope sensitivity as outlined in Chapter 5

(Section 5.3.2). In such a model the inputs are filtered in the cochlea, nonlinearly distorted and lowpass filtered. The average response of an MSO neuron to such inputs will therefore be of the form

$$r(\tau | \phi) = \frac{1}{T} \int_0^T dt v_I(t) v_C(t + \tau | \phi) * \kappa(\tau) \quad (8.27)$$

where  $\kappa(\tau)$  is the model of carving inhibition as outlined in Chapter 3 (Section 3.2),  $v_I(t)$  is the ipsilateral input, and  $v_C(t + \tau | \phi)$  is the contralateral input for an ITD  $\tau$  and an IPD  $\phi$ . The inputs are given by

$$v_I(t) = f_I [h_I(t) * s(t)] * \lambda_I(t) \quad (8.28)$$

$$v_C(t + \tau | \phi) = f_C [h_C(t) * s(t + \tau | \phi)] * \lambda_C(t) \quad (8.29)$$

where  $s(t | \phi)$  is the noise stimulus,  $h_I(t)$  and  $h_C(t)$  are the ipsilateral and contralateral cochlea-filter impulse responses,  $f_I(\cdot)$  and  $f_C(\cdot)$  are the nonlinearities, and  $\lambda_I(t)$  and  $\lambda_C(t)$  are the lowpass filter impulse responses.

For such inputs the expected response can be equivalently rewritten as

$$r(\tau | \phi) = \frac{1}{T} \int_0^T dt v_I(t) v_C(t + \tau | \phi) * \kappa(\tau) * \lambda_X(\tau) \quad (8.30)$$

$$v_I(t) = f_I [h_I(t) * s(t)] \quad (8.31)$$

$$v_C(t + \tau | \phi) = f_C [h_C(t + \tau | \phi) * s(t)] \quad (8.32)$$

where  $\lambda_X(\tau)$  is the cross-correlation of the lowpass component impulse responses.

Let the nonlinear inputs given in (8.31) and (8.32) be defined in terms of their power series

$$v_I(t) = \sum_{j=0}^{\infty} a_j [h_I(t) * s(t)]^j \quad (8.33)$$

$$v_C(t + \tau | \phi) = \sum_{k=0}^{\infty} b_k [h_C(t + \tau | \phi) * s(t)]^k \quad (8.34)$$

Using these inputs in (8.30), predicts the response:

$$r(\tau) = \lambda_X(\tau) * \kappa(\tau) * \sum_{j=0}^{\infty} \sum_{k=0}^{\infty} a_j b_k Z_{j,k}(\tau | \phi) \quad (8.35)$$

where  $Z_{j,k}(\tau | \phi)$  is the cross-correlation of the ipsilateral filtered stimulus to the  $j^{\text{th}}$  power and the contralateral filtered stimulus to the  $k^{\text{th}}$  power

$$Z_{j,k}(\tau | \phi) = [h_I(t) * s(t)]^j * [h_C(t | \phi) * s(t)]^k \quad (8.36)$$

Expressing the convolutions and the cross-correlation in (8.36) as integrals gives

$$Z_{n,m}(\tau | \phi) = \frac{1}{T} \int_0^T dt \int d\sigma_1 \cdots \int d\sigma_{j+k} \prod_{u=1}^j s(t - \sigma_u) h_I(\sigma_u) \prod_{v=j+1}^{j+k} s(t + \tau - \sigma_v) h_C(\sigma_v | \phi) \quad (8.37)$$

This can in turn be decomposed to

$$\mathbf{Z}_{j,k}(\tau | \phi) = \int d\sigma_1 \cdots \int d\sigma_{j+k} \mathbf{U}_{j+k}(\boldsymbol{\sigma}) \mathbf{h}_I(\sigma_1) \cdots \mathbf{h}_I(\sigma_j) \mathbf{h}_C(\sigma_{j+1} + \tau | \phi) \cdots \mathbf{h}_C(\sigma_{j+k} + \tau | \phi) \quad (8.38)$$

where  $\boldsymbol{\sigma}$  is an  $N$ -tuple of the integration variables arising from the convolutions and  $\mathbf{U}_N(\boldsymbol{\sigma})$  is the  $(N-1)^{\text{th}}$ -order correlation of the noise stimulus

$$\begin{aligned} \mathbf{U}_N(\boldsymbol{\sigma}) &= \frac{1}{T} \int_0^T dt \mathbf{s}(t - \sigma_1) \cdots \mathbf{s}(t - \sigma_N) \\ &\approx \langle \mathbf{s}(\sigma_1) \cdots \mathbf{s}(\sigma_N) \rangle \end{aligned} \quad (8.39)$$

Consider the case for  $N = 2$ . If two variables  $\sigma_1$  and  $\sigma_2$  are not equal, then  $\mathbf{s}(\sigma_1)$  and  $\mathbf{s}(\sigma_2)$  will be independent, with the consequence that  $\mathbf{U}_2(\boldsymbol{\sigma})$  will be the square of the first moment of the noise process. If the variables are equal then  $\mathbf{s}(\sigma_1) = \mathbf{s}(\sigma_2)$ , and  $\mathbf{U}_2(\boldsymbol{\sigma})$  will be the second moment.

$$\mathbf{U}_2(\boldsymbol{\sigma}) = \begin{cases} \langle \mathbf{s}(\sigma) \rangle^2 & \sigma_1 \neq \sigma_2 \\ \langle \mathbf{s}(\sigma)^2 \rangle & \sigma_1 = \sigma_2 \end{cases} \quad (8.40)$$

More generally, the value of  $\mathbf{U}_N(\boldsymbol{\sigma})$  depends upon the partitioning of the  $\boldsymbol{\sigma}$  variables based on equality. Let  $q_\sigma$  be the partition of  $\{1, \dots, N\}$  defined by the equivalence relation  $\diamond_\sigma$ , such that

$$a \diamond_\sigma b \equiv \sigma_a = \sigma_b \quad (8.41)$$

This results in a set of equivalence classes each corresponding to a different element of  $\boldsymbol{\sigma}$ . If  $\sigma_1$  and  $\sigma_2$  are in the same equivalence class then  $\sigma_1 = \sigma_2$ . If  $q_\sigma$  contains  $n_1$  equivalence classes containing only one element,  $n_2$  classes containing two elements, and so on, the value of  $\mathbf{U}_N(\boldsymbol{\sigma})$  will be

$$\mathbf{U}_N(\boldsymbol{\sigma}) = \mu_1'^{n_1} \mu_2'^{n_2} \cdots \mu_N'^{n_N} \quad (8.42)$$

where  $\mu_n'$  denotes the  $n^{\text{th}}$  moment of the noise stimulus. Since the probability density function of the noise process is defined to be symmetrical around zero mean, then the odd-order moments will all be zero. Therefore, if any equivalence class contains an odd number of elements,  $\mathbf{U}_N(\boldsymbol{\sigma})$  will be zero. If  $N$  is odd this cannot be avoided, with the consequence that  $\mathbf{U}_N(\boldsymbol{\sigma})$  will also be zero in this circumstance.

$$\mathbf{U}_N(\boldsymbol{\sigma}) = \begin{cases} 0 & n_1 \neq n_3 \neq \cdots \neq 0 \\ \mu_2'^{n_2} \mu_4'^{n_4} \cdots \mu_{\lfloor N/2 \rfloor}'^{n_{\lfloor N/2 \rfloor}} & n_1 = n_3 = \cdots = 0 \end{cases} \quad (8.43)$$

Putting (8.43) back into (8.38), it can be seen that the integration need only be considered for values of  $\boldsymbol{\sigma}$  where the partition  $q_\sigma$  is a member of  $\mathcal{Q}_N$ , the set of all partitions of  $\{1, \dots, N\}$  where each equivalence class contains an even number of elements

$$\begin{aligned} \mathbf{Z}_{j,k}(\tau | \phi) &= \int_{q_\sigma \in \mathcal{Q}_{j+k}} d\sigma_1 \cdots d\sigma_{j+k} \mathbf{U}_{j+k}(\boldsymbol{\sigma}) \mathbf{h}_I(\sigma_1) \cdots \mathbf{h}_C(\sigma_{j+k} + \tau | \phi) \\ &= \sum_{q \in \mathcal{Q}_{j+k}} \prod_{c \in q} \mu_{|c|}' \int d\sigma \mathbf{h}_I(\sigma_j)^{|c \leq j|} \mathbf{h}_C(\sigma_{j+1} + \tau | \phi)^{|c > j|} \end{aligned} \quad (8.44)$$

In general, the response of the neuron will be dependent on several terms of the form  $(h_I^{n_1} \star h_C^{m_1})(h_I^{n_2} \star h_C^{m_2}) \dots$  where each  $n_a + m_a$  is even. No further simplification was possible.

# BIBLIOGRAPHY

---

- Agmon-Snir H, Carr CE & Rinzel J (1998). The role of dendrites in auditory coincidence detection. *Nature* **393**:268–272.
- Barnes-Davies M, Barker MC, Osmani F & Forsythe ID (2004). Kv1 currents mediate a gradient of principal neuron excitability across the tonotopic axis in the rat lateral superior olive. *Eur. J. Neurosci.* **19**:325–333.
- Batra R, Kuwada S & Fitzpatrick DC (1997). Sensitivity to interaural temporal disparities of low- and high-frequency neurons in the superior olivary complex. I. Heterogeneity of responses. *J. Neurophysiol.* **78**:1222–1236.
- Beckius GE, Batra R & Oliver DL (1999). Axons from anteroventral cochlear nucleus that terminate in medial superior olive of cat: observations related to delay lines. *J. Neurosci.* **19**:3146–3161.
- Brand A, Behrend O, Marquardt T, McAlpine D & Grothe B (2002). Precise inhibition is essential for microsecond interaural time difference coding. *Nature* **417**:543–547.
- Brugge JF, Anderson DJ & Aitkin LM (1970). Responses of neurons in the dorsal nucleus of the lateral lemniscus of cat to binaural tonal stimulation. *J. Neurophysiol.* **33**:441–458.
- Carr CE & Konishi M (1990). A circuit for detection of interaural time differences in the brain stem of the barn owl. *J. Neurosci.* **10**:3227–3246.
- Chan JC, Yin TC & Musicant AD (1987). Effects of interaural time delays of noise stimuli on low-frequency cells in the cat's inferior colliculus. II. Responses to band-pass filtered noises. *J. Neurophysiol.* **58**:543–561.
- Clack JA (1997). The evolution of tetrapod ears and the fossil record. *Brain Behav. Evol.* **50**:198–212.
- Colburn HS (1973). Theory of binaural interaction based on auditory-nerve data. I. General strategy and preliminary results on interaural discrimination. *J. Acoust. Soc. Am.* **54**:1458–1470.
- Crow G, Rupert AL & Moushegian G (1978). Phase locking in monaural and binaural medullary neurons: Implications for binaural phenomena. *J. Acoust. Soc. Am.* **64**:493–501.
- Cumming BG & Parker AJ (1997). Responses of primary visual cortical neurons to binocular disparity without depth perception. *Nature* **389**:280–283.

- Dean I, Harper NS & McAlpine D (2005). Neural population coding of sound level adapts to stimulus statistics. *Nat. Neurosci.* **8**:1684–1689.
- Evans EF (2001). Latest comparisons between physiological and behavioural frequency selectivity. In *Physiological and psychophysical bases of auditory function*, ed. Breebaart DJ, Houtsma AJM, Kohlrauch A, Prijis VF & Schoonhoven R, 382–387. Maastricht: Shaker.
- Fitzpatrick DC, Batra R, Stanford TR & Kuwada S (1997). A neuronal population code for sound localization. *Nature* **388**:871–874.
- Funabiki K & Konishi M (2005). Intracellular Study of Auditory Coincidence Detector Neurons in Owls. *Assoc. Res. Otolaryngol. Abs.* **28**:43.
- Gabor D (1946). Theory of Communication. *J. Inst. Electr. Eng.* **93**:429–457.
- Goldberg JM & Brown PB (1969). Response of binaural neurons of dog superior olivary complex to dichotic tonal stimuli: some physiological mechanisms of sound localization. *J. Neurophysiol.* **32**:613–636.
- Gould AL (1969). A regression technique for angular variates. *Biometrics* **25**:683–700.
- Green DM & Swets JA (1974). *Signal Detection Theory and Psychophysics*. New York: Krieger.
- Grothe B & Sanes DH (1993). Bilateral inhibition by glycinergic afferents in the medial superior olive. *J. Neurophysiol.* **69**:1192–1196.
- Grothe B & Sanes DH (1994). Synaptic inhibition influences the temporal coding properties of medial superior olivary neurons: an in vitro study. *J. Neurosci.* **14**:1701–1709.
- Hahn SL (1996). *Hilbert transforms in signal processing*. Boston: Artech House.
- Hancock KE & Delgutte B (2004). A physiologically based model of interaural time difference discrimination. *J. Neurosci.* **24**:7110–7117.
- Harper NS & McAlpine D (2004). Optimal neural population coding of an auditory spatial cue. *Nature* **430**:682–686.
- Ingham NJ & McAlpine D (2004). Spike-frequency adaptation in the inferior colliculus. *J. Neurophysiol.* **91**:632–645.
- Ingham NJ & McAlpine D (2005). GABAergic inhibition controls neural gain in inferior colliculus neurons sensitive to interaural time differences. *J. Neurosci.* **25**:6187–6198.
- Jeffress LA (1948). A place theory of sound localisation. *J. Comp. Physiol. Psychol.* **41**:35–39.
- Johnson DH (1980). The relationship between spike rate and synchrony in responses of auditory-nerve fibers to single tones. *J. Acoust. Soc. Am.* **68**:1115–1122.
- Joris PX, Carney LH, Smith PH & Yin TC (1994a). Enhancement of neural synchronization in the anteroventral cochlear nucleus. I. Responses to tones at the characteristic frequency. *J. Neurophysiol.* **71**:1022–1036.
- Joris PX, Smith PH & Yin TC (1994b). Enhancement of neural synchronization in the anteroventral cochlear nucleus. II. Responses in the tuning curve tail. *J. Neurophysiol.* **71**:1037–1051.

- Joris PX & Yin TC (1992). Responses to amplitude-modulated tones in the auditory nerve of the cat. *J. Acoust. Soc. Am.* **91**:215–232.
- Joris PX (2003). Interaural time sensitivity dominated by cochlea-induced envelope patterns. *J. Neurosci.* **23**:6345–6350.
- Joris PX, Sande BVD & van der Heijden M (2005). Temporal damping in response to broadband noise. I. Inferior colliculus. *J. Neurophysiol.* **93**:1857–1870.
- Kapfer C, Seidl AH, Schweizer H & Grothe B (2002). Experience-dependent refinement of inhibitory inputs to auditory coincidence-detector neurons. *Nat. Neurosci.* **5**:247–253.
- Kopp-Scheinflug C, Lippe WR, Dörrscheidt GJ & Rübsamen R (2003). The medial nucleus of the trapezoid body in the gerbil is more than a relay: comparison of pre- and postsynaptic activity. *J. Assoc. Res. Otolaryngol.* **4**:1–23.
- Kuwada S, Fitzpatrick DC, Batra R & Ostapoff EM (2006). Sensitivity to interaural time differences in the dorsal nucleus of the lateral lemniscus of the unanesthetized rabbit: comparison with other structures. *J. Neurophysiol.* **95**:1309–1322.
- Louage DHG, Joris PX & van der Heijden M (2006). Decorrelation sensitivity of auditory nerve and anteroventral cochlear nucleus fibers to broadband and narrowband noise. *J. Neurosci.* **26**:96–108.
- Louage DHG, van der Heijden M & Joris PX (2004). Temporal properties of responses to broadband noise in the auditory nerve. *J. Neurophysiol.* **91**:2051–2065.
- Louage DHG, van der Heijden M & Joris PX (2005). Enhanced temporal response properties of anteroventral cochlear nucleus neurons to broadband noise. *J. Neurosci.* **25**: 1560–1570.
- Magnusson AK, Kapfer C, Grothe B & Koch U (2005). Maturation of glycinergic inhibition in the gerbil medial superior olive after hearing onset. *J Physiol* **568**:497–512.
- Marcelja S (1980). Mathematical description of the responses of simple cortical cells. *J. Opt. Soc. Am.* **70**:1297–1300.
- Mardia KV & Jupp PE (2000). *Directional Statistics*. Chichester: Wiley.
- Marquardt T & McAlpine D (2001). Simulation of binaural unmasking using just four binaural channels. *Assoc. Res. Otolaryngol. Abs.* **24**:87.
- McAlpine D, Jiang D & Palmer AR (1996). Interaural delay sensitivity and the classification of low best-frequency binaural responses in the inferior colliculus of the guinea pig. *Hear. Res.* **97**:136–152.
- McAlpine D, Jiang D & Palmer AR (2001). A neural code for low-frequency sound localization in mammals. *Nat. Neurosci.* **4**:396–401.
- McAlpine D, Jiang D, Shackleton TM & Palmer AR (1998). Convergent input from brainstem coincidence detectors onto delay-sensitive neurons in the inferior colliculus. *J. Neurosci.* **18**:6026–6039.
- McAlpine D & Palmer A (2002). Binaural Bandwidths of Inferior Colliculus Neurons Measured Using Interaurally-Delayed Noise. *Assoc. Res. Otolaryngol. Abs.* **25**:40.

- Mossop JE & Culling JF (1998). Lateralization of large interaural delays. *J. Acoust. Soc. Am.* **104** :1574–1579.
- Moushegian G, Rupert AL & Gidda JS (1975). Functional characteristics of superior olivary neurons to binaural stimuli. *J. Neurophysiol.* **38**:1037–1048.
- Nieder A & Wagner H (2000). Horizontal-disparity tuning of neurons in the visual forebrain of the behaving barn owl. *J. Neurophysiol.* **83**:2967–2979.
- Ohzawa I, DeAngelis GC & Freeman RD (1990). Stereoscopic depth discrimination in the visual cortex: neurons ideally suited as disparity detectors. *Science* **249**:1037–1041.
- Ohzawa I, DeAngelis GC & Freeman RD (1997). Encoding of binocular disparity by complex cells in the cat's visual cortex. *J. Neurophysiol.* **77**:2879–2909.
- Overholt EM, Rubel EW & Hyson RL (1992). A circuit for coding interaural time differences in the chick brainstem. *J. Neurosci.* **12**:1698–1708.
- Palmer AR, Shackleton TM & McAlpine D (2002). Neural mechanisms of binaural hearing. *Acoust. Sci. Tech.* **23**:61–68.
- Rayleigh, Lord (1907). On our perception of sound direction. *Philos. Mag.* **13**:214–232.
- Read JCA, Parker AJ & Cumming BG (2002). A simple model accounts for the response of disparity-tuned V1 neurons to anticorrelated images. *Vis. Neurosci.* **19**:735–753.
- Reyes AD, Rubel EW & Spain WJ (1996). In vitro analysis of optimal stimuli for phase-locking and time-delayed modulation of firing in avian nucleus laminaris neurons. *J. Neurosci.* **16**:993–1007.
- Rothman JS, Young ED & Manis PB (1993). Convergence of auditory nerve fibers onto bushy cells in the ventral cochlear nucleus: implications of a computational model. *J. Neurophysiol.* **70**:2562–2583.
- Rothman JS & Manis PB (2003a). Differential expression of three distinct potassium currents in the ventral cochlear nucleus. *J. Neurophysiol.* **89**:3070–3082.
- Rothman JS & Manis PB (2003b). Kinetic analyses of three distinct potassium conductances in ventral cochlear nucleus neurons. *J. Neurophysiol.* **89**:3083–3096.
- Rothman JS & Manis PB (2003c). The roles potassium currents play in regulating the electrical activity of ventral cochlear nucleus neurons. *J. Neurophysiol.* **89**:3097–3113.
- Sanger TD (1988). Stereo disparity computation using Gabor filters. *Biol. Cybern.* **59**:405–418.
- Scott LL, Mathews PJ & Golding NL (2005). Posthearing developmental refinement of temporal processing in principal neurons of the medial superior olive. *J. Neurosci.* **25**:7887–7895.
- Seidl AH & Grothe B (2005). Development of sound localization mechanisms in the Mongolian gerbil is shaped by early acoustic experience. *J. Neurophysiol.* **94**:1028–1036.
- Shackleton TM, McAlpine D & Palmer AR (2000). Modelling convergent input onto interaural-delay-sensitive inferior colliculus neurones. *Hear. Res.* **149**:199–215.

- Shackleton TM, Skottun BC, Arnott RH & Palmer AR (2003). Interaural time difference discrimination thresholds for single neurons in the inferior colliculus of Guinea pigs. *J. Neurosci.* **23**:716–724.
- Shamma SA, Shen NM & Gopaldaswamy P (1989). Stereausis: binaural processing without neural delays. *J. Acoust. Soc. Am.* **86**:989–1006.
- Shneiderman A & Oliver DL (1989). EM autoradiographic study of the projections from the dorsal nucleus of the lateral lemniscus: a possible source of inhibitory inputs to the inferior colliculus. *J. Comp. Neurol.* **286**:28–47.
- Siveke I, Pecka M, Seidl AH, Baudoux S & Grothe B (2006). Binaural response properties of low-frequency neurons in the gerbil dorsal nucleus of the lateral lemniscus. *J. Neurophysiol.* **96**:1425–1440.
- Skottun BC (1998). Sound localization and neurons. *Nature* **393**:531.
- Skottun BC, Shackleton TM, Arnott RH & Palmer AR (2001). The ability of inferior colliculus neurons to signal differences in interaural delay. *Proc. Natl. Acad. Sci. USA* **98**:14050–14054.
- Slee SJ, Higgs MH, Fairhall AL & Spain WJ (2005). Two-dimensional time coding in the auditory brainstem. *J. Neurosci.* **25**:9978–9988.
- Smith PH (1995). Structural and functional differences distinguish principal from nonprincipal cells in the guinea pig MSO slice. *J. Neurophysiol.* **73**:1653–1667.
- Smith PH, Joris PX & Yin TC (1993). Projections of physiologically characterized spherical bushy cell axons from the cochlear nucleus of the cat: evidence for delay lines to the medial superior olive. *J. Comp. Neurol.* **331**:245–260.
- Smith PH, Joris PX & Yin TC (1998). Anatomy and physiology of principal cells of the medial nucleus of the trapezoid body (MNTB) of the cat. *J. Neurophysiol.* **79**:3127–3142.
- Spitzer MW & Semple MN (1995). Neurons sensitive to interaural phase disparity in gerbil superior olive: diverse monaural and temporal response properties. *J. Neurophysiol.* **73**:1668–1690.
- Svirskis G, Kotak V, Sanes DH & Rinzel J (2002). Enhancement of signal-to-noise ratio and phase locking for small inputs by a low-threshold outward current in auditory neurons. *J. Neurosci.* **22**:11019–11025.
- Svirskis G, Kotak V, Sanes DH & Rinzel J (2004). Sodium along with low-threshold potassium currents enhance coincidence detection of subthreshold noisy signals in MSO neurons. *J. Neurophysiol.* **91**:2465–2473.
- Tollin DJ & Yin TCT (2005). Interaural phase and level difference sensitivity in low-frequency neurons in the lateral superior olive. *J. Neurosci.* **25**:10648–10657.
- Tsuchitani C (1977). Functional organization of lateral cell groups of cat superior olivary complex. *J. Neurophysiol.* **40**:296–318.
- Wagner H & Frost B (1993). Disparity-sensitive cells in the owl have a characteristic disparity. *Nature* **364**:796–798.

- Wagner H, Mazer JA & von Campenhausen M (2002). Response properties of neurons in the core of the central nucleus of the inferior colliculus of the barn owl. *Eur. J. Neurosci.* **15**:1343–1352.
- Yin TC & Chan JC (1990). Interaural time sensitivity in medial superior olive of cat. *J. Neurophysiol.* **64**:465–488.
- Yin TC, Chan JC & Carney LH (1987). Effects of interaural time delays of noise stimuli on low-frequency cells in the cat's inferior colliculus. III. Evidence for cross-correlation. *J. Neurophysiol.* **58**:562–583.
- Yin TC, Chan JC & Irvine DR (1986). Effects of interaural time delays of noise stimuli on low-frequency cells in the cat's inferior colliculus. I. Responses to wideband noise. *J. Neurophysiol.* **55**:280–300.
- Young SR & Rubel EW (1983). Frequency-specific projections of individual neurons in chick brainstem auditory nuclei. *J. Neurosci.* **3**:1373–1378.
- Zhou Y, Carney LH & Colburn HS (2005). A model for interaural time difference sensitivity in the medial superior olive: interaction of excitatory and inhibitory synaptic inputs, channel dynamics, and cellular morphology. *J. Neurosci.* **25**:3046–3058.